TOWARDS LIGHT SHEET MICROSCOPY-BASED HIGH THROUGHPUT IMAGING AND CRISPR OPTOGENETICS

Federico Maria Gasparoli

A Thesis Submitted for the Degree of PhD
at the
University of St Andrews

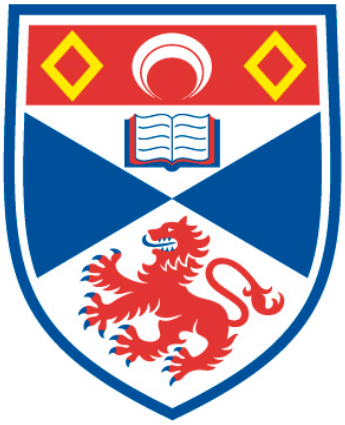

2018

Towards Light Sheet Microscopy-based High Throughput Imaging and CRISPR Optogenetics

Federico Maria Gasparoli

University of
St Andrews

This thesis is submitted in partial fulfilment for the degree of

Doctor of Philosophy (PhD)

at the University of St Andrews

October 2018

Declaration

Candidate's declaration

I, Federico Maria Gasparoli, do hereby certify that this thesis, submitted for the degree of PhD, which is approximately 45,000 words in length, has been written by me, and that it is the record of work carried out by me, or principally by myself in collaboration with others as acknowledged, and that it has not been submitted in any previous application for any degree.

I was admitted as a research student at the University of St Andrews in September 2014.

I received funding from an organisation or institution and have acknowledged the funder(s) in the full text of my thesis.

Date Signature of candidate

Supervisor's declaration

I hereby certify that the candidate has fulfilled the conditions of the Resolution and Regulations appropriate for the degree of PhD in the University of St Andrews and that the candidate is qualified to submit this thesis in application for that degree.

Date Signature of supervisor

Permission for publication

In submitting this thesis to the University of St Andrews we understand that we are giving permission for it to be made available for use in accordance with the regulations of the University Library for the time being in force, subject to any copyright vested in the work not being affected thereby. We also understand, unless exempt by an award of an embargo as requested below, that the title and the abstract will be published, and that a copy of the work may be made and supplied to any bona fide library or research worker, that this thesis will be electronically accessible for personal or research use and that the library has the right to migrate this thesis into new electronic forms as required to ensure continued access to the thesis.

I, Federico Maria Gasparoli, confirm that my thesis does not contain any third-party material that requires copyright clearance.

The following is an agreed request by candidate and supervisor regarding the publication of this thesis:

Printed copy

Embargo on all of print copy for a period of 3 years on the following ground(s):

- Publication would preclude future publication

Supporting statement for printed embargo request

Publication would preclude further publication. I aim of publishing this work within a 3 years period.

Electronic copy

Embargo on all of electronic copy for a period of 3 years on the following ground(s):

- Publication would preclude future publication

Supporting statement for electronic embargo request

Publication would preclude further publication. I aim of publishing this work within a 3 years period.

Title and Abstract

- I require an embargo on the title and abstract but I understand that the title will be used in the graduation booklet.

Date Signature of candidate

Date Signature of supervisor

Underpinning Research Data or Digital Outputs

Candidate's declaration

I, Federico Maria Gasparoli, hereby certify that no requirements to deposit original research data or digital outputs apply to this thesis and that, where appropriate, secondary data used have been referenced in the full text of my thesis.

Date Signature of candidate

Acknowledgments

To my supervisor Dr Paul Reynolds for his helpful advice and availability. Thank you for making my writing process such an enjoyable experience.

To Professor Frank J. Gunn-Moore for his support and suggestions.

To Dr Maciej Antkowiak, I am grateful for the opportunity you have given to me. Starting my PhD by your side taught me a lot more than I could have ever imagined. I have learned from you to innovate as a scientist and that science should always be viewed from a broad and multidisciplinary perspective.

To Rebeca, thank you for the countless discussions and brainstorming sessions which empowered my ability to generate original ideas.

To Wardiya, who motivated me and lifted my expectations through these pasts few years. Working with you inspired me and this journey would not have been the same without you.

Finally, to my parents and my sister Martina, there are no words to describe how thankful I am for your presence and encouragement through this adventure.

Funding

This work was supported by the University of St Andrews Ashworth Legacy and the Wellcome Trust Institutional Strategic Support Fund (ISSF).

Abstract

High Throughput Imaging (HTI) has an important role in the High Throughput/Content Screening process (HTS/HCS). It is widely used in the drug discovery process and in a wide range of other applications including studies focused on cell cycle, cell proliferation, cell migration, apoptosis, protein expression, protein localization, signalling pathways or stem cell development and differentiation. Nowadays, most of the HCS experiments are performed on two-dimensional (2D) monolayer of cells cultured on planar plastic substrates which do not reflect the complex 3D architecture of a living tissues where the cells interact between each other and with the ExtraCellular Matrix (ECM). Currently, the state-of-the-art HCS systems that can be used for high throughput imaging of 3D cell culture models are based on confocal microscopy. Even though very efficient, these machines can reach the million-dollar price and thus might be affordable to big industry and phenotypic screening centres but not to most of smaller realities such as academic laboratories. This thesis project proposes a solution to link light sheet microscopy, one of the best techniques for the imaging of 3D cell culture models, with the currently available HTS/HCS platforms: the development of the affordable and user-friendly HT-LISH microscope first prototype have the potential to offer automated light sheet microscopy-based HTI capabilities for the study of 3D samples to industries, screening centres and also to smaller laboratories, where a lower throughput level is eventually required.

Another important part of this PhD thesis is focused on CRISPR-based genome editing which during the recent decades has become an invaluable tool in cell and tissue biology. CRISPR interference (CRISPRi) and activation (CRISPRa) systems have been developed to allow the users to up-or down-regulate any gene of interest in a relative simple manner. Even though emerged as powerful techniques to regulate the gene expression levels, these tools lack in spatiotemporal resolution. In order to study and understand genetic patterns specific to a certain type of tissue it is important to achieve a precise control over the CRISPRi/a systems so that they can be selectively targeted to small populations of cells (spatial resolution) or be activated and de-activated at will (temporal resolution). This work, describes the development and the characterization

of the Red Light CRISPR system, a novel CRISPR-based tool for precise gene regulation experiments that relies on the interaction of the Phytochrome B (PhyB) and Phytochrome-Interacting Factor 6 (PIF6), two light sensitive protein from the plant *Arabidopsis Thaliana* that dimerize under red light at 660 nm and separate when illuminated with infrared light at 740 nm. The Red Light CRISPR system fuses together the non-invasive and highly spatiotemporal resolved technique of optogenetics with the "easy to use" and efficient CRISPR approach. This system is thus joining the already available range of optogenetics tools that enable a precise spatiotemporal control of the CRISPR system and, in particular, it introduces for the first time a red/infrared light-based CRISPR inducible system.

Table of Content

List of Figures

List of Tables

Chapter 1

Introduction

1.1 List of Abbreviations

1.2 High Throughput and High Content Screening

1.3 High Content Screening, Three-Dimensional Cell Culture Models and Light Sheet Microscopy

1.4 The Clustered Regularly Interspaced Short Palindromic Repeats (CRISPR) System

1.5 The Clustered Regularly Interspaced Short Palindromic Repeats (CRISPR) System and Optogenetics

1.6 Summary of the Aims of this Work

1.1 List of Abbreviations

2D - Two-Dimensional
3D - Three-Dimensional
Cas - CRISPR-associated protein
cr-RNAs - CRISPR-RNAs
CRISPR - Clustered Regularly Interspaced Short Palindromic Repeats
CRISPRa - CRISPR activation
CRISPRi - CRISPR interference
crRNAs - CRISPR RNAs
dCas9 - “dead” Cas9
ECM - ExtraCellular Matrix
gRNA - guide RNA
HCA - High Content Analysis
HCS - High Content Screening
HT-LISH - High Throughput Light Sheet Microscope
HTI - High Throughput Imaging
HTS - High Throughput Screening
KRAB - KRuppel Associated Box
NM - Neisseria meningitides
PAM - Protospacer Adjacent Motif
PhyB - Phytochrome B
PIF6 - Phytochrome-Interacting Factor 6
pre-crRNAs - pre-CRISPR RNAs
Sa - Staphylococcus Aureus
SP - Streptococcus Pyogenes
SPIM - Single/Selective Plane Illumination Microscope
ST - Streptococcus Thermophilus
TALEN - Transcription Activator-Like Effector Nucleases
tetO - Tetracycline Operator
TetR - Tetracycline Repressor
tracrRNA - trans-activating crRNA
WT - Wild Type
ZFNs - Zinc Fingers

1.2 High Throughput and High Content Screening

High throughput screening or HTS is a technology developed in the 1980s by the pharmaceutical sector mainly for the drug discovery process [1]. This concept was born to overcome the very low throughput that could be achieved by traditional biochemical and pharmacological methods where only 20 to 50 compounds could be screened per week [1]. With the evolution of technology in both hardware and software, HTS became a practical method for the automated screening of a large number of synthetic compounds in a relatively short period of time with the aim of identify those capable of interacting with the target of interest [1]. At the beginning of the 1990s, the main focus of this approach was stressed on the speed of the HTS platforms; the goal was to screen as many compounds in the shortest time as possible. Therefore, there was the idea that the best systems were those with the highest reading speed [2]. The traditional samples used were homogeneous solutions of synthetic compounds screened against pre-selected protein targets analysed with a simple "mix and read" approach [2]. In order to extract more meaningful information from the screening process, cell-based assays in multi-well plates were later developed [2] consisting in the limited measurement in parallel of one or two averaged signals from the population of cells grown in each well [3, 4]. This approach was thus excluding from the readout any possible difference occurring between single cells [3, 4]. Over the years, the HTS did not have the expected huge impact in the drug discovery process as the productivity have seen a decrease in the number of successfully developed drugs reaching the pharmaceutical market [5, 6]. There was therefore the need of implementing the screening process with a new approach that could allow for more sophisticated automated cell-based high throughput assays where a multi-parametric analysis could be focused at a single cell level. One of the key protagonist that enabled the achievement of such challenging approach was the rapidly expanding field of fluorescence microscopy [7]. Hardware technological advances led to the development of fast, automated High Throughput Imaging (HTI) systems that were relying on fluorescence as source of information. Single cells phenotypes could be simply visualized with fluorescence proteins or markers [8]. The novel HTI in combination with the high throughput technologies and the development

of multi-parametric automated analysis systems (High Content Analysis - HCA) gave birth to the concept of the High Content Screening (HCS) also defined as phenotypic screening [7, 9]. In HCS, a large dataset of fluorescent images is acquired and analysed in a fully automated process and the information extracted can lead to the generation of precise phenotypic maps of each single cell [9]. It is interesting to mention that the majority of the "New Molecular Entities" (NMEs - molecules that have not been previously approved/evaluated) approved by the US FDA (Food and Drug Administration) between 1999 and 2012 were discovered following the phenotypic screening approach applied in drug screening studies; several of these molecules related to the oncology, neuroprotection, antiviral, and inflammation areas are advancing in the clinical trials [10]. The phenotypic profiles obtained with the HCS approach can elucidate physiologic or disease mechanisms as a consequence of for instance drug treatments or genetic perturbations [2, 9]. The readout is not limited to a maximum of two features in parallel but the combined use of the wide range of fluorescent proteins/markers nowadays available can lead to the simultaneous evaluation of multiple parameter for each single cell in one single assay [9, 11]. Moreover, the introduction of environmental chambers on the HTI stations, allows to perform live-cell imaging experiments [9], thus enabling the study of cellular processes that are regulated in a spatiotemporal-dependent manner [2, 9]. HCS is having an important impact in the entire drug discovery and development pipeline which aims to evaluate the activity, safety and toxicity of possible novel therapeutic compounds on *in vitro* cultures [2, 12, 13]. This cell-based approach has the potential to extract deeper and so more meaningful information than the traditional methods with a direct consequence of better selecting promising drug candidates and thus reducing the expenses of the entire drug discovery process because the costs are increasing as a compound proceeds in the pipeline [2, 12].

HTI combined with HCA has not been limited to the drug discovery process but it has been implemented for several applications including, among others, assays focused on the study of cell cycle, cell proliferation, cell migration, apoptosis, protein expression, protein localization, signalling pathways or stem cell development and differentiation [2, 11-13].

Figure 1 summarises the main components of the entire HCS process.

The first step is to define the question(s) that needs to be answered by the assay (Figure 1). The goal is to design an experiment that gives a multi-parametric phenotypic readout that is reproducible and scalable [7]. This process includes for instance the choice of the

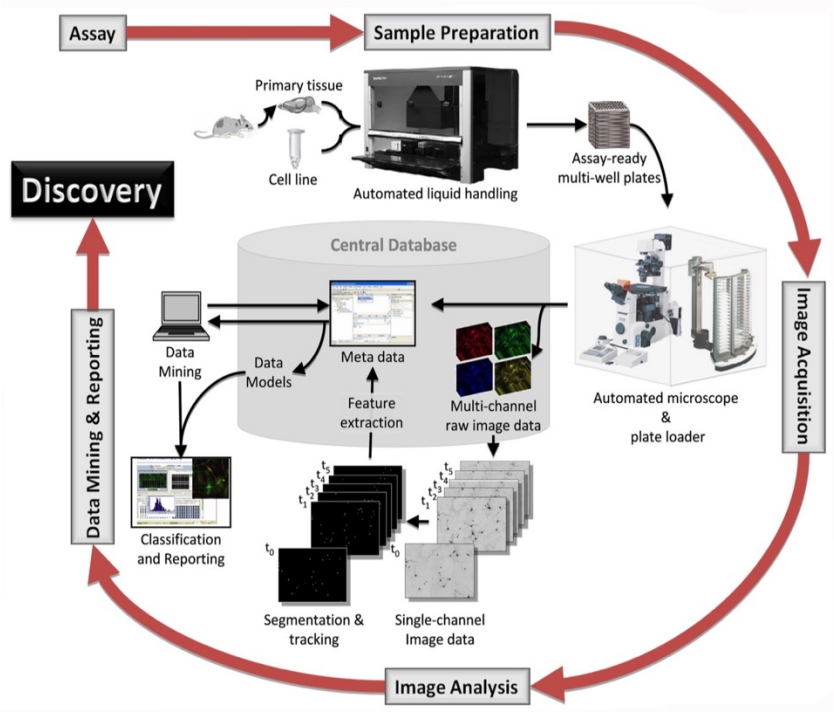

Figure 1 - Schematic summary of the main components of the High Content Screening approach. From [9].

cell type, the well plate format, if live of fixed cells are required, the experimental timescale, and the fluorophores to label the targets of interest [4, 7, 9]. Because HCS is a multi-parametric method that relies on multiple fluorescence markers, it is fundamental to evaluate the fluorophores spectral overlap together with their compatibility with the excitation light source(s) and the filter sets available on the high throughput imaging platform that will be used for the screening [4, 7]. Before starting the whole experiment, it is necessary to perform a preliminary pilot small-scale test aiming to assess the robustness of the assay and its feasibility in a high throughput manner (large scale) [4, 7, 9]. Once all the parameters are established, the next step is to automate the assay for the HCS process. Automation is the key features for a large scale high throughput approach as the other HCS steps, sample preparation, image acquisition and image analysis (Figure 1), must be performed in a fully automated

manner. During the sample preparation, it is fundamental to minimise any technical variation in-between the large number of samples for instance in terms of cell number, reagents volumes and staining procedures [4]. Therefore, this HCS step is usually performed with liquid-handling robots that precisely prepare the multi-well plates with high efficiency and reproducibility [4, 9]. Robotic arms then transfer one by one the multi-well plates to the high throughput imaging platform to perform the next essential and crucial HCS step of automated image acquisition. Image resolution, magnification and field(s) of view together with focus and exposure time for each fluorescence channel must be precisely determined depending on the sample that is used and the features that need to be characterized [4]. The high throughput microscope will thus acquire several images for each multi-well plate in an automated manner. All the data/images have to be then transferred, stored and analysed in order to extract meaningful biological information from the assay [4, 7, 9]. Automated Image analysis includes image processing, object segmentation, cell tracking, intensity or textures measurements, feature extraction and statistical analysis [4, 7, 9]. All these parameters can be then translated in a precise phenotypic cells characterization (appearance, development, behaviour, ...) that can possibly elucidate the biological questions that were designed in the assay [4, 7, 9].

This thesis will be focusing on the image acquisition step of the HCS process describing the development of a high throughput imaging system prototype based on light sheet microscopy.

1.3 High Content Screening, Three-Dimensional Cell Culture Models and Light Sheet Microscopy

Nowadays, most of the HCS experiments are performed on two-dimensional (2D) monolayer of cells cultured on planar plastic substrates [2, 14-16]. Over the years, due to their simplicity, the screenings on 2D cell cultures have proven to be a convenient model to test possible drug candidates and are still useful in the discovery process [15, 16]. However, it is commonly accepted that these 2D planar systems are considerably different when compared to the complex three-dimensional (3D) architecture of human tissues and organs [17-21]. In natural tissues, different cells types assume polarized structures and interact with each other and with the variety of proteins present in the extracellular matrix (ECM). This synergistic interplay is fundamental to define the properties and the functions of tissues [17, 22-25]. Cell culture monolayers do not maintain these 3D features and therefore, in order to extract more meaningful information and thus produce better outcomes from HCS experiments, the use of more complex 3D cell culture models that better mimic the physiology of human tissues have to be considered. Currently, there is a vast range of biologically-relevant 3D models available; this group includes among others permeable membranes filter inserts, scaffold-based models, microcarriers, cellular spheroids or organoids [16, 17, 26]. They vary depending on their complexity/tissue similarity and their possible use in automated screening experiments [16, 17, 26]. Therefore, different 3D models are more indicated for different cell-based studies. For instance, cellular and multi-cellular spheroids started gaining popularity in HTS/HCS to model and study cancer [15, 16, 21, 27]. They are aggregates of cells that form a heterogeneous environment with physiological cell-cell and cell-extracellular matrix (ECM) interactions. As in cancer, spheroids express different gradients of oxygen, nutrients and metabolites. These 3D models have also a gene expression pattern very similar to the one found in cancer tissues [15-17, 27].

One of the most advanced form of *in vitro* 3D cell culture models are the organoids, 3D organ-specific cells aggregates derived from primary or stem cells cultures that are able to self-organise in organ-like structures[28]. Organoids have been demonstrated to exhibit various levels of organ-specific 3D architectures and functions and can therefore

be considered as highly suitable models for translational studies and 3D phenotypic screenings [28]. The development and use of more biologically-relevant 3D models evidently requires dedicated microscopy techniques as conventional imaging platforms that are perfect for thin 2D cells monolayers do not possess sufficient volumetric imaging capabilities [21, 29]. The main issues when imaging 3D cell culture models with fluorescence microscopy are for instance related to the samples dimension and optical density: thick specimens have highly scattering properties that may prevent the light to penetrate in depth [18, 29, 30]. In addition, fluorophores photobleaching and light-induced phototoxicity (mostly if live fluorescence imaging is required) must be considered [18, 29, 30]. These microscopy-related issues become more challenging in HTS/HCS as the whole imaging process needs to be fully automated.

In the high throughput imaging (HTI) platforms and more in fluorescence microscopy, in order to perform a significant post-acquisition quantitative analysis and to extract phenotypic features from the 3D culture models, an automated fluorescent microscope requires among others optical section capabilities, a high signal-to-noise ratio, fast image acquisition of multiple fluorescence channels and low photobleaching; if biological processes need to be followed over time, low phototoxicity is a requirement and the microscopes have to be equipped with environmental control chambers [18, 27, 31].

Currently, the state-of-the-art HCS systems that can be used for high throughput imaging of 3D cell culture models are based on confocal microscopy [2, 27]. In this technique, optical sectioning is achieved by using pinholes that block out-of-focus light. Examples are the PerkinElmer's Operetta and Opera Phenix or the BD Biosciences's BD Pathway, advanced HTI platforms based on confocal spinning disk design that offer automated, high resolution and fast acquisition of 3D models [27]. Even though the available HTI systems enable efficient HTS/HCS applications, the cost of these machines can be very high and reach the million dollars price [2]. In addition, they are developed to achieve a very high throughput that might be necessary for screening experiments performed by pharmaceutical industries or phenotypic screening centres but not for smaller realities such as for instance in academia.

Therefore, due to the elevated cost and throughput, these HTI platforms might be easily accessible to big pharmaceutical industries or phenotypic screening centres but probably not to academic laboratories.

Even though most of the 3D HTI systems are based on confocal microscopy, this is not the only technique suitable for the imaging of 3D cell culture models. The 2014 Nature *methods of the year* light sheet fluorescence microscopy is demonstrating to be an optimal technique for the imaging of "living sample in three dimensions with relatively low phototoxicity and at high speed" [32, 33].

Light sheet fluorescence microscopy is a wide-field microscopy technique where illumination and detection are performed through two distinct and orthogonal optical pathways. There are two independent objectives placed at 90 degrees to each other: the first, illumination objective, is used to illuminate the specimen with a thin sheet of laser light and the second, detection objective, is used to collect the fluorescence coming from the sample (Figure 2A). Importantly, the illuminated plane is precisely aligned with the focal plane of the detection pathway so that the specimen is excited only in a thin, well-defined plane imaged in focus by the detection objective (Figure 2B). As a result, a precise optical sectioning is achieved as the out-of-focus light is drastically

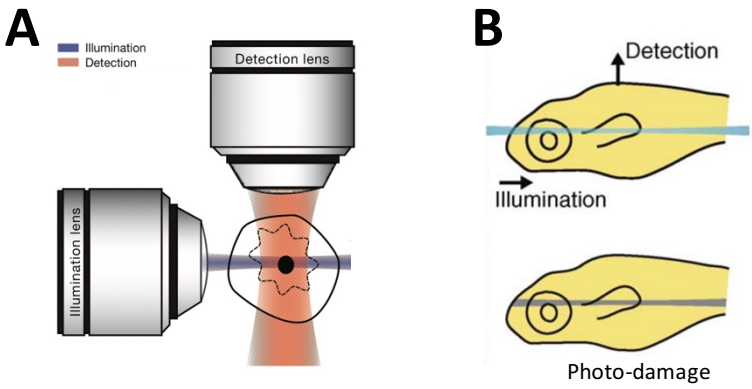

Figure 2 - Light Sheet Fluorescence Microscopy principle. (A) In light sheet microscopy, an illumination and a detection objective are placed at 90 degrees to each other and are used to illuminate the sample with a thin sheet of laser light (Illumination objective) and to collect the fluorescence coming from the specimen illuminated plane (detection objective). The illuminated plane is precisely aligned with the focal plane of the detection objective. The sample is placed precisely at the intersection of the two orthogonal pathways. Adapted from [41] (B) The illumination strategy with a thin sheet of light results in a precise optical sectioning of the sample only at the focal plane of the detection objective: the out of focus light is drastically limited and therefore also photobleaching and mostly light photo-damage are significantly reduced. Adapted from [31].

limited; thus, also photo-damage and photobleaching are significantly reduced (Figure 2B) enabling imaging over long periods of time [33-37]. This is a huge advantage of light sheet compared to confocal microscopy. In this latter, optical sectioning is achieved with the use of one or more (in spinning disk systems) pinhole(s) that remove the out-of-focus light. However, for each frame acquired, the sample is always illuminated below and above the focal plane of the objective. When considering the acquisition of a sample volume, it means that each plane of the specimen is illuminated multiple times within the 3D scan and this can lead to unwanted photobleaching and/or phototoxicity.

In most of the light sheet microscopy configurations, the sample is placed at the intersection of the two orthogonal pathways (Figure 2A): by scanning the entire specimen through the light sheet (or the light sheet through the sample in more advanced systems), for each position, single 2D images can be acquired and then processed to obtain one final highly resolved 3D image. In most of the light sheet microscopes, the sample can also be rotated around its axis and thus images of different angles can be acquired [33, 35, 38]. The basic light sheet fluorescence microscopy system is called SPIM or Single/Selective Plane Illumination Microscope [39] and it can be easily assembled following the open source instructions from the OpenSPIM project web site [40, 41] (http://openspim.org/). As shown in Figure 3, the basic SPIM building unit [42] is composed of four main parts: (1) the illumination unit, which include one or more laser light sources, the illumination objective and a cylindrical lens coupled with an aperture slit, both necessary for the generation of a thin sheet of light; (2) the detection unit, that is placed orthogonally in respect to the illumination unit and includes the detection objective, fluorescence emission filter(s) and a CCD camera; (3) the stage unit, which includes a sample chamber that holds the specimen at intersection of the illumination and detection optical paths and allows for its movements (x, y, z and rotation); and finally (4) the control unit, which comprises a computer and the software to control all the microscope components. Over the years, because of its simple geometry and versatility of the design, light sheet microscopy has undergone a large number of implementations aiming at increasing resolution, penetration depth, field of view, acquisition speed and more [33, 43]. This technology is emerging as one of the

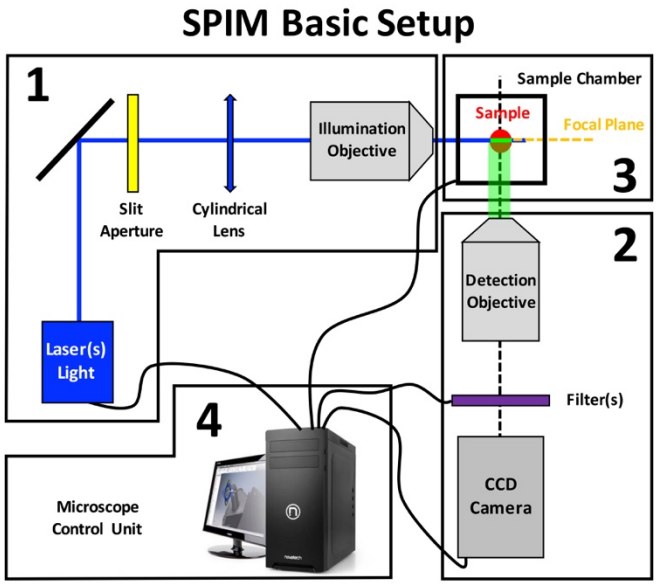

Figure 3 - Diagram of the basic building unit of the Single/Selective Plane Illumination Microscopy (SPIM). (1) Illumination unit, which include one or more laser light sources, the illumination objective and a cylindrical lens coupled with an aperture slit, both necessary for the generation of a thin sheet of light. (2) Detection unit, that is placed orthogonally in respect to the illumination unit and includes the detection objective, fluorescence emission filter(s) and a CCD camera. (3) Stage unit, which includes a sample chamber that holds the specimen at intersection of the illumination and detection optical paths and allows for its movements (x, y, z and rotation). (4) Control unit, which comprises a computer and the software to control all the microscope components.

most suitable microscopy technique for the imaging of 3D cell culture models [27] however, when this thesis project started in 2014, light sheet microscopy had not yet been successfully applied to HTI for the automated screening of biologically-relevant complex 3D models. One possible explanation can be found in the orthogonal design of most of the light sheet microscopes: as mentioned before, two objectives are placed at 90° from each other and are used for the illumination of the sample and for the collection of the emitted fluorescence signal (Figure 2A). In addition, the specimen must be inserted exactly at intersection of the two orthogonal optical paths (Figure 2A). Therefore, in order to reach an HTI approach, the difficult challenge is to introduce an automated loading of multiple samples in-between the two objectives. As described later in this thesis (Chapter 2 - Section 2.2), a first attempt towards the development of a light sheet microscope with high throughput capabilities was made by Gualda *et al*. with the SPIM-Fluid [44]. Their design is based on fluidics, a technology focused on the study and manipulation of fluids at the milli-micrometre scale, and flow cytometry. Throughout a controlled pump system, the samples are first loaded into a tube mounted

between the illumination and detection objectives in the sample chamber and then scanned one at a time through the light sheet. In this way, the entire volume of the specimens can be acquired in a fast manner allowing the microscope to be potentially used in high throughput studies [44]. However, the precise control of this fluidic approach, the positioning of the samples as well as for instance the treatment of the specimens with different drugs at different concentrations might be challenging key features that have to be considered. Moreover, the SPIM-Fluid is a system specifically designed for this purpose and it is not compatible with any of the already existing High Throughput/Content Screening (HTS/HCS) platforms. On the contrary, one of the aim of this thesis project was to find a solution to link light sheet microscopy and 3D cell culture models with the currently available HTS/HCS systems. In this work, the design and the development of a High Throughput Light Sheet Microscope prototype named HT-LISH is reported. The HT-LISH microscope capabilities in terms of 3D and high throughput imaging will be described. As in most of the HTS/HCS platforms, the system allows for a fast and automated scan of single or multiple 3D samples in commercially available multi-well plate formats. The HT-LISH microscope prototype is compatible with any currently available inverted microscope; it can be seen as an external box of limited size that can be easily attached to any inverted microscope from one of its side ports. This approach can introduce high throughput capabilities for the screening/imaging of 3D models while maintaining a conventional epi-fluorescent function if needed. Inverted microscopes are widely spread in most of the academic laboratories and also in various microscopy based high throughput stations used by industries or phenotypic screening centres. This “add-on” feature together with its reduced costs compared to the currently state-of-the-art HTI systems have the potential to offer automated HTI capabilities for the study of biologically-relevant 3D models also to smaller laboratories where a lower throughput level is eventually required.

1.4 The Clustered Regularly Interspaced Short Palindromic Repeats (CRISPR) System

During the recent decades genome editing has become an invaluable tool in cell and tissue biology. In this experimental approach, a gene of interest is silenced or a section of DNA is, inserted, replaced, or removed from the genome. Typically, it is used to interfere with the original expression level, structure or function of the gene-encoded protein and to study the effects of this modification in order to understand the gene/protein function in a biological process [45]. In genome engineering, small genomic insertion or deletion, gene integration or knockdown, gene regulation as well as generation of transgenic animals can be achieved. The application of genome editing techniques to study human biology processes can lead to a better understanding of human pathologies and therefore to the further development of new disease treatment focused on gene therapy [46, 47]. The recently discovered Type II Clustered Regularly Interspaced Short Palindromic Repeats (CRISPR)/CRISPR-associated protein 9 (Cas9) system can provide a flexible, efficient and simple to use molecular biology tool that covers several genome engineering strategies, from gene disruption to gene regulation [45].

The history of the CRISPR/Cas system goes back to 2002, when Leo Schouls of the National Institute of Public Health in Bilthoven and his colleagues identified the CRISPR sequences in the bacteria genome, short conserved repeated sequences interspaced by non-repetitive sequences named spacers [48]. In 2005, Haft *et al.* described the implication of the CRISPR-associated proteins (Cas) in the CRISPR system [49] and then, in 2007, scientists from Danisco provided the first biological evidence for its function: they found that the CRISPR system was a type of bacteria defence mechanism by showing that it was possible to modify the resistance of *Streptococcus Thermophilus* (ST) to phages by simply adding or deleting spacers DNAs complementary to the phages genome [48, 50, 51]. Currently, we know that the CRISPR/Cas system is indeed a bacteria/archaea adaptive immune system which provides resistance against invading genetic elements such as viruses and phages [45, 52]. In general, in bacteria and archaea the CRISPR complex recognises an invading foreign DNA through CRISPR RNAs (crRNAs) and cleaves it through the Cas proteins [45, 53]. This defence mechanism can be divided

in three stages [45, 52]. The CRISPR loci contain conserved repeated sequenced interspaced by protospacers which are generated during the first “adaptation” phase of the defence mechanism. The Cas proteins process the invading foreign genomes in small DNA sequences which are then integrated in the CRISPR loci as protospacers between two repeated sequences [45, 52, 53]. Typically, a very short sequence (3-6 nt) located next to the protospacer in the foreign DNA called Protospacer Adjacent Motif (PAM) is necessary for the generation/integration of the protospacer in the CRISPR loci [45, 54, 55]. In the second stage, called “CRISPR Expression”, pre-CRISPR RNAs (pre-crRNAs) are transcribed and then cleaved in CRISPR-RNAs (cr-RNAs) from the CRISPR loci on the base of its protospacers [45, 52, 56]. In the third stage, called “interference”, if a crRNA matches an invading foreign DNA region, the CRISPR complex is activated and the foreign nucleic acid is specifically recognized and bound by the crRNA-CRISPR complex and then cleaved by the Cas proteins; the absence of the PAM sequence in the CRISPR locus prevents any self-cleaving activity [45, 52, 56].

From the analysis of various bacteria and archaea species, more than 40 different Cas protein families were identified [49]. While in the adaptation phase of the CRISPR/Cas system the Cas proteins involved are conserved (Cas1 and Cas2) in the other two stages they change depending on the prokaryotic species. Based on these variances, the CRISPR/Cas system is classified in three different types: type I, type II and type III [57].

In the type I and type III systems (which are similar to each other) specialised Cas endonucleases process the pre-crRNAs in mature crRNAs: each crRNA is then assembled into a multi-Cas complex with the ability to recognise, bind and cleave the invading foreign DNA complementary to the crRNAs sequences [57, 58]. The type II system, however, works with a different mechanism in which a trans-activating crRNA (tracrRNA) binds to the repeated sequences of pre-crRNA forming a “dual RNA” tracrRNA-crRNA; this complex is processed by the double-stranded (ds) RNA-specific ribonuclease RNase III together with a Cas protein called Cas9 and the invading foreign dsDNA is then cleaved in both its sense and anti-sense strands (Double Strand Brakes) [57, 58].

In genome engineering (in bacterial, mammalian and plant cells), the type II mechanism was demonstrated to be the simplest and therefore the most popular of the CRISPR/Cas system types as its activity is performed by a single protein, Cas9, which is only guided by a dual tracrRNA-crRNA. [45, 58-60]. Moreover, the actual application of this system was made easier by Martin Jinek *et al.* [58] who designed a chimeric guide RNA (gRNA) containing the essential part of both tracrRNA and crRNA and thus able to directly guide the CRISPR/Cas9 complex.

Therefore, the only necessary parts of the type II CRISPR/Cas9 system for genome engineering experiments are the Cas9 protein and the gRNAs which can be targeted to any specific sequence in the genome of interest. It follows that the type II CRISPR/Cas9 system is the most widely used in genome engineering [45]. Importantly, different bacteria species code for different Cas9 proteins that respond to specific gRNAs.

The gRNAs are normally composed of 20 nucleotides that perfectly match the sequence of the target DNA of interest. For instance, a gRNA sequence can be found in the form 5'-G**NNNNNNNNNNNNNNNNNNNN**NGG-3' where NGG (in red) is the PAM sequence (in the DNA target) and the **N**s in bold represents the gRNA nucleotides sequences. As mentioned before, the PAM (Protospacer Adjacent Motif) is a conserved sequence that has to be present downstream the DNA target sequence to allow the CRISPR system to recognise and bind the DNA target. As for Cas9, the PAM sequence is different and Cas9-specific depending on the bacteria species: for instance, NGG in *Streptococcus Pyogenes* (SP) can drive only SPCas9, NNAGAAW in *Streptococcus Thermophilus* (ST) can drive only STCas9, NNGRRT in *Staphylococcus Aureus* (Sa) can drive only SaCas9 or NNNNGATT in *Neisseria Meningitides* (NM) can drive only NMCas9 [53, 61, 62]. Therefore, these Cas9-gRNA pairs can be used in combination to achieve orthogonal genome engineering capabilities [53, 62]. In order to be functional, the gRNA expression plasmid has to contain the following essential components: the U6 RNA Polymerase III promoter, the gRNA protospacer sequence, a scaffold and a terminator [58, 63, 64]. While the gRNA sequence has to be chosen and designed specifically for the gene of interest, the other parts can be found in the published and widely available plasmids. The Cas9 from *Streptococcus Pyogenes*, SPCas9 (with its specific gRNA), is the most commonly used

[45]. The Cas9 protein(s) contains two endonuclease domains, a HNH nuclease domain which cleaves the DNA strand complementary to the gRNA sequence, and a RuvC-like nuclease domain that cleaves the non-complementary DNA strand [45, 58]. This Wild Type (WT) version of Cas9 has been widely used in genome editing for instance to perform gene knockout or knockin experiments in both *in vitro* and *in vivo* [45, 53, 65]: the cleavage activity of Cas9 allows to disable or modify the targeted genes of interest in order to analyse their function(s) in normal or diseased states. Importantly, over the years the CRISPR system and thus the Cas9 proteins (or the gRNAs) has been engineered to perform several different experiments that do not entirely exploit the cleaving activity of this tool. An interesting and promising approach involved the mutations (D10A and H840A) of both the HNH and RuvC-like nuclease domains of the WTCas9. This catalytically inactive version of the protein has been called “dead” Cas9 or dCas9 as the modification represses the original cleavage action of Cas9 but not the specific gRNA-mediated binding properties [45, 58, 65, 66]. It means that dCas9 can recognise and bind a specific DNA sequence in a gRNA-dependent manner without any nuclease activity. This CRISPR/dCas9 system has, among others, two main epigenetic applications which are focused on gene regulation experiments. The so called CRISPR interference or CRISPRi has been used in bacteria to down-regulate the expression of gRNA-targeted genes of interest [66]. In CRISPRi, dCas9 is co-transfected with the gRNA which is targeting a coding region of a gene of interest. As a result, dCas9 binds to the DNA and represses the transcription as the RNA polymerase is blocked by the presence of dCas9 [66]. However, this approach is highly efficient only in prokaryotes [66]. Therefore, CRISPRi has been implemented to successfully achieve a significant level of gene down-regulation also in mammalian cells by fusing the transcriptional repressor KRuppel Associated Box (KRAB) to the dCas9 protein [67]. A similar approach has been exploited to engineer CRISPR activation systems or CRISPRa. The dCas9 protein has been fused with several transcription activators, such as VP64 [67-69], VPR [70], or the SunTag system [71], to successfully achieve a precise up-regulation of one or more genes of interest defined by the specific gRNAs. CRISPRi and CRISPRa offer a precise, selective and easy to use system for both gene repression and activation while maintaining an

epigenetic behaviour: dCas9 binds to a specific DNA sequence without any nuclease activity while the transcription effectors regulate the gene expression.

1.5 The Clustered Regularly Interspaced Short Palindromic Repeats (CRISPR) System and Optogenetics

The CRISPR/dCas9-based systems emerged as a powerful technique to regulate the gene expression levels, however, one of the main disadvantages was their lack in spatial and temporal resolution. In order to study and understand genetic patterns specific to a certain type of tissue it is important to achieve a precise control over the CRISPR/dCas9 system(s) so that it can be selectively targeted to small populations of cells (spatial resolution) or be activated and de-activated at will (temporal resolution). When this PhD project started in 2014, the inducible promoters available to control the CRISPR system expression did not have these important features [66, 72].

One of the aim of this thesis project was to develop a light inducible CRISPR/dCas9 system for gene regulation that can be precisely controlled in space and time using light as an external trigger. In this way, any genetic pathway could be targeted and thus studied at single cell level, over time. In this approach, distinctive to the emerging field of optogenetics, exogenous light-sensitive functional proteins are expressed in cells and then light is used to control their activity and consequently modify the cellular behaviour [73-75] . Although optogenetics was initially developed for neuroscience, it can be also applied to other fields of biomedical research where there is the need to precisely control defined events in space and time with the aim to directly interact and study the mechanisms behind biological processes [73-75]. When this thesis project started in 2014, several light-sensitive proteins for optogenetics experiments were available [73, 76, 77] and some of them have been used to develop light inducible gene regulation tools based on Zinc Fingers (ZFNs), Transcription Activator-Like Effector Nucleases (TALEN) or Tetracycline Repressor/Operator (TetR/tetO) system [78-81]. Compared to the type II CRISPR/Cas9 system, ZNFs or TALEN need complex and time-consuming protein engineering [53, 82] and the TetR system requires a specific number of tet operator (tetO) repeats upstream the gene of interest sequence [80]. Over the last years, the CRISPR system has been coupled with optogenetics to create several tools for different applications. Examples are the “caged” Cas9 system developed by Hemphill *et al*. [83] where the Cas9 is active only upon illumination with UV light or the

photoactivatable “split” Cas9 published by Nihongaky *et al*. [84] where Cas9 has been divided in two subunits that can be re-assembled under blue light. Polstein *et al*. [85] and Nihongaky *et al*. [86] exploited the CRISPR system to control the expression level of a gene of interest upon blue light illumination. In a different approach, Jain *et al*. [87] engineered the “CRISPR-plus”, a novel method to photocage the gRNAs activity under UV illumination.

In this thesis project, a red-light-sensitive optogenetic tool based on the type II CRISPR/SPdCas9 system named Red Light CRISPR system was developed using the pair of proteins Phytochrome B (PhyB) and Phytochrome-Interacting Factor 6 (PIF6) form the plant *Arabidopsis Thaliana* which dimerize under red illumination (660 nm) and separate under infrared (740 nm) light. This pair of proteins has been previously used for gene regulation in mammalian cells and yeasts but not coupled with the CRISPR systems [80, 81, 88].

1.6 Summary

In summary, this PhD thesis project had multiple aims which were focused on microscopy, in relation to HTI, and molecular biology, in regard to optogenetics-based genome engineering.

Chapter 2 is proposing a new possible strategy to link light sheet microscopy and 3D cell culture models with the currently available High Throughput/Content Screening (HTS/HCS) platforms. In this work, the design and the development of a High Throughput Light Sheet Microscope prototype named HT-LISH is reported. Section 2.3 describes a detailed development, characterization and control of the HT-LISH microscope. Section 2.4 presents different experiments aiming to evaluate and show the possible applications/imaging capabilities that can be achieved with this system, from a basic imaging of 3D cell culture models, to a more advanced acquisition of multiple 3D specimens in an automated manner. This chapter concludes in section 2.5 with an analysis of the system in relation to its potential application in HTI studies together with future implementation aiming to improve the HT-LISH microscope.

Chapter 3 is focusing on molecular biology and presents a novel CRISPR/dCas9-based light inducible optogenetics system for a precise control of gene expression with high spatial and temporal resolution. This tool uses light as external trigger and is based on a pair of light sensitive proteins, Phytochrome B (PhyB) and Phytochrome-Interacting Factor 6 (PIF6), which dimerize under red illumination (660 nm) and separate under infrared light (740 nm). The development and the properties of this tool, named Red Light CRISPR system, are presented in section 3.3. The design, operation and all the step necessary to assemble the final version of the system are described in detail in sections 3.3.1, 3.3.2 and 3.3.3. Section 3.3.4 evaluates the spatial resolution of the Red Light CRISPR system by showing the light-based activation of the tool only in defined regions of a cell culture plate. The thesis proceeds with section 3.3.5 where the activity of the Red Light CRISPR system is evaluated in combination with an orthogonal light inducible CRISPR system responding to blue illumination. The conclusive section 3.5 containing

the analysis of the system is preceded by section 3.4 that first evaluates the possibility to express the Red Light CRISPR system in cellular spheroid when transfected with Lipofectamine 3000 (section 3.4.1) and then proposes a HT-LISH microscope implementation aiming to lay the foundation for future on-stage HT-LISH microscope-based optogenetics experiments on 3D models (section 3.4.2). In particular, the upgraded microscope is used to perform experiments aiming to optically control the expression level of genes of interest in cellular spheroids with the Red Light CRISPR system (section 3.4.3).

Chapter 2

Light Sheet Microscopy for High Throughput Imaging of Three-dimensional Cell Culture Models

2.1 List of Abbreviations

2.2 Background

2.3 Development and Characterization of the HT-LISH Setup

2.3.1 OPM, iSPIM and SCAPE Microscopy

2.3.2 The use of a Single Objective in the HT-LISH Microscope

2.3.3 Magnification and HT-LISH Microscope: How to Precisely Assemble the System

2.3.4 Numerical Aperture and Theoretical Resolution of the HT-LISH Microscope

2.3.5 The LISH Scanning System in the HT-LISH Microscope

2.3.6 Theoretical and Experimental Characterization of the Light Sheet in the HT-LISH Microscope

2.3.6.1 Light Sheet Theory

2.3.6.2 Experimental validation of Light Sheet Parameters

2.3.7 Experimental Characterization of the Scanning System in the HT-LISH Microscope

2.3.8 Theoretical and Experimental Pixel Size Characterization of the HT-LISH Microscope

2.3.9 Experimental Characterization of the Point Spread Function (PSF) of the HT-LISH Microscope

2.3.10 Volumetric Imaging with the HT-LISH Microscope

2.3.11 Controlling the HT-LISH Microscope

2.3.12 Summary: the current version of the HT-LISH microscope

2.4 Applications of the HT-LISH System

2.4.1 HT-LISH microscope for the Imaging in 3 Dimensions with Multiple Channels

2.4.2 HT-LISH microscope for the Imaging in 5 Dimensions: Multi-channel Time Lapse

2.4.3 HT-LISH microscope for Automated Imaging of 3D Models

2.5 Discussion and Future Directions

2.1 List of Abbreviations

All the components of the microscope assembled in this work with the respective abbreviations can be found in the Supplementary Material (Chapter 6 - Section 6.1.1).

2D - Two-Dimensional
$2W_0$ - Light Sheet Thickness
$2Z_r$ - Light Sheet Rayleigh Range
3D - Three-Dimensional (xyz)
4D - four dimensional (xyzt)
5D - five dimensional (xyzct)
a_{nmax} - Size along the X Dimension of the Black Pixel Column (Section 3.10)
BFP - Objective Back Focal Plane
DAQ - Data Acquisition (Card)
dBFP - Diameter of Objective Back Focal Plane
DSLM - Digital Scanned Laser Light Sheet Fluorescence Microscopy
dZ - Step Size of the Scanning Mirror (Section 3.10)
f - Lens Focal Length
FOV - Field of View
FUCCI - Fluorescent Ubiquitination-based Cell Cycle Indicator
FWHM - Full Width Half Maximum
GUI - Graphic User Interface
HCS - High Content Screening
HT-LISH - High Throughput Light Sheet
HT/C - High Throughput/Content
HTI - High Throughput Imaging
HTS - High Throughput Screening
IPS - Image Pixel Size
iSPIM - inclined Single Plane Illumination Microscopy
LISH - Light Sheet
LWD - Long Working Distance
M - Magnification
M_f - final magnification
M_{tot} - total magnification
n - Refractive Index
n_1, n_2, ..., n_{max} - Frame Number (Section 3.10)
NA - Numerical Aperture
n_a - Refractive Index Air
$NA_{actualmax}$ - Actual Maximum Numerical Aperture
NA_{max} - Maximum Numerical Aperture
n_g - Refractive Index Glass
n_o - Refractive Index Oil
n_w - Refractive Index Water
OPM - Oblique Plane Microscopy
PPS - Physical Pixel Size

PSF - Point Spread Function
R - Resolution
R_A - Axial Resolution
R_L - Lateral Resolution
SCAPE - Swept Confocally-Aligned Planar Excitation
SPIM - Selective Plane Illumination Microscope
TM - Total Magnification
X_{new} - New Image Size along the X Dimension (Section 3.10)
$X_{origina}$ - Original Image Size along the X Dimension (Section 3.10)
$Y_{original}$ - Original Image Size along the Y Dimension (Section 3.10)
Z_n - μm size of scan related to the frame n (Section 3.10)
Z_{nmax} - μm size of the entire scan (Section 3.10)
λ - Wavelength of light

2.2 Background

As mention in Chapter 1.3, one of the aim of this thesis project was to find a solution to link Light Sheet (LISH) Microscopy and Three-Dimensional (3D) cell culture models with the currently available High Throughput/Content Screening (HTS/HCS) platforms. Based on the literature, there are not practical solutions for implementing LISH Microscopy towards the already established High Throughput Imaging (HTI) technologies. A possible explanation for this gap can be found in the orthogonal configuration of conventional LISH microscopes: commonly in LISH imaging there are two objectives, one for illumination and one for detection that have to be placed at 90 degrees to each other and the sample has to be inserted exactly in between them (Figure 2A). To reach an HTI approach, multiple samples have to be automatically loaded in-between the objectives. The first step towards the development of a light sheet microscope with HTI capabilities was made by Gualda *et al*. with the so called SPIM-Fluid (Figure 4) [44] . This system is based on the Selective Plane Illumination Microscope (SPIM) design [38, 39] and it consists of a sample chamber with inside an FEP tube placed at 45 degrees from the two

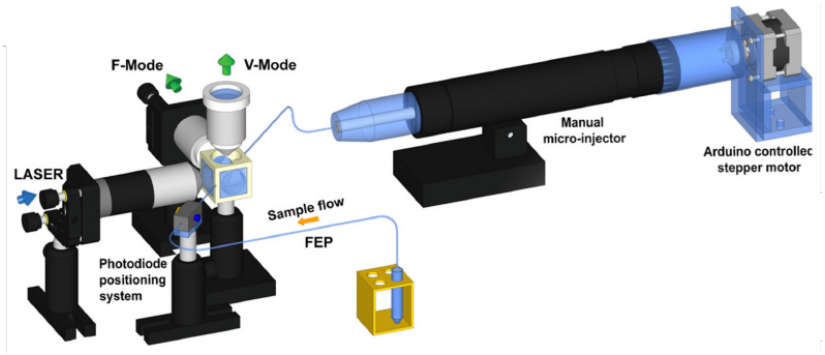

Figure 4- Schematic of the SPIM-Fluid system. Adapted from [44].

objectives. A pump system allows the samples to move inside the tube. In this way, the specimens can be scanned and thus imaged when passing through the sheet of light in a high throughput manner. As any other OpenSPIM-based light sheet microscopes also this setup can be further implemented to improve the image quality for example with the addition of another illumination objective or by changing the illumination source (e.g. two-photon laser or laser beam shaping).

This strategy, could be in principle a good solution for a high throughput light sheet microscope but the main goal for this work was to assemble a system compatible with any epi-fluorescence inverted microscope currently available on the market. [36].
Therefore, it was necessary to assemble a light sheet system that uses the single objective lens commonly present on an inverted microscope for both the illumination and detection. A possible solution was found in the design of the so called Oblique Plane Microscopy (OPM) which was first published in 2008 by Chris Dunsby [89] and then more recently implemented as Swept Confocally-Aligned Planar Excitation (SCAPE) microscopy by the Hillman group [90].

In this chapter, the design and the development of a High Throughput Light Sheet Microscope prototype based on the OPM and SCAPE microscopy design and named HT-LISH is reported. The HT-LISH microscope capabilities in terms of 3D and high throughput imaging will be fully described. The system is compatible with any currently available inverted microscope and allows for a fast and automated scan of single or multiple 3D samples in commercially available multi-well plate formats. This setup represents the “automated image acquisition” stage (Figure 1 - Chapter 1) of the entire HTS/HCS process and for the reasons mentioned above, it can easily fit with the antecedent “automated sample handling” stage (Figure 1 - Chapter 1).

2.3 Development and Characterization of the HT-LISH Microscope

2.3.1 OPM, iSPIM and SCAPE Microscopy

Oblique Plane Microscopy (OPM) is a light sheet based technique developed by Chris Dunsby in 2008 [89] and then taken up by Cutrale and Gratton in 2012 [91] with the inclined Single Plane Illumination Microscopy (iSPIM). Differently from conventional light sheet microscopes, this design relies on a single objective for both illumination and detection while maintaining all the LISH main features including low photobleaching, low phototoxicity and optical sectioning capabilities. The Dunsby 2008 design is shown in Figure 5 and is similar (almost identical) to the iSPIM published in 2012. In this scheme, the lens L3 is the single objective used for both illumination and detection. It is relayed with a second objective, labelled as L6, through a pair of lenses, L4 and L5. This optical

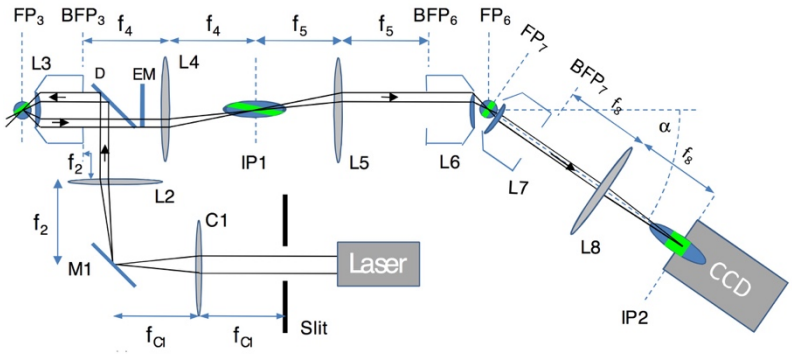

Figure 5 - Diagram of the Oblique Plane Microscope (OPM): M, mirror; L, spherical lens; C, cylindrical lens; f_x, focal length of lens x; FP_x, focal plane of lens x; BFP_x, back focal plane of lens x; D, dichroic filter; EM, emission filter; IP, imaging plane for CCD camera. Adapted from [89].

path is ending with a further "microscope" composed by a third objective, L7, a further lens, L8, and a CCD camera. As can be noticed, this last arm is not mounted along the optical axes of the other two objectives but it is tilted by a specific angle. The sheet of light is created through a cylindrical lens (C1) and is then focused on a mirror (M1). This mirror is regulated so that light is hitting the objective L3 not in the centre of the back aperture (Back Focal Plane - BFP) but on the side. In this way, due to the working principle of lenses, a sheet of light that is illuminating the sample at a specific angle is generated. The position and therefore the angle can be adjusted with the mirror M1.

The fluorescence from the "tilted" imaged plane is then collected back from the same objective L3 and is projected onto a CCD camera following the optical path mentioned above. In order to acquire a 3D stack, Dunsby in 2008 and Cutrale and Gratton in 2012 mounted the sample onto a motorized micrometre stage that was used to move the specimen through the light sheet along the horizontal direction. A series of contiguous images can thus be collected and eventually processed to obtain a fully 3D reconstructed model of the sample. The interesting feature here is that the microscope is imaging the sample through a single lens (L3) which can be considered as the objective of an inverted microscope as shown by Cutrale and Gratton in 2012 [91] and by the same Dunsby in 2011 and 2016 [92-94]. The other optical parts and the light source can instead be mounted outside the microscope body through a side port. Importantly, samples do not need any particular mounting like in conventional LISH and they can therefore be imaged using standard commercially available (multi) well plates.

In any type of optical microscope, there is an objective which is coupled with a tube-lens (TL). In order to obtain the magnification labelled on the objective, the tube-lens focal length (f_{TL}) has to be specific depending on the objective manufacturer (e.g. Zeiss TL = 164.5 mm). Because of the lens principle, the image of an object that is placed at the focal plane of the objective is projected in the so-called Image Plane (IP) at a distance f_{TL} after the tube-lens. In conventional LISH imaging, the sheet of light (and thus the illumination objective) is perfectly perpendicular to the optical axes of the detection objective and therefore the projected image of the sample in the Image Plane (black dashed line in Figure 6A) remains perpendicular to the detection optical axes (Figure 6A). Depending on the objective magnification (M), it is magnified laterally (M=M) and axially ($M \approx M^2$). In OPM, the sheet of light is coming out from the objective and is sectioning the sample at a specific angle (Figure 6B) and therefore it is not perpendicular to the optical axes of the single objective used. It follows that also the projected image in the Image Plane (black dashed line in Figure 6B) lies at an angle to the optical axes and due to spherical aberrations, it is heavily distorted [89, 92] (Figure 5 - IP1 and Figure 6B). This phenomenon is stronger in the areas far from the Image Plane (axial magnification $M \approx M^2$) [89, 92]. To collect the image of the sample it is thus not sufficient

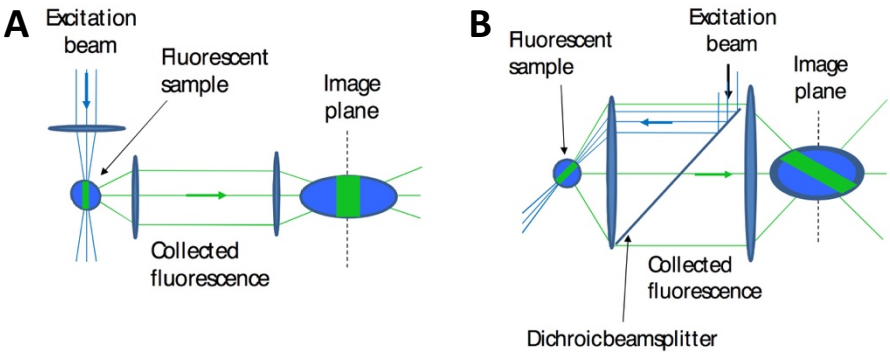

Figure 6 - Conventional Light Sheet vs Oblique Plane Microscopy. (A) Schematic of conventional light sheet microscopy: Illumination and Detection are perpendicular to each other and the projected image is perpendicular to the detection optical axes. (B) Schematic of Oblique Plane Microscopy: Illumination and Detection are performed with a single objective. The light is sectioning the sample at a specific angle and therefore, in the image plane, also the projected image is tilted and heavily distorted. Adapted from [89].

to tilt and place a CCD camera in this image plane (black dashed line Figure 6B and IP1 in Figure 5). It is therefore necessary to re-image the image plane with a second de-magnifying pair of lens and objective that in Figure 5 are labelled as L5 and L6. The image created by this second objective is the precise projection of the image acquired by the first objective (Figure 5 L3) and it is tilted as much as the angle of incidence of the light sheet (Figure 5 FP6, FP7). To maintain a high lateral and axial image resolution, the total magnification from the first to the second objective needs to be equal in the axial and lateral dimensions [89, 92]. All the optical laws regulating the optical path will be described and discussed in the next sub-chapters (from 2.2 to 2.10). As mentioned before, in order to acquire the final image, a "detection arm" as in conventional LISH microscopes composed of a further objective (L_7) and a tube-lens (L8) needs to be installed before the CCD camera [89, 92]. It has to be placed in front of the second objective at a specific angle from the optical axes equal to the angle of incidence of the sheet of illumination [89, 92].

In a second version of the system, Dunsby [92] modified the design of the OPM by changing the illumination path of the light sheet to achieve fast LISH scanning through the sample (Figure 7). In particular, the light sheet now passes through the second objective (O2) first, is focused through a set of lenses (T2 and T1) and is then illuminating the sample through the first objective with a sheet of light tilted at a specific angle,

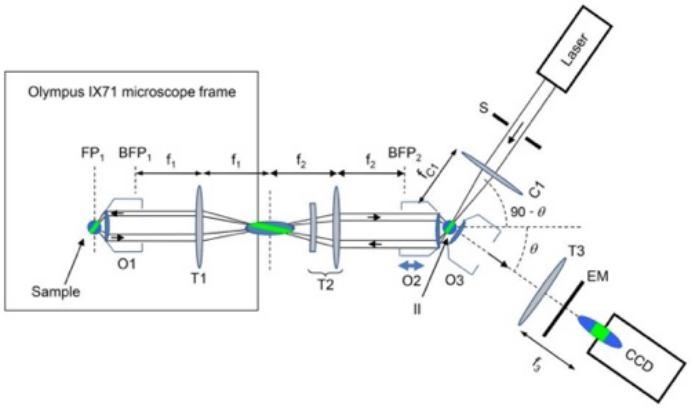

Figure 7 - Diagram of the Dunsby new version of the Oblique Plane Microscope. Ox, objective lens, Tx, tube lens; FPx, focal plane of objective Ox; BFPx, back focal plane of objective Ox; fx, focal length of Tx; C1, cylindrical lens; II, intermediate image of the sample; EM, emission filter; S, slit. Adapted from [92].

exactly as in the previous design. This is possible because O1 and O2 are precisely relayed and the LISH is entering in the second objective (O2) with a precise angle which is therefore maintained also at O1 (Figure 7). The rest of the setup remains the same as in the previous system. With this new configuration, the authors could achieve fast LISH scanning through the sample by changing the position of the second objective along the axial direction (O2 optical axes). This rapid movement of O2 is driven by a piezo-electric objective actuator. With this configuration, the OPM were capable of imaging 3D calcium dynamics in rat cardiomyocytes [92].

The Hillman lab revisited the OPM microscopy concept and developed the Swept Confocally-Aligned Planar Excitation (SCAPE) microscopy [90]. While the overall design is substantially the same as in Dunsby OPM 2008, the main difference is in the mechanism of the acquisition of the images. In fact, they exploited the principle of Digital Scanned Laser Light Sheet Fluorescence Microscopy (DSLM) [37] (Figure 8) to scan the light sheet through the sample instead of using a piezo-electric actuator (or a motorized stage to scan the specimen through the sheet of light). A scanning mirror is placed in a plane conjugate with the BFP of the objective with the function of changing the angle of incidence of the light at the BFP of the objective resulting in a rapid vertical scan of the laser beam in the sample plane thus generating a thin sheet of light (Figure 8). In SCAPE, Hillman and collaborators used this principle to rapidly scan the tilted LISH through the sample so that for each movements of the mirror corresponds the

acquisition of the entire illuminated plane. This improvement makes the SCAPE a very fast volumetric light sheet microscope which has been used for example to image a freely moving Drosophila or the calcium dynamics in a *in vivo* mouse brain [90].

A HT imaging station requires a certain level of speed to scan multi-well plates in a rapid manner. As it will be fully described later in the chapter, the HT-LISH microscope developed in this work is mounting a mirror-based scanning system similar to the one found in SCAPE.

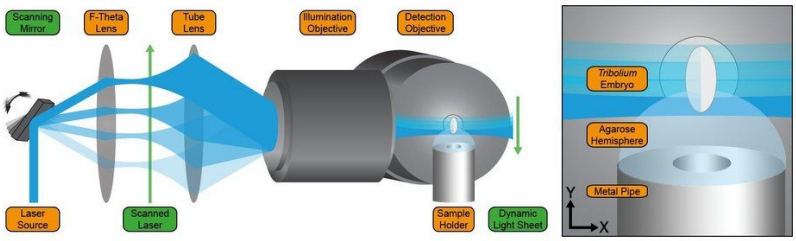

Figure 8 - Diagram showing the Digital Scanned Laser Light Sheet Fluorescence Microscope (DSLM). A scanning mirror is placed in a plane conjugate with the BFP of the objective with the function of changing the angle of incidence of the light at the BFP of the objective. This results in a rapid vertical scan of the laser beam in the sample plane thus generating a thin sheet of light. Adapted from [37].

2.3.2 The use of a Single Objective in the HT-LISH Microscope

One of the key points of the HT-LISH microscope is the use of a single objective that is illuminating the sample with a sheet of light tilted of a specific angle that can be called γ. For a perfect condition, in conventional LISH microscopes the illumination plane and the detection plane are at 90 degrees from each other (Figure 9A). Therefore, in OPM-based microscopes, the system is closer to the perfect orthogonal configuration when the angle γ is very small (close to 0 degrees) (Figure 9B). Obviously, it is not possible to

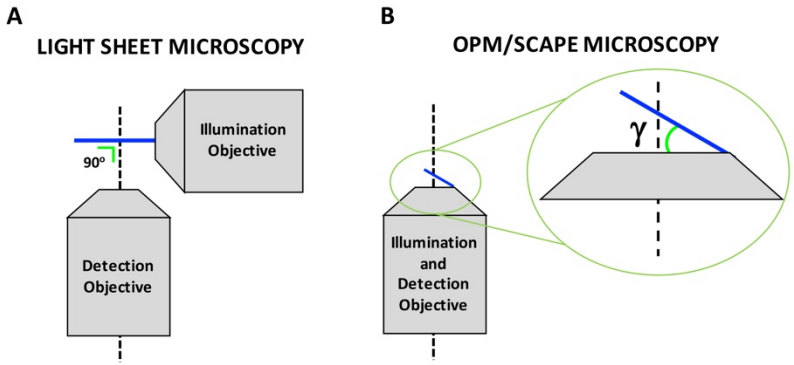

Figure 9 - Conventional Light Sheet vs OPM/SCAPE Microscopy imaging configuration. (A) In conventional LISH microscopy, the illumination and detection planes are at 90 degrees from each other. (B) In OPM/SCAPE-based systems the light sheet is sectioning the sample with a γ tilt angle.

reach a 0 degrees tilt ($\gamma = 0$) directly from a single lens but with the use of high numerical aperture (NA) objective, the γ angle can be as small as about 26-30 degrees and the same objective can be used also for the detection [89-95].

The NA is a measure of how much light can be collected and emitted by the objective. It can be calculated as follow:

$$NA = n \cdot \sin\alpha$$

where n is the refractive index of the medium between the objective and the sample and α is the half angle of the cone of light emitted or collected by the objective (Figure 10). Therefore, with high NA small γ angles can be reached (Figure 10). With air

objectives, it is hard to have NA greater than 0.95 but as suggested by the equation above, higher NA can be achieved by incrementing the medium refractive index (n). Objectives that can be used with immersion media (immersion objectives) can reach NA as high as 1.4 with oil immersion. This is because commonly, between the sample and the objective there is a layer of glass from ether a coverslip or a multi-well plate. Glass has a refractive index n_g of 1.515, much higher than air, n_a = 1, higher than water, n_w = 1.33, and almost identical to oil, n_o = 1.51. As shown in Figure 11A, the relationship between refraction and light angle of incidence is described by the Snell's law:

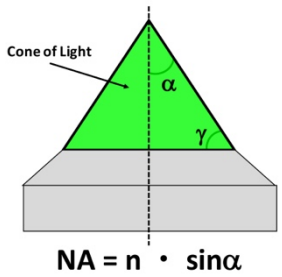

Figure 10 - Numerical Aperture (NA). The NA is a measure of how much light can be collected and emitted by an objective. With high NAs, small γ angle can be achieved.

$$n_1 \cdot \sin\phi_1 = n_2 \cdot \sin\phi_2$$

When considering an ideal situation where ϕ_1 is equal for three different objectives, one air, one water and one oil immersion (Figure 11B, C, D), the light behaviour is dissimilar. In the first case (air - Figure 11B), because $n_g >>> n_a$, the angle ϕ_2 is much bigger than ϕ_1 and the rays of light are heavily bended so that the cone of light that can be collected by the air objective is reduced. In the second situation (water - Figure 11C), where $n_g > n_a$, the angle ϕ_2 is slightly bigger than ϕ_1 with a consequent reduction of the tilt of the rays of light. The water immersion objective can therefore collect a wider cone of light thus achieving higher NA than air objectives.
In the third case (oil - Figure 11D), where $n_g \approx n_o$, the angle ϕ_2 will be almost equal to ϕ_1 and the entire cone of light can thus be collected by the oil immersion objective.

It is important to mention that the conditions in Figure 11BCD represents ideal situations where the sample is touching the glass coverslip/bottom dish. When focusing on applications that require 3D imaging deep in a living sample (or even if the specimen is not touching the glass) such as LISH microscopy, the presence of spherical aberrations

has to be considered. Aberrations are caused by the further refractive index mismatches between the samples themselves and the mainly water-based imaging medium (n = 1.33). Biological samples have a refractive index which is actually close to the one of water. Therefore, the use of water immersion objectives is preferred. As shown in Figure 11E and 11F, when compared to water immersion objectives, oil immersion objectives cannot exploit their full NA capacity because $\phi_4 < \phi_1$ and this leads to unwanted aberrations.

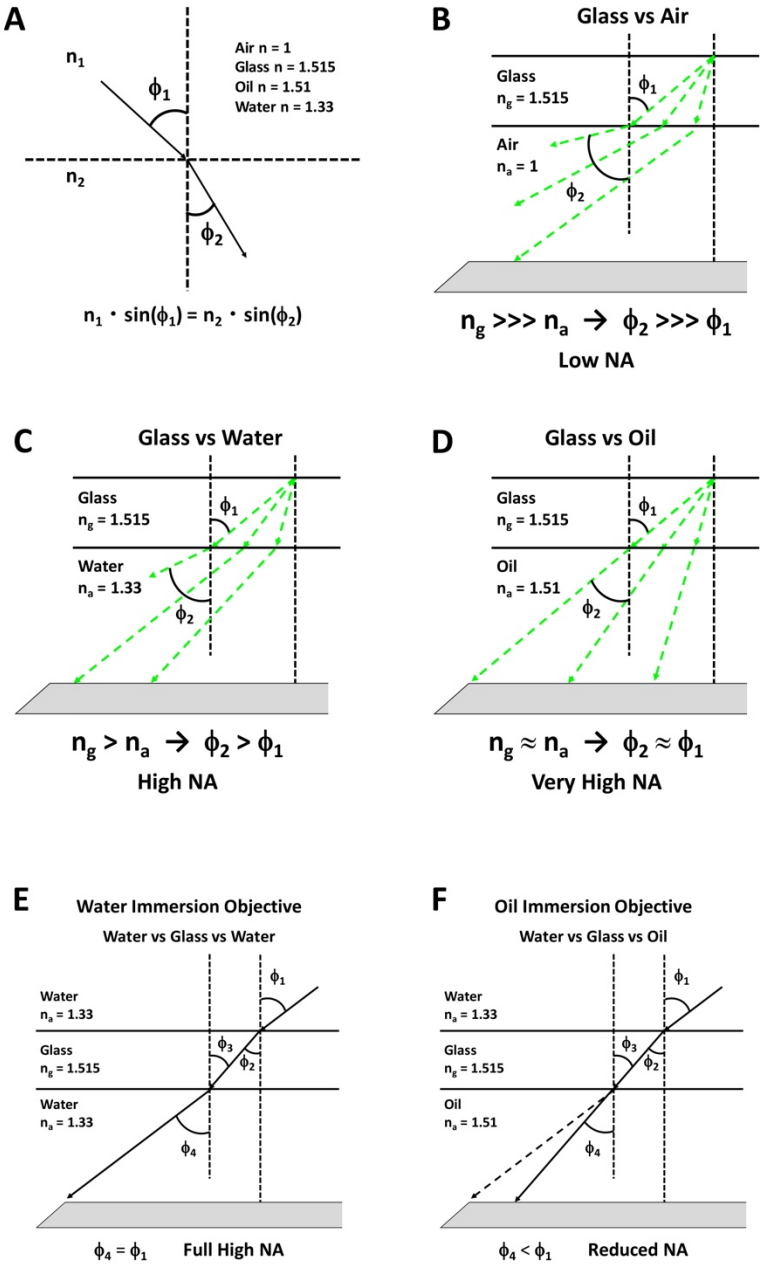

Figure 11 - Snell's law and refractive index.
(A) The Snell's law. (B, C, D) Ideal microscopy situations where a sample is touching the glass coverslip/bottom of the dish. ϕ_1 is equal for three different objectives, one air (B), one water (C) and one oil (D) immersion. In (B), because $n_g>>>n_a$, the angle ϕ_2 is much bigger than ϕ_1 and the rays of light are heavily bended so that the cone of light that can be collected by the air objective is reduced. In (C), because $n_g>n_a$, the angle ϕ_2 is slightly bigger than ϕ_1 with a consequent reduction of the tilt of the rays of light. Water immersion objectives can therefore collect a wider cone of light thus achieving higher NA than air objectives. In (D), because $n_g \approx n_o$, the angle ϕ_2 will be almost equal to ϕ_1 and the entire cone of light can thus be collected by the oil immersion objective. (E, F) Microscopy imaging situations where 3D imaging deep in a living sample is required. Biological samples have a refractive index which is close to the one of water ($\phi_4 = \phi_1$) and therefore the use of water immersion objectives is preferred (E). Oil immersion objectives cannot exploit their full NA capacity because $\phi_4 < \phi_1$ and this leads to unwanted aberrations (F).

For the reasons explained above, a Zeiss 40x 1.2 NA Water Immersion (W) (n_w=1.33) objective that was available in the laboratory was considered as a valid objective for the HT-LISH microscope. Going back to the key point of using a single objective to illuminate the sample with a sheet of light tilted of a specific γ angle (Figures 9B and 10), with this objective, the maximum α angle (Figure 10) that can be achieved is:

$$NA = n_w \cdot \sin\alpha \rightarrow \alpha = \sin^{-1}(NA/ n_w) = \sin^{-1}(1.2/1.33) = \mathbf{64^o}$$

The smallest γ tilt angle (Figure 10) achievable with this objective is therefore:

$$\gamma = 90-\alpha = 90-64 = \mathbf{26^o}$$

It can be concluded that with this objective the sample can be illuminate by a sheet of light with a maximum tilt γ angle not smaller than 26°. It means that if the light is hitting the first objective at the far end of its BFP, a LISH with a 26° γ angle is generated; by shifting the position of the light towards the centre of the back aperture (BFP), sheets of light with increasing γ angle can be obtained (Figure 12). This is a key concept that will be discussed in detail in section 2.3.4 where the NA of the HT-LISH microscope will be fully characterised.

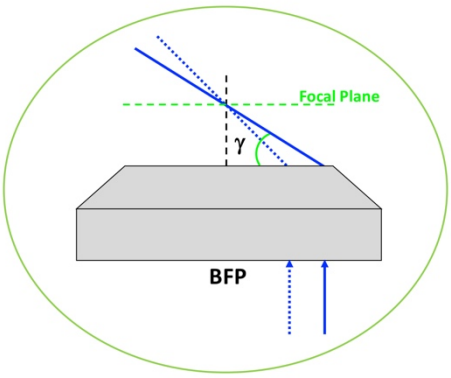

Figure 12 - Generation of tilted light sheet in OPM/SCAPE based microscopy. In OPM/SCAPE based microscopy, to generate a light sheet with a tilt γ angle, the light is hitting the illumination (and detection) objective at the end of its BFP. By shifting the position of the light towards the centre of the back aperture (BFP), sheets of light with increasing γ angle are obtained.

This is important also because as shown in Figure 13, if the LISH γ angle is too small, the depth (z) that can be reached in the sample is as well reduced. The maximum depth (z) (Figure 13) depends on the LISH length ($2Z_r$) and on the γ angle as follow:

$$z = 2Z_r \cdot \sin \gamma$$

$2Z_R$ is a LISH parameter that I will describe later in the chapter (Section 2.3.6 and 2.4.1). Here is important to note that for a given value of $2Z_r$, smaller γ means small z. Therefore, a balance between the angle γ and z is also required.

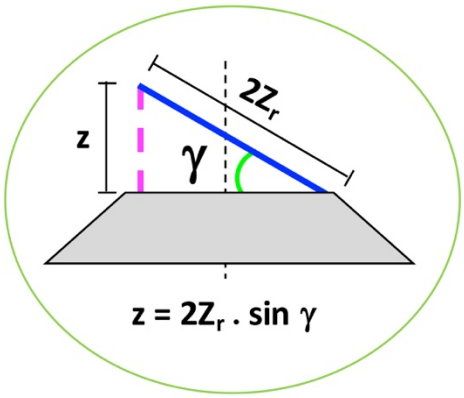

Figure 13 - Relationship between Light Sheet γ angle, maximum depth (z) achievable and Light Sheet length ($2Z_r$). Smaller γ angle means smaller z.

2.3.3 Magnification and HT-LISH Microscope: How to Precisely Assemble the System

Magnification is an important parameter that has to be considered.

In general, magnification (M) is a number indicating the apparent enlargement (not the physical size) of an object. The image obtained considering a thin spherical lens (L_1) and an object (o) that is placed before the lens focal point (f_1) (Figure 14A), will have a magnification equal to the ratio between the height of the object (o) and the height of the image (i). It corresponds to the distance (d_i) of the image from the lens (L_1) and the distance of the object (d_o) from the lens (L_1) (Figure 14A):

$$M = o/i = d_i/d_o$$

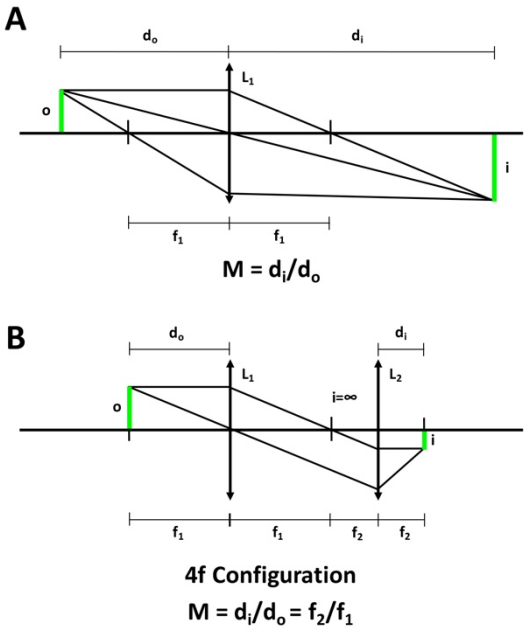

Figure 14 - Magnification. (A) Magnification (M) is equal to the ratio between the height of the object (o) and the height of the image (i). It corresponds to the distance (d_i) of the image from the lens (L_1) and the distance of the object (d_o) from the lens (L_1). (B) 4f Configuration: particular case when the object (o) is placed at the focal plane of the lens (L_1). In order to generate an image, a second lens (L_2) has to be placed in the optical path and if the two lenses are separated of a distance equal to the sum of their focal lengths ($f_1 + f_2$), an image will be generated at the focal plane (f_2) of the second lens (L_2) with a magnification equal to the ratio between their focal lengths ($M=f_2/f_1$).

A particular case occurs when the object (o) is placed at the focal plane of the lens (L_1) (Figure 14B). In this situation, the rays of light will not meet in a precise point after the lens and the image will be projected at infinity. Therefore, in order to generate an image, a second lens (L_2) has to be placed in the optical path. In particular, if the two lenses are separated of a distance equal to the sum of their focal lengths (Figure 14B - $f_1 + f_2$), an image will be generated at the focal plane (f_2) of the second lens (L_2) with a magnification equal to the ratio between the distance (d_i) of the image from the second lens (L_2) and the distance of the object (d_o) from the first lens (L_1). It follows that the magnification is given by the ratio of the focal lengths of the two lenses:

$$M = d_i/d_o = f_2/f_1$$

This situation where two lenses are separated of a distance equal to the sum of their focal lengths is called 4f configuration. If the two focal distances are equal, the magnification is 1.

As mentioned before (section 2.3.1), in a OPM-based system, the magnification M from the first objective (O1) to the second objective (O2) has to be equal in lateral and axial dimensions [89, 92]. A Nikon 40x 0.95 NA Air objective was available as O2. The f of the tube-lens for a Nikon objective is 200mm; It means that O2 coupled with a 200 mm lens gives a magnification of 40 times, exactly the same as O1. It follows that, when relayed in 4f, the overall magnification is equal to 1 as the sample is first magnified 40x and then de-magnified 40x. However, to ensure the M is equal both in lateral (M=M) and axial ($M \approx M^2$) dimensions, M needs to be equal to the ratio of the objective refractive indexes [89, 92]. This is because O1 is a Water immersion ($n_w = 1.33$) and O2 is an Air objective ($n_a = 1$).

In Figure 15 is schematized a situation where an image (I) of an object (O) is projected by an array of lenses mounted in a 4f configuration; the two sides of the lens array have refractive indexes n_1 and n_2.

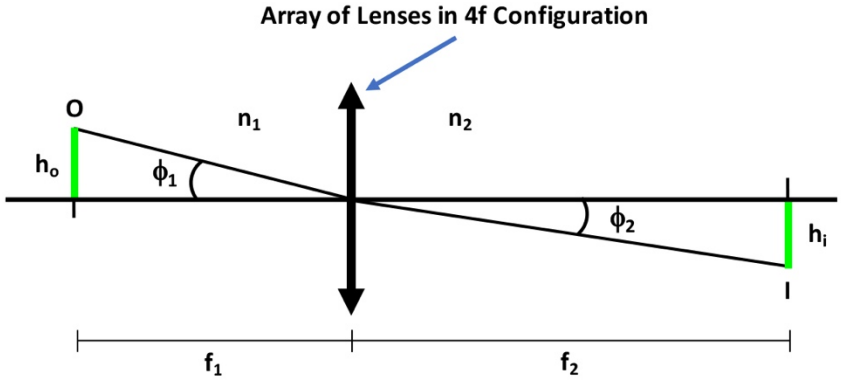

Figure 15 - Schematized optical situation where an image (I) of an object (O) is projected by an array of lenses mounted in a 4f configuration with different refractive indexes. If the two sides of the lens array have different refractive indexes n_1 and n_2, the magnification (M) is equal to: $M = h_i/h_o = n_1/n_2 \cdot f_2/f_1$

For trigonometric laws, $\tan\phi_1 = h_o/f_1$ and $\tan\phi_2 = h_i/f_2$. For small angle approximation, $\tan\phi = \sin\phi$. The Snell's law states that:

$$n_1 \cdot \sin\phi_1 = n_2 \cdot \sin\phi_2$$

Thus:

$$n_1 \cdot h_o/f_1 = n_2 \cdot h_i/f_2 \quad \rightarrow \quad h_i/h_o = n_1/n_2 \cdot f_2/f_1$$

Because the magnification M is equal to h_i/h_o (beginning of this subchapter) we can conclude that:

$$M = h_i/h_o = n_1/n_2 \cdot f_2/f_1$$

Therefore, if the refractive indexes are different, the magnification of a 4f configuration system is not simply given by the ratio of the lenses focal length (Figure 14B) but the ratio of the refractive indexes must be considered.

It follows that for the HT-LISH system where both O1 and O2 are 40x:

$$M = nO1/nO2 = n_w/n_a = 1.33/1 = 1.33$$

In order to achieve that, a pair of lenses (L1 and L2) in a 4f configuration were introduced in the middle of the HT-LISH microscope path between the tube-lenses TL1 and TL2 (f=200 mm) so that their magnification was equal to 1.33 (Figure 16). This solution was adopted also because of the introduction of the scanning system that will be describe later on in section 2.3.5. The pair of lenses that mounted in 4f have f = 75 mm (L1 - installed after TL1) and f = 100 mm (L2 - installed after L1) (Figure 16). The overall magnification (M_{tot}) of the HT-LISH microscope is therefore:

$$M_{tot} = 40 \cdot (100/75) \cdot (1/40) = 1.33$$

For the third part of the microscope, a Nikon 40x 0.6 NA Long Working Distance (LWD) objective was used as O3 and it was coupled with a 200 mm tube-lens (TL3) (Figure 16) to achieve 40x magnification. As previously explained (section 2.3.1), the key point is that O3 has to be placed in front of O2 at a specific angle from the optical axes equal to the angle of incidence of the sheet of illumination (γ - Figures 9B and 10). Therefore, a LWD objective is here required otherwise O3 will physically touch O2 before reaching the common focal point.

The final magnification (M_f) of the HT-LISH microscope is therefore:

$$M_f = 40X \cdot 1.33x \cdot (1/40x) \cdot 40x = 53.2x$$

The basic scheme of the HT-LISH microscope that was assembled in this work is shown in Figure 16. The parts list of all the components used to assemble the HT-LISH microscope can be found in the Supplementary Material (Chapter 6 - Section 6.1.1).
Starting from the left of the figure, the Zeiss tube-lens (TL1) is placed at 164.5 mm from the BFP of the Zeiss 40x 1.2 NA W (O1). The image of the sample is therefore magnified 40 times and projected at 164.5 mm from the BFP of the Zeiss tube-lens (Image Plane IP1). O1 is relayed in a 4f configuration with the second objective, O2 (Nikon 40x 0.95 NA Air) through the pair of lenses L1 and L2 (f=75 mm and f=100 mm - M=1.33) and the tube lens TL2 (f=200 mm). The final arm of the microscope includes the third objective O3 (Nikon 40x 0.6 NA LWD Air) coupled with the tube lens TL3 (f=200 mm) and a Andor Zyla 5.5 sCMOS camera (Figure 16).

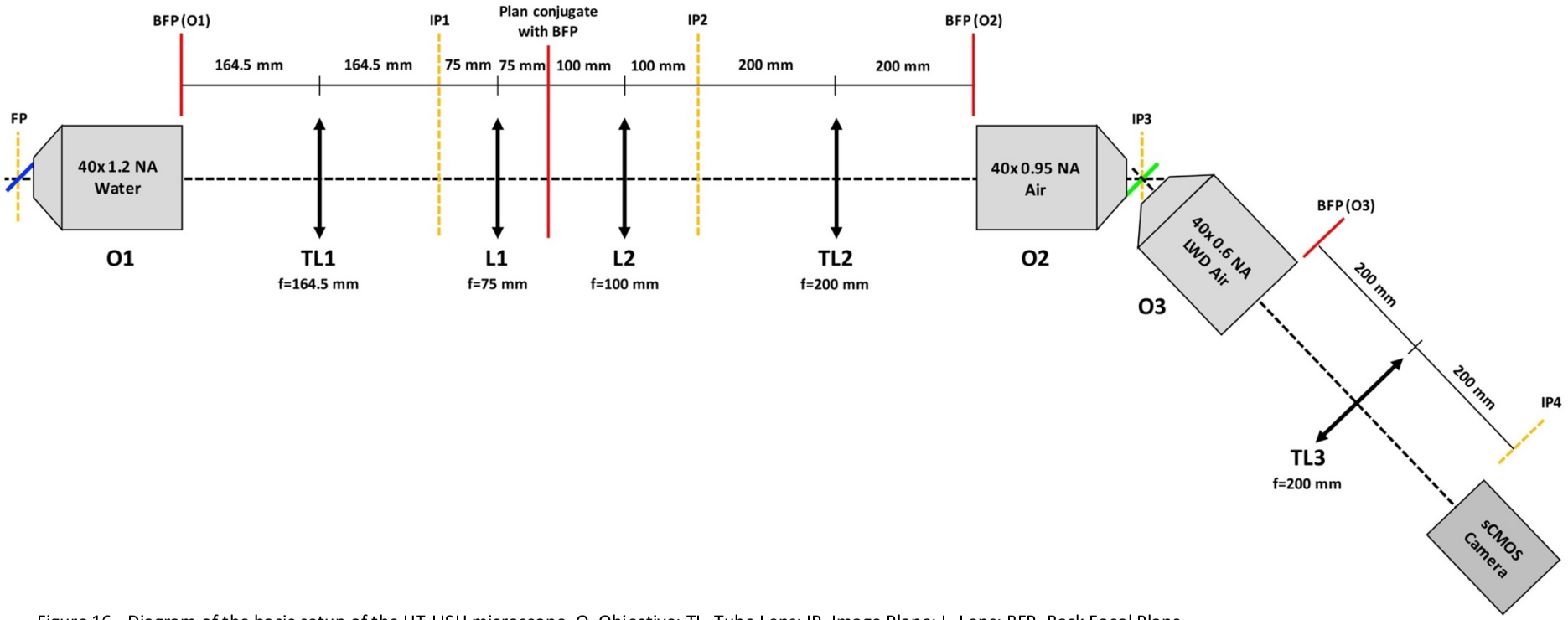

Figure 16 - Diagram of the basic setup of the HT-LISH microscope. O, Objective; TL, Tube Lens; IP, Image Plane; L, Lens; BFP, Back Focal Plane.

2.3.4 Numerical Aperture and Theoretical Resolution of the HT-LISH Microscope

Previously in the chapter the term resolution was mentioned. This, among others (e.g. magnification and numerical aperture), is a key parameter that defines an optical microscope. It is therefore fundamental to analyse it in depth for the HT-LISH microscope. In optical microscopy, resolution (R) can be described as the shortest distance between two close points in a sample that can be still distinguished as separate objects. It means that more details and information can be extracted from an image.

Lateral resolution (R_L), the resolution calculated along the lateral dimensions (x, y) can be defined by the following Ernst Abbe equation:

$$R_L = \lambda/2NA = \lambda/2 \cdot n \cdot \sin\alpha$$

where λ is the wavelength of the collected light.
Axial resolution (R_A), the resolution calculated along the axial dimension (z - depth), in LISH microscopy mainly depends on the thickness of the sheet of light ($2W_o$), parameter explained in detail is section 3.6.

The Abbe equation above suggests that high NA, and consequently high n, are linked with better resolution and thus the use of high NA objectives is preferred. In the HT-LISH, as in OPM and SCAPE, resolution and therefore the total NA of the system doesn't depend only on O1 but also O2 and O3 have to be considered. Taking into account only O1 (Zeiss 40x 1.2 NA W), for λ = 0.510 μm, the calculated lateral resolution (R_L) is:

$$R_L = \lambda/2NA = 0.510/2 \cdot 1.2 = 212 \text{ nm}$$

Nonetheless, the image collected by O1, before reaching the camera is passing through first O2 and then O3. For a perfect system, the same NA should be maintained along all the optical path so that all the information collected from O1 are conserved. For the HT-LISH setup, it means that both O2 and O3 should be water immersion objectives with

the same 1.2 NA as O1. However, because of the physical position, it is very difficult to mount two water immersion objectives at this point of the optical path (Figure 15 - O2, O3, IP3). Therefore, a pair of air objectives was considered as the most suitable solution.

Considering O2, in order to calculate what is the minimum NA for an air objective to maintain all the information collected from O1, the α angle described before in the chapter (Figure 10) has to be taken into account. The α angle for O1 is 64^{o}. It follows that it is necessary to use an air objective able to perform with the same α angle. This can be calculated as shown below:

$$NA = n \cdot \sin\alpha \rightarrow NA = 1 \cdot \sin(64) = 0.898 \approx 0.9$$

This simple operation suggests that an air objective with a numerical aperture ≥ 0.9 should be used (in fact $0.9 \cdot 1.33 \approx 1.2$). As mentioned, O2 is a Nikon 40x 0.95 NA Air objectives with a numerical aperture higher than 0.9 and it is therefore a very suitable objective for this purpose. For this air objective, the maximum α (Figure 10) is:

$$NA = n_a \cdot \sin\alpha_2 \rightarrow \alpha_2 = \sin^{-1}(NA/ n_a) = \sin^{-1}(0.95/1) \approx 72^{o}$$

Because α_2 is a bigger than the α angle in O1 (64^{o}), the full NA of O2 is not entirely exploited and therefore it can be stated that between O1 and O2, O1 is the objective that is limiting the NA of the system.

Finally, also O3 has to be considered. As explained before, the image projected at the focal plane of O2 is tilted as much as the γ angle (Figure 10 and 12) of incidence of the light sheet in O1 (Figure 15 FP, IP3). As in conventional two-objectives LISH microscopy, the illumination and collections beams must be separated of 90^{o} [89]. It means that the optical axes of the objective O3 needs to be perpendicular to the tilted image projected by O2. Therefore, as shown in Figure 17A, the optical axes of O3 (red dashed line) requires to be at γ^{o} from the optical axes of O2 (black dashed line). At this point of the

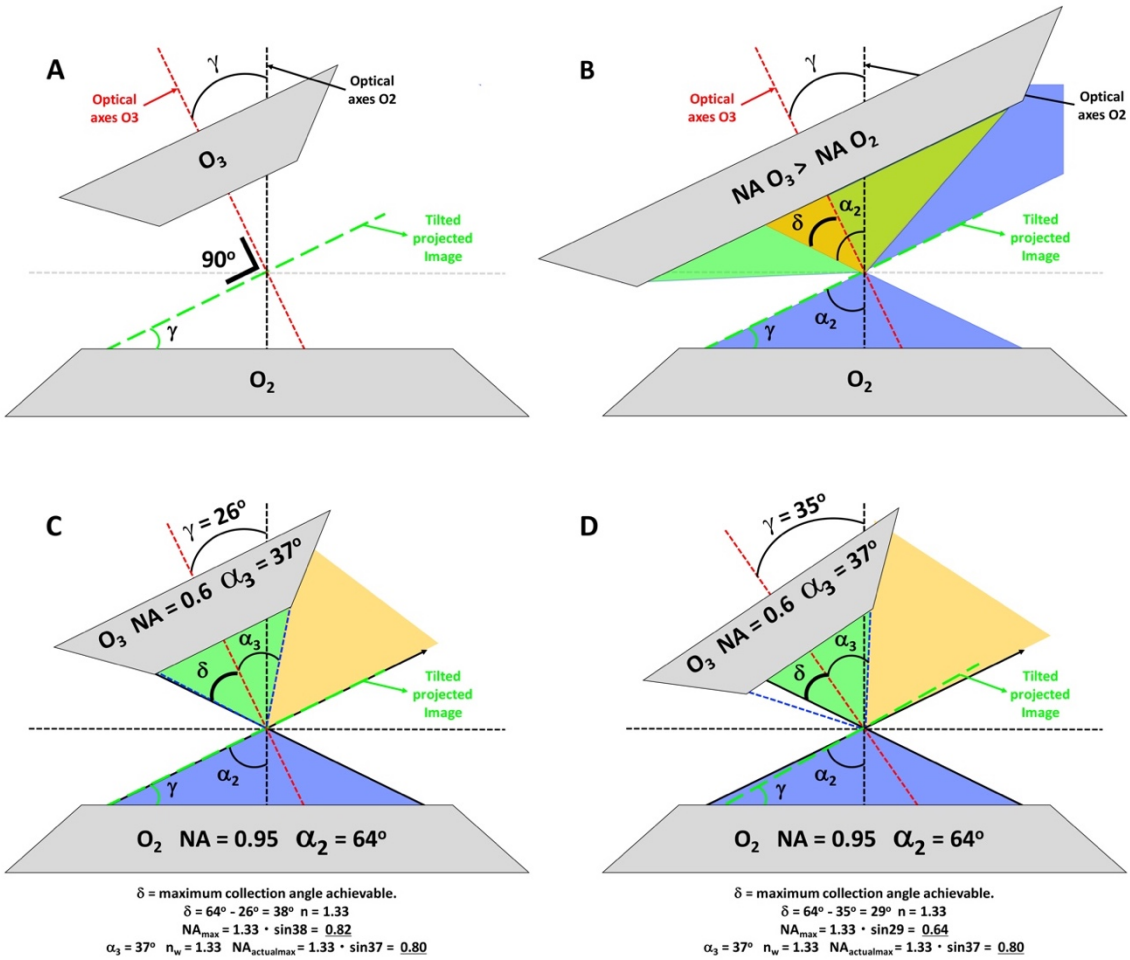

Figure 17 - Schematic representation of the Numerical Aperture (NA) of the HT-LISH microscope. (A) In the HT-LISH system, the optical axes of O3 (red dashed line) requires to be at γ^{o} (Light Sheet tilt angle) from the optical axes of O2 (black dashed line). (B) Due to the γ tilt, with O3 it is not possible to conserve all the information collected from the NA of O1 and O2. This does not strictly depend on the NA of O3. In fact, even if the NA of O3 (green) is larger than the NA of O2 (blue), only a smaller portion of information can be collected (light green and orange regions). (C) Graphical representation of the maximum NA achievable with a 40x 1.2 NA water immersion objective as O1, a 40x 0.95 NA Air objective as O2 and a 40x 0.6 NA LWD Air objective as O3. (D) Graphical representation of the NA of the HT-LISH microscope achievable with a γ tilt angle of 35 ^{o} and the objectives (O1, O2 and O3) indicated in (C).

optical path, due to this tilt, it is practically impossible to conserve all the information collected from O1 and projected from O2. And this does not strictly depend on the NA of O3. In fact, as shown in Figure 17B, even if the NA of O3 (green) is larger than the NA of O2 (blue), only a smaller portion of information can be collected (light green and orange regions).

The maximum NA (NA_{max}) achievable with the tilted configuration is represented by the orange triangle in Figure 17B and depends on the angle δ. It can be calculated by subtracting the γ tilt angle value from the maximum α angle value (α_2) (Figure 10 - α) of O2:

$$\delta = \alpha_2 - \gamma$$

the maximum NA (NA_{max}) achievable is thus:

$$NA_{max} = n \cdot \sin\delta$$

Because the images are collected with a water immersion objective (O1), here the refractive index of water: $n = n_w = 1.33$ needs to be considered. If for instance the objective used was an oil immersion, the refractive index of oil needs to be considered.

As shown in Figure 17C and as explained before, the α_2 angle that can be achieved with O2 is limited by the NA of O1 and is 64^o. The smallest γ tilt angle is therefore 26^o ($90^o - 64^o$). It follows that with the HT-LISH system the maximum NA (NA_{max}) achievable is:

$$\delta = \alpha_2 - \gamma = 64^o - 26^o = \mathbf{38^o}$$

$$NA_{max} = n \cdot \sin\delta = 1.33 \cdot \sin 38 = \mathbf{0.82}$$

This NA, for $\lambda = 0.510\ \mu m$, gives a maximum theoretical lateral resolution (R_L) of:

$$R_L = \lambda/2NA_{max} = 0.510/2 \cdot 0.82 = 310\ nm$$

Importantly, this is true only if the NA of the third objective O3 matches the calculated maximum NA (NA_{max}). For this purpose, a Nikon 40x 0.6 NA LWD Air objective was used. This choice was made because, as mentioned before, O3 needs to have a LWD and to fully exploit the maximum NA (NA_{max}) achievable of 0.82, it is necessary to use an objective with a NA α angle (α_3) close to the 38^o value of the δ angle calculated before. In fact, with this objective (O3):

$$NA = n_a \cdot \sin\alpha_3 \rightarrow \alpha_3 = \sin^{-1}(NA/\ n_a) = \sin^{-1}(0.6/1) \approx 37^o$$

Considering again that the images are collected with a water immersion objective (O1), the refractive index of water n = n_w = 1.33 has to be taken into account. It follows that the use of O3 enables to almost perfectly match the maximum NA (NA_{max}) achievable of 0.82 (Figure 17C). In fact, the actual maximum NA ($NA_{actualmax}$) is:

$$NA_{actualmax} = n_w \cdot \sin\alpha_3 = 1.33 \cdot \sin 37 = \mathbf{0.8}$$

In this case, for λ = 0.510 μm, the theoretical best lateral resolution achievable is:

$$R_L = \lambda/2 \cdot NA_{actualmax} = 0.510/2 \cdot 0.80 = 319 \text{ nm}$$

It can be therefore concluded that in a OPM-based setup also the third objective (O3) is a factor that can limit the NA and thus the best resolution achievable.

In the assembly of the first prototype of the HT-LISH microscope presented in this work, the LISH tilt γ angle was set at 35° (Figure 17D). In this configuration, the actual maximum NA ($NA_{actualmax}$) achievable is:

$$\delta = \alpha_2 - \gamma = 64^\circ - 35^\circ = \mathbf{29^\circ}$$

$$NA_{actualmax} = n \cdot \sin\delta = 1.33 \cdot \sin 29 = \mathbf{0.64}$$

This NA, for λ = 0.510 μm, gives a maximum theoretical lateral resolution (R_L) of:

$$R_L = \lambda/2NA_{actualmax} = 0.510/2 \cdot 0.64 = 398 \text{ nm}$$

2.3.5 The LISH Scanning System in the HT-LISH Microscope

Another fundamental part of the HT-LISH microscope is the scanning system. This is important because it enables a fast image acquisition and speed is one of the requirements of an HT platform. As mentioned in the first part of this chapter, the HT-LISH microscope exploits the scanning principle used in SCAPE microscopy which is similar to the DSLM (Digital Scanned Light Sheet Fluorescence Microscopy) scanning system. The DSLM is a LISH microscope with the conventional orthogonal two-objective configuration but uses a different strategy to generate the sheet of light. In DSLM, a scanning mirror is positioned in a plane conjugate with the BFP of the illumination objective along the optical axes (Figure 18A). A laser beam is first focused on the scanning mirror, is then reflected through a pair of lenses (L1 and TL) and is finally hitting the objective in the centre of the BFP. In this way, the sample is illuminated only in a

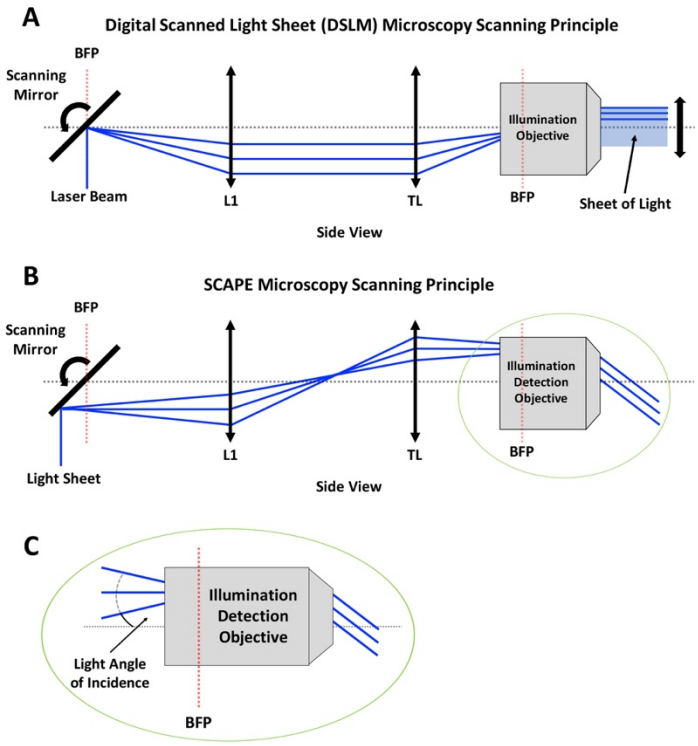

Figure 18 - Graphical representation of scanning systems. (A) Graphical representation of the DSLM scanning principle (see Figure 8). (B, C) Graphical representation of SCAPE and HT-LISH microscopes scanning system. In order to generate a tilted sheet of light, the laser is focused on the side of the scanning mirror and is thus directed to the edge of the BFP of the objective. By changing the mirror position, also the angle of incidence of the LISH at the BFP of the objective is changed and therefore a sheet of light that is scanned through the sample with a specific angle is obtained.

very small region with a thin beam of light. When the scanning mirror is quickly changing its position, this thin beam of light is entering in the centre of the objective back aperture with different angles; as a result, the beam is rapidly scanned through the sample in the vertical direction thus generating a thin sheet of light (Figure 18A). SCAPE microscopy is using this configuration with two main differences. First of all, a light sheet is generated with a cylindrical lens (as in conventional SPIM) before bouncing on the scanning mirror (Figure18 B). Second, based on the OPM design, in order to generate a tilted sheet of light, the laser is focused on the side of the scanning mirror and therefore is directed to the edge and not to the centre of the BFP of the objective. In this way, by changing the mirror position, also the angle of incidence of the LISH at the BFP of the objective is changed and therefore a sheet of light that is scanned through the sample with a specific angle is obtained (Figure 18BC).

The first design of the SCAPE developed by the Hillman group is shown in Figure 19 [90]. As in OPM, there is a three objectives configuration with the addition of a scanning mirror. Here it is important to notice that the light collected from the objective is following the same optical path as the illumination and is reflected back to the scanning mirror.

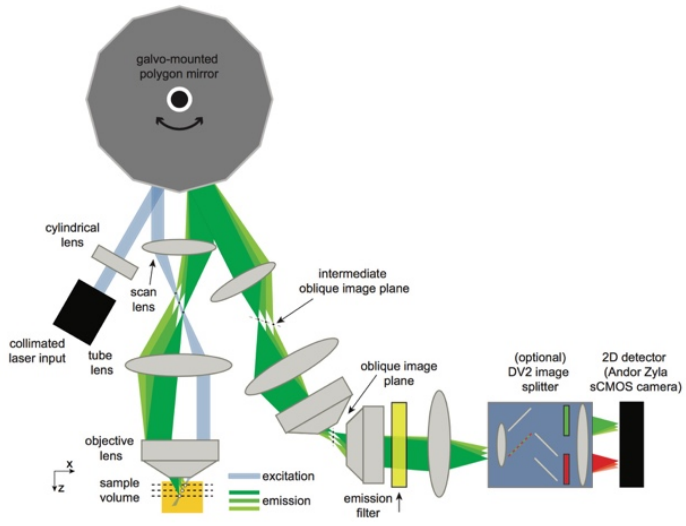

Figure 19 - Graphical representation of the Swept Confocally-Aligned Planar Excitation (SCAPE) Microscope. Adapted from [90].

This is a key principle. With this setup, the LISH is physically moved through the sample by changing the position of the scanning mirror of specific scanning angles. As a result,

the images of the illuminated planes will be re-projected at different positions for different angles and therefore impossible to collect with a static camera. To solve this issue, the collected light has to be de-scanned. This can be achieved by ether using the same scanning mirror as was done in SCAPE, or by directing the collected light to a different scanning mirror that is de-scanning the images by the same angle [90]. In this way, the images projected will be all static. In order to scan the light sheet, the original version of SCAPE (Figure 19) [90] is mounting a rotating polygon mirror. During the acquisition, for every rotation, a facet of the mirror is used to scan the light sheet through the sample and the adjacent facet is used to de-scan the collected light. Because the point of contact between two adjacent facets is precisely aligned along the optical axes of the objective, the adjacent facet is able to reflect only half of the total light collected from the objective (Figure 19). As a result, only half of the full NA of the illumination and detection objective is used with a consequent decreasing of image resolution.

To overcome this issue, on the HT-LISH system a conventional “flat” scanning mirror (as in Figure 18B) was installed. As in SCAPE, it was aligned along the optical axes but the entire surface of the mirror was used for both the scanning and de-scanning processes. It follows that all the light collected from the objective O1 can be reflected with a consequent exploitation of the full O1 NA.

The scheme of the HT-LISH microscope assembled in this work is shown in Figure 20.
The light sheet (blue line) was first reflected by a steering mirror (StM1) which was conjugated with the focal plane (FP) of the objective O1 (Image Plane 5 - IP5). It was used to direct the light to the side of the BFP of O1 to create the tilted illumination sheet. After that, the beam (blue line) was first reflected by a dichroic mirror (DM) and then by the scanning mirror (ScM). As mentioned before, the ScM lied on a plane conjugated with the BFP of O1. In this way, the light sheet could be rapidly scanned through the sample. The fluorescence coming from the imaged plane (green line) was collected back

by O1 and was following backwards the same optical path. The light was then de-scanned by the same ScM and directed to the objective O2.

The parts list of all the components used to assemble the HT-LISH microscope can be found in the Supplementary Material (Chapter 6 - Section 6.1.1).

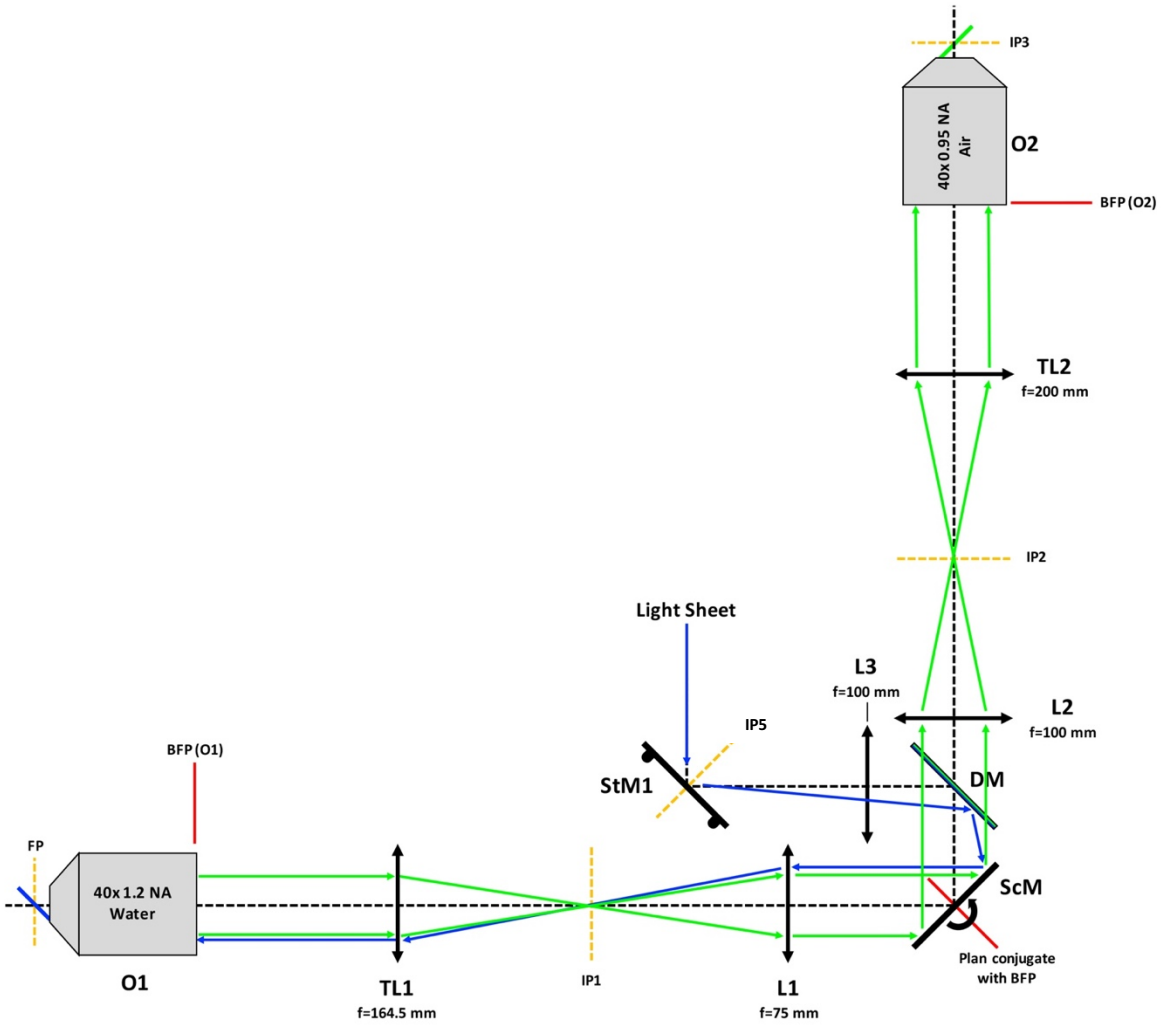

Figure 20 - Diagram of the HT-LISH microscope equipped with the scanning system. O, Objective; BFP, Back Focal Plane; TL, Tube Lens; IP, Image Plane; L, Lens; ScM, Scanning Mirror; DM, Dichroic Mirror; StM, Steering Mirror. The blue line indicates the illumination light, the green line shows the collected light.

2.3.6 Theoretical and Experimental Characterization of the Light Sheet in the HT-LISH Microscope

2.3.6.1 Light Sheet Theory

In the *HT-LISH* system, as in SCAPE and OPM, the light sheet is created through a cylindrical lens. This type of lens is peculiar because it focuses the light only along one dimension while the other remains unaffected. As a result, when a beam is passing through a cylindrical lens, a sheet of light is generated.

As shown in Figure 21, there are three main important parameters that must be consider: the width, the thickness and the length of the sheet of light.

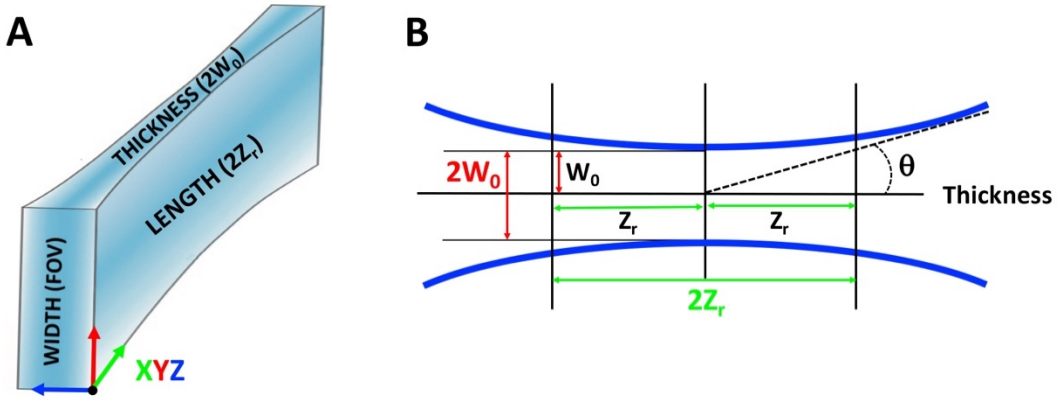

Figure 21 - Light Sheet parameters. (A) Graphical representation of a light sheet showing the light sheet width (FOV), length ($2Z_r$) and thickness ($2W_0$). (B) Graphical representation of a light sheet viewed from the top showing the light sheet length ($2Z_r$) and thickness ($2W_0$).

First, the width defines the field of view (FOV) of the light sheet or in other words the portion of the sample that is illuminated along one dimension. In the case of this setup it represents the vertical (y) dimension of each image acquired (Figure 21A). This parameter depends only on the vertical size of the laser beam used to create the light sheet and on the optical path magnification.

Second, the thickness of the light sheet, $2W_0$ (Figure 21B), can be used to define the axial (z) resolution of a light sheet microscope (Figure 21A). It can be theoretically calculated with the following Gaussian equation:

$$2W_0 = 2\lambda/n\pi\theta$$

where λ is the wavelength of the laser light, n is the refractive index of the immersion medium and θ is the angle indicated in Figure 21B that can be obtained knowing the NA of the light sheet.

Third, the length of the light sheet defines the depth of field and, as indicated in Figure 21A, it represents the opposite dimension of the width which in this case is the horizontal axes (x) of each image acquired. It is also called "Rayleigh range" and it is indicated by $2Z_r$ (Figure 21B). It depends the on optical path magnification and it is strictly related with half-thickness (W_0) and with the horizontal size of the laser beam used to create the light sheet. In fact, a vertical slit with an adjustable aperture is installed before the cylindrical lens to control the horizontal size of the laser beam.
The length is calculated with the following equation:

$$2Z_r = 2n\pi W_0^2/\lambda$$

where λ is the wavelength of the laser light, n is the refractive index of the immersion medium and W_0 is the half thickness of the light sheet.

It follows that the thinner is the light sheet, the better is the axial resolution but the depth of field is shorter which means that only a small portion of the sample can be illuminated (and thus imaged). Vice versa, a thick light sheet corresponds to greater depth of field but with a lower axial resolution.

The light sheet optical path of the HT-LISH microscope is shown in Figure 22.
Starting from the laser box (488 nm) there were two lenses in a 4f configuration, L5 and L6, that had f = 75 mm and f = 250 mm respectively. This telescope was used to increase the laser beam size which was originally of about 1 mm. The laser was then reflected by two steering mirrors, StM2 and StM3, and was directed towards the vertical slit (Slit). The cylindrical lens (Cyl) was installed after the slit. It is important to notice that this lens had f = 50 mm and it was mounted 50 mm after the vertical slit aperture. The optical path continued in a 4f configuration with the lens L4, f = 200 mm, with a further steering mirror (lying in the IP4 plane conjugated with the focal plane FP of the objective O1) and with the lens L3, f = 100 mm. After this point, as already described, the dichroic mirror DM, the scanning mirror ScM, the lens L1, f = 75 mm, and the tube lens TL1, f = 164.5 mm, were installed before the objective O1 (Zeiss 40x 1.2 NA Water).

The parts list of all the components used to assemble the HT-LISH microscope can be found in the Supplementary Material (Chapter 6).

As explained above, the width (FOV) of the light sheet depends on the vertical size of the laser beam used to create the light sheet and on the magnification. Because of the telescope formed by the lenses L5 and L6, the circular beam diameter at the slit level is 3.3 mm (M = 250/75 = 3.3x). The cylindrical lens (cyl) is mounted so that it is focusing the laser beam only in the vertical direction and is therefore affecting the width (and not the thickness) of the final light sheet. The magnification from the slit to the objective O1 is given by:

$$M = L4/Cyl \cdot L1/L3 \cdot 1/40x = 200/50 \cdot 75/100 \cdot 1/40 = 0.075x$$

It follows that the width or the FOV of the light sheet on the focal plane (FP) of O1 is:

$$3.3\ mm \cdot 0.075x = 0.2475\ mm = 247.5\ \mu m$$

where 3.3 mm is the beam diameter at the slit level. Therefore, in this setup configuration, the FOV of the light sheet along the y dimension (Figure 22) is of 247.5 μm.

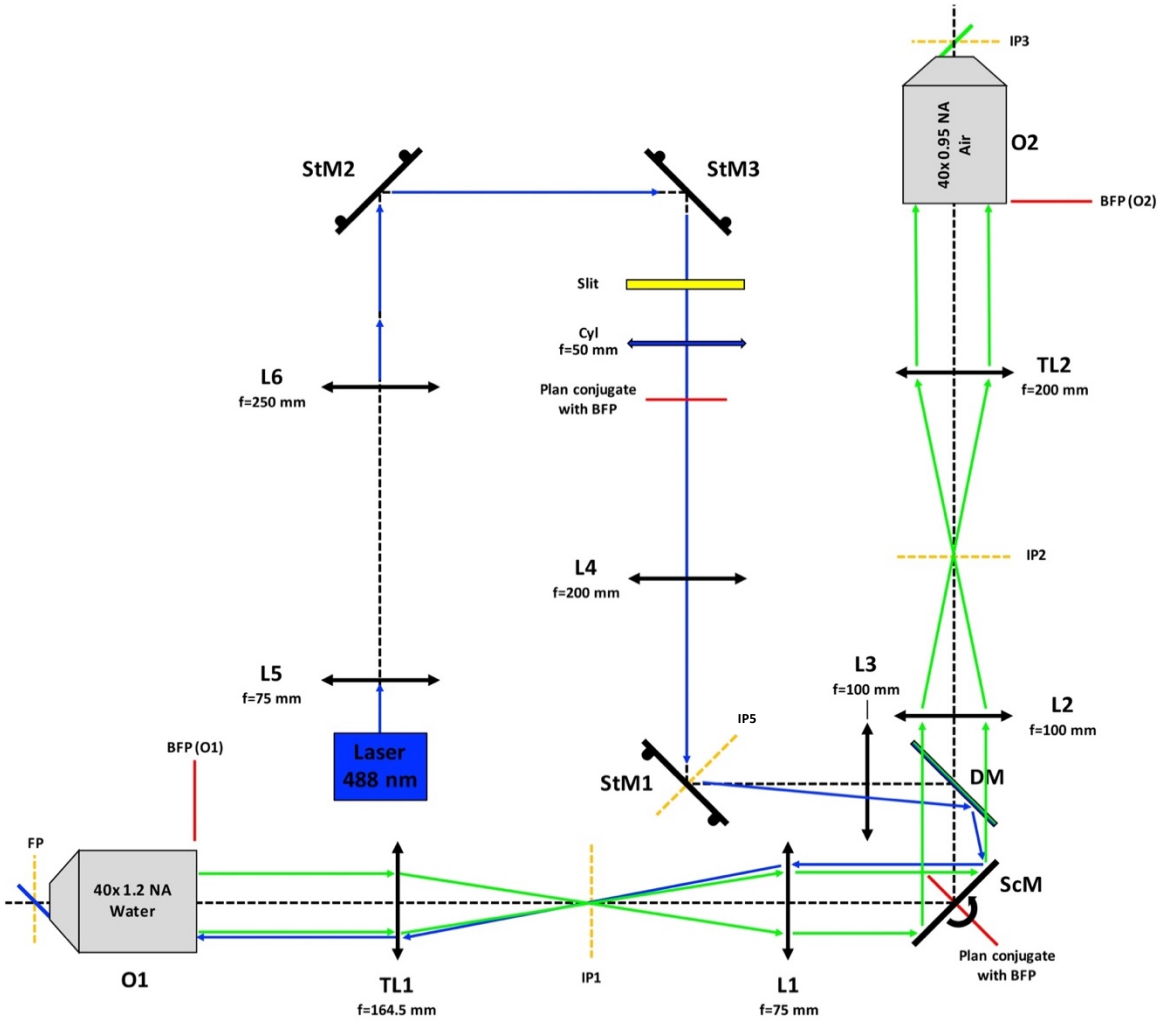

Figure 22 - Diagram of the HT-LISH microscope showing also the light sheet optical path. O, Objective; BFP, Back Focal Plane; TL, Tube Lens; IP, Image Plane; L, Lens; ScM, Scanning Mirror; DM, Dichroic Mirror; StM, Steering Mirror; Cyl, Cylindrical lens. The blue line indicates the illumination light, the green line shows the collected light.

As mentioned before, the thickness $2W_0$ and the Rayleigh range $2Z_r$ (length or depth of field) of the light sheet are strictly interconnected. In order to theoretically calculate thickness and Rayleigh range, there are several parameters that have to be considered: O1 BFP diameter, O1 NA, light sheet NA, magnification (from the BFP of O1 to the slit) and the horizontal size of the laser beam.

The BFP diameter of the objective O1 ($dBFP_{O1}$) depends on the focal length (f_{O1}) and the NA of O1 (NA_{O1}) and can be obtained as follow:

$$dBFP_{O1} = 2 \cdot f_{O1} \cdot NA_{O1}$$

f_{O1} is calculated dividing the focal length of the objective tube lens by the objective magnification. It follows that for O1 the focal length f_{O1} is:

$$f_{O1} = TL1/40x = 164.5/40 = 4.11 \text{ mm}$$

$dBFP_{O1}$ is thus equal to:

$$dBFP_{O1} = 2 \cdot 4.11 \cdot 1.2 = 9.86 \text{ mm}$$

Knowing the BFP diameter of the objective O1 ($dBFP_{O1}$), allows to calculate the size of the light sheet (LISH) at the BFP of O1 as a function of the light sheet NA by solving the simple proportion:

$$NA_{O1}/dBFP_{O1} = \text{NA LISH Wanted}/ \text{LISH at } BFP_{O1}$$

and

$$\text{LISH at } BFP_{O1} = (dBFP_{O1} \cdot \text{NA LISH Wanted})/NA_{O1}$$

The result is in mm and it can be converted in μm by multiply the value obtained by 1000 and represents the size in the horizontal dimension of the light sheet beam at the BFP of O1.

In order to calculate the size of the aperture of the slit and thus control thickness ($2W_0$) and length ($2Z_r$), the magnification from the BFP of O1 to the slit ($M_{BFPO1toSlit}$) has to be considered. Importantly, in this setup the cylindrical lens (Cyl) focuses the beam only in

the vertical direction, the horizontal dimension that can be controlled with the slit aperture, remains unaffected. It follows that the magnification $M_{BFPO1toSlit}$ that has to be considered is given by the lenses L4, L3, L1 and TL1 (and not Cyl because the beam passing through it is unaffected). It is therefore:

$$M_{BFPO1toSlit} = L4/L3 \cdot TL1/L1 = 200/100 \cdot 75/164.5 = 0.9118x$$

By multiplying the size in the horizontal dimension of the light sheet (LISH at BFP_{O1} in μm) for the magnification $M_{BFPO1toSlit}$, the slit aperture size can be obtained for each light sheet NA.

As a result, different light sheet NAs and thus different values of light sheet thickness and Rayleigh range can be achieved by varying the slit openings. It is important to mention that higher light sheet NAs generates thinner sheet of light with higher axial resolution but shorter Rayleigh range.

In Table 1 are listed different values of light sheet NA with the correspondent theoretical light sheet thickness, Rayleigh range and Slit aperture size.

Therefore, different NAs of the light sheet and thus different openings of the Slit can be chosen depending on the sample that has to be imaged.

Theoretical LISH THICKNESS and LENGTH (µm)												
NA LISH	**0.020**	**0.027**	**0.033**	**0.036**	**0.040**	**0.047**	**0.053**	**0.060**	**0.067**	**0.080**	**0.093**	**0.107**
Lambda (µm)	0.488	0.488	0.488	0.488	0.488	0.488	0.488	0.488	0.488	0.488	0.488	0.488
n Water	1.33	1.33	1.33	1.33	1.33	1.33	1.33	1.33	1.33	1.33	1.33	1.33
Angle DEG (LISH)	0.86162	1.14886	1.43613	1.55105	1.72344	2.01079	2.29819	2.58565	2.87317	3.44844	4.02406	4.60009
Angle RAD (LISH)	0.01504	0.02005	0.02507	0.02707	0.03008	0.03509	0.04011	0.04513	0.05015	0.06019	0.07023	0.08029
Wo	**7.77**	**5.82**	**4.66**	**4.31**	**3.88**	**3.33**	**2.91**	**2.59**	**2.33**	**1.94**	**1.66**	**1.45**
LISH Thickness = 2Wo	**15.53**	**11.65**	**9.32**	**8.63**	**7.77**	**6.66**	**5.82**	**5.18**	**4.66**	**3.88**	**3.33**	**2.91**
Zr	**516.45**	**290.49**	**185.90**	**159.37**	**129.08**	**94.83**	**72.59**	**57.35**	**46.45**	**32.24**	**23.68**	**18.12**
Rayleigh range = 2Zr	**1032.90**	**580.97**	**371.79**	**318.74**	**258.17**	**189.65**	**145.18**	**114.70**	**92.89**	**64.48**	**47.35**	**36.24**

SLIT APERTURE SIZE (µm)												
NA LISH	**0.020**	**0.027**	**0.033**	**0.036**	**0.040**	**0.047**	**0.053**	**0.060**	**0.067**	**0.080**	**0.093**	**0.107**
NA O1	1.2	1.2	1.2	1.2	1.2	1.2	1.2	1.2	1.2	1.2	1.2	1.2
dBFP O1 (mm)	9.87	9.87	9.87	9.87	9.87	9.87	9.87	9.87	9.87	9.87	9.87	9.87
$M_{BFPO1toSlit}$	0.91185	0.91185	0.91185	0.91185	0.91185	0.91185	0.91185	0.91185	0.91185	0.91185	0.91185	0.91185
SLIT Aperture size (µm)	**150**	**200**	**250**	**270**	**300**	**350**	**400**	**450**	**500**	**600**	**700**	**800**

Table 1 - Theoretically calculated values of light sheet thickness ($2W_0$) and Rayleigh range ($2Z_r$) in function of Slit aperture size and light sheet NA.

2.3.6.2 Experimental validation of Light Sheet Parameters

In order to experimentally confirm the calculated thickness of the light sheet, a compact CCD camera was temporarily added to the optical path and installed at the IP2 level, a plane conjugated with the focal plane of O1 (after the scanning mirror (ScM) and the lens L2) (Figure 22).

To precisely calculate the pixel size of this CCD camera at IP2 (and thus to obtain the images scale bar), a Brightfield image (a white LED array was mounted over O1 for Brightfield imaging) of a stage micrometre ruler with 10 μm divisions was acquired (Figure 23A).

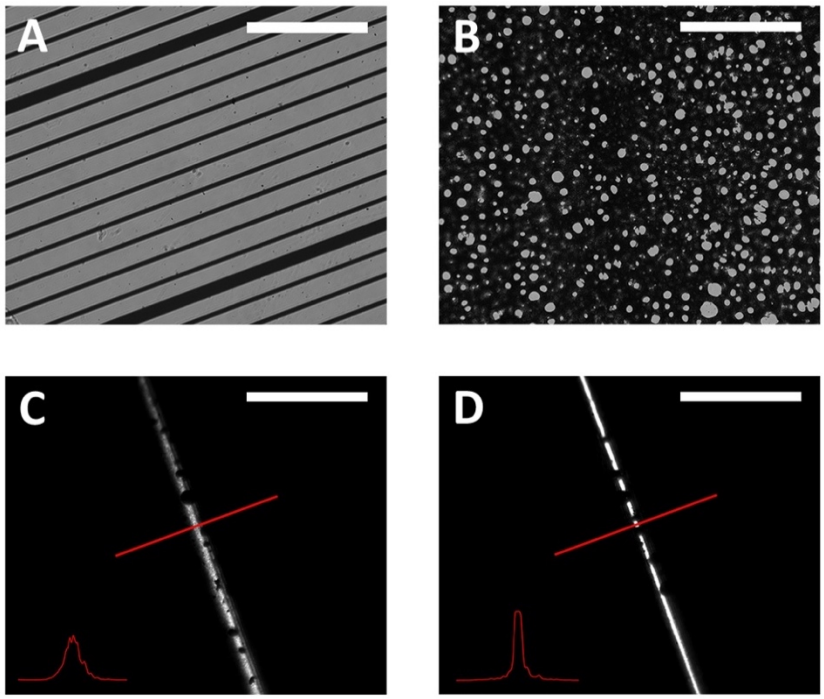

Figure 23 - Laser Light Collimation. (A) Brightfield image of a stage micrometre ruler with 10 μm divisions. (B) Fluorescence image of a glass bottom cell culture plate covered with the ink from a marker that is fluorescent in the GFP channel when illuminated with blue light (488 nm). (C, D) Fluorescence image of the cross section (thickness) of a light sheet generated with non-collimated (C) and collimated (D) 488 nm laser light. Scale bar 50 μm.

A glass bottom cell culture plate was covered with the ink from a marker that is fluorescent in the GFP channel when illuminated with blue light (488 nm) (Figure 23B).

It was used to visualize the light sheet along its thickness on the camera(s) (Figures 23C, 23D and 24).
For this characterization, the steering mirror StM1 was used to direct the light sheet beam to the centre of the BFP of O1. As a result, the light sheet was coming out straight from O1 and the light sheet thickness could thus be measured.
It is important to mentioned that to perform these measurements and for a correct operation of the entire microscope, the laser beam has to be collimated. It means that after the expansion (telescope with lenses L5 and L6 - Figure 22), the laser light rays must be parallel to each other and to the optical axes (Figure 23D) or the light sheet will not be properly focused on the focal plane of O1 (Figure 23C).

In Figure 24 are shown the fluorescence images of the light sheet for the different slit openings listed in Table 1 (white number on the top right corner of the images). Using an ImageJ plugin, in order to measure the light sheet thickness, the Full Width Half Maximum (FWHM - measurement of the width of a fluorescent object at the point where its intensity is 50% of the maximum) for each image was calculated along a line (red line) perpendicular to the light sheet.

As shown in Table 2, the measured FWHM values are in line with the theoretically calculated ones. In fact, there is a very small difference between the light sheet thickness values theoretically calculated in section 2.3.6.1 and the FWHM measured. This is indicating that the light sheet path of HT-LISH microscope is well aligned in terms of both magnification and slit position.

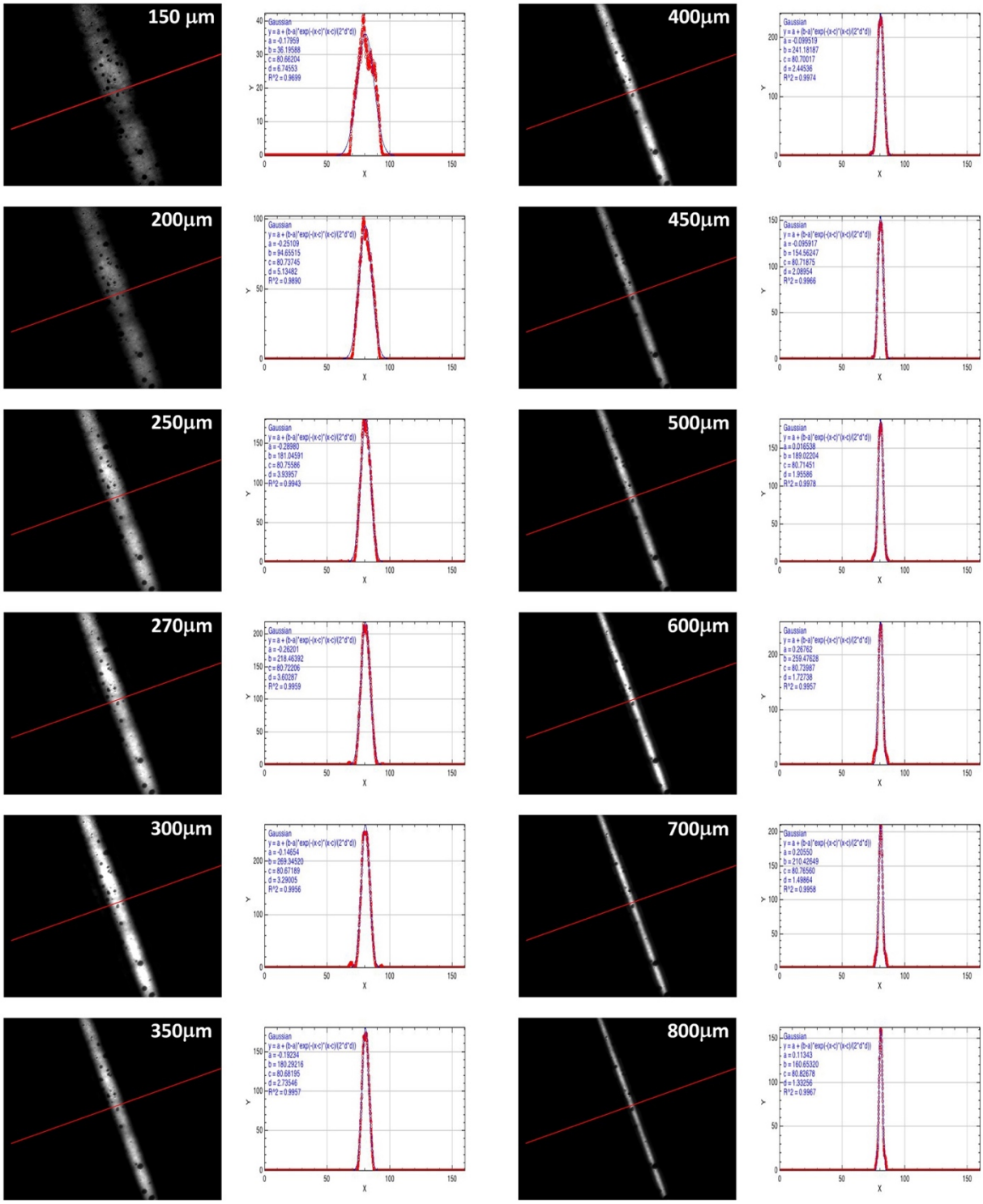

Figure 24 - Fluorescence images and intensity plots of the light sheet cross section (thickness - $2W_0$) for the different slit openings (white number on the top right corner of the images - listed in Table1). In order to measure the light sheet thickness, the Full Width Half Maximum (FWHM) for each image is calculated along a line (red line) perpendicular to the light sheet (see Table 2).

Measured LISH THICKNESS (µm)												
NA LISH	0.020	0.027	0.033	0.036	0.040	0.047	0.053	0.060	0.067	0.080	0.093	0.107
SLIT Aperture size (mm)	150	200	250	270	300	350	400	450	500	600	700	800
LISH Thickness = 2Wo	15.53	11.65	9.32	8.63	7.77	6.66	5.82	5.18	4.66	3.88	3.33	2.91
LISH Thickness Measured	15.88	12.09	9.28	8.48	7.75	6.44	5.76	4.92	4.61	4.07	3.53	3.14

Table 2 - Comparison between theoretically calculated and measured values of light sheet thickness ($2W_0$) for different Slit opening size.

2.3.7 Experimental Characterization of the Scanning System in the HT-LISH Microscope

As previously mentioned, the scanning system installed on the microscope is used to rapidly scan the light sheet through the sample. To achieve that, the scanning mirror is changing its position depending on the input voltage that it is receiving. Therefore, a specific voltage value defines a precise z step of the scan that remains constant along the entire image acquisition process. It is therefore important to fully characterise the scanning system in order to understand the relationship between each voltage input value and the z step size in μm at the sample level. Knowing the z step size is fundamental for a volumetric imaging system as it is required for the reconstruction of the three-dimensional volume of the sample.

To precisely calculate this correlation, the HT-LISH microscope setup was temporarily modified as for the light sheet experimental characterization. The compact CCD camera was again installed in the Image Plane 2 (IP2) after the scanning mirror (ScM) (Figure 22). A series of contiguous Brightfield images of the previously mentioned stage micrometre ruler with 10 μm divisions were acquired for specific voltage inputs values. As shown in Figure 25A, by measuring the movement of one selected division line of the ruler (red line) along the different frames of the scan, the precise conversion voltage to μm could be calculated. For this setup, a voltage step value of 0.1535 Volt corresponds to step size of 10 μm at the sample level (Figure 25A). For the scanning mirror used in this microscope, because the response to the voltage input values is linear, this measurement is enough to determine the voltage value for any μm step size required during the imaging process. For instance, a step size of 1 μm corresponds to an input voltage value of 0.01535 Volt. The maximum scan rage is around 250 μm ($\approx \pm 1.9$ Volt)

To confirm that the light sheet in the IP2 (Figure 22) is static because de-scanned by the scanning mirror, a further 10 μm step acquisition of Brightfield images and fluorescent images of the light sheet (using the marker sample as previously described) was performed. As shown in Figure 25B, the light sheet remained as expected in a constant position along the entire scan while only the Brightfield images were moving in the background.

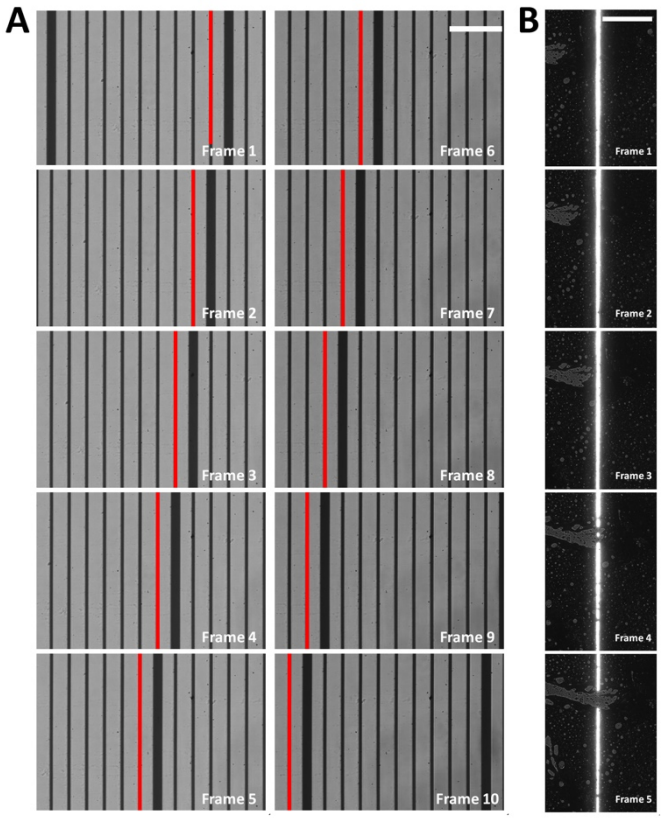

Figure 25 - Characterization of the HT-LISH microscope scanning system. (A) Characterization of the scanning mirror μm step size. A Stack of contiguous Brightfield images of a stage micrometre ruler with 10 μm divisions were acquired for specific voltage inputs values. By measuring the movement of a selected division line of the ruler (red line) along the different frames of the scan, the precise conversion voltage to μm can be calculated. (B) Stack (5 frames) of Brightfield images of a fluorescent marker overlaid with fluorescence images of the light sheet. As expected, the light sheet is de-scanned and it remains in a constant position along the entire stack while only the Brightfield images are moving in the background. This is because the Brightfield light is positioned over O1, therefore is neither scan through the sample nor de-scanned. Scale bar 30 μm.

2.3.8 Theoretical and Experimental Pixel Size Characterization of the HT-LISH Microscope

When using any type of microscope, in order to precisely extract spatial information from the images acquired, it is necessary to consider the relationship between the real size of the sample and the Physical Pixel Size (PPS) on the CCD camera chip that is used. This allows a precise spatial quantification (size) of all the elements present in an imaged and permits the accurate selection of the image scale bar. In general, this relationship depends mainly on the magnification of the system. It is sufficient to know the Physical Pixel Size (PPS) of the camera chip and the Total Magnification (TM) of the microscope to calculate the Image Pixel Size (IPS) and therefore the real dimension of the sample:

$$IPS = PPS/TM$$

The microscope setup presented in this work is equipped with a Andor Zyla 5.5 sCMOS camera that has a Physical Pixel Size (PPS) of 6.5 μm x 6.5 μm. The magnification of the system from Objective 1 (O1) to Objective 2 (O2) is 1.33x and from Objective 3 (O3) to the camera is 40x (Section 2.3.3 - Figure 15). The final magnification is therefore 53.2x (1.33x・40x). It follows that the Image Pixel Size (IPS) is:

$$IPS = 6.5/53.2 = 0.1222\ \mu m$$

It means that on the images acquired, the size of each pixel should be 0.122 μm in both X and Y dimensions. However, as previously explained, O3 and the camera are actually tilted (Sections 2.3.1, 2.3.3 and 2.3.4) of a specific γ angle (Light Sheet angle of incidence - Section 2.3.2) respect to the optical axes of O2. This concept is schematised in Figure 26. It follows that the imaged planes perpendicular to O1 and O2 (red panels 3D View) are not perpendicular to O3 and the spatial information collected by this latter objective are thus different (green panels 3D View). It is essential to consider the γ tilt angle to properly calculate the IPS in the lateral dimensions. As shown in Figure 26, this angular displacement is affecting only the horizontal dimension X of the image, the vertical

dimension Y remains unaffected as the image plane is rotated along this axis. Following the trigonometric laws, the new horizontal dimension indicated with X^I can be obtained:

$$X^I = X \cdot \cos\gamma$$

As a result, the correct pixel size of the images acquired can be calculated. Both the coordinates X and Y measures 0.122 μm and the γ tilt angle was set to 35 degrees (Section 2.3.4 - Figure 17D). Therefore, X^I is:

$$X^I = X \cdot \cos\gamma \rightarrow X^I = 0.122 \cdot \cos 35 = 0.1000\ \mu m$$

In conclusion, the theoretical calculations suggest that the Image Pixel Size (IPS) of the HT-LISH setup assembled in this work are 0.1000 μm in X and 0.1222 μm in Y and the pixel ratio Y/X is 1.22 (=1/cos35).

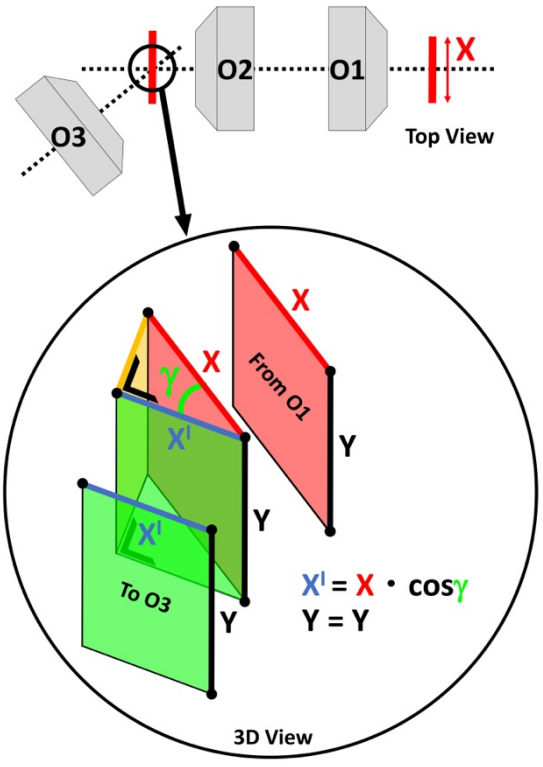

Figure 26 - Graphical representation of the X and Y image coordinates in the HT-LISH microscope.

To experimentally verify the calculated Image Pixel Size (IPS), as shown in Figure 27, a Brightfield image of the stage micrometre ruler with 10 μm divisions already used in sections 3.6 and 3.7 was acquired.

As explained above, the 35 degrees angular displacement is affecting only the X^I dimension of the image (Figure 26). To make sure that the measurements on the image were corresponding to the real size of the ruler, the ruler was positioned with the 10 μm division lines perpendicular to the Y axes and not to the X^I axes of the image (Figure 27). In this way, the Image

Pixel Size (IPS) along the Y dimension could be experimentally measured.

As highlighted by the red line in Figure 27, the first step was to measure on the image how many pixels correspond to the known 10 μm distance of the ruler division lines. This process suggested that 10 μm are equal to 84 pixels in the image; this indicates that the experimentally calculated Image Pixel Size (IPS - one pixel) along the Y dimension is 0.1190 μm. As estimated before, the image pixel ratio Y/X has to be of 1.22 (=1/cos35), therefore the Image Pixel Size along the X dimension is 0.0975 μm (0.1190μm/1.22).

The theoretically and experimentally obtained values (0.1000 μm X - 0.122 μm Y vs 0.0975 μm X - 0.1190 μm Y) are very close to each other, suggesting that in terms of magnification the microscope is well aligned (Table 3). The Field of view (FOV) of the HT-LISH microscope is of 250 μm in X and 257 μm in Y (Andor Zyla sCMOS camera sensor XY: 2560 x 2160).

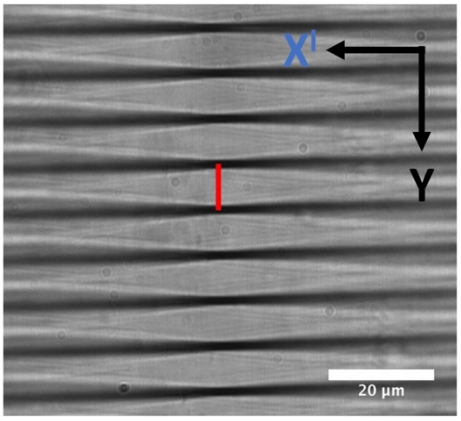

Figure 27 - HT-LISH microscope Brightfield image of a stage micrometre ruler with 10 μm divisions. Due to the angular tilt between O2 and O3, the ruler division lines are in focus only in the central part of the image and defocused on the sides. By measuring how many pixels correspond to the known 10 μm distance of the ruler division along the Y dimension (red line), it is possible to calculate the image pixel size (IPS) in X' and Y (see Table 3).

	Image Pixel Size (μm)	
	Theoretical	Experimental
IPS X	0.1000	0.0975
IPS Y	0.1220	0.1190

Table 3 - Theoretically and experimentally calculated Image Pixel Size values.

2.3.9 Experimental Characterization of the Point Spread Function (PSF) of the HT-LISH Microscope

The ability of an optical microscope to resolve a light point source is limited by the diffraction of light. In fluorescence microscopy, it means that in the image acquired with an ideal and precisely aligned optical system, the size in the lateral and axial dimensions (X, Y and Z) of a point source are equal to the diffraction limit values in X, Y and Z. It follows that in the image plane, a point source smaller then this diffraction limit will appear blurred along all three dimensions. The diffraction limit can therefore be used to define the resolution of an optical system.

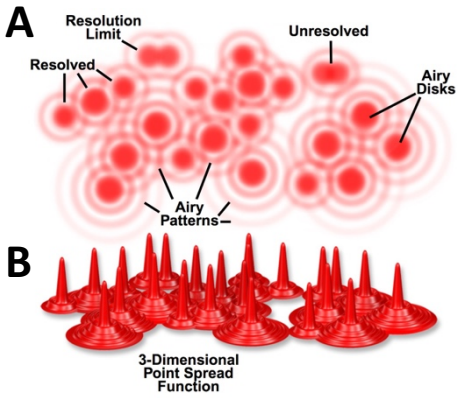

Figure 28 - 2D (A) and 3D (B) representation of the Point Spread Function (PSF). From microscopyu.com.

As shown in Figure 28A, in the XY image plane, a light point source appears as an Airy disk or, in other words, as a high intensity central spot surrounded by a series of concentric interspersed dark or low intensities regions. Resolution can be defined as the shortest distance between two closely spaced Airy disks that can be still distinguished as two separate entities.

As explained in Section 2.3.4, the lateral resolution (R_L) and thus the diffraction limit in X and Y, can be described by the following Abbe Lateral Resolution equation:

$$R_L = \lambda/2NA_{actualmax}$$

Differently, along the axial dimension, the diffraction limited Airy disk appears as an elongated elliptical pattern and, as shown in Figure 28B, can be seen as the 3D projection of the Airy disk. As previously mentioned, axial resolution in LISH microscopy mainly depends on the light sheet thickness $2W_0$.

The Airy disk intensity distribution along the three dimensions X, Y and Z is defined as Point Spread Function or PSF. The measure of the PSF can therefore be used as a quantification of the resolution of an optical system.

As previously calculated in Section 2.3.4, the theoretical lateral resolution (R_L) achievable with the HT-LISH microscope assembled in this work was 398 nm. The Ernst Abbe equations above used to calculate lateral resolution describe only one of the possible ways to define the concept of resolution. Another equation was formulated by Lord Rayleigh and states that two light point sources can be resolved when the central spot of the Airy disk of one point source overlaps with the first dark region surrounding the central spot of the Airy disk of the other point source.
Rayleigh Lateral Resolution (R_L) is defined as:

$$R_L = 0.61\lambda/NA$$

The HT-LISH setup assembled in this work could therefore achieve a Rayleigh lateral resolution of 486 nm.
However, to experimentally characterize the resolution of an optical system, the measure of the Full Width Half Maximum (FWHM) of the PSF is considered as a useful and simple criterion. This is because if the PSFs of two light point sources are closer than their width, they cannot be resolved as separated entities.

The experimental characterization of the PSF for the HT-LISH microscope was therefore performed by measuring the FWHM of fluorescent beads measuring 200 nm in size (smaller than the diffraction limit achievable) with a fluorescence emission peak at 510 nm. The beads were placed onto a glass bottomed dish and immersed in a low-melting point agarose solution to create a 3D beads distribution (Material and Method - Chapter 5). It is essential to acquire the images of the beads under same conditions and microscope settings that will be used to image the actual samples; in this case the

following parameters were used: Slit Opening: 270 μm, LISH Thickness $2W_0$: 8.6 μm, Rayleigh range $2Z_R$: 318.7 μm.

In regard to this experiment, it is important to mentioned that the objectives O2 and O3 used in the HT-LISH optical path were re-imaging the samples in air without a glass coverslip. Air objective are assembled to image the sample through a glass coverslip and therefore their use without this material cannot guarantee the absence of aberrations. Because the glass coverslips can have different thickness, some air objectives are provided with a correction collar which allows the user to change the distance of some lenses inside the objective to match the glass thickness. The objective used in the HT-LISH system had the correction collar which could be used to partially contain the aberrations due to the challenging re-imaging conditions. Therefore, images of the beads were acquired for different correction collar combinations.

As shown in Figure 29, three beads per condition were analysed and the FWHM along the X and Y dimension were determined using a plugin for the ImageJ software.

The FWHM values obtained are listed in Table 4.

First of all, it is visible that the various combinations of the correction collar generated very different values of FWHM, introducing different grades of optical aberrations.

It is also interesting to observe from Table 4 that while the values calculated along the Y dimension remained constant over the different collar combinations, the FWHM along the X axes was more variable. As described in section 3.8, this can be explained by the fact that only the horizontal dimension of the images was affected by the tilt of the image plane and not the vertical; along the X axes the presence of aberration can therefore be more pronounced. This can also explain why the XY resolution was not perfectly isotropic (X=Y).

The collar correction combination of 0.11 for O2 and 0 for O3 provided the best results achievable with an almost isotropic lateral resolution of 0.7 μm in X and 0.6 μm in Y (Table 4). Therefore, all the further imaging experiments were performed using this collar correction combination.

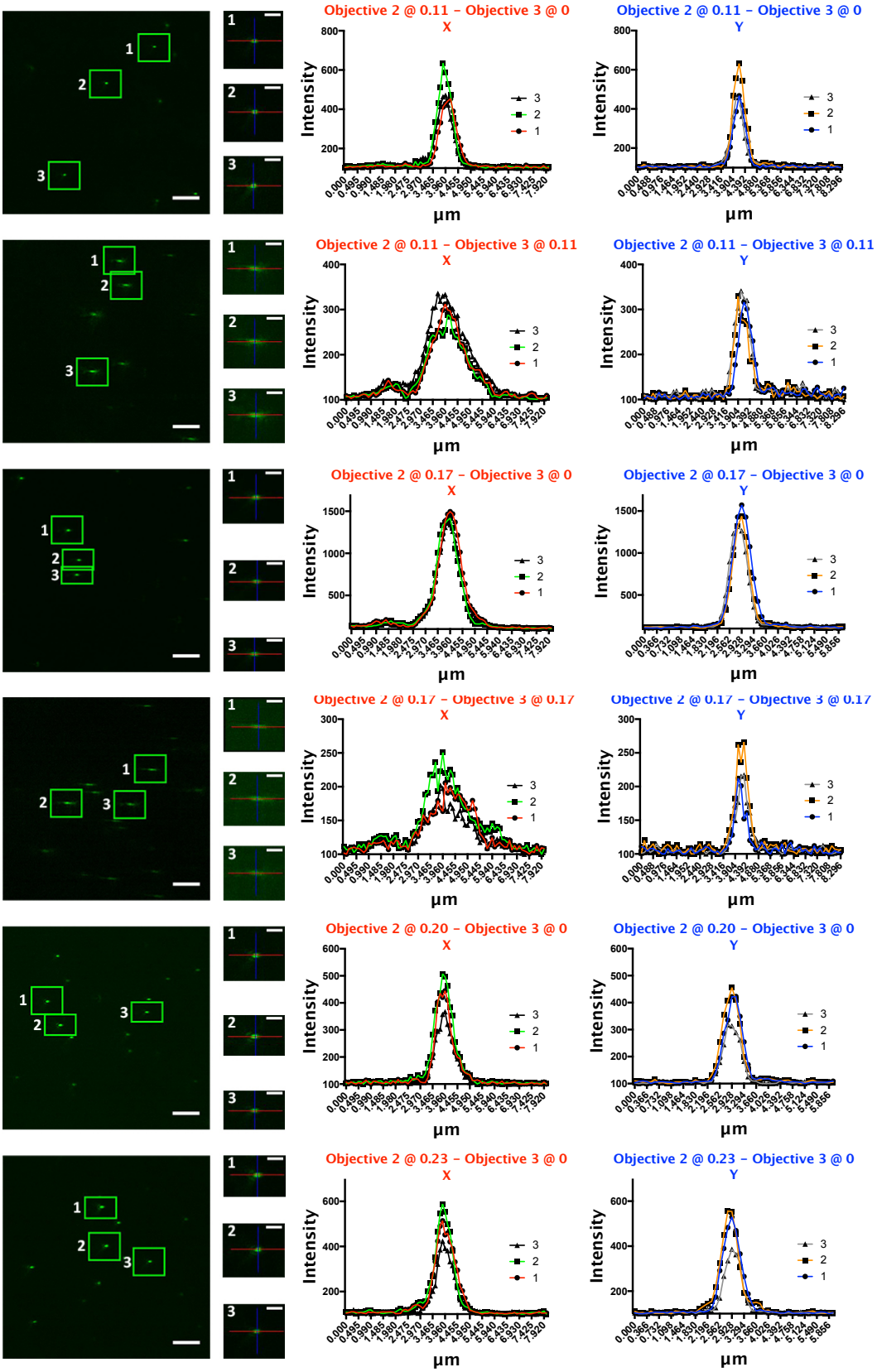

Figure 29 - Experimental calculation of the HT-LISH microscope lateral resolution (X and Y). Fluorescence images of 200 nm fluorescent beads were acquired with different O2 and O3 correction collar combination. The graphs show the intensity distribution of single beads along the X and Y dimension. This information are used to calculate the FWHM and thus the lateral resolution achievable with the HT-LISH microscope (see Table 4). Scale bar large images, 10 µm; Scale bar single beads images, 3 µm.

	O2 @ 0.11 - O3 @ 0		O2 @ 0.11 - O3 @ 0.11		O2 @ 0.17 - O3 @ 0		O2 @ 0.17 - O3 @ 0.17		O2 @ 0.20 - O3 @ 0		O2 @ 0.23 - O3 @ 0	
	µm ± StD		µm ± StD		µm ± StD		µm ± StD		µm ± StD		µm ± StD	
X	**0.7**	0.040	**1.6**	0.162	**1.0**	0.025	**1.8**	0.139	**0.8**	0.072	**0.8**	0.068
Y	**0.6**	0.007	**0.7**	0.024	**0.6**	0.041	**0.6**	0.079	**0.6**	0.003	**0.6**	0.033

Table 4 - Calculated FWHM values along the X and Y dimensions of 200 nm fluorescent beads acquired with the HT-LISH microscope using different correction collar combinations.

However, it has to be mentioned that these values were higher than the theoretically calculated ones, suggesting that the microscope was not perfectly aligned and that aberrations can thus distort the images.

Leaving aside that O2 and O3 as explained above were re-imaging without a glass coverslip, the most probable source of this issue could be that the collected light was not travelling perfectly parallel to the optical axes of the detection path. It means that the lenses and the mirrors used in the system were slightly out of axes between each other and therefore a more precise work should be carried out in order to correct for this. Nonetheless, the purpose of this work is to present a prototype of a fully functional imaging setup for the automated high throughput imaging of 3D models using light sheet microscopy. Even if the images acquired with the HT-LISH microscope were not perfectly aberrations-free, the resolution of the system was acceptable for the experimental purposes of this work mentioned above. Therefore, the correction of this misalignment was not considered as a priority at that time.

It can be also considered that, on a theoretical level, the image of an object is given by the convolution of the real object and the PSF. It means that by performing a deconvolution of the image with the PSF, the resolution can be improved. An example of this process is shown in Figure 30 where the FWHM of the deconvolved 0.11-0 collar combination image was calculated along the X and Y dimensions. Deconvolution was performed using the "2D Iterative Deconvolution" plugin in the ImageJ software.
As shown in Table 5, the resolution could be improved as the measured FWHM from the deconvolved image is 0.5 µm in X and 0.4 µm in Y, values smaller than the ones calculated before.

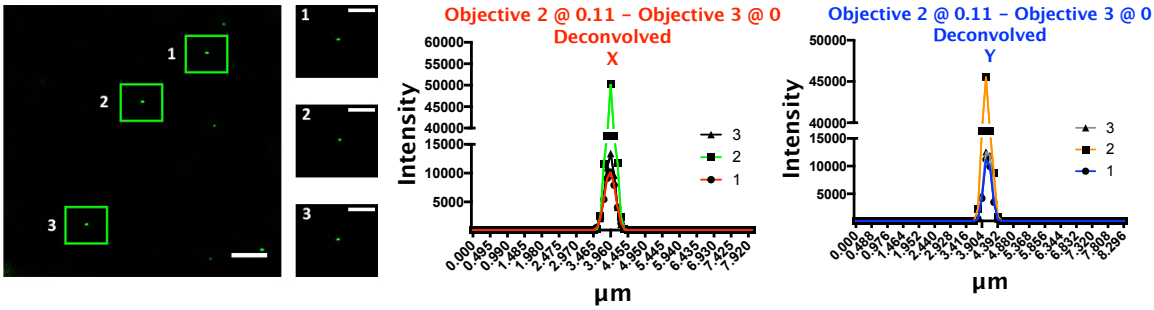

Figure 30 - Deconvolved fluorescence images of 200 nm fluorescent beads acquired with the HT-LISH microscope using the O2 @ 0.11 and O3 @ 0 correction collar combination. The graphs show the intensity distribution of single beads along the X and Y dimension. This information are used to calculate the FWHM and thus the lateral resolution achievable with the HT-LISH microscope after deconvolution (see Table 5). Scale bar large images, 10 µm; Scale bar single beads images, 3 µm.

	O2 @ 0.11 - O3 @ 0 Deconvolved	
	µm ± StD	
X	0.5	0.010
Y	0.4	0.032

Table 5 - Calculated FWHM values along the X and Y dimensions of the deconvolved 200 nm fluorescent beads images in Figure 30.

Considering axial resolution, previously in this work it has been mentioned that in LISH microscopy it mainly depends on the light sheet thickness $2W_0$. Therefore, because of the LISH parameters used in this experiment, the axial resolution should be equal to 8.6 µm. However, because the beads imaged with the microscope were much smaller than this $2W_0$ value (200nm vs 8.6 µm), a specification has to be made. It is not possible that the PSF along the Z axis of a 200nm beads is 48 times (8.6µm /0.200µm) bigger the size of the beads itself. Therefore, in this case, the Axial Resolution (R_A) can be defined by the following Ernst Abbe Axial Resolution (R_A) equation:

$$R_A = 2\lambda/NA^2$$

For the HT-LISH system, Axial Resolution (R_A) was thus equal to:

$$R_A = 2\lambda/NA_{actualmax}^2 = 2 \cdot 0.510/0.64^2 = 2.5\ \mu m$$

As for lateral resolution, this is not the only way to define axial resolution; another equation derived from the Rayleigh principle suggests that Axial Resolution (R_A) is:

$$R_A = 2\lambda n/NA^2$$

And for the HT-LISH system:

$$R_A = 2\lambda n/NA^2 = \ 2 \cdot 0.510 \cdot 1.33/0.64^2 = 3.3\ \mu m$$

In both cases, these values can be decreased by using a thinner light sheet ($2W_0 < R_A$ calculated values).

To experimentally measure the axial resolution of the HT-LISH microscope, a similar FWHM quantification used for the lateral resolution was performed. The 3D fluorescent beads sample was imaged also along the axial dimension maintaining the same collar correction (0.11-0), imaging and microscopy conditions mentioned before. A series of contiguous images were acquired with a step size of 100 nm. A 3D stack of the beads was thus collected and, as shown in Figure 31, single beads were displayed as orthogonal projection along the XY, XZ and YZ planes.

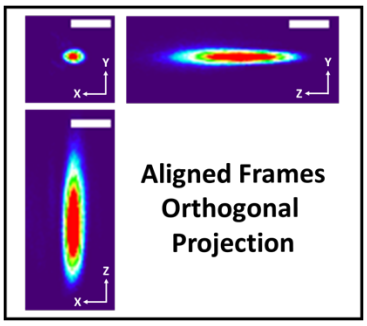

Figure 31 - Orthogonal projection along the XY, XZ and YZ planes of a single 200 nm fluorescent beads acquired with the HT-LISH microscope. Scale bar 2 μm.

The FWHM in the Z dimension measured on the XZ plane is highlighted in Table 6 and was equal to 5μm. Also in this case, the microscope misalignment was affecting the axial resolution which appeared therefore worse that the one theoretically calculated.

Importantly, as shown in Figure 31, before performing any measurements along the axial dimension, all the frames of the 3D stack had to be aligned to each other. This is because the volume acquired by the HT-LISH microscope has a rhomboid shape that needs to be processed in order to obtain a proper 3D reconstruction of the sample. This concept is extensively explained in the next section (2.3.10).

	O2 @ 0.11 - O3 @ 0
	µm
X	0.7
Y	0.6
Z	5

Table 6 - Measured FWHM along the X, Y and Z dimensions of the bead in Figure 31.

2.3.10 Volumetric Imaging with the HT-LISH Microscope

In conventional two objectives LISH microscopy, in order to reconstruct the 3D volume of a sample, it is sufficient to directly stack together the raw images acquired as illumination and detection are perfectly perpendicular to the sample (Figure 32A). Instead, the HT-LISH microscope assembled in this work is a light sheet-based system that is using a single objective for both illumination and detection. In order to acquire a 3D volume, the sheet of light is scanned along the axial direction (Z) through the sample at a precise angle γ. As shown in Figure 32B, due to this tilt, the 3D volume acquired has a rhomboid shape. Therefore, for the image reconstruction, it is not sufficient to stack

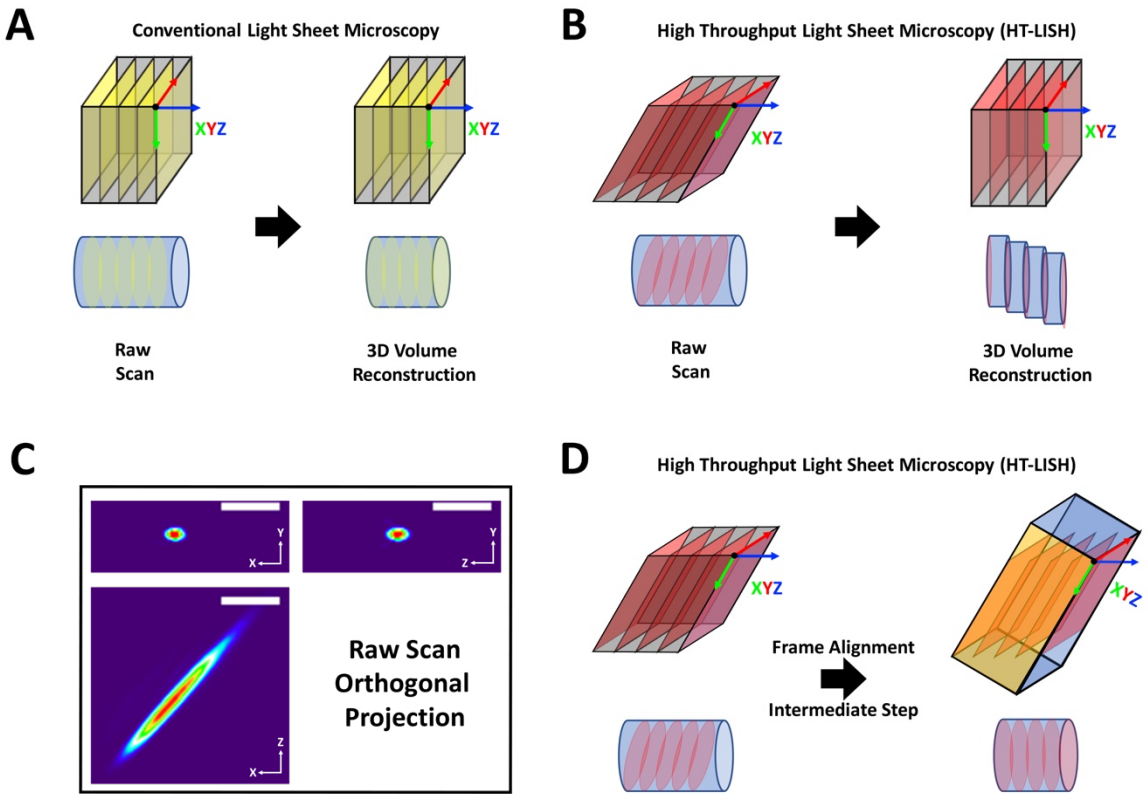

Figure 32 - Volumetric imaging with the HT-LISH microscope. (A) In conventional two objectives LISH microscopy, in order to reconstruct the 3D volume of a sample, it is sufficient to directly stack together the raw images acquired as illumination and detection are perfectly perpendicular to the sample. (B) This cannot be done with the HT-LISH microscope; the light sheet is scanned along the axial direction (Z) through the sample at a precise angle γ, therefore the 3D volume acquired has a rhomboid shape. It follows that it is not sufficient to stack together the raw frames or the real 3D spatial information of the sample are lost as the sample volume is stretched into an "unreal" shape. This is visualised in (C) where the orthogonal projection of the 200 nm fluorescent bead shown in Figure 31 is displayed directly from the raw scan. Scale bar 2 μm. (D) In order to properly reconstruct the 3D volume of a sample acquired with the HT-LISH microscope, it is necessary to perform an intermediate step where all the frames of the scan are aligned to each other.

together the raw frames or the real 3D spatial information of the sample are lost as the sample volume is stretched into an “unreal” shape (Figure 32B). This can be visualized in Figure 32C by displaying the orthogonal projection of the raw stack of the fluorescent bead used to characterise the axial PSF in Figure 31. For instance, it is not difficult to notice that the projection of the bead in the XZ plane looks very elongated and it is not parallel to the Z axes as in Figure 31. The image in this plane is in fact rotated of an angle equal to the tilt angle γ of the illumination sheet of light, in this case 35 degrees. It follows that to properly reconstruct the 3D volume of the sample maintaining the spatial information, it is necessary to perform an intermediate step where all the frames of the scan are aligned to each other (Figure 32D).

To perform this image processing in a rapid and automated way, a custom-made Matlab script was used (Supplementary Material - Chapter 6 - Section 6.1.2). The script principle is described in Figure 33. Starting from the top of the figure, the red lines correspond to single frames of the stack (n_1, n_2, ..., n_{max}) viewed from the top along their X dimension. They are ordered from the first (n_1) to the last (n_{max}) along the acquisition direction (Z). The scan angle γ between the Z axes and each frame is highlighted in green and, as described in section 3.4, for the HT-LISH was set to 35 degrees. The distance between the frames is defined as dZ and corresponds to the step size of the scanning mirror in μm. The grey area indicates the original rhomboid shape of the volume acquired (viewed from the top).

A simple method for the frames alignment is to add black pixel to each image along the X axes (a_n - black lines) so that the position of each frame in the sample is conserved but the rhomboid shape (Figure 32BD) of the volume is transformed in a squared shape. This is highlighted by the orange area in Figure 33 which corresponds to the XZ plane in Figure 32D (orange plane). Importantly, the image dimension along the Y axes remains the same as the original ($Y_{original}$) while the new size in X (X_{new}) is equal to the original pixel dimension in X ($X_{original}$ - red line) plus the black pixel added (a_{nmax}).

As shown in the bottom part of Figure 33, this concept can be more simply visualized by analysing the XY plane of each new frame. As can be noticed, each image has a column

of black pixel on the right, on the left or on both sides depending on their position in the sample.

The new size along the X dimension (X_{new}) is however constant for all the frames and is equal to:

$$X_{new} = X_{original} + a_{nmax}$$

$X_{original}$ in the HT-LISH measures 2560 pixels (Andor Zyla sCMOS camera). The parameter a_{nmax} can be calculated with trigonometry:

$$a_{nmax} = Z_{nmax} \cdot \sin\beta$$

where Z_{nmax} is the μm size of the entire scan along the Z dimension. It can be obtained by multiplying the scan step size dZ by the total number of frames n_{max}:

$$Z_{nmax} = dZ \cdot n_{max}$$

The angle β strictly depends on the scan angle γ (angle of incidence of the light sheet - Figure 12 section 2.3.2) and, as shown in Figure 33, is equal to:

$$\beta = 90 - \gamma$$

In the HT-LISH microscope β is equal to 55 degrees (90° - 35°).
Using these calculations, the Matlab script is creating an array of X_{new} by $Y_{original}$ black pixels.
This process is followed by the estimation of how many black pixels (a_n) need to be added on the left side of each image:

$$a_n = Z_n \cdot \sin\beta$$

where n is the frame number and Z_n is the μm size of scan related to the frame taken into account:

$$Z_n = dZ \cdot n$$

The a_n value is in μm and is converted in pixels by multiplying it with the image pixel size (IPS - section 3.8) in the X direction.

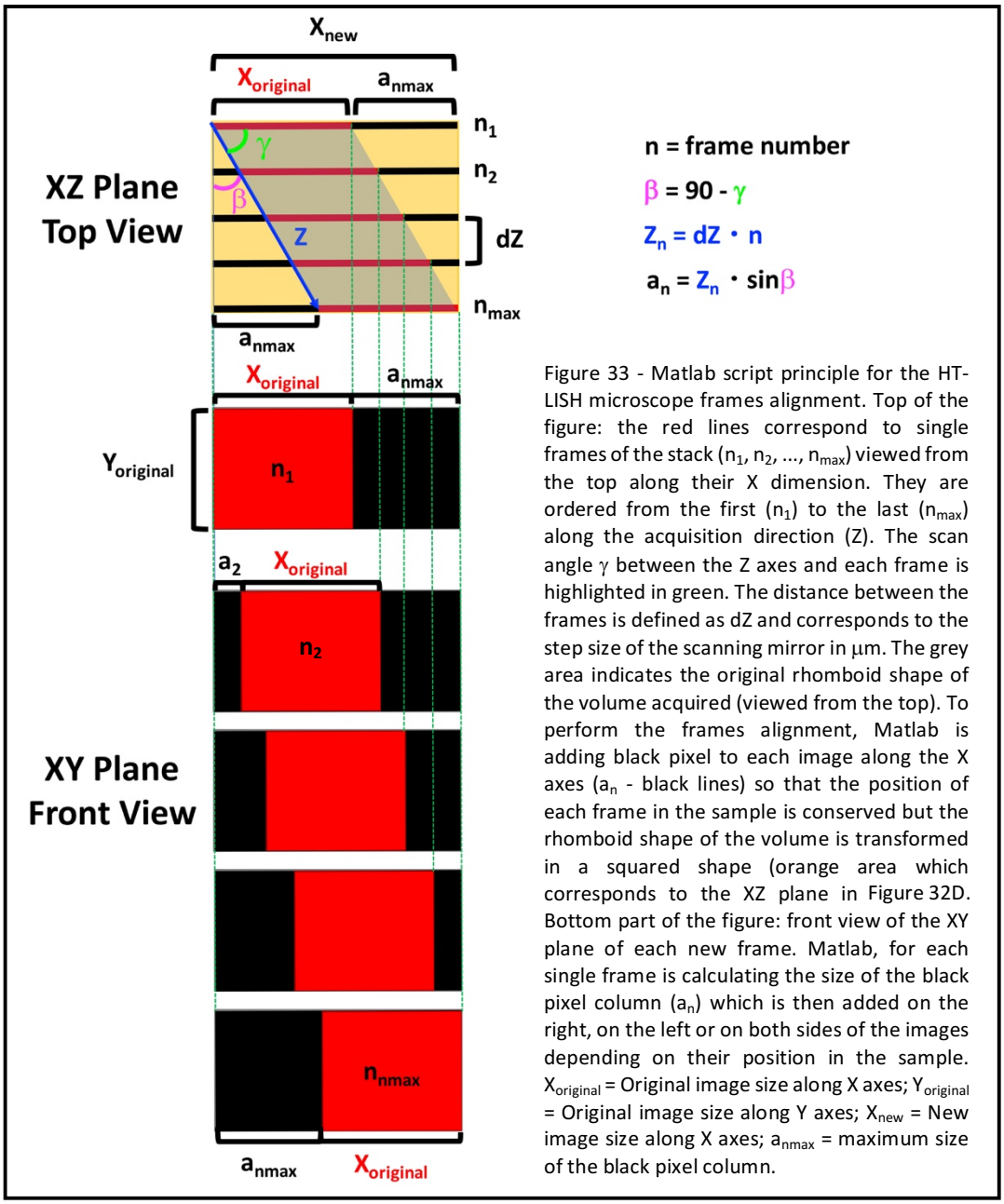

Figure 33 - Matlab script principle for the HT-LISH microscope frames alignment. Top of the figure: the red lines correspond to single frames of the stack (n_1, n_2, ..., n_{max}) viewed from the top along their X dimension. They are ordered from the first (n_1) to the last (n_{max}) along the acquisition direction (Z). The scan angle γ between the Z axes and each frame is highlighted in green. The distance between the frames is defined as dZ and corresponds to the step size of the scanning mirror in μm. The grey area indicates the original rhomboid shape of the volume acquired (viewed from the top). To perform the frames alignment, Matlab is adding black pixel to each image along the X axes (a_n - black lines) so that the position of each frame in the sample is conserved but the rhomboid shape of the volume is transformed in a squared shape (orange area which corresponds to the XZ plane in Figure 32D. Bottom part of the figure: front view of the XY plane of each new frame. Matlab, for each single frame is calculating the size of the black pixel column (a_n) which is then added on the right, on the left or on both sides of the images depending on their position in the sample. $X_{original}$ = Original image size along X axes; $Y_{original}$ = Original image size along Y axes; X_{new} = New image size along X axes; a_{nmax} = maximum size of the black pixel column.

Matlab is first automatically calculating the a_n value for each frame of the scan and is then inserting each image in the created array leaving a black pixel column on the left side of the image measuring a_n by $Y_{original}$ pixels (Figure 33).
For example, when considering the second frame (n=2) with a dZ of 1 μm:

$$Z_2 = 2 \cdot 2 = 4\ \mu m \qquad \text{and} \qquad a_2 = 4 \cdot \sin 35 = 2.3\ \mu m$$

It means that the second frame has to be inserted in the new array (X_{new} by $Y_{original}$ pixels) leaving 2.3 μm (a_2 - Figure 33) of black pixels from the left side.

Matlab was executing this script in a very fast way, it took less than a minute to obtain a new 3D series of aligned images. After this process, as in conventional light sheet microscopy, for the reconstruction of the sample 3D volume it is sufficient to stack together the new images.

In order to verify the performance of the Matlab script in a more relevant model than fluorescent beads, a volumetric acquisition with the HT-LISH microscope assembled in this work is shown in Figure 34. The sample consisted of a culture of HeLa cells stably expressing a fluorescent cell cycle indicator called FUCCI (Fluorescent Ubiquitination-based Cell Cycle Indicator) [96]. This construct will be discussed more in detail in section 2.4. Briefly, the nuclei of the cells change fluorescence depending on the cell cycle phase: they turn green if the cell is in the S/G2/M phase, red if in G1 and orange if in G1/S.
Before the imaging step, in order to create a 3D distribution, the HeLa cells were re-suspended in a solution of a low-melting point agarose (Material and Method - Chapter 5).
Figure 34 shows the orthogonal projections and the Maximum Intensity Projection (MIP) of the sample from the original raw data and from the data corrected with the Matlab script.

First of all, as explained before (Figure 32C), the orthogonal projections form the original raw scan showed that the nuclei of the cells were elongated and rotated (A and B) compared to the projections from the corrected images (D and E). Moreover, focusing on the MIP from the original raw data (C), it was evident how the spatial information are lost as, for instance, the size of all the single nuclei could not be determined when compared to the MIP of the corrected stack (F).

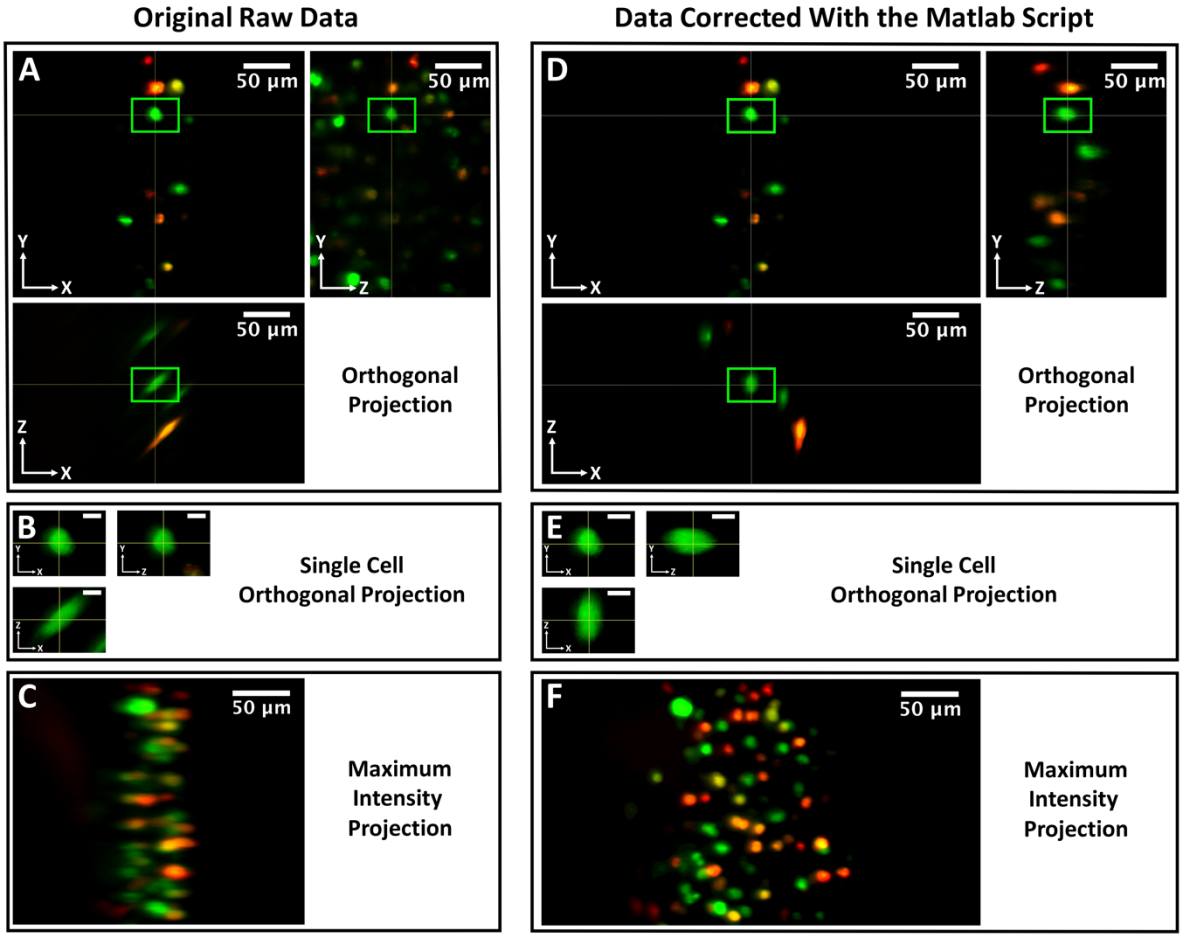

Figure 34 - Comparison between raw and corrected data of a volumetric acquisition of a 3D distribution of HeLa-FUCCI cells with the HT-LISH microscope. To create a 3D distribution, the HeLa cells were re-suspended in a solution of a low-melting point agarose. (A, D) Orthogonal projection of raw data (A) and corrected data with the Matlab script (D). (B, E) Orthogonal projection of raw data (B) and corrected data with the Matlab script (E) of a single cell. Scale bar 3 µm. (C, F) Maximum Intensity Projection (MIP) of the entire scan from the raw data (C) and from the data corrected with the Matlab script (F). Acquisition parameters: LISH thickness ($2W_0$), 8.6 µm; Rayleigh range ($2Z_r$), 319 µm; Step size, 1 µm; Number of frames, 193; Exposure time green channel, 100 ms; Exposure time red channel, 250 ms.

Figure 35 shows different views of the 3D volume of the HeLa-FUCCI sample reconstructed in 3 dimensions after the intermediate step of the frame alignment performed with the custom-made Matlab script.

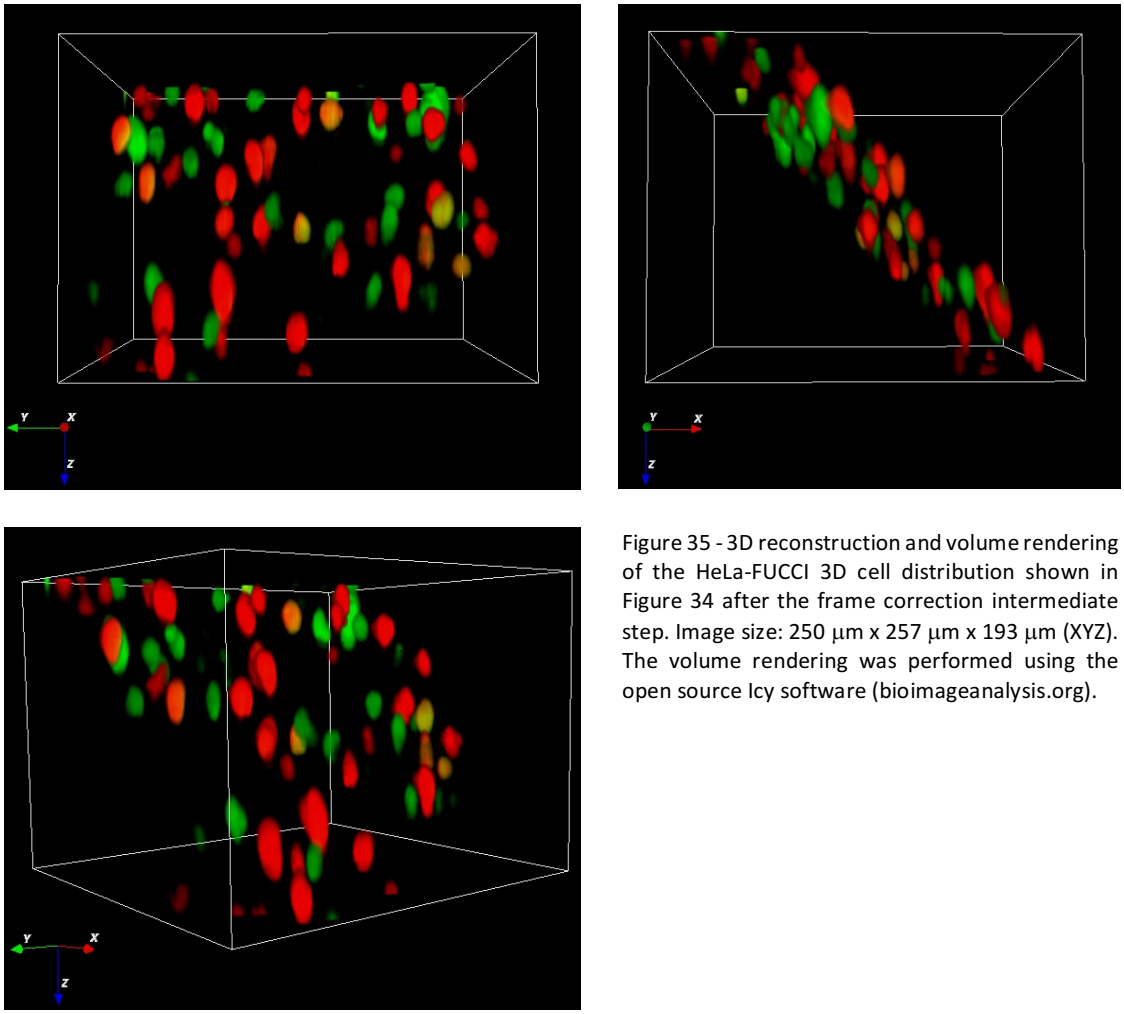

Figure 35 - 3D reconstruction and volume rendering of the HeLa-FUCCI 3D cell distribution shown in Figure 34 after the frame correction intermediate step. Image size: 250 μm x 257 μm x 193 μm (XYZ). The volume rendering was performed using the open source Icy software (bioimageanalysis.org).

2.3.11 Controlling the HT-LISH Microscope

As previously described in this work, to acquire a 3D volume, the HT-LISH microscope is using a tilted thin sheet of laser light (Toptica Photonics iBeam Smart 488-S) that is scanned through the sample with a scanning mirror (Cambridge Technologies 6M2412B40S100S1, 6240HA, 67124H-1, 611240, 6010-25-040). A camera (Andor Zyla 5.5 sCMOS) is automatically acquiring an image for each position of the light sheet in the sample. Therefore, there was the need of a precise synchronization between the scanning mirror, the camera and the laser light. In order to achieve long term imaging of living samples, a Stage Top Incubator (okolab H301-K-FRAME) was mounted on the microscope. In addition, one fundamental feature of the microscope assembled in this work, is the ability of acquiring multiple samples in an automated way. This guarantees its application in high throughput studies. This was realized by installing on the system a motorized stage (Marzhauser SCAN IM 130 x 85 00-24-625-0000) which obviously has to communicate with all the other hardware of the microscope.

In order to control all the different part of the HT-LISH microscope prototype and to guarantee a precise synchronization between them, a combination of three software was used: MicroManager, LabVIEW and Andor Solis. The entire system was controlled by a custom assembled desktop computer running Windows 7 and equipped with a Gigabyte GA-Z170X Intel Z170 motherboard mounting an Intel Core i7 6700K CPU @ 4.00 GHz processor and 16 GB of RAM. Importantly, the Andor Zyla sCMOS camera of the HT-LISH microscope requires a writing speed of 1.1 GB/s to properly work. The PC was therefore equipped with 4 Samsung 850 Evo Basic 250 GB Writing Speed 520 MB/s SSDs linked in RAID 0 so that a theoretical writing speed of 2.08 GB/s was achieved.

A scheme of the connections between the hardware and the software of the HT-LISH microscope is shown in Figure 36.

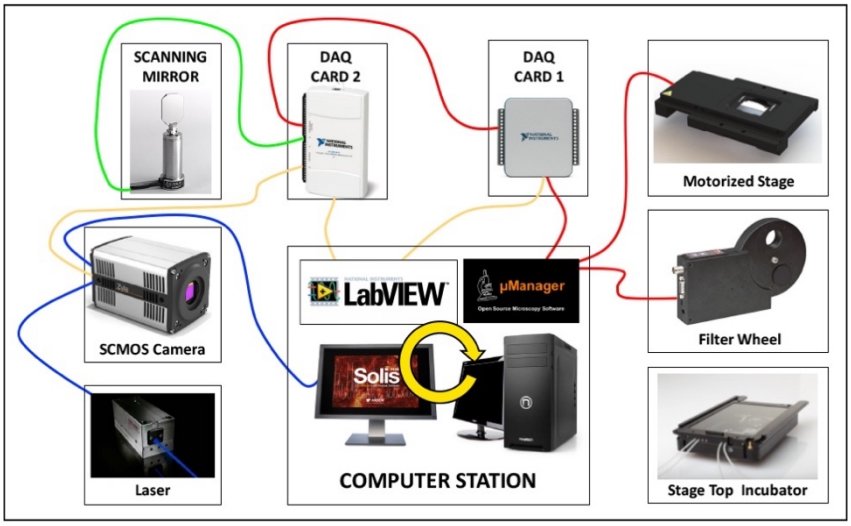

Figure 36 - Diagram showing the connections between the hardware and the software of the HT-LISH microscope.

LabVIEW is a system engineering software from National Instrument™ that offers a graphical programming approach for the custom configuration of any hardware. It is using a Data Acquisition (DAQ) card to send or receive analogic or digital signals that can be used to control any type of instrument. In the HT-LISH system two DAQ cards were used. The DAQ card 1 (National Instrument™ 3008 - Figure 36) was programmed to simply trigger/start the image acquisition (from MicroManager), the DAQ card 2 (National Instrument™ 6211 - Figure 36) was instead used to precisely control the synchronization between the scanning mirror and the Andor Zyla sCMOS camera. Importantly, the DAQ card 2 was under direct control of DAQ card 1. As previously explained in section 2.3.7, the scanning mirror changes its angle depending on the input voltage value that is receiving and for each position the camera is acquiring an image of the sample. The DAQ card 2 was therefore programmed with LabVIEW (LabVIEW program diagram in Supplementary Material - Chapter 6 -Section 6.1.3) to step different voltage values to the scanning mirror (Figure 37 - green line) so that for each step the camera was automatically acquiring an image (Figure 37 - blue line). This process was repeated for each fluorescence channel that needed to be acquired (Figure 37). Importantly, the Laser box (Toptica Photonics iBeam Smart 488-S) was directly linked to

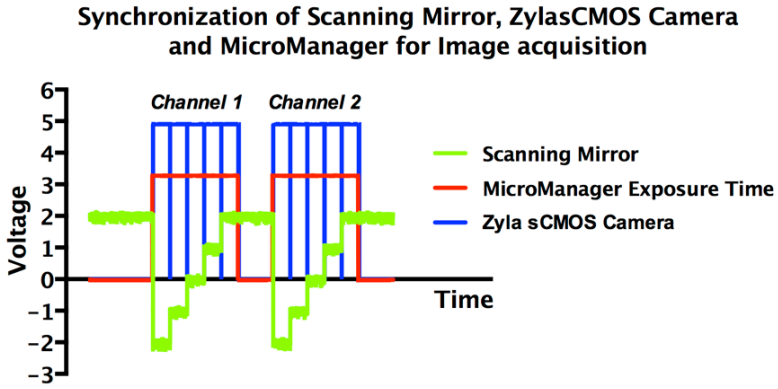

Figure 37 - Graph displaying the synchronization between the scanning mirror (green line), the Andor Zyla sCMOS camera (blue line) and the exposure time controlled by the MicroManager software (red line).

the camera so that the light was automatically switched on only when the camera was acquiring. The laser power was instead controlled with the software provided by the Laser box manufacturer.

The Graphic User Interface (GUI) created with LabVIEW and shown in Figure 38 was designed for the acquisition of two fluorescence channels and allowed the user to choose the length of the scan (Number of frames), the starting voltage (Starting Voltage), the step size of the scanning mirror (Increment) and the camera exposure (Exposure time (per frame)) independently for each channel.

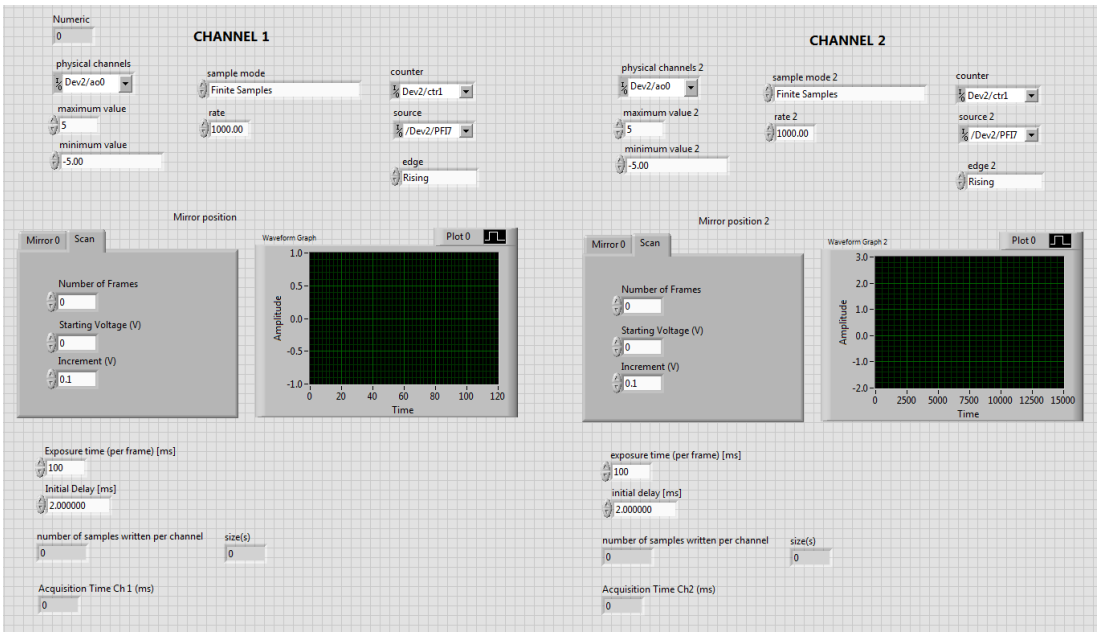

Figure 38 - Custom-made LabVIEW Graphic User Interface (GUI).

In Figure 37, the number of frames was set to 5, the starting voltage was set to -2 Volts, the increment was set to 1 volt and the camera exposure time was set to 100 ms.

MicroManager (Open Imaging) is an open source software that has been developed to control any type of microscopes. In the HT-LISH system, MicroManager was used to trigger the entire image acquisition process and mainly controlled the motorized stage and the filter wheel (Thorlabs FW102C) for the different fluorescence channels. Through the *Multiple-Dimension Acquisition* panel shown in Figure 39, this software allowed to set how many fluorescence channels needed be acquired and the relative camera exposure time. Importantly, as shown by the red line in figure 37, the camera exposure time selected had to match the length (time) of the scan of each channel. The *Multiple-Dimension Acquisition* panel also enabled to perform time-lapse experiments and it consented to control the motorized stage positions. This latter setting is very important for the HT-LISH microscope as it introduced the high throughput approach so that multiple samples could be imaged in different fluorescence channels (and eventually also over time) in a fully automated way. As mentioned above, MicroManager was selected as the principal trigger of the entire image acquisition process. When pressing the *Acquire!* button (Figure 39), this software was sending an impulse to the DAQ card 1 (Figure 36) which in turns triggered the DAQ card 2 (Figure

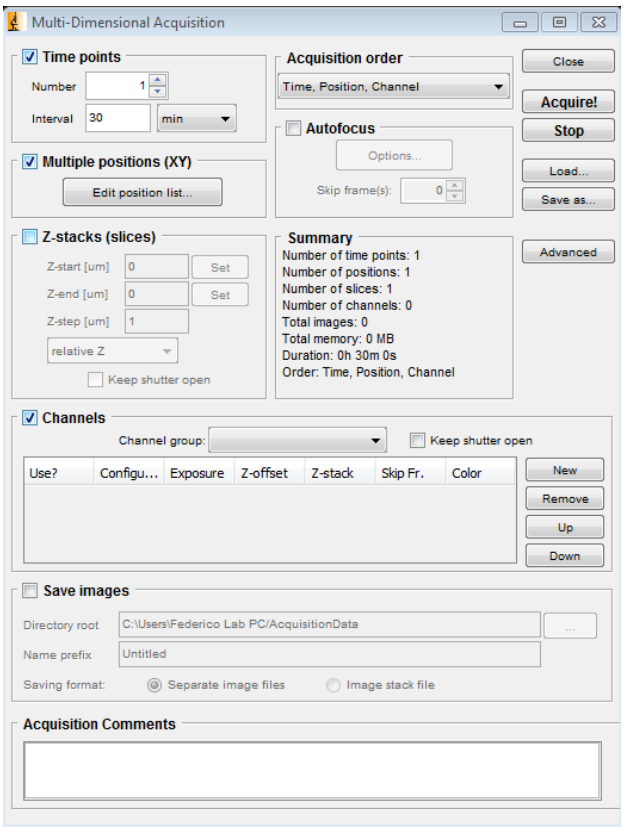

Figure 39 - MicroManager *Multi-Dimensional Acquisition* panel. It allows to set how many fluorescence channels can be acquired and the relative camera exposure time. It also enables to perform time-lapse experiments and it consents to control the motorized stage positions.

36) and the image acquisition could thus start. This process was repeated every time there was a new trigger signal within the image acquisition ether given by the change of the fluorescence filter or by the movement of the motorized stage to a different position.

In summary, this is how the HT-LISH microscope acquisition has been programmed to operate. Once all the parameters are set, MicroManager triggers the DAQ card 1 which in turn triggers the DAQ card 2. The acquisition starts and a series of images are collected by the camera for each different position of the scanning mirror. If the acquisition of multiple channels is selected, every time the filter wheel is changing the fluorescent filter, a new impulse is sent and the acquisition process is repeated for the other channel. Moreover, if multiple samples are selected, after each scan, the motorized stage moves to different location. Every time is reaching a new imaging position a new impulse triggers the DAQ card 1 and, for each fluorescence channel selected, the image acquisition process starts again. This happens also when performing time lapse experiments: for each time points selected, Micromanager automatically triggers the DAQ card 1.

The physical image acquisition was performed using the Andor Solis software. From the software GUI shown in Figure 40 it can be notice that the *Acquisition Mode* of the camera was set to *Kinetic Series* which means that multiple images were automatically acquired. The length of this series could be set in the *Kinetic Series Length* panel and it had to be equal to the scan length set in LabVIEW plus one frame (because LabVIEW start counting from 0 while MicroManager from 1). The *Trigger Mode* had to be set on *External Exposure* which means that the camera will start acquiring only when triggered by an external input that was also defining the camera exposure time for each frame. As explained before, in the HT-LISH microscope this was controlled by the custom LabVIEW program through the DAQ card 2. These settings were sufficient if the image acquisition was required for one channel, in one image position and for one time point. In the opposite case, a custom-made Andor script needed to be used. It was utilized to keep the camera always sensitive to any input coming from an external source (in this case

the DAQ card 2). Within the script, the number of acquisition could be set depending on the number of fluorescence channels, positions or time points that needed to be acquired. For instance, if the user needs to acquire two channels, this number has to be set on 2. If there is the necessity to image two channels for two samples in two different position, the number has to be set on 4.

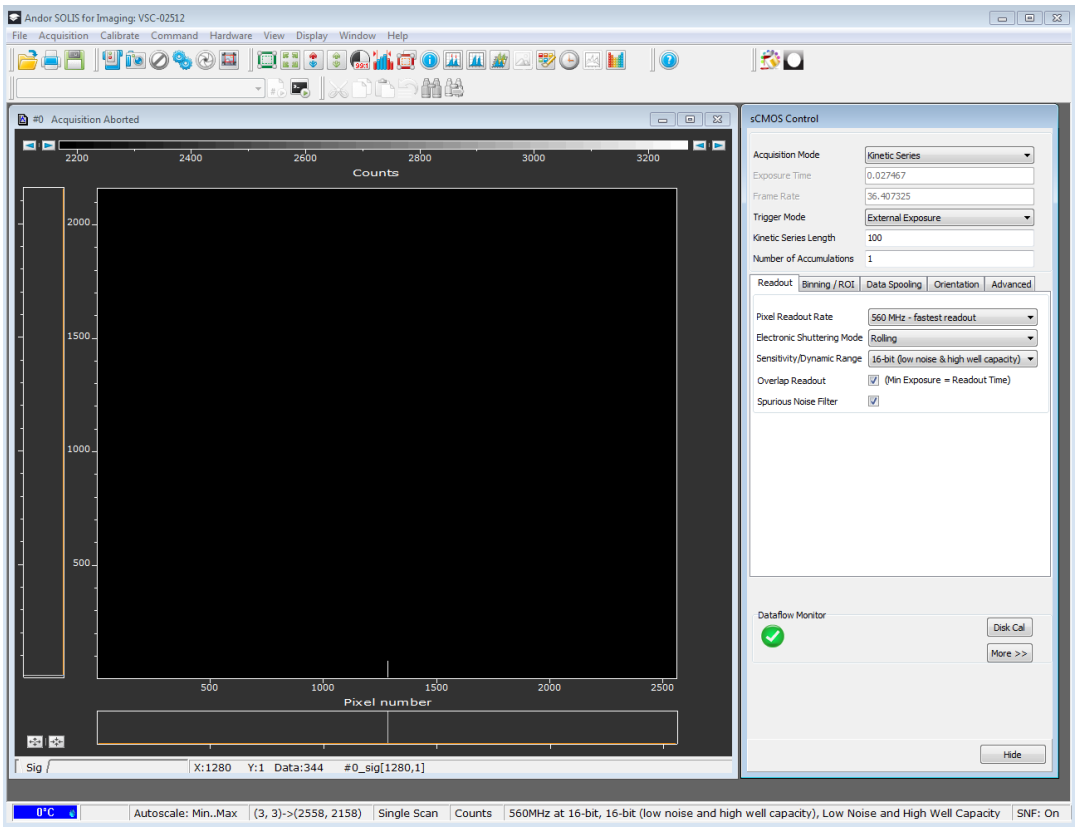

Figure 40 - Andor Solis software Graphic User Interface (GUI) to controls the Andor Zyla sCMOS camera.

2.3.12 Summary: the current version of the HT-LISH microscope

In Figure 41 is presented the complete scheme of the current version of the HT-LISH microscope assembled in this work. The parts list of all the components used in this system can be found in the Supplementary Material (Chapter 6 - Section 6.1.1).

A summary of the HT-LISH microscope essential features/parameters is presented below.

Magnification:
The HT-LISH microscope currently mounts three 40x objectives, a Zeiss 40x 1.2 NA Water Immersion objective as O1, a Nikon 40x 0.95 NA Air objective as O2 and a Nikon 40x 0.6 NA Long Working Distance (LWD) objective as O3. **The overall Magnification (M_f) of the system is 53.2x** (Section 2.3.3).

Field of view (FOV):
The HT-LISH microscope **FOV** is of **250 μm in X and 257 μm in Y** (Section 2.3.8).

Numerical Aperture (NA):
The **NA** of the HT-LISH microscope is **0.64** (Section 2.3.4).

Light Sheet:
The light sheet is generated with a **cylindrical lens** (Cyl) (Section 2.3.6).
The light sheet thickness (**$2W_0$**) and length (Rayleigh Range **$2Z_r$**) can be controlled by an **adjustable vertical slit** (Slit) (Section 2.3.6).
The maximum FOV of the light sheet (**width**) is of **247 μm** (Y dimension on the camera chip) (Section 2.3.6).

Camera:
The HT-LISH microscope is mounting a **Andor Zyla 5.5 sCMOS Camera** (Section 2.3.3).

Scanning System:

The light sheet is scanned through the sample with a **SCanning Mirror** (ScM) installed in a plane conjugate with the Back Focal Plane (BFP) of the objective O1 (Section 2.3.5).

Voltage to μm conversion: **1 μm = 0.01535 Volt** (Section 2.3.5).

The maximum **scan rage** (Z) is around **250 μm** (≈ ±1.9 Volt) (Section 2.3.5).

Scanning Angle (γ):

The objective O1 is illuminated the samples with a sheet of light tilted of **35°**. The objective O3 and the Andor Zyla 5.5 sCMOS camera are thus tilted of 35° from the optical axes of the objective O2 (Section 2.3.4).

Experimentally calculated resolution:

X = 0.7 μm, Y = 0.6 μm and Z = 5 μm (Section 2.3.9).

Laser:

Blue Laser at **488 nm**.

Figure 42 is showing photographs of some HT-LISH microscope components.

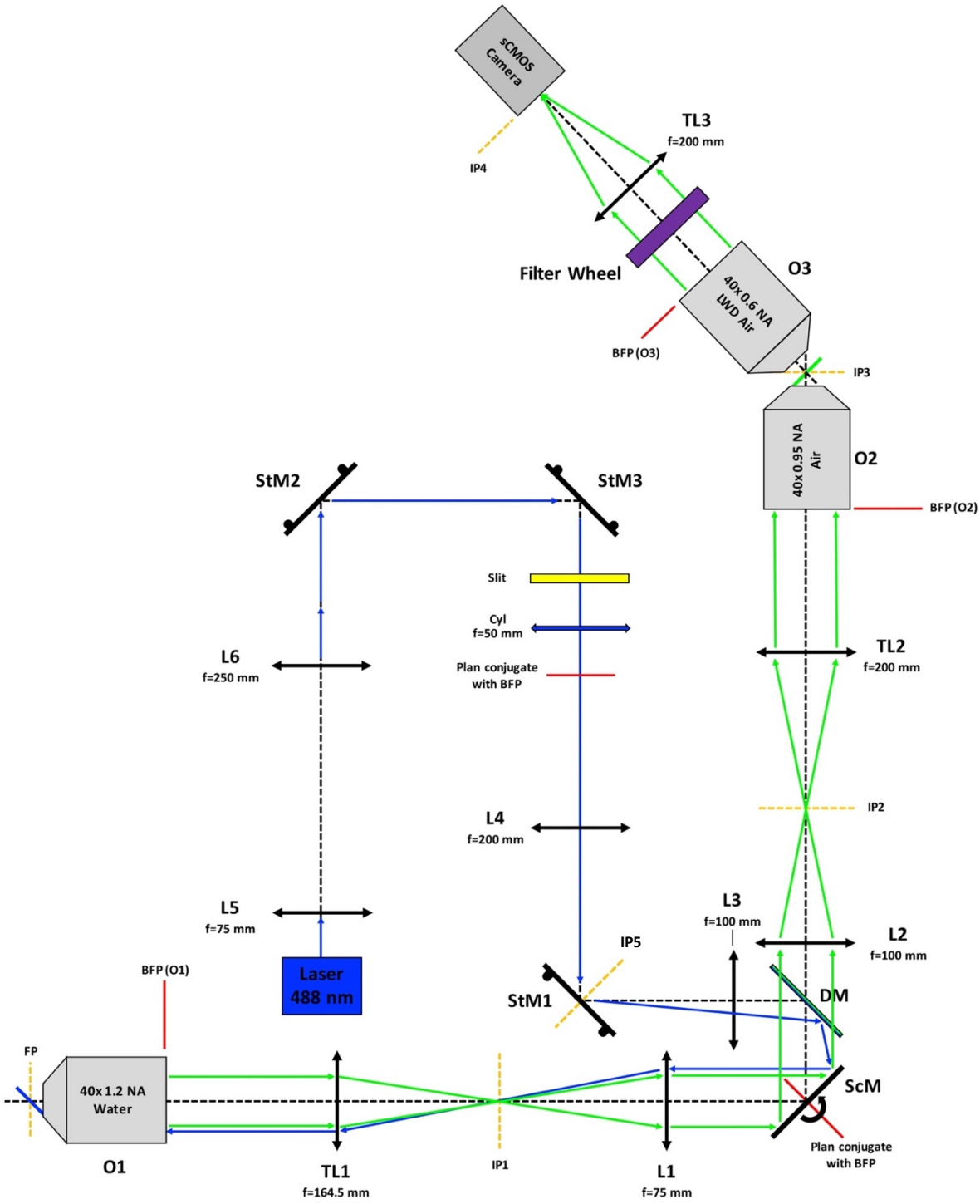

Figure 41 - Complete diagram of the current version of the HT-LISH microscope assembled in this work. O, Objective; BFP, Back Focal Plane; TL, Tube Lens; IP, Image Plane; L, Lens; ScM, Scanning Mirror; DM, Dichroic Mirror; StM, Steering Mirror; Cyl, Cylindrical lens. The blue line indicates the illumination light, the green line shows the collected light.

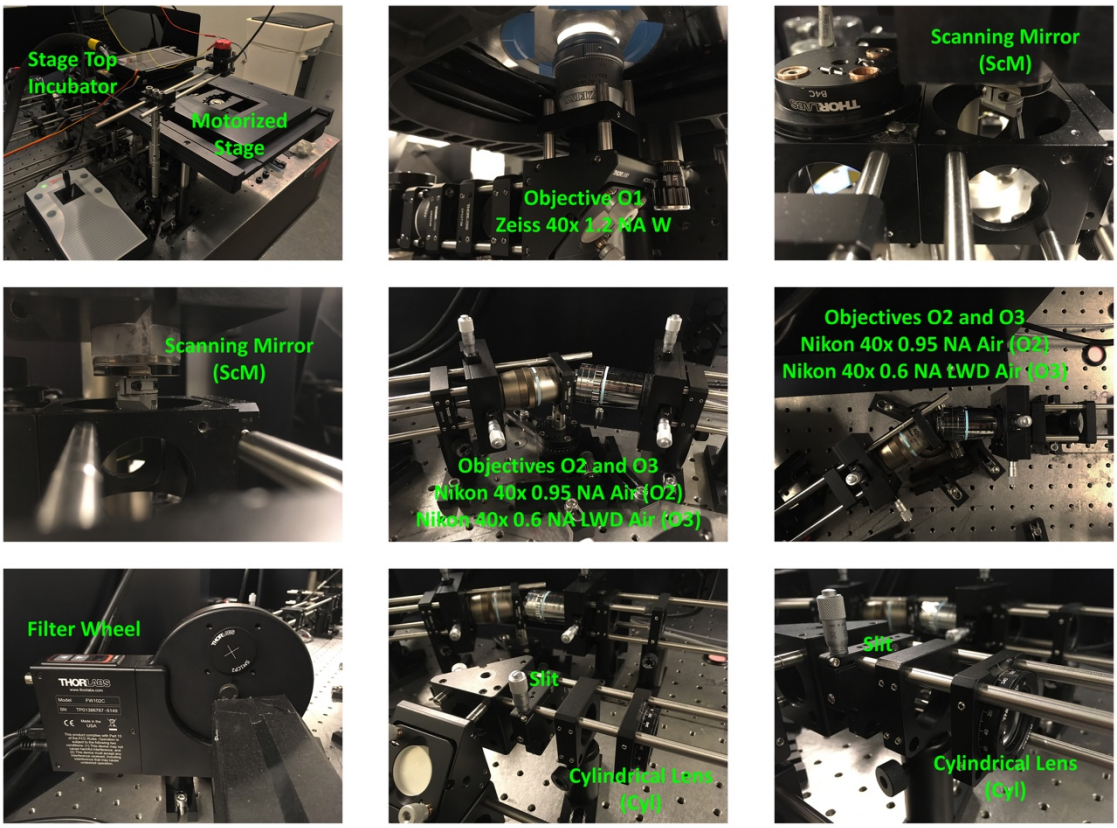

Figure 42 - Photographs of some components of the HT-LISH microscope developed in this work.

2.4 Applications of the HT-LISH System

This section presents the capabilities of the HT-LISH microscope prototype assembled in this work in terms of automated volumetric imaging. The results highlight its ability to acquire stack of images in 3 dimensions (3D - xyz), in 3 dimensions with multiple channels (3D - xyzc) and in 4/5 dimensions (3D over time/multi-channel xyzct) with a particular focus on the main application in High Throughput Imaging studies.

2.4.1 HT-LISH microscope for the Imaging in 3 Dimensions with Multiple Channels

The HT-LISH system developed in this work is a light sheet microscope and as such, it should be able to image 3D models in their depth. A first demonstration of this capability has been presented in Figure 34 (section 2.3.10) where a 3D distribution of HeLa cells expressing a fluorescent cell cycle indicator (FUCCI) was successfully imaged and rendered in 3D (Figure 35).

The 3D distribution of HeLa-FUCCI cells presented in Figures 34 and 35 is a relatively simple specimen to image; the cells are distant from each other thus the light scattering is reduced. Cellular spheroids are a more suitable 3D model to evaluate the capabilities of the HT-LISH microscope. In fact, as explained in the introduction chapter (Chapter 1) of this work, cellular and multi-cellular spheroids started gaining popularity in cancer research [15, 16, 27] as they can better simulate the tumour behaviour [15-17, 27]. They are in fact aggregates of cells that form a heterogeneous environment with physiological cell-cell and cell-extracellular matrix (ECM) interactions. As in cancer, spheroids express different gradient of oxygen, nutrients and metabolites. These 3D cell culture models have also a gene expression pattern very similar to the one found in cancer tissues [15-17, 27]. The dens architecture makes the spheroids a more challenging sample to image due to the increased light scattering.
Therefore, the HeLa-FUCCI cell line was used to produce cellular spheroids (Material and Methods - Chapter 5) that were then imaged with the HT-LISH microscope. An example is shown in Figures 43 where the volume of two different 350/400 μm HeLa-FUCCI

cellular spheroid was acquired. The fluorescence images in Figure 43A correspond to the Maximum Intensity Projection (MIP) of the HeLa-FUCCI spheroids in the red and green

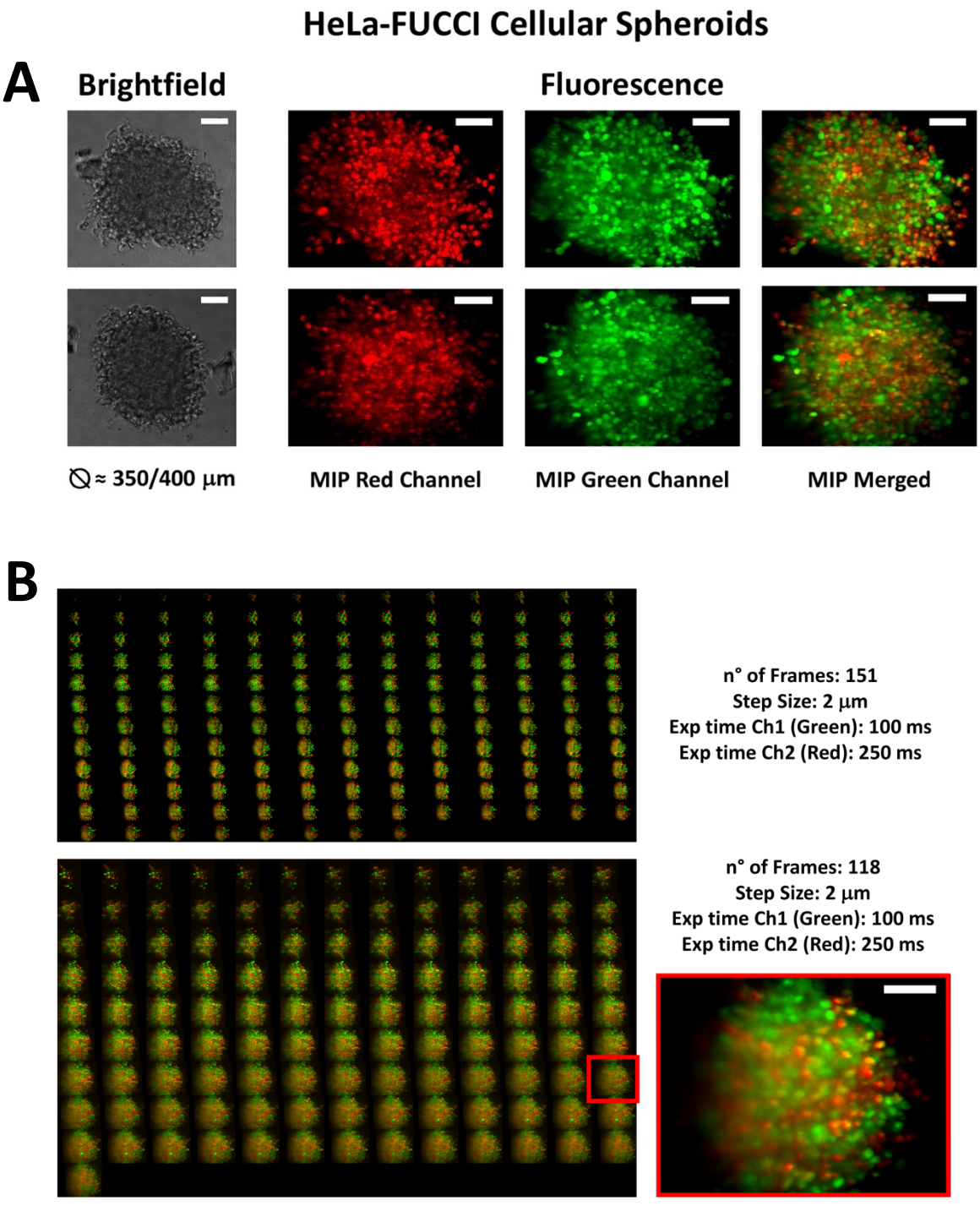

Figure 43 - HT-LISH microscope for the Imaging in 4 Dimensions. (A) Brightfield and two channels fluorescence Maximum Intensity Projection (MIP) images of two 350/400 μm HeLa-FUCCI spheroids. (B) Single frame 2D visualisation of the spheroids in (A). Acquisition parameters: LISH thickness ($2W_0$), 8.6 μm; Rayleigh range ($2Z_r$), 319 μm; Step size, 2 μm; Number of frames, 151 (top) and 118 (bottom); Exposure time green channel, 100 ms; Exposure time red channel, 250 ms. Scale bar Brightfield images, 100 μm; Scale bar Fluorescence images, 50 μm.

channels. For the first sample, 151 frames per channel were acquired, for the second, 118 frames. For both the samples, the light sheet thickness ($2W_0$) was set to 8.6 μm, the Rayleigh range ($2Z_r$) to 319 μm (Section 2.3.6 - Table1) and the step size to 2 μm.
In Figure 43B each of the frames (151 or 118) and thus all the different planes of the spheroid are visualised as a single 2D image.

These results validated one of the capability of the HT-LISH microscope prototype developed in this work. The microscope enabled the multiple fluorescent channels volumetric imaging of a 3D models which in this case is represented by a cellular spheroid.

It is important to highlight that for the HT-LISH system, as mentioned in section 2.3.2 (Figure 13), the depth (z) that can be reached in the sample depends on the LISH tilt γ angle and the LISH Rayleigh range $2Z_r$:

$$z = 2Z_r \cdot \sin\gamma$$

The γ angle is set to 35° (Section 2.3.4) and the Rayleigh range to 319 μm therefore, the maximum depth z that can be reached by the HT-LISH microscope with the current settings is:

$$z = 2Z_r \cdot \sin\gamma \quad \rightarrow \quad z = 319 \cdot \sin 35 = 183\ \mu m$$

As represented in Figure 44, it means that it is not possible to acquire the entire volume of a 350/400 μm cellular spheroid but only a portion of it can be imaged (as for the samples in Figure 43). This is related with the final magnification (M_f) of the system; the HT-LISH microscope developed in this work has a final magnification of 53.2x (40x times 1.33 - Section 2.3.3). For these type of samples, a more suitable magnification would be

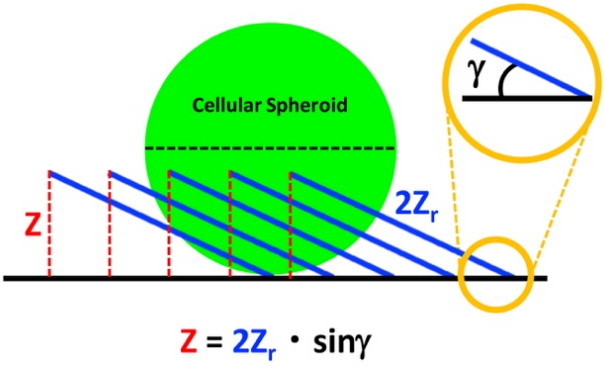

Figure 44 - Graphical representation of the relationship between Light Sheet γ angle, maximum depth (z) achievable and Light Sheet length ($2Z_r$) in the HT-LISH microscope. Smaller γ angle means smaller depth (z) and thus a smaller portion of the sample can be imaged.

a 26.6x, easily achievable by using three objectives (O1, O2 and O3 - Figure 41) with a 20x magnification. As mentioned in section 2.3.1, in order to obtain the magnification labelled on the objective, the tube-lens focal length (f_{TL}) has to be specific depending on the objective manufacturer. For instance, Nikon tube lenses need to have a 200 mm focal length, Zeiss tube lenses 164.5 mm. If the objectives are fully corrected for optical aberration within their body, it is possible to change the magnification by using tube lenses with a different focal length. For instance, a Nikon 40x coupled with a 100 mm tube lens will give a magnification of 20x. In a Zeiss imaging system, the situation is different. Optical aberrations are only partially corrected in Zeiss objectives, and a 164.5 mm Zeiss tube lens is specifically required to guarantee an aberration-free imaging system. Zeiss sells only tube lenses with a focal length of 164.5 mm, therefore, the use of a tube lens with a shorter focal length from another manufacturer would reduce the magnification but the images acquired would be highly distorted by optical aberration. It follows that this strategy could not be applied to the HT-LISH microscope as only the Zeiss 40x 1.2 NA water Immersion objective was available as O1. If a 20x magnification wants to be achieved, the only solution is to replace it with a 20X objective or, for instance, with a Nikon high NA water immersion objective whose magnification can be calibrated depending on the tube lens used.

Regarding the experiment performed in Figure 43, a further important specification has to be made. The FUCCI construct is based on a pair of plasmids called FUCCI Green and FUCCI Red [96] . FUCCI Green is based on the green fluorescent protein monomeric Azami Green (mAG), FUCCI Red on the red shifted fluorescent protein monomeric Kusabira Orange2 (mKO2). The Fluorescent spectrum of mAG and mKO2 is illustrated in Figure 45. FUCCI Green has an excitation peak at 492 nm and an emission peak at 505 nm. FUCCI Red is excited at 551 nm and emits at 565 nm. It follows that blue light and green light are valid choices to excite FUCCI Green and FUCCI Red respectively. The HT-LISH microscope is only equipped with a 488 nm laser (blue light) which is an optimal

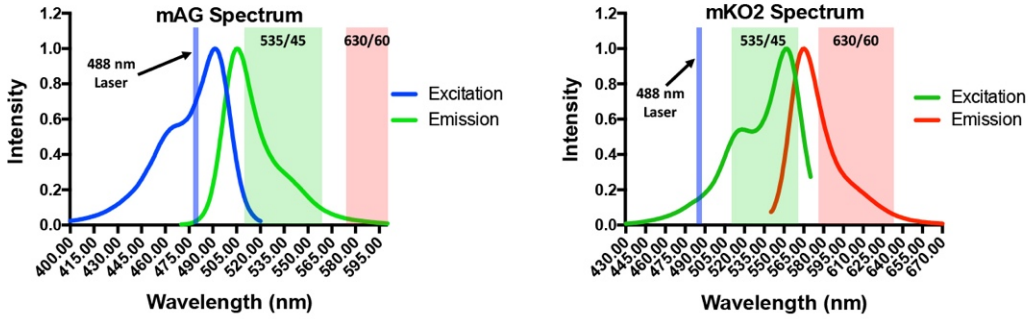

Figure 45 - Fluorescent spectrum of Azami Green (mAG) and Kusabira Orange2 (mKO2) from FUCCI Green and FUCCI Red respectively. The HT-LISH microscope is equipped with only a 488 nm laser. (A) Emission filters used in the HT-LISH microscope: 535/45 nm for the green channel and 630/60 nm for the red channel. The 630/60 nm filter is not optimal for the collection of the mKO2 fluorescence signal but it is however required to avoid the overlap with the mAG emission wavelength. The 535/45 nm emission filter is sufficient but not optimal to collect the mAG fluorescent signal and, more important, there is a clear wavelength overlap with the fluorescence coming from the mKO2 protein. (B) Ideal emission filters for the imaging of FUCCI Green and FUCCI Red: 510/43 nm for the green channel and 630/60 nm for the red channel.

wavelength for the excitation of FUCCI green but not for FUCCI red. However, from the spectrum of mKO2 in Figure 45, it can be noticed that, even if minimally, the 488 nm light can be used also for the illumination of FUCCI red. Obviously, the exposure time or the light power have to be increased.

Because a single wavelength is used to excite two different fluorophores, the separation between the green and red fluorescence is only determined by the emission filters. As indicated in Figure 45, for mAG, a 535/45 nm emission filter was available, for mKO2 a 630/60 nm filter was used. From the mKO2 spectrum it can be observed that the 630/60 nm filter is not optimal for the collection of the mKO2 fluorescence signal but it is

however required to avoid the overlap with the mAG emission wavelength (only a negligible signal from mAG is picked up by this filter). The situation is different for the 535/45 nm filter. From the mAG spectrum in Figure 45, it can be noticed that this emission filter is sufficient but not optimal to collect the mAG fluorescent signal. And more important, there is a clear wavelength overlap with the fluorescence coming from the mKO2 protein. However, this issue was solved with a simple image post processing step performed with an ImageJ plugin called *Spectral Unmixing*: the user can calculate the wavelength overlap ratio between the two fluorophores that is then used to correct the fluorescence signal from each image. This strategy was also applied to the other FUCCI-based experiments described in this section 2.4.

2.4.2 HT-LISH microscope for the Imaging in 5 Dimensions: Multi-channels Timelapse

As previously mentioned in this work, the HT-LISH microscope is equipped with a stage top incubator. This guarantees the supply of gas (CO_2) to the sample while maintaining a precise level of temperature and humidity. Therefore, the specimens can be kept alive over long periods of time directly on the microscope stage. This feature should enable the HT-LISH to perform time lapse experiments and thus to precisely follow a cellular process of interest over time (4/5D imaging).

The HeLa-FUCCI cell line can be an interesting sample for this experiments as the nucleus of each cell is changing fluorescence depending on the cell cycle phase. Therefore, this cell line is a perfect specimen to follow over time.
As in the previous section, the HeLa-FUCCI cells were used to produce a cellular spheroid (≈200 μm) (Material and Methods - Chapter 5). For the image acquisition process, the spheroid was placed in a glass bottom dish with a solution of low-melting agarose and culture medium to minimize the sample movements due to any environmental vibrations. The spheroid was imaged over a period of 24 hours with a time interval of 30 min. A total of 131 frames per time-point were acquired in two channels (red and green) with a LISH thickness ($2W_0$) of 8.6 μm, a Rayleigh range ($2Z_r$) of 319 μm (Section 2.3.6 - Table 1) and a step size of 2 μm.

The results of this experiment are visualised in Figure 46. In particular, Figure 46A shows Maximum Intensity Projection (MIP) of the HeLa-FUCCI spheroids over different time-points. By focusing the attention on singe nuclei, it can be noticed that over a period of 24 hours some of the cells are going through different cell cycle phases. Figure 46B displays the images of single nuclei corresponding to the highlighted regions in Figure 46A (yellow squares 1, 2, 3 and 4). For instance, it can be observed that the cells indicated with a white arrow are cycling from the G1 (red) to the S/G2/M (green) phase passing through the G1/S (orange) cell cycle phase.

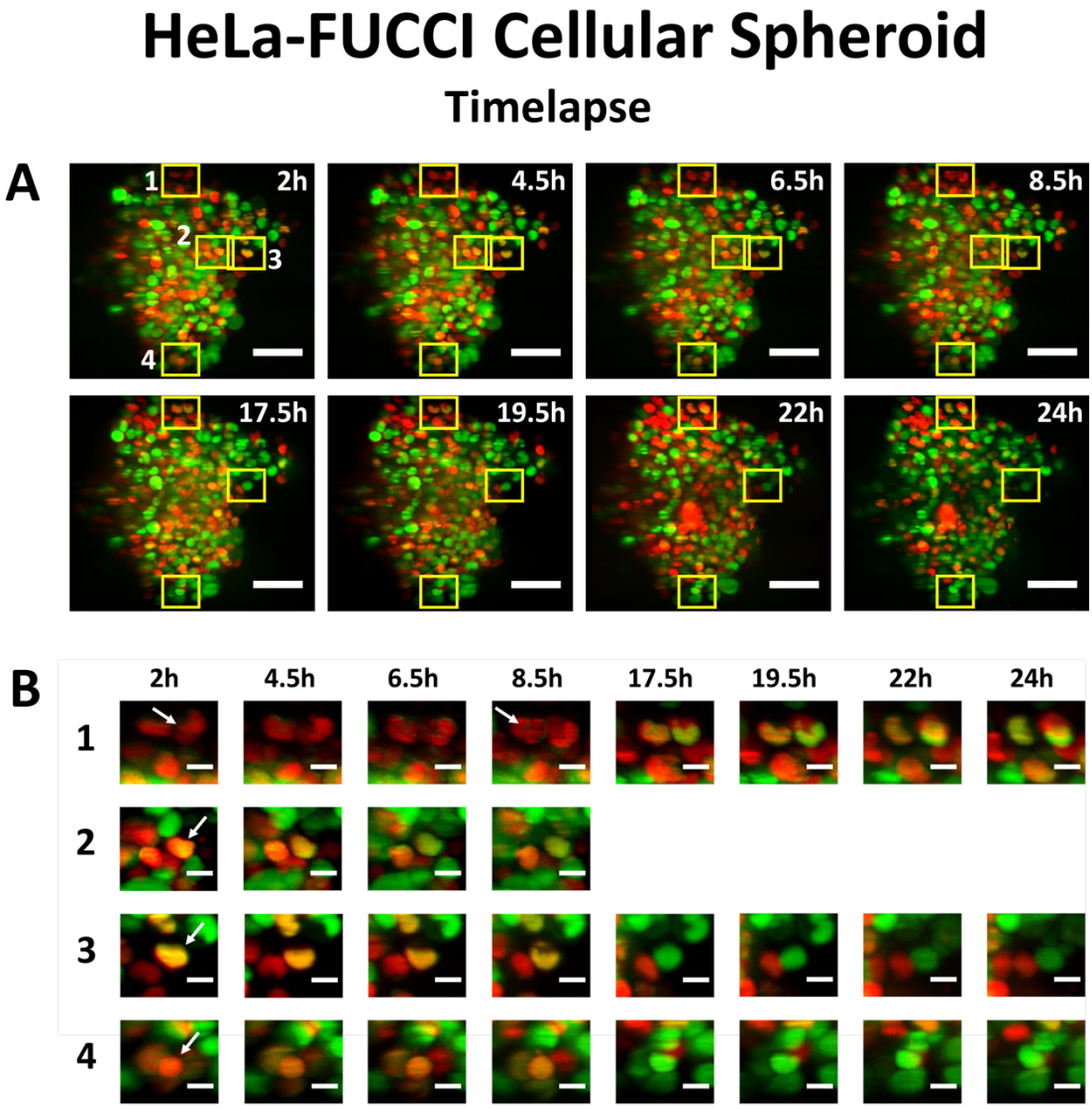

Figure 46 - Timelapse of HeLa-FUCCI Cellular Spheroids. Panel (A) shows the Maximum Intensity Projection (MIP) of a ≈200 μm HeLa-FUCCI spheroid recorded with the HT-LISH microscope over a 24 hours period (t=2h, 4,5h, 6.5h, 8.5h, 17.5h, 19.5h, 22h and 24h). Scale bar, 100 μm. Panel (B) displays MIP images of single nuclei corresponding to the 1, 2, 3 and 4 regions highlighted with the yellow squares and in panel (A). The cells indicated by the white arrows are cycling through different cell cycle phases, from G1 (red) to G1/S (orange) to S/G2/M (red). Scale bar, 10 μm.

These results suggested that the HT-LISH is actually capable to perform 5D imaging experiments of 3D cell culture models where a cellular process, in this case the cell cycle, is followed over time in 3 dimensions with multiple channels.

2.4.3 HT-LISH microscope for Automated Imaging of 3D Models

The results described in section 2.4.1 and 2.4.2 demonstrate that the HT-LISH microscope is able to acquire the volume of a 3D sample in 3, 4 and 5 dimensions. This is a common feature of any light sheet-based systems. However, as stated at the beginning of this chapter, the microscope assembled in this work has a further important implementation, relatively new to light sheet imaging. The HT-LISH should in fact enable the automated volumetric imaging of 3D models following a high throughput approach.

Previously in this work it has been mentioned that FUCCI (Fluorescent Ubiquitination-based Cell Cycle Indicator) [96] is a fluorescent cell cycle indicator. As it is highly relevant for the experiments presented in this section, it is necessary to describe it more in depth. The FUCCI cell cycle reporter is based on the observation that during the G1 phase of the cell cycle, there is a nuclear accumulation of the DNA replication licensing factor Cdt1 which is then degraded during the S/G2/M phases [96] (Figure 47A). This degradation is due to the action of Geminin, a direct inhibitor of Cdt1. Geminin is accumulating during the S/G2/M phases of the cell cycle and it is degraded by

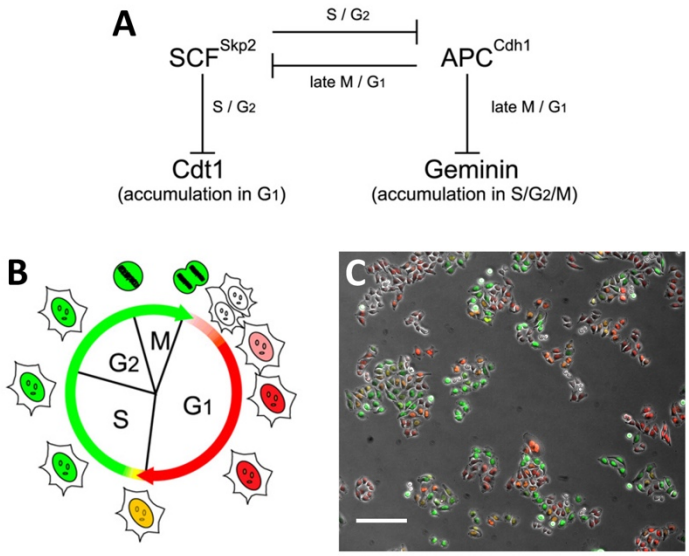

Figure 47 - Fluorescent Ubiquitination-based Cell Cycle Indicator (FUCCI). (A) Schematic principle behind the FUCCI construct. (B, C) Schematic (B) and fluorescence image (C) of cells progressing through the stages of the cell cycle. Scale bar (C), 200 µm. (A, B) adapted from [96].

proteolysis in the G1 phase [96]. The authors exploited the cell cycle-dependent inverse oscillation of Cdt1 and Geminin to assemble two different plasmids: FUCCI Green where human Geminin is fused to a green reporter (mAG - monomeric Azami Green) and FUCCI Red where human Cdt1 is fused to a red shifted reporter (mKO2 - monomeric Kusabira Orange2). When co-transfected, the nuclei of the cells emit different fluorescence signals depending on Geminin and Cdt1 levels: they turn green if the cell is in the S/G2/M phase, red if in G1 and orange if in G1/S (Figure 47BC). Therefore, the cell cycle phase can be clearly distinguished and thus this construct has the potential to be used in drug screening studies where the action of a chemotherapeutic compound aiming to arrest the cell cycle of cancerous cells is tested.

For the experiments performed in this section, a drug called Etoposide, a chemotherapeutic agent used in cancer treatments [97], was used. It works as an inhibitor of the Topoisomerase II, a key enzyme involved in the cell cycle that is highly expressed in the G2/M phase [98]. The action of Etoposide can thus be visualized with the FUCCI constructs as the cells will be very fluorescent in the green channel because of a cell cycle arrest in the G2/M phase [99]. To evaluate the activity of this drug on the HeLa-FUCCI line, the cells were first grown in 2D (96 well plate) and treated for a 24 hours period with different concentration of Etoposide: 0.5, 1, 2.5 and 5 μM. DMSO was used as control. The results of this experiment are illustrated in Figure 48. As previously reported [99], the fluorescence images show that increasing concentration of Etoposide induced cell cycle arrest in the G2/M phase. In particular, a concentration greater than 0.5 μM was required to fully block the cell cycle. These data are supported by the flow cytometry analysis presented in the graph in Figure 48. It is in fact visible that in DMSO the cells are for ≈50 % in the G1 phase, for ≈25% in the G1/S phase and for ≈15% in the S/G2/M phase; instead, when treated with an Etoposide concentration greater that 0.5 μM, HeLa-FUCCI are for 90% in the S/G2/M cell cycle phase.

Nowadays, from an imaging point of view, it is not difficult to perform this experiment (2D culture) with a 2D high throughput/content (HT/C) approach. There are several

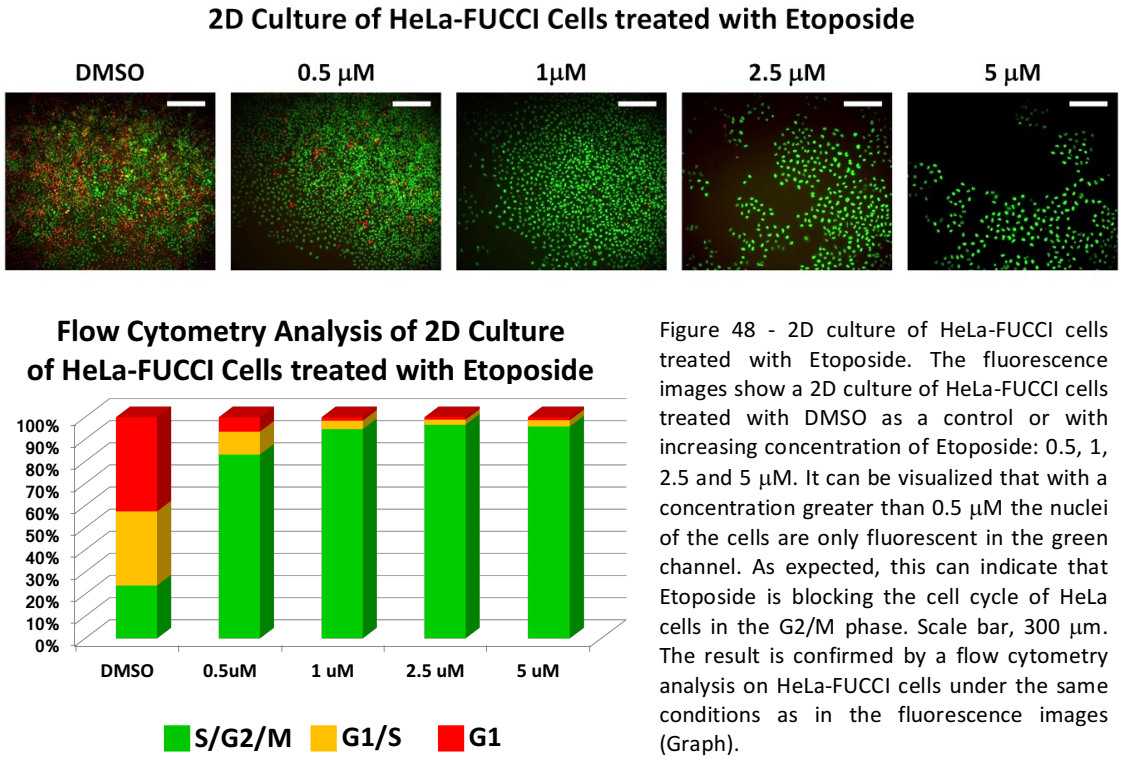

Figure 48 - 2D culture of HeLa-FUCCI cells treated with Etoposide. The fluorescence images show a 2D culture of HeLa-FUCCI cells treated with DMSO as a control or with increasing concentration of Etoposide: 0.5, 1, 2.5 and 5 μM. It can be visualized that with a concentration greater than 0.5 μM the nuclei of the cells are only fluorescent in the green channel. As expected, this can indicate that Etoposide is blocking the cell cycle of HeLa cells in the G2/M phase. Scale bar, 300 μm. The result is confirmed by a flow cytometry analysis on HeLa-FUCCI cells under the same conditions as in the fluorescence images (Graph).

possibilities for the automated imaging/screening of 2D cell cultures. Interestingly, this type of HT imaging can be carried out in any laboratory provided with an epi-fluorescent microscope and a motorized stage. The challenge is to develop a similar system that still relies on epi-fluorescence microscopes but is focused on the automated imaging of 3D models as they proved to better mimic the real tissues 3D architecture [17-21]. In this regard, the HT- LISH microscope designed and assembled in this work has the potential to be a valid first prototype. In order to evaluate the high throughput imaging performance of the HT-LISH system, the same experiment described above for the 2D cell culture was replicated in 350/400 μm HeLa-FUCCI cellular spheroids (Material and Methods - Chapter 5). The volume of five spheroids treated with DMSO or with different concentration of Etoposide (0.5, 1, 2.5 and 5 μM) were acquired in a fully automated process. This experiment was performed with a LISH thickness ($2W_0$) of 8.6 μm, a Rayleigh range ($2Z_r$) of 319 μm (Section 2.3.6 - Table1) and a step size of 2 μm. Each spheroid was sectioned in 146 frames.

The working principle of the HT-LISH microscope is illustrated in Figure 49. The locations of the five samples were stored in MicroManager and the HT-LISH microscope through

the motorized stage was capable to move through the different positions while acquiring a two channel (red and green channels) 3D stack of images for each spheroid. The result of the experiment is shown in Figure 50 and Figure 51.

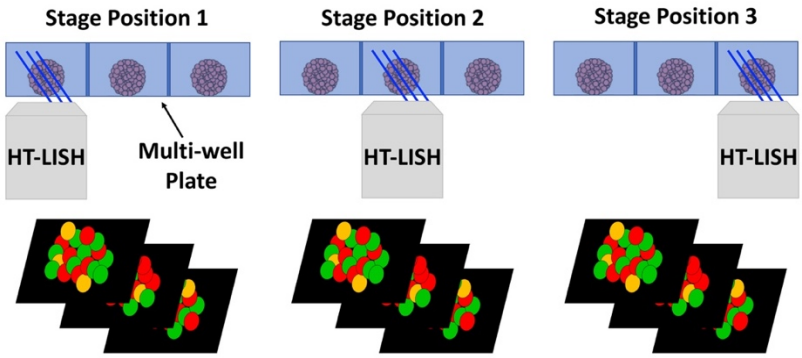

Figure 49 - Diagram illustrating the HT-LISH microscope working principle during a high throughput imaging experiment. The locations of the samples are stored in MicroManager and the HT-LISH microscope through the motorized stage is moving through the different positions while acquiring a two channel (red and green channels) 3D stack of images for each specimen.

Figure 50 is presenting the Maximum Intensity Projection (MIP) of the five spheroids in both the red and green channels. In Figure 51 each of the 146 frames and thus all the different planes of the spheroid can be visualised as a single two channel 2D image. The results show that also in the HeLa-FUCCI spheroids Etoposide is fully arresting the cell cycle in the G2/M phase with concentration greater than 0.5 μM.

Even though from a visual point of view the cell cycle arrest is displayed by the FUCCI construct, a more in-depth analysis of the volumetric images acquired could not be performed due to the large size of the data as for a proper image analysis a more powerful computer station is required. However, the aim of this experiment was to evaluate the HT-LISH microscope capability of performing automated imaging experiments. The system is designed for applications such as fluorescence-based drug or genetic screening that need to be applied on more complex cell culture models than the conventional 2D cell monolayer. In addition, a fundamental feature for a high throughput/content platform is the speed of the entire scan as it is not very practical if the imaging of multiple samples at one time-point requires several days of acquisition. In this experiment, for each spheroid, the exposure time per frame for the red and green

channel was of 250 ms and 100 ms respectively (Figure 51). If the movement of the filter wheel is considered, it means that each sample was acquired in about 53 seconds. Therefore, including the stage movements, the total acquisition time for the imaging of five spheroids was around 4 minutes and 45 seconds, a value that makes the HT-LISH microscope a fast volumetric high throughput/content imaging system.

In conclusion, as described in section 2.4.2, the possibilities of this microscope are not limited to the 3D imaging only at one time-point but cellular processes can be tracked over time. Therefore, the HT-LISH system can be also exploited for a fast volumetric imaging of multiple samples, each followed over several time-points (4/5D Imaging).

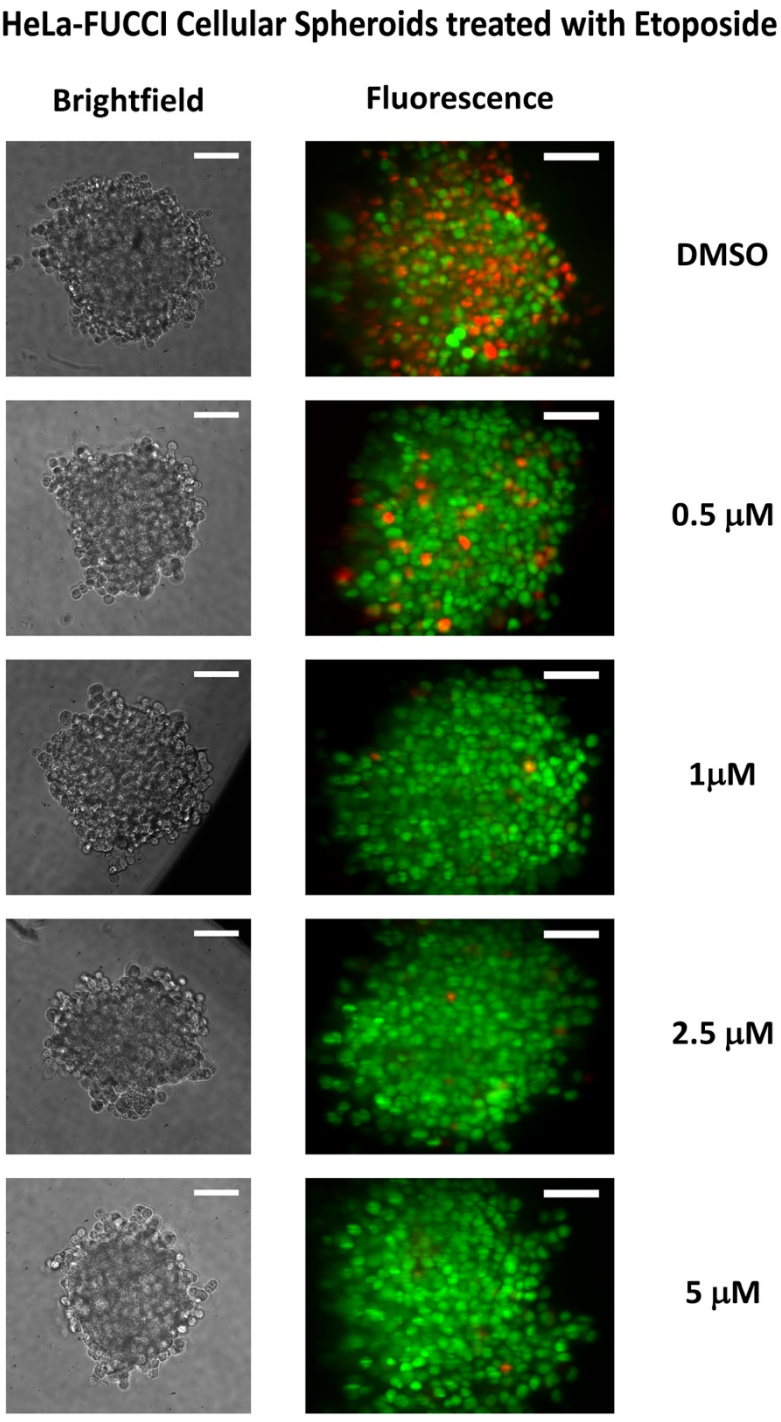

Figure 50 - Brightfield and two channel fluorescence Maximum Intensity Projection images of HeLa-FUCCI cellular spheroids treated with Etoposide. The sample are treated with DMSO as a control or with the same Etoposide concentration as in Figure 48: 0.5, 1, 2.5 and 5 μM. It can be visualized that with a concentration greater than 0.5 μM the nuclei of the cells are only fluorescent in the green channel, indicating that Etoposide induces the cell cycle arrest of HeLa cells in the G2/M phase. Acquisition parameters: LISH thickness ($2W_0$), 8.6 μm; Rayleigh range ($2Z_r$), 319 μm; Step size, 2 μm; Number of frames, 146; Exposure time green channel, 100 ms; Exposure time red channel, 250 ms. Scale bar Brightfield and fluorescence images, 100 μm.

Single Frames Visualization of HeLa-FUCCI Cellular Spheroids treated with Etoposide

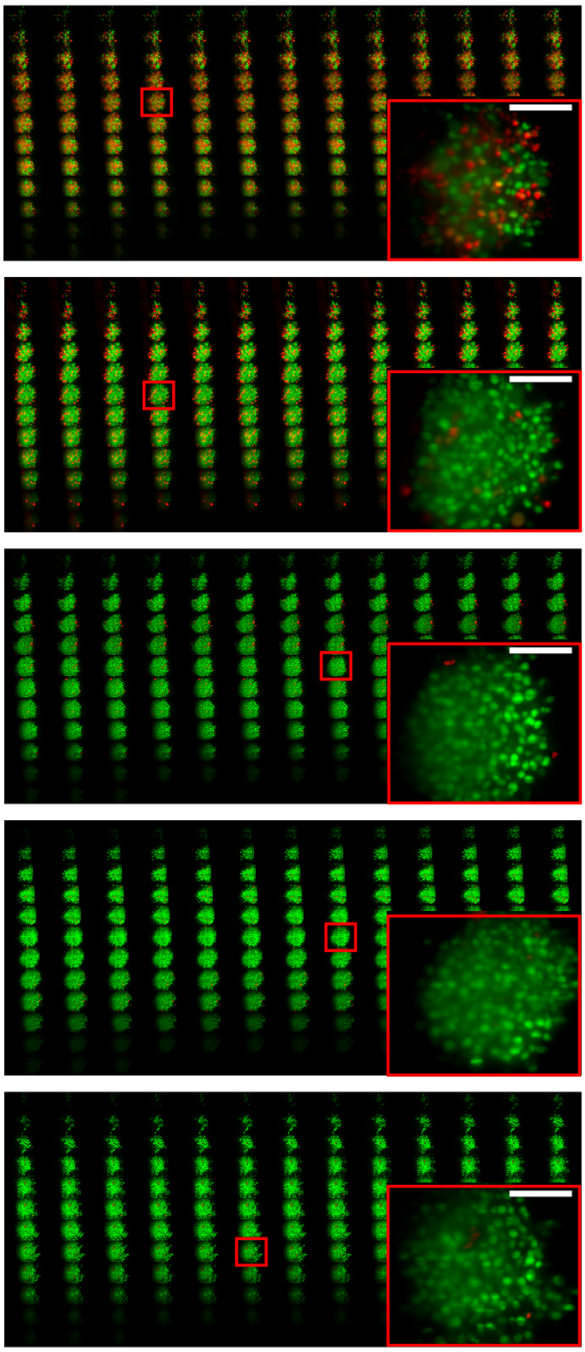

Figure 51 - Single frame 2D visualisation of the spheroids in Figure 50.

2.5 Discussion and Future Directions

This chapter described the design, the assembly, and the characterization of the HT-LISH first prototype, a single objective-based light sheet microscope. The proof-of concept experiments reported in this work primarily suggest that this system, as other light sheet microscopes, is capable to perform a fast image acquisition of biologically-relevant 3D cell culture model in 3 dimensions (3D - xyz), in 3 dimensions with multiple channels (3D - xyzc) and in 4/5 dimensions (3D over time/multi-channel - 4/5D - xyz(c)t).

In section 2.4.1 the HT-LISH microscope was used to image 350/400 μm HeLa-FUCCI cellular spheroids (Figure 43 - section 2.4.1). These experiments primarily suggested that the system is capable of acquiring the volume (3D imaging) of the 3D samples in two channels (3D multi-channel imaging).

Importantly, the maximum depth z (Figure 44 - section 2.4.1) that can be achieved with the current HT-LISH microscope prototype is of ≈183 μm, therefore it was not possible to image the entire volume of the 350/400 μm spheroids but only a portion was acquired. As described in section 2.4.1, this is due to the final magnification (M_f) of the system which is currently of 53.2x and depends on the use of 40x objectives. By halving the magnification, a greater volume of the samples could be acquired.

In addition, the experiments described in section 2.4.1 highlighted an issue regarding the imaging of the FUCCI constructs; the HT-LISH microscope currently mounts only a blue laser light source at 488 nm, wavelength that is optimal for the excitation of FUCCI green (mAG fluorescent protein) but not ideal for FUCCI red (mKO2 fluorescent protein) (Figure 45 - section 2.4.1). A combination of emission filters (535/45 nm for mAG and 630/60 nm for mKO2) and post-acquisition image processing (*Spectral Unmixing* plugin in ImageJ) enabled a precise discrimination between the fluorescence signal coming from these two FUCCI constructs. However, while the filter used for mKO2 was not optimal but necessary to avoid spectral overlap with FUCCI green, a better solution for the collection of the mAG fluorescence signal would be to use a 510/42 nm emission filter if a green laser is not available. This strategy would be more suitable for both the collection of the mAG fluorescence and the reduction of the mAG/mKO2 spectral overlap in the green channel.

Section 2.4.2 reports the capability of the HT-LISH microscope prototype to perform two channels long-term imaging of 3D cell culture models (5D imaging) while following cellular processes, such as the cell cycle, over time. The maximum intensity projection (MIP) of HeLa-FUCCI spheroids at different time points in Figure 46 (section 2.4.2) suggested that the cell cycle of HeLa cells could be followed over time at single cell level. As for the previous experiments in section 2.4.1, also in this case, because of the high magnification, only a portion of the spheroid could be imaged and the ImageJ *Spectral Unmixing* plugin was used to discriminate between FUCCI green and FUCCI red.

One of the main features and application of the HT-LISH is the ability of acquiring multiple 3D samples in an automated manner, thus opening new possibilities for light sheet microscopy, one of the most suitable techniques for the imaging of 3D cell culture models, to join the world of HTI and HCS. In section 2.3.4, a proof-of-concept experiment is presented. It was based on the automated imaging of different HeLa-FUCCI cellular spheroids treated with increasing concentration of Etoposide, a drug that it is known to arrest the cell cycle in the G2/M transition phase (Figures 51 and 52 - section 2.4.2). Even though with the same volume size/magnification issues and post-acquisition image processing described above, the results suggested that only an Etoposide concentration greater than 0.5 μM was capable to block the HeLa cell cycle in the G2/M phase (green fluorescence from FUCCI constructs). It is important to mention that the outcome of this experiment can be different depending on the size of the spheroids: larger spheroids (500/600 μm) were reported to better mimic the tumor environment [100]. Therefore, the use of bigger spheroids could lead to more reliable results. However, this was a proof-of-concept experiment aiming to evaluate the automated imaging feature of the HT-LISH microscope. Moreover, as previously mentioned, the spheroid size that can be imaged with the current HT-LISH microscope prototype is limited because of the too high magnification.

As described in Chapter 1 and Chapter 2 of this work, one of the main aim of this thesis project was to find a solution to link light sheet microscopy and 3D cell culture models

with the currently available High Throughput/Content Screening (HTS/HCS) platforms. First of all, contrary to the majority of the light sheet microscopes where the sample preparation can be very challenging, the HT-LISH prototype allows for the scan of multiple 3D samples in commercially available multi (or single) well plate formats as in most of the HTS/HCS systems.

Second, the system developed in this work is fully compatible with any currently available inverted microscope. This is a fundamental aspect if the goal mentioned above wants to be reached as inverted microscopes are widely spread in various microscopy based HTI stations used by industries or phenotypic screening centres as well as in most of the academic laboratories. As shown in Figure 52, the HT-LISH can be seen as an external box of limited size that can be easily attached to any inverted microscope. The single illumination and detection objective (O1 - Figure 41 section 2.3.12) with its tube lens (TL1 - Figure 41 section 2.3.12) can be considered as the objective and the tube lens

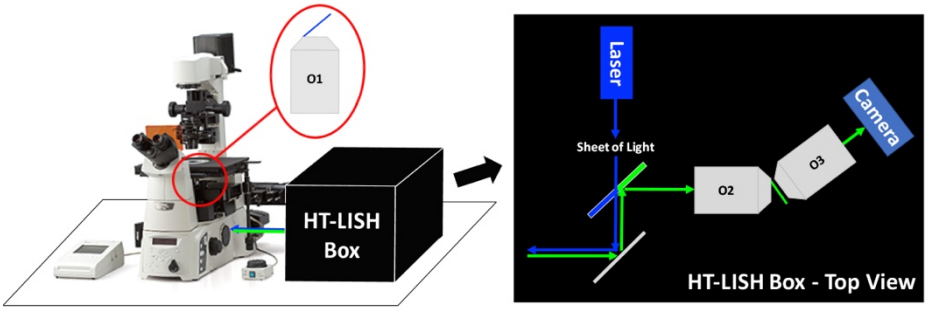

Figure 52 - HT-LISH box. The HT-LISH microscope can be seen as an external box of limited size that can be easily attached to any inverted microscope. The single illumination and detection objective O1 (with its tube lens TL1 - Figure 41 section 2.3.12) can be considered as the objective (and the tube lens) already mounted on the inverted microscope while the rest of the optical path, including the light source(s), the scanning system and the camera(s) can be attached as an "add-on" through one of the side ports.

already mounted on the inverted microscope while the rest of the optical path, including the light source(s), the scanning system and the camera(s) can be attached as an "add-on" through one of the side ports. This also offers the possibility to use the already established commercially available robotic arms for the automated sample loading. It follows that inverted microscope-based HTI platforms could be potentially implemented with the HT-LISH functionality without substantially changing their structure. This is even more relevant considering smaller academic realities that might not be capable to

afford the expensive 3D HTI machines currently available on the market but still require a certain level of throughput for an automated imaging of multiple biologically-relevant 3D cell culture models. These laboratories could implement their inverted microscope with the HT-LISH box and thus have access to a versatile platform that offers the possibility to image single or multiple 3D samples in 3, 4 or 5 dimensions (x, y, z, multi-channel, over time) with high acquisition speed while maintains the classic epi-fluorescence or Brightfield microscopy features if needed.

A third important aspect of the HT-LISH microscope prototype is that the system is very user friendly. The use of all the microscope features, from the basic 3D imaging to the more complex acquisition of multiple 3D samples, it is very simple and not more challenging than operating a confocal microscope. Once the light sheet parameters wanted are set, the user can easily place the specimens in commercially available glass bottom dishes, find the samples and the focal plane of interest with either Brightfield or fluorescence illumination, set the scanning parameters through the LabVIEW and/or MicroManager GUI and start the acquisition (section 2.3.11). As fully described in section 2.3.11, the HT-LISH prototype is currently controlled with multiple software. However, in future versions of the system the microscope hardware components could be all precisely controlled by only one software, for instance LabVIEW, thus making the HT-LISH operation even simpler and more user friendly.

In addition, also the Matlab script developed for the necessary frame alignment process described in section 2.3.10 does not include any particularly challenging step. The script is fast and the spatial conversion requires less than a minute, also with heavy datasets.

The current version of the HT-LISH microscope is a prototype and, as such, it requires further implementations in terms of hardware, software and optics.

The first upgrade that is required should be focused on the alignment of the HT-LISH microscope. In fact, as explained in section 2.3.9, this directly influences the resolution and thus, in order to increase image quality and consequently extract more precise information from an eventual following image analysis, a more careful alignment must be performed.

A second and very relevant implementation concerns the automated imaging capabilities of the HT-LISH microscope. Even though it has a great potential in HTI applications, with the current prototype it is not yet possible to achieve a very high throughput. This is mainly because of the software used to control the system (section 2.3.11). MicroManager does not offer an automated detection of the samples but the stage position(s) has to be manually selected. The same is happening with the selection of the focal plane as the current version of the HT-LISH is equipped with a motorized stage that allows only the movement along the X and Y axes. To implement an automated control also along the Z axes, it would be sufficient to install the HT-LISH on an inverted microscope capable of a Z stage movement. The hardware "evolution" obviously needs to be paired with a software implementation: for instance, a custom-made all-in-one software script (e.g. in LabVIEW) that provides an automated sample detection along the X, Y and Z axes, could offer both a much higher throughput and, as mentioned before, an easier operation.

A further upgrade required for the HT-LISH microscope should be focused on the magnification as different applications require higher or lower magnification depending on the samples that need to be analysed. The current HT-LISH prototype has a final magnification (M_f) of 53.2x that is limiting the Field of View (FOV). As described above and in section 2.4.1, reducing the magnification (for instance with the use of 20x objectives or Tube Lenses with shorter focal lengths) will guarantee a bigger FOV with the possibility to image 3D samples, such as cellular spheroids, through their entire volume.

The HT-LISH microscope is currently mounting only one laser line at 488 nm which is limiting the number of fluorophores that can be used. Therefore, in order to bring the system closer to a potential use in HTI experiments, the addition of one or more laser wavelengths (e.g. a green laser) could increase the number of phenotypic features that could be extracted and analysed from the 3D stack acquired with the microscope. It follows that also more emission filters will be required but the filter wheel already installed in the optical path can accommodate up to six fluorescence filters.

Moreover, this light source upgrade should not be focused only in terms of wavelength but also in regard to the illumination strategy. For instance, the use of two-photon excitation (instead of multiple one-photon laser lines) could improve the image resolution together with the penetration depth that can be achieved with the light sheet.

One last and fundamental upgrade that is required to fully transform the HT-LISH microscope in a valuable HTI station is focused on “miniaturization”. As described above, the final goal is to enclose the system in a box of limited size so that can be considered as an add-on of an inverted microscope. To do so, the optical path needs to be simply re-designed and implemented with shorter focal length lenses and/or different optical paths so that the overall size of the microscope can be significantly decreased.

With or without further implementations, the HT-LISH microscope has one principal drawback that is however common with the current HTI platform as well as with light sheet microscopy in general. The control and operation of advanced microscopy systems require powerful computer stations in terms of both processor and RAM. Moreover, the image acquisition of 3D samples produces a huge amount of data that need to be stored and handled. Therefore, a dedicated and performant setup is required as a poor computer power will limit the entire microscope capabilities and thus, in regard to the HT-LISH, will also affect the throughput and acquisition speed features. In addition, another important characteristic of the HT-LISH that could be considered as a drawback is related to the magnification; compared to other microscopes, the magnification of the HT-LISH is basically fixed and it would be very challenging to change. In fact, as explained in section 2.3.3, in the HT-LISH the magnification does not depend only on the illumination and detection single objective O1 (Figure 41 - section 2.3.12) but also the enlargement power of the second objective O2 (Figure 41 - section 2.3.12) must be taken into account (together with its NA). If a different magnification wants to be used, either O1 and O2 or their tube lenses (TL1 and TL2 - Figure 41 - section 2.3.12) have to be changed considering that the magnification between O1 and O2 requires to be of 1.33x (for water immersion objectives as O1 - section 2.3.3).

In conclusion, even though with some drawbacks, the overall design and operation could make the HT-LISH a versatile and user-friendly microscopy multi-station with a fast light sheet-based 3D (xyz), 4D (xyzt) and 5D (xyzct) imaging capabilities that could bring the HTI approach of biologically-relevant 3D cell cultures models in any laboratory, academic and non, that are provided with an inverted microscope/inverted microscopy-based platform. Once miniaturized and fully implemented (as described above) the HT-LISH could become a very powerful and versatile inverted microscopy add-on; this system could have a future impact in 3D HTI-based research (e.g. drug or genetic screening) and it would be very interesting to perform proper automated imaging tests when installed on commercially available inverted microscopy-based HTI platforms.

Chapter 3

The Red Light CRISPR/dCas9 System for the Optical Control of Gene Expression

3.1 List of Abbreviations

3D - Three-Dimensional (xyz)
4D - Four Dimensional (xyzt)
5D - Five Dimensional (xyzct)
apo-PhyB - Form of PhyB not light sensitive
Cas9 - CRISPR-associated protein 9
CRISPR - Clustered Regularly Interspaced Short Palindromic Repeats
CRY2 - CRYptochrome2
dCas9 - “dead” Cas9
DMD - Digital Micromirror Device
GFP - Green Fluorescent Protein
GS - polyglycine-serine flexible linker
KRAB - KRuppel Associated Box
MIP - Maximum Intensity Projection
NLS - Nuclear Localisation Sequences
PAM - Protospacer Adjacent Motif
PCB - PhycoCyanoBilin
PhyB - Phytochrome B
PhyB-Pfr - PhyB in the “far-red absorbing” state
PhyB-Pr - PhyB in the “red adsorbing” state
PIF6 - Phytochrome-Interacting Factor 6
SP - Streptococcus Pyogenes
ST - Streptococcus Thermophilus
TetR - Tetracycline Repressor
TR - Transcription Regulator
VPR - fusion protein of three transcription activators, VP64, p65 and Rta

3.2 Background

During the recent decades genome editing has become a fundamental tool for the study of cell and tissue biology. This approach can lead to a better understanding of human pathologies and therefore to the further development of new disease treatment focused on gene therapy [46, 47]. The recently discovered Type II Clustered Regularly Interspaced Short Palindromic Repeats (CRISPR)/CRISPR-associated protein 9 (Cas9) system can provide a flexible, highly efficient and easy to use genome engineering tool [45].

Briefly, the CRISPR system relies on the action of Cas9, a protein that has two endonuclease domains capable of cleaving the DNA: a double strand brake (DSB) is generated as one endonuclease cleaves the complementary DNA strand and the other cleaves the non-complementary DNA strand [45]. In order to recognise, bind and then cleave the DNA target in a highly specific manner, Cas9 has to be driven by a guide RNA (gRNA). The gRNAs are sequences of about 20 nucleotides that perfectly match the sequence of the DNA target which in turn has to contain to its end a short conserved sequence called Protospacer Adjacent Motif (PAM) [45]. This PAM sequence may vary depending on the bacteria species: for instance, NGG in *Streptococcus Pyogenes* (SP) or NNAGAAW in *Streptococcus Thermophilus* (ST) [53, 61]. The wild type Cas9 protein, due to its DNA cleaving activity, it is not suitable for gene regulation experiments. The ability to control the gene expression levels in cells and tissues is fundamental for a precise understanding of cellular (mal)functions as the molecules involved in biological processes are not arranged in a random fashion but follows a specific combination of genetic patterns [101, 102]. In addition, the expression level of one or multiple genes in various cells and tissues can induce significantly different effects depending on both time and space [103]. More recently, a mutated version of Cas9, called “dead” Cas9 (dCas9), was established by mutating the two endonuclease sites. This modification represses the original cleavage action of Cas9 but not the specific binding properties [45, 58, 65, 66]. Therefore, the CRISPR/dCas9 complex maintains an epi-genetic behaviour: dCas9 binds to a specific DNA sequence without any nuclease activity. The protein in this configuration has been used for direct gene regulation experiments: by fusing dCas9

with transcription activators, such as VP64, VPR, or the SunTag system, or transcription repressors, such as KRAB, it is possible to precisely up-regulate or down-regulate one or more genes of interest defined by the specific gRNAs [45, 67-71]

The main disadvantage of these CRISPR system variants is their lack of spatial and temporal resolution. In order to study and understand genetic patterns specific to a certain type of cell or tissue it is important to achieve a precise control over the CRISPR/dCas9 system so that it can be selectively targeted to small populations of cells (spatial resolution) or be activated and de-activated at will (temporal resolution). For this purpose, an ideal solution was found in optogenetics, an approach that combines molecular and optical methods to control specific cellular function in living tissue [73, 74].

The aim of this work was therefore to use optogenetics to develop a light inducible CRISPR/dCas9 system for gene regulation that can be precisely controlled in space and time using light as an external trigger. In this way, any genetic pathway can be targeted and thus studied at single cell level, over time. In this approach, characteristic to the emerging field of optogenetics, exogenous light-sensitive functional proteins are expressed in cells and then light is used to control their activity and consequently modify the cellular behaviour [73-75].

This chapter presents the development of the Red Light CRISPR/dCas9 system, a novel CRISPR-based optogenetics tool that provides active on/off switching control by using light sensitive proteins that can be activated by red light and actively deactivated under infrared illumination.

3.3 Development of the Red Light CRISPR System

3.3.1 Designing the Red Light CRISPR System

The Red Light CRISPR/dCas9 system developed in this work is based on the *Streptococcus Pyogenes* (SP) dCas9 and relies on two *Arabidopsis Thaliana* proteins that dimerize under red illumination (660 nm) and separate under infrared (740 nm) light: the Phytochrome B (PhyB) and the Phytochrome-Interacting Factor 6 (PIF6) [80, 81, 104, 105].

The main advantage of using this pair of light sensitive proteins is the bi-stable switching feature: the PhyB-PIF6 pair can actively and instantaneously be switched between stable On and Off states by shining red and infrared light respectively [81, 104].
Moreover, red light penetrates tissues much deeper than for instance blue light with also much lower phototoxicity, feature important mostly if long term live imaging experiments need to be performed [81, 104].
The choice of a red shifted pair of light sensitive proteins is even more significant if the light activation is combined with fluorescence microscopy in which blue light is commonly used for imaging of GFP-based fluorophores.
Importantly, the PhyB protein by itself is not light sensitive (apo-PhyB) (Figure 53) but it has to be covalently bound [81, 104] to the chromophore PhycoCyanoBilin (PCB). This bond transforms the Phytochrome B into its “red adsorbing” state (Pr) (Figure 53). The red light can then induce PhyB-Pr to change its conformation and to interact with PIF6. At this stage PhyB is in a stable “far-red absorbing” state (Pfr) as only the use of infrared light can rapidly detach PIF6 from PhyB: in this way, the phytochrome goes back to its Pr state ready to be re-activated if illuminated with red light (Figure 53) [81, 104, 105]. Therefore, if PhyB and PIF6 are transfected into cells, in order to make them light sensitive, the PCB must be added to the cell culture medium.

This step can be considered as a limitation of the system for two main reasons. First of all, PCB by itself is very light sensitive and has to be handled in complete dark conditions

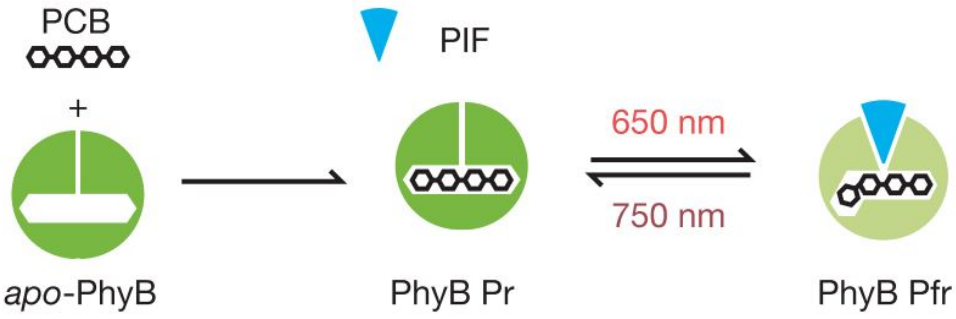

Figure 53 - The PhyB-PIF6 interaction depends on the chromophore PhycoCyanoBilin (PCB). apo-PhyB covalently binds to PCB to form a light-sensitive protein. PhyB undergoes conformational changes between the Pr and Pfr states catalysed by red and infrared light, reversibly associating with the PIF domain only in the Pfr state. Adapted from Levskaya et al. [105].

or under green safelight (532 nm) otherwise it will become inactive [81]. Secondly, PCB has a half-life of 1 hour in the culture medium and it is sufficient to convert into the Pr state only the PhyB proteins already expressed (PhyB-Pr then remains stably active). If long term (ideally more than 24h) light control experiments have to be performed, fresh PCB-medium has to be replaced to allow new PhyB proteins to become active (Pr state) [81].

However, the two "disadvantages" mentioned above can be turned into advantages if considering a cell line stably expressing the Red Light CRISPR/dCas9 system. A cell line as such can be very useful as any gene of interest can be simply targeted by transfecting only specifically designed gRNAs. Moreover, this stable line can be cultured following conventional procedures (not necessarily in dark conditions) since PhyB is not active without the presence of PCB in the culture medium and thus the system cannot be activated. In contrary, cells stably expressing other systems (such as the blue-light - based inducible systems [85, 86]), are immediately sensitive to light and therefore, after the generation, they have to be handled always in complete dark conditions to avoid unwanted protein interaction (mostly if the experiment requires the activation of the system only in a specific region).

The basic working principle of the Red Light CRISPR/dCas9 system developed in this work is illustrated in Figure 54. The SP-dCas9 protein is fused with PIF6 and PhyB with a Transcription Regulator (TR) (1); the use of red light (660 nm) results in a stable PhyB-

PIF6 bond (2) and thus in the transcription regulation of the targeted gene of interest (3). By shining infrared light (740 nm), the system will be deactivated (4). If exposed to red light, the system can be switched on again.

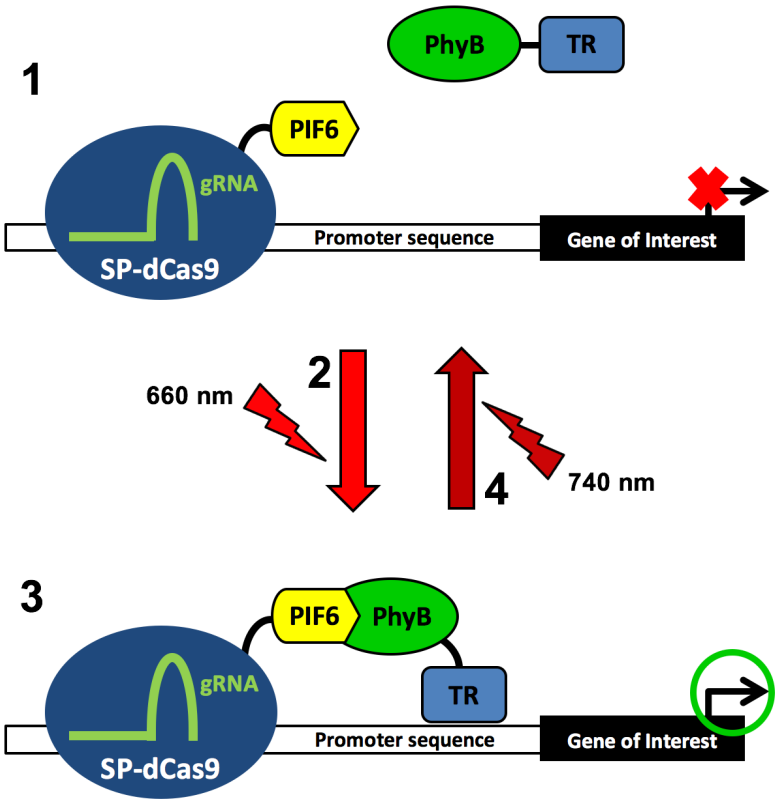

Figure 54 - Schematic working principle of the Red Light CRISPR/dCas9 system. Without any illumination (1), dCas9-PIF6 is bound to the DNA but there is no transcription regulation as PhyB-TR is not linked to PIF6. When illuminated with red light (2), PhyB undergoes a conformational change and it stably binds to PIF6. The system is now active and can thus induce target up- or down-regulation (3). This process is reversible (4): under infrared illumination, PhyB and PIF6 are detached and the transcription regulation is blocked. If exposed to red light, the system can be switched on again (1-4).

3.3.2 Building a versatile LED platform for the light experiments

The initial step was to assemble a red and infrared LEDs platform required for the activation and inactivation of the Red Light CRISPR/dCas9 system. The experiments were carried out directly inside the cell culture incubator using black walls 96 well plates (Perkin Elmer 6005182) therefore, also the LED box was built using this type of plate. In particular, red LEDs at 660 nm (Digi-Key 1125-1084-ND) and Infrared LEDs at 740 nm (Digi-Key 1125-1075-ND) were mounted into the wells of a black walls 96 well plates (the number of LEDs vary depending on the experiments) (Figure 55A). The LEDs were placed under control of one or more Arduino UNO microcontroller depending on the number of LEDs used (Figure 55B). This configuration enables direct and independent programming of switching and power regulation of each single LED. The custom-made

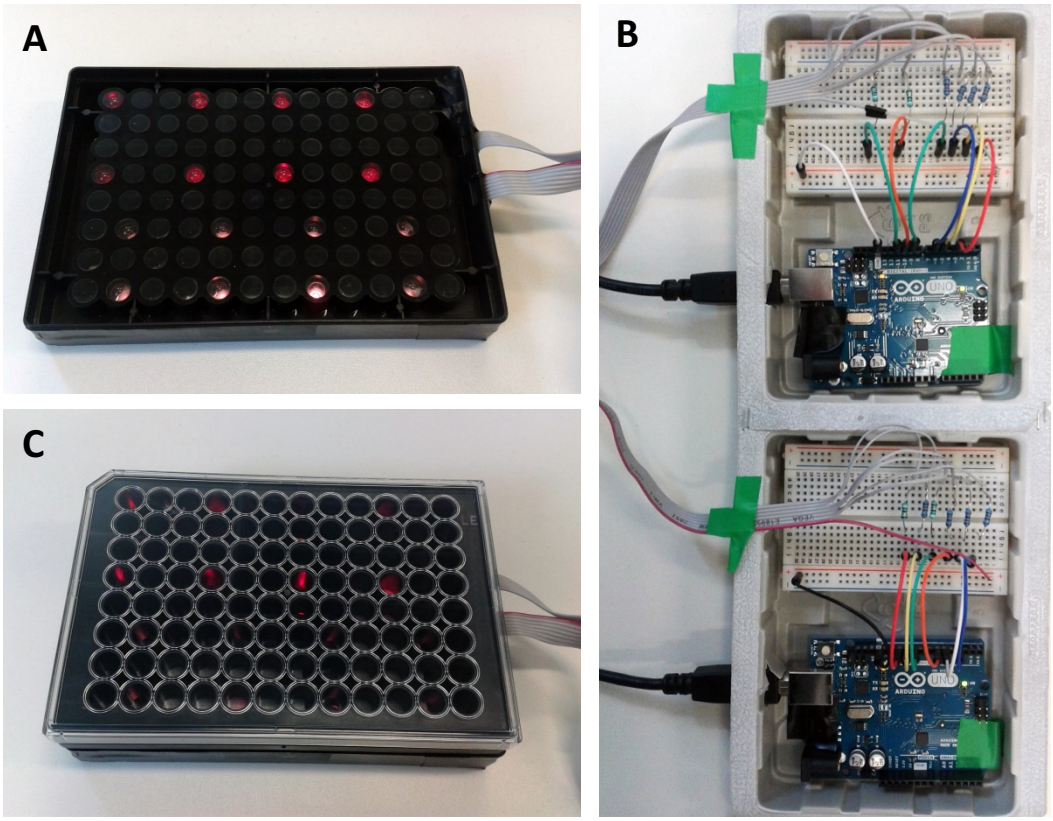

Figure 55 - Red and infrared LEDs platform. (A) Red LEDs at 660 nm (Digi-Key 1125-1084-ND) and Infrared LEDs at 740 nm (Digi-Key 1125-1075-ND) are mounted into the wells of a black walls 96 well plates; the number of LEDs vary depending on the experiments. (B) In order to have full control in terms of time and power, the LEDs are placed under control of one or more Arduino UNO microcontroller depending on the number of LEDs used. (C) For each light experiment, the black walls 96 well plate with the cells transfected with the Red Light CRISPR/dCas9 system is positioned directly onto the LEDs box so that the transfected wells are precisely matching the wells hosting the LEDs (the LED plate is placed upside-down, with the lid on the bottom).

Arduino UNO code can be found in the Supplementary Material (Chapter 6 - Section 6.2.1). As shown in Figure 55C, for each light experiment, the black walls 96 well plate with the transfected cells is positioned directly onto the LEDs box so that the transfected wells are precisely matching the wells hosting the LEDs; while both the 96 well plates (LEDs and cells) are placed inside the incubator, the Arduino UNO system remains outside.

The LEDs power is evaluated using a power meter (Thorlabs PM100USB).

All light experiments were carried out using continuous illumination (24 or 3 hours) with a power of ≈0.200 mW/cm^2 for red LEDs and ≈1 mW/cm^2 for infrared LEDs. For spatial resolution experiments, the red LEDs are set to a power of 0.080/0.100 mW/cm^2.

3.3.3 Development of the Red Light CRISPR System

3.3.3.1 Requirements for the Red Light CRISPR System

The diagram in Figure 54 illustrates only the working principle of the Red Light CRISPR System and highlights that it is composed of two different plasmids. The first one represents the CRISPR part of the system where the dCas9 protein is fused with the Phytochrome-Interacting Factor 6 (PIF6). The second plasmid contains the Phytochrome B (PhyB) fused with the regulatory element (Transcription Regulator - TR) that can control the expression level of the gene of interest targeted by the CRISPR system. In order to assemble these two fusion proteins plasmids and to guarantee their correct functionality, several variables had to be considered.
Therefore, this section (3.3.3) of the thesis presents the complete development of the Red Light CRISPR System including the assembly of a set of plasmids that differ in terms of fusion proteins position, protein length, Nuclear Localisation Sequences (NLSs) and transcription regulators (TRs).

First of all, based on the literature, two truncated versions of the Phytochrome B (PhyB) protein were selected, PhyB (1-908) and PhyB (1-650). The first one contains both the N- and C- terminal of the Phytochrome, while the second corresponds only to the N-terminal photosensory core of the entire PhyB protein which is required for the binding of both PCB and PIF [80, 81, 105]. Both these PhyB versions were reported to interact well with the PIF counterpart [80, 81, 105]. In addition, also the Phytochrome-Interacting Factor (PIF) has been previously used with different lengths, however, the PIF version corresponding to the first 100 aa, PIF6 (1-100), was selected as it was reported to provide better binding to its partner Phytochrome B [80, 105].

Due to the relatively large sizes of both the PhyB versions (908 or 650 amino acids) and dCas9 (1368 amino acids), the choice was to fuse the dCas9 with PIF6 (dCas9-PIF6) and the Phytochrome with a transcription regulator (PhyB-TR). In contrast, the dCas9-PhyB fusion (about 7 Kb in sequence) would have made the plasmid significantly large in size

and thus very difficult to transfect into cells. In this regard, for all the experiments, the two components of the Red Light CRISPR system were co-transfected with Lipofectamine 3000 together with a gRNA and a fluorescence reporter plasmid. It follows that also a possible low transfection efficiency had to be considered.

Another fundamental key point of the Red Light CRISPR system is the localisation of the fusion proteins within the cells (once transfected). In fact, in order to induce gene overexpression or down-regulation, both dCas9-PIF6 and PhyB-TR have to be present in the nucleus at the same time. The dCas9 protein must be localized in the nucleus in order to bind to the nuclear DNA target and PhyB must translocate into the nucleus in order to bind to PIF6 and thus induce the TR activity. In this sense, the addition of Nuclear Localisation Sequences (NLSs) within the fusion proteins has been reported to solve this possible issue and therefore, based on previously published constructs [80, 81, 85, 86], also the insertion of NLSs in the constructs assembled was considered.

In addition, sequences working as spacers (*e.g.* Glycine-Serine linkers) in-between the fusion proteins are reported to be important for the correct folding and thus function of each protein [78, 80, 106]. Therefore, also this element was considered when assembling the constructs.

As mentioned in section 3.2 of this chapter, several transcription regulators have been successfully fused with the dCas9 protein to obtain an important up- or down-regulation of the targeted gene of interest. In regard to gene down-regulation experiments, the direct fusion with the Kruppel associated box (KRAB) has demonstrated to significantly reduce the gene expression level [67]. However, it was previously reported that this process provides detectable repression of a fluorescence reporter plasmid only after several days post-transfection [67]. Therefore, the first version of the Red Light CRISPR system developed in this work is focused on optical gene up-regulation as it can be performed within a period of 24/48 hours post-transfection [68, 107].

To conclude, in order to estimate the efficiency of each set of plasmids, the light-induced up-regulation of a gRNA-targeted fluorescent reporter plasmid was evaluated by microscopy and flow cytometry. In particular, a first screening was based on epi-fluorescence imaging: if there was a detectable difference in terms of fluorescent signal between the fluorescent reporter alone, the activated (Red light) and the non-activated (Infrared light) system, a flow cytometry analysis was performed. In this way, the system efficiency could be precisely quantified.

3.3.3.2 Road to the functional version of the Red Light CRISPR System

As mentioned in the previous section, the development of the Red Light CRISPR system required the study of set of plasmids that differ in terms of fusion proteins position, protein length, Nuclear Localisation Sequences (NLS) and transcription regulators (TRs). In Table 7 there is a summary of all the versions of the Red Light CRISPR system that were assembled in this work. The detailed cloning strategy and sequence for each construct can be found in the Supplementary Material (Chapter 6 - Section 6.2.2). This section of the thesis presents the full process behind each single version of this CRISPR optogenetics tool.

Name	PIF6 Plasimd	PhyB Plasmid	Activator	Reporter Plasmid	Figure(s)
RED1	Flag-NLS-**dCas9**-NLS-PIF6	PhyB (**1-908**)-NLS-VP64-2A-GFP	VP64	8xgRNA-mCherry	56, 58, 59
RED2	Flag-NLS-**dCas9**-NLS-PIF6	3xNLS-PhyB (**1-908**)-NLS-VP64-2A-GFP	VP64	8xgRNA-mCherry	56, 58, 59
RED3	Flag-PIF6-Flag-NLS-**dCas9**-NLS-PIF6	PhyB (**1-908**)-NLS-Gateway Linker-VPR	VPR	8xgRNA-eGFP	61, 62, 64
RED4	Flag-PIF6-Flag-NLS-**dCas9**-NLS-PIF6	3xNLS-PhyB (**1-908**)-NLS-Gateway Linker-VPR	VPR	8xgRNA-eGFP	62, 65
RED5	Flag-PIF6-Flag-NLS-**dCas9**-NLS-PIF6	PhyB (**1-650**)-NLS-Gateway Linker-VPR	VPR	8xgRNA-eGFP	62, 66, 67
RED6	**dCas9**-NLS-GS Linker-PIF6	PhyB (**1-650**)-NLS-Gateway Linker-VPR	VPR	8xgRNA-eGFP	68, 69, 70, 71, 72
RED7	**dCas9**-NLS-GS Linker-PIF6	PhyB (**1-650**)-GS Linker-VPR	VPR	8xgRNA-eGFP	69, 73, 74, 76, 77, 78, 80, 81, 82, 83, 85, 86, 89

Table 7 - Summary of all the versions of the Red Light CRISPR system assembled in this work.

3.3.3.2.1 ***RED1*** *and* ***RED2***

The first step towards the Red Light CRISPR system was to assemble the plasmid containing the CRISPR part. The N-terminus of PIF6 was thus fused with the C-terminus of dCas9 (Figure 56). The dCas9 protein cloned in this plasmid was coming from the dCas9-VP64 construct developed by Perez-Pinera *et al*. [68] where two NLS sequences are inserted at the N- and C-terminus of dCas9 to help this large protein to translocate into the nucleus. For this reason, both the NLS sequences were maintained also in the dCas9-PIF6 plasmid. This fusion is based on the Muller *et al*. [80] system where the N-terminus of PIF6 was fused to the C-terminus of the tetracycline repressor protein (TetR). For the activator plasmid, the most straightforward approach was to base the design on the optogenetics system developed by Konermann *et al*. [78] where the blue light sensitive CIB1 protein is fused with the transcription activator VP64 linked with the green fluorescent protein (GFP) in a 2A bicistronic sequence as expression marker. The activator-GFP domain was first amplified by PCR and then fused with the long version of the Phytochrome B, PhyB (1-908) (Figure 56).

The plasmids obtained after this cloning process were therefore: Flag-NLS-dCas9-NLS-PIF6 and PhyB (1-908)-NLS-VP64-2A-GFP (Figure 56) (Plasmids 10 and 12 - Supplementary Material - Chapter 6 - Section 6.2.2). These two constructs represent the first version of the Red Light CRISPR system that was denominated **RED1** (Table 7).

RED1	**Flag-NLS-dCas9-NLS-PIF6**
	PhyB (1-908)-NLS-VP64-2A-GFP
RED2	**Flag-NLS-dCas9-NLS-PIF6**
	3xNLS-PhyB (1-908)-NLS-VP64-2A-GFP

Figure 56 - Plasmids structure of the **RED1** and **RED2** systems.

Together with RED1, also **RED2** was developed and it differs because of the addition of three Nuclear Localization sequences (NLSs) in front of the PhyB protein (Figure 56): 3xNLS-PhyB (1-908)-NLS-VP64-2A-GFP (Plasmids 13 - Supplementary Material - Chapter 6 - Section 6.2.2). This design is based on the plasmid configuration developed by

Nihongaki *et al*. [86] where the presence of three NLSs in their blue light-sensitive CRISPR/dCas9 tool significantly improved the system efficiency.

Due to the presence of GFP in the PhyB-VP64 construct, to evaluate the **RED1** and **RED2** systems a red-shifted fluorescent reporter plasmid designed by a colleague (Rebeca Diaz) was used. It expressed the mCherry fluorescent protein under control of a minimal CMV promoter with the aim of minimizing the fluorescence basal expression level without any targeted activation (Figure 57). Moreover, eight repetition sequences in the form 5'-AAAGGTCGAGAAACTGCAAA**AGG**-3' were inserted upstream from the minimal promoter (Figure 57) (Plasmids 7 - Supplementary Material - Chapter 6 - Section 6.2.2). This repetition represents the CRISPR binding site and therefore also a suitable gRNA plasmid targeting the sequence above was assembled (Rebeca Diaz) (Plasmids 9 - Supplementary Material - Chapter 6 - Section 6.2.2).

The mechanism of action of **RED1** and **RED2** is schematised in Figure 58.

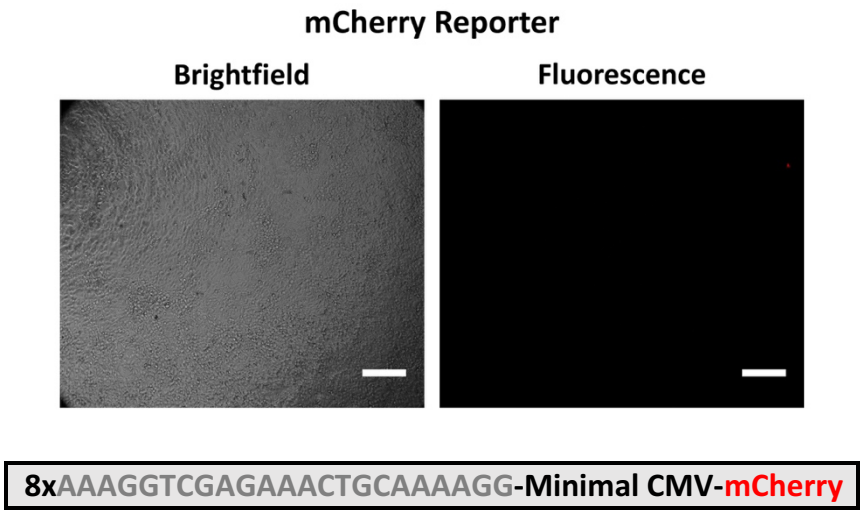

Figure 57 - mCherry reporter plasmid. The mCherry fluorescent protein is under control of a minimal CMV promoter with the aim of minimizing the fluorescence basal expression level (fluorescence image). Eight repetition sequences in the form 5'-AAAGGTCGAGAAACTGCAAA**AGG**-3' that represents the CRISPR binding site are inserted upstream from the minimal promoter. Scale bar, 200 μm.

The **RED1** and **RED2** systems together with the mCherry reporter and the gRNA plasmids were transfected in HEK 293 cells. In addition, the reporter construct was transfected by itself for the calibration of the fluorescence basal level signal. After an incubation period (24 hours), the PCB was added and the **RED1** and **RED2** samples were exposed to

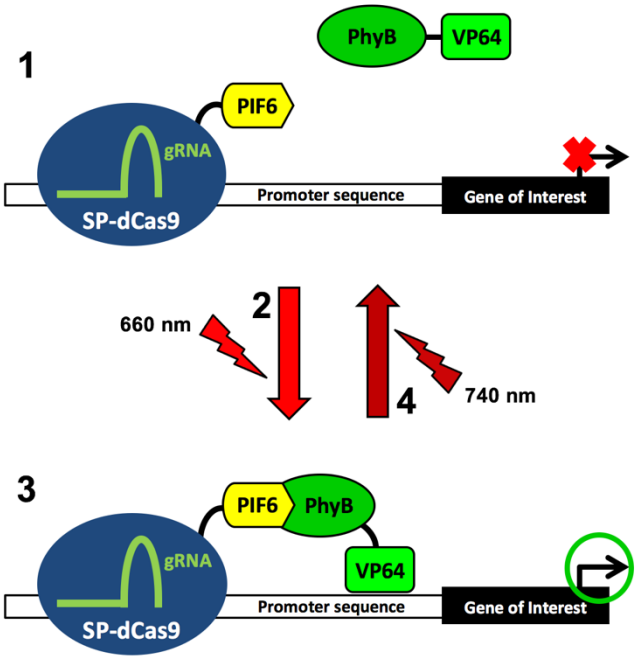

Figure 58 - Schematic working principle of **RED1** and **RED2** systems (see Figure 54).

continuous red or infrared illumination for 24 hours. A series of images were acquired with an epi-fluorescence microscope and the fluorescence coming from the wells transfected with the systems under red and infrared light were compared with the control (mCherry reporter plasmid alone) while maintaining the same microscope settings. As shown in Figure 59, even though this experiment was performed multiple times, an evident mCherry upregulation above the basal level could not be detected from both **RED1** and **RED2**.

Assuming that dCas9 was binding correctly to the mCherry reporter plasmid, three potential reasons were considered to explain the failure of both the **RED1** and **RED2** systems in this configuration. First of all, PhyB and PIF6 could not fold correctly. The direct fusion respectively with VP64 and dCas9 could prevent the proteins from a proper configuration and thus VP64 could not act as transcription activator. Secondly, PhyB (1-908) and PIF6 could not interact with each other or their bond was not strong enough [80]. Third, even if VP64 produced positive results in terms of gene overexpression when combined with other CRISPR tools, the Red Light CRISPR system could require a stronger activator.

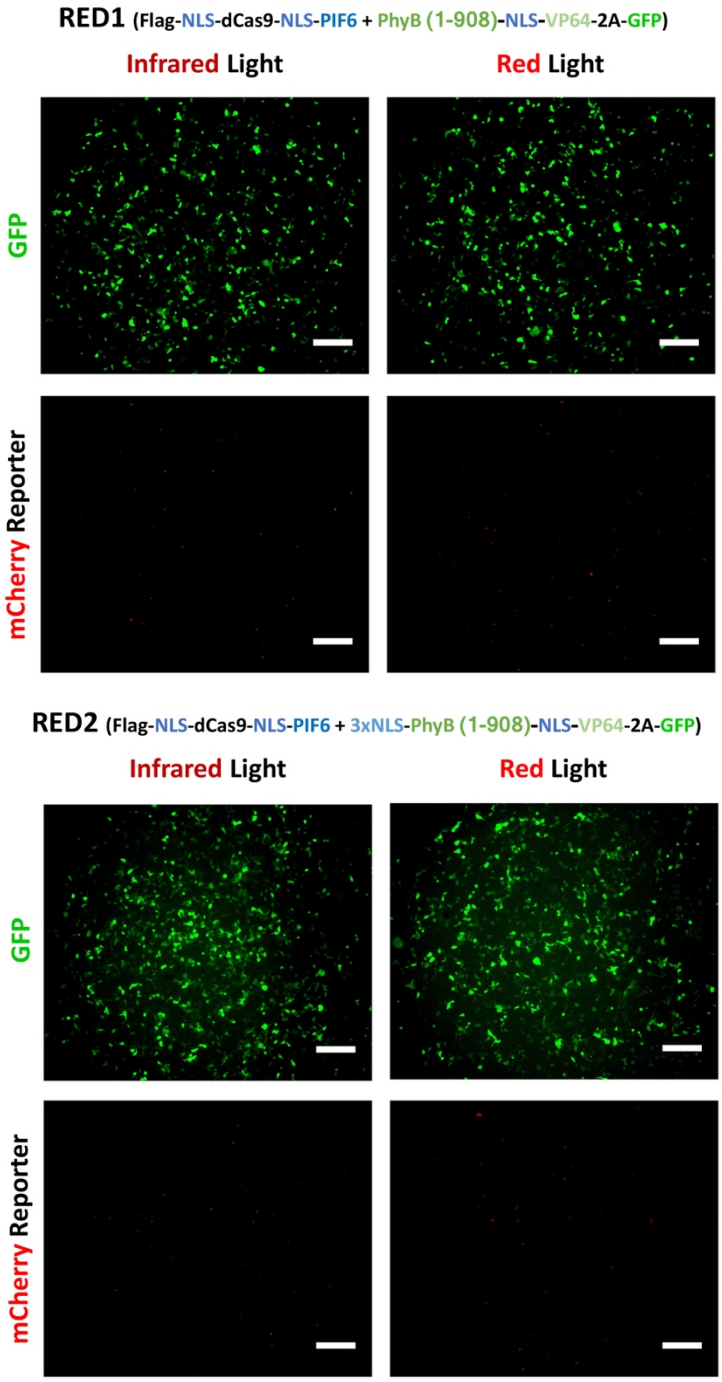

Figure 59 - **RED1** and **RED2** mCherry up-regulation. Fluorescence images of **RED1** and **RED2** co-transfected in HEK 293 cells with the mCherry reporter and the gRNA plasmids and illuminated with red or infrared light (for 24 hours after the addition of PCB). The mCherry reporter plasmid alone was transfected as control. The GFP signal is coming from the GFP tag present in the activator plasmids (Figure54). With both the systems, an evident mCherry up-regulation above the basal level cannot be detected. Scale Bar, 200 μm.

*3.3.3.2.2 **RED3** and **RED4***

The next version of the system, **RED3** (Table 7), was therefore developed taking into account the possible issues explained above.

To exclude the weak transcription activator hypothesis, VP64 was replaced with a stronger activator, VPR, developed by Chavez *et al.* [70]. VPR is a fusion protein of three transcription activators, VP64, p65 and Rta and, when fused with dCas9, was demonstrated to provide superior up-regulation capabilities (Figure 60).

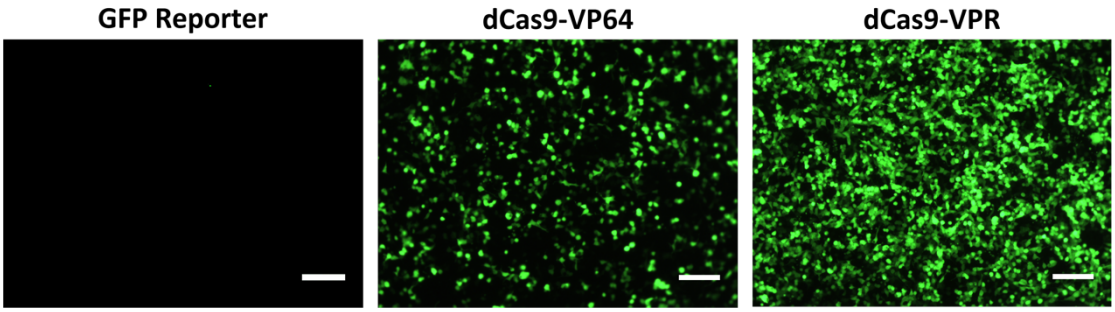

Figure 60 - Comparison between the transcription regulators VP64 and VPR (*VP64, p65 and Rta)* for the overexpression of a GFP fluorescent reporter plasmid. Scale bar, 100 μm.

Therefore, a new plasmid was assembled where the PhyB (1-908) C-terminus was fused with VPR (Figure 61). Moreover, to overcome any misfolding issue of the Phytochrome B, a Gateway linker sequence of 22 aa from the original dCas9-VPR plasmid [70] was cloned in-between PhyB (1-908) and VPR (Figure 61). The activator plasmid for **RED3** was therefore: PhyB (1-908)-NLS-Gateway Linker-VPR (Plasmids 15 - Supplementary Material - Chapter 6 - Section 6.2.2). In principle, the linker should increase the space between PhyB and VPR and thus help the Phytochrome to maintain a proper configuration.

RED3	**Flag-PIF6-Flag-NLS-dCas9-NLS-PIF6**
	PhyB (1-908)-NLS-Gateway Linker-VPR

Figure 61 - Plasmids structure of the **RED3** system.

Regarding the CRISPR part of the system, also the dCas9-PIF6 plasmid used in **RED1** and **RED2** was modified. Polstein *et al*. [85] successfully achieve optical gene up-regulation by fusing two CIBN molecules to the dCas9 protein, one on each side. Therefore, the dCas9-PIF6 fusion plasmid from the previous **RED1** and **RED2** systems was modified by adding a further PIF6 protein upstream the dCas9 (N-Terminus) (Figure 61): Flag-PIF6-Flag-NLS-dCas9-NLS-PIF6 (Plasmids 14 - Supplementary Material - Chapter 6 - Section 6.2.2). In this way, when illuminated with red light, two molecules of PhyB-VPR should bind to the two PIF6 proteins fused to dCas9 and in principle induce a stronger overexpression. The mechanism of action of **RED3** is schematised in Figure 62.

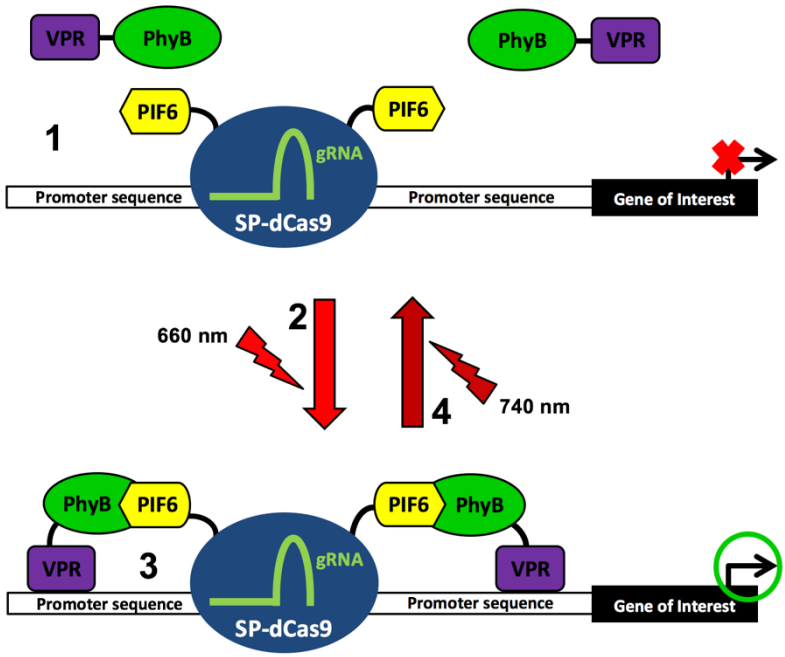

Figure 62 - Schematic working principle of the **RED3** systems (see Figure 54).

Importantly, for the **RED3** experiments, because the PhyB-VPR plasmid did not co-express a GFP tag anymore, a GFP reporter was used instead of the mCherry plasmid. Also in this construct, the fluorescent protein is under control of a CMV minimal promoter and it is preceded by eight gRNA target repetitions (Figure 63) (Plasmids 8 - Supplementary Material - Chapter 6 - Section 6.2.2). The use of a GFP reporter plasmid instead of the mCherry one was also motivated by the improved quality of any flow cytometry analysis as the available machine did not have a green laser necessary to

efficiently excite mCherry (but only a blue light source). The GFP reporter was characterized by flow cytometry to be certain that the addition of PCB in the culture media was not influencing the fluorescence level (Supplementary Material - Chapter 6 - Section 6.2.3).

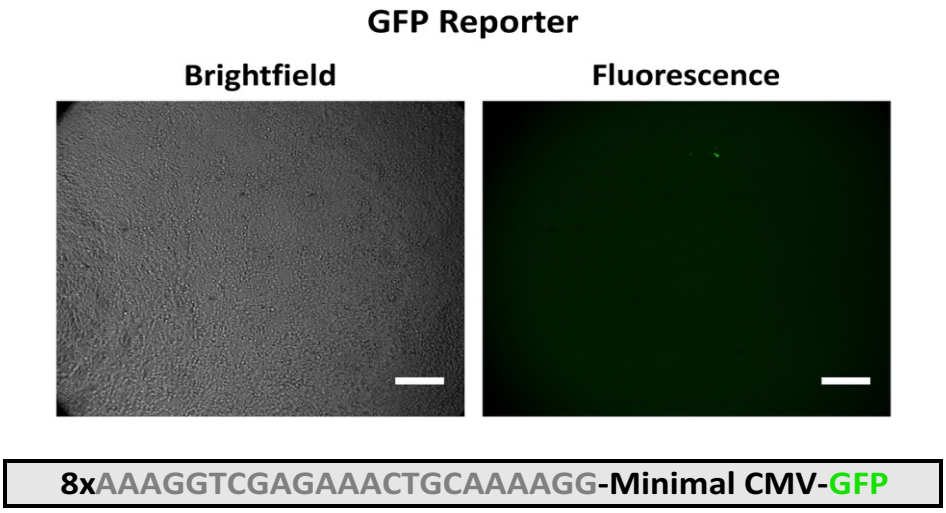

Figure 63 - GFP reporter plasmid. The GFP fluorescent protein is under control of a minimal CMV promoter with the aim of minimizing the fluorescence basal expression level (fluorescence image). Eight repetition sequences in the form 5'-AAAGGTCGAGAAACTGCAAA**AGG**-3' that represents the CRISPR binding site are inserted upstream from the minimal promoter. Scale bar, 200 μm.

The **RED3** system were co-transfected with GFP reporter and gRNA plasmids in HEK 293 cells and illuminated with red or infrared light. The GFP reporter construct was also transfected by itself for the calibration of the fluorescence basal level signal. As shown in Figure 64, the epi-fluorescence microscopy analysis (on multiple experiments) did not show any significant GFP up-regulation; only very few cells transfected with the **RED3** system and illuminated with red light seemed to express GFP over the basal level.

As for the previous constructs, a Red Light CRISPR system version, **RED4** (Table 7), with three NLSs on the N-Terminus of PhyB was assembled: 3xNLS-PhyB (1-908)-NLS-Gateway Linker-VPR (Figure 65) (Plasmids 16 - Supplementary Material - Chapter 6 - Section 6.2.2). However, the same results as for **RED3** were obtained (Data not shown).

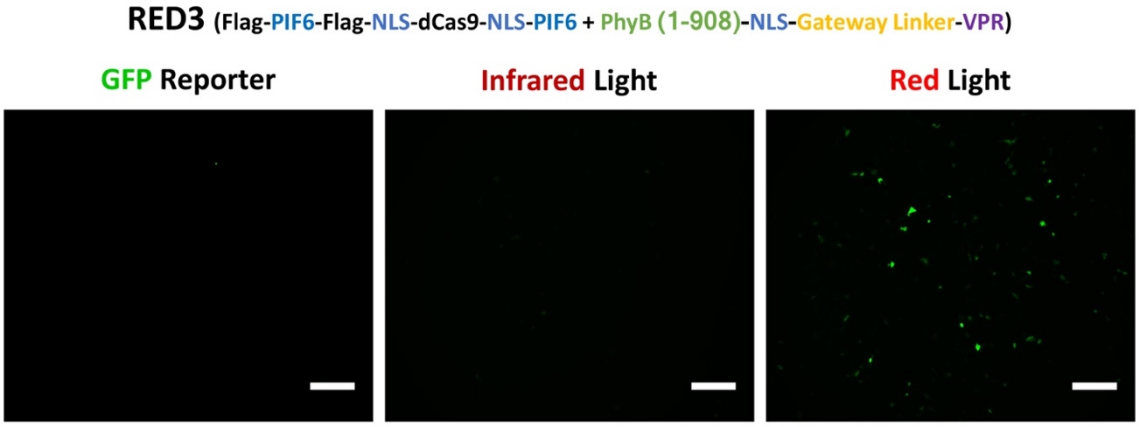

Figure 64 - **RED3** GFP up-regulation. Fluorescence images of **RED3** co-transfected in HEK 293 cells with the GFP reporter and the gRNA plasmids and illuminated with red or infrared light (for 24 hours after the addition of PCB). The GFP reporter plasmid alone was transfected as control. With **RED3**, an evident GFP up-regulation above the basal level cannot be detected. Scale Bar, 200 μm.

RED4	**Flag-PIF6-Flag-NLS-dCas9-NLS-PIF6**
	3xNLS-PhyB (1-908)-NLS-Gateway Linker-VPR

Figure 65 - Plasmids structure of the **RED4** system.

These experiments might suggest that the co-localisation of both PhyB-VPR and PIF6-dCas9-PIF6 inside the nucleus should unlikely be an issue. In fact, as previously reported [68, 80, 85], the presence of NLSs in both the plasmids should guarantee the nuclear translocation. In addition, VPR was demonstrated to provide a strong fluorescent reporter plasmid up-regulation in human cells when directly fused to dCas9 [70]. Therefore, one of the possible explanations for the failure of the **RED3** and **RED4** systems could be an incorrect folding or poor interaction between PhyB and PIF6.

*3.3.3.2.3 **RED5***

As mentioned in section 3.3.3.1, the Phytochrome B has been previously used in two different versions [80, 81, 105]. The PhyB protein cloned in **RED1**, **RED2**, **RED3** and **RED4** contains both the N- and C- terminal of the Phytochrome and corresponds to 908 amino acids (PhyB (1-908)). PhyB (1-908), in the optogenetics system for protein translocation experiments developed by Levskaya *et al.* demonstrated to well interact with the PIF6 counterpart [105]. However, an equal result was achieved in the tetracycline-based optogenetics system developed by Muller *et al*. [80]. Here, a 650 amino acids truncated version of the Phytochrome B, PhyB (1-650), was used. It corresponding to the only N-terminal photosensory core of the entire Phytochrome B, the minimal protein portion necessary for PCB and PIF6 binding. These two different approaches suggest that Phytochrome B and the Phytochrome-Interacting Factor 6 always interact with each other, but the strength of their binding can be influenced by the kind of proteins they are fused with. It follows that a probable reason for which the **RED1**, **RED2**, **RED3** and **RED4** systems failed in the up-regulation of the fluorescent reporter could be an incorrect or poor interaction between PhyB (1-908) and PIF6. Therefore, in the **RED5** system (Table 7), PhyB (1-908) was replaced with the 650 amino acids truncated version of PhyB: PhyB (1-650)-NLS-Gateway Linker-VPR (Figure 66) (Plasmids 17 - Supplementary Material - Chapter 6 - Section 6.2.2). The mechanism of action of **RED5**, equal to **RED3** and **RED4**, is schematised in Figure 62 above.

RED5	**Flag-PIF6-Flag-NLS-dCas9-NLS-PIF6**
	PhyB (1-650)-NLS-Gateway Linker-VPR

Figure 66 - Plasmids structure of the **RED5** system.

HEK 293 cells were co-transfected with the **RED5** system, the GFP reporter and the gRNA plasmids and were exposed to continuous red or infrared illumination for 24 hours. The GFP reporter plasmid alone was transfected as control. The fluorescence microscopy images in Figure 67 show that with the **RED5** system a detectable GFP reporter up-regulation could be achieved. It was observed that, under equal camera exposure time

and excitation light intensity, the difference in GFP expression given by **RED5** under red illumination over the system under infrared light or the GFP reporter alone is evident. Therefore, to precisely quantify **RED5** efficiency, a further flow cytometry analysis was performed (plots in Figure 67). The result of this experiment is visualised in the graph in Figure 67. First of all, the data confirmed that the GFP signal from **RED5** under red light was actually higher when compared with cells transfected with the GFP reporter alone (about 3.5 times - statistically significant, $p<0.05$, ANOVA), meaning that the Red Light CRISPR system in this configuration was capable of up-regulating the GFP fluorescence reporter. This suggested that the 650 amino acids truncated version of PhyB was a key requirement for a correct development of the Red Light CRISPR system. On the other hand, the flow cytometry analysis (Figure 67) showed that, even though statistically significant, the difference in GFP expression between the **RED5** system under red and infrared illumination was very limited. Moreover, the data seemed to highlight that the system under infrared light was also inducing statistically significant GFP up-regulation. These two drawbacks of **RED5** could be explained considering that the PIF6 protein was reported to behave as a transcription activator in *Arabidopsis Thaliana* [105], which means that PIF6 by itself could up-regulate the GFP gene when dCas9 is bound to its target.

The ideal solution to this possible issue could be to modify the entire Red Light CRISPR system by switching the fusion proteins: dCas9 fused with PhyB (1-650) and PIF6 fused with the transcription activator VPR. However, the CRISPR part of the system would result in a 11.5 kb plasmids (with a dCas9-VPR fusion protein of 2044 amino acids) therefore very difficult to transfect with Lipofectamine 3000.

The fact remains that also in the previously optogenetics tool based on the PhyB-PIF pair of proteins developed by Muller *at al*. [80], the use of infrared light did not induce any significant up-regulation of the targeted gene of interest. Moreover, the **RED5** system, in its current configuration was probably not strong enough to induce a significant up-regulation of any endogenous gene of interest, under either red or infrared illumination.

The **RED5** system was therefore considered as a new starting point for the development of the Red Light CRISPR system. The dCas9-PIF6 fusion could be ameliorated starting again from the use of a single PIF6 protein with the aim of reducing the background activity under infrared light.

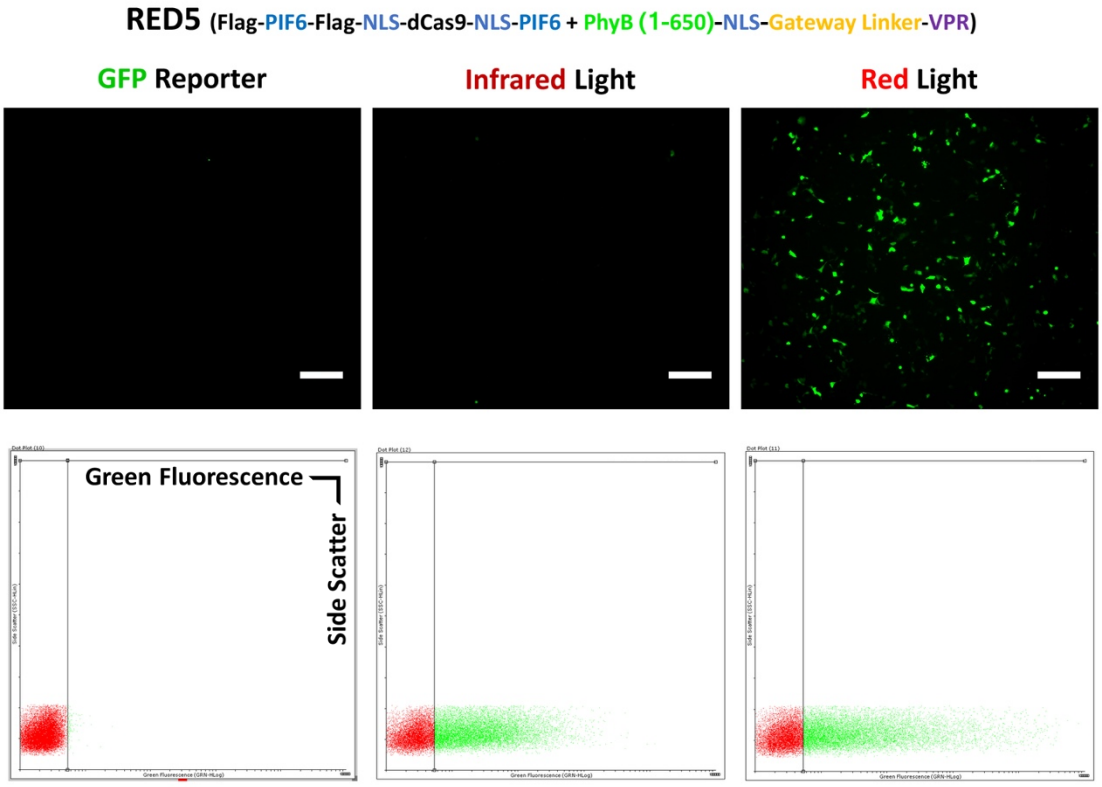

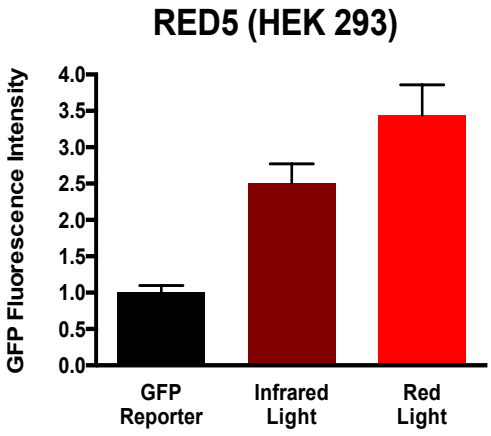

Figure 67 - **RED5** GFP up-regulation. Fluorescence images and flow cytometry analysis of **RED5** co-transfected in HEK 293 cells with the GFP reporter and the gRNA plasmids and illuminated with red or infrared light (for 24 hours after the addition of PCB). The GFP reporter plasmid alone was transfected as control. It is visible that **RED5** is capable to induce a detectable GFP up-regulation above the basal level. This result is confirmed by the flow cytometry graph where it can be observed that the GFP signal from **RED5** under red light is actually higher when compared to cells transfected with the GFP reporter alone or with **RED5** under infrared illumination (n=3, statistically significant, ANOVA - $p<0.05$). Moreover, the data seems to highlight that **RED5** under infrared light is also inducing GFP up-regulation (n=3, statistically significant, ANOVA - $p<0.05$). The flow cytometry plots represent the number of cells below (red) and above (green) an arbitrary GFP threshold (0.5% of un-transfected cells - Material and Method section, chapter 5). Scale Bar, 200 μm.

3.3.3.2.4 RED6

In the new version named **RED6** (Table 7), the CRISPR part of the system was similar but not identical to the fusion in **RED1** and **RED2** where only one PIF6 protein was used. In particular, in **RED6** the N-terminus of PIF6 was fused with the human-optimized-sequence dCas9 protein from Chavez *at al.* [70] through a standard 10 aminoacid polyglycine-serine flexible linker (GS) linker [105]. Moreover, only one NLS was cloned in-between dCas9 and PIF6 as in the original dCas9-VPR construct [70] this fusion protein did not show any nuclear translocation issues. The new CRISPR part of the system obtained was therefore: dCas9-NLS-GS Linker-PIF6 (Plasmids 19 - Supplementary Material - Chapter 6 - Section 6.2.2). The **RED6** pair of plasmids is illustrated in Figure 68 and the mechanism of action in Figure 69.

RED6	**dCas9-NLS-GS Linker-PIF6**
	PhyB (1-650)-NLS-Gateway Linker-VPR

Figure 68 - Plasmids structure of the **RED6** system.

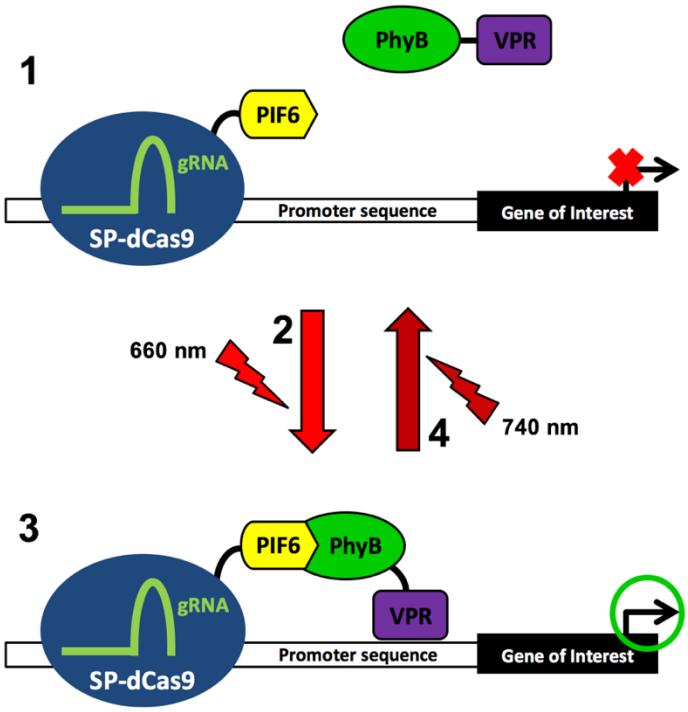

Figure 69 - Schematic working principle of the **RED3** systems (see Figure 54).

As for the previous experiments, HEK 293 cells were co-transfected with the **RED6** system, the GFP reporter and the gRNA plasmids and were exposed to continuous red or infrared illumination for 24 hours. The GFP reporter plasmid alone was transfected as control. From the fluorescence microscopy images in Figure 70, an evident

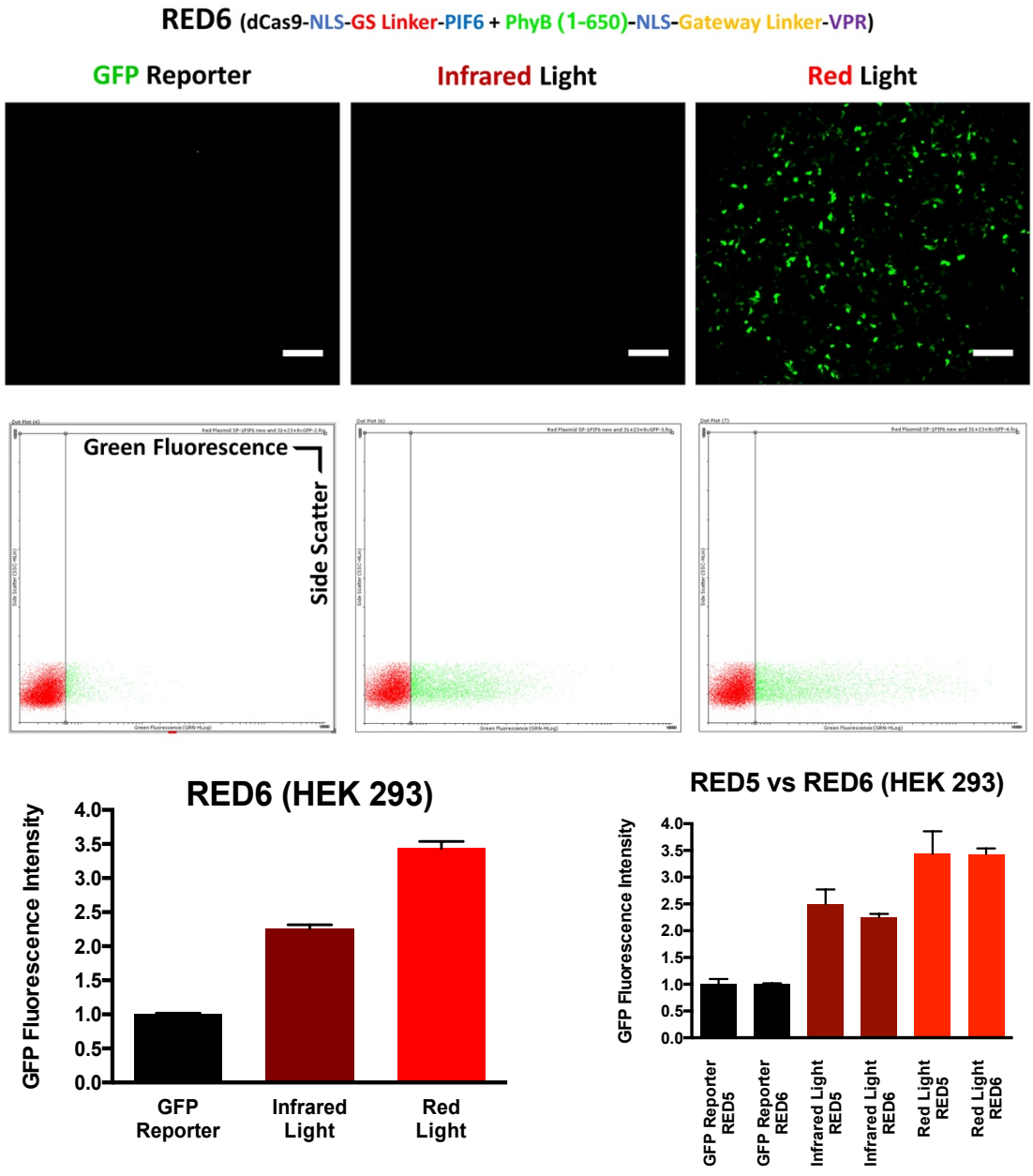

improvement in terms of GFP up-regulation efficiency between the **RED5** (Figure 67) and **RED6** systems it is not visible. This was confirmed by the flow cytometry analysis in Figure 70 (plots and graphs) where it can be observed that there is not a clear difference between the two systems under red or infrared illumination.

This experiment suggested that under red illumination, the CRISPR part of the system with only one PIF6 protein (**RED6**) was sufficient to achieve the same GFP up-regulation level as in the previous version with two PIF6 molecules fused up- and downstream the dCas9 protein (**RED5**). Moreover, this also indicated that the use of a single NLS sequence in-between dCas9 and PIF6 was sufficient for the nuclear translocation of this fusion protein. In addition, the unwanted GFP overexpression under infrared illumination remained the same even by reducing the PIF6 protein number.

The priority was to increase the system efficiency under red illumination. In this regard, as explained in section 3.3.3.1, the transfection efficiency had to be considered. The CRISPR-based and the activator plasmids in **RED6** were 9.8 kb and 9 kb respectively and they required to be transfected with high efficiency to achieve the translation of multiple copies of the fusion proteins. Therefore, transfection efficiency was considered as a possible limiting factor for a proper evaluation of the Red Light CRISPR system. Until this point, all the experiments were performed using HEK 293 cells. As shown in Figure 71, with this cell line, for the **RED6** system a maximum transfection efficiency around 20% could be achieved.

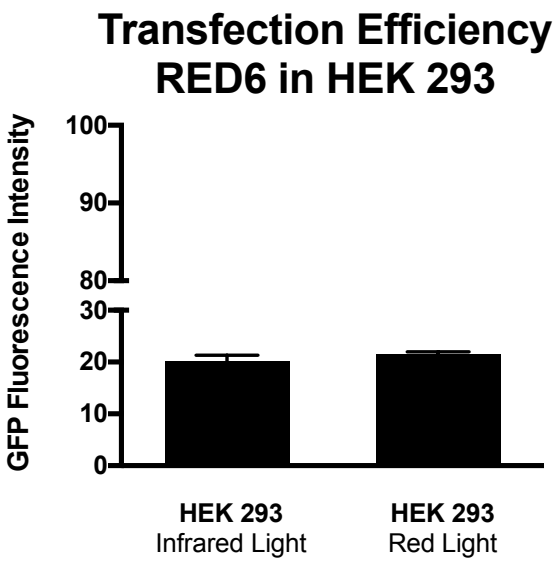

Figure 71 - Transfection Efficiency of **RED6** in HEK 239 cells measured by flow cytometry. The data represent the percentage of cells over the GFP basal fluorescence level (GFP reporter alone) transfected with **RED6** under red or infrared illumination. The measured transfection efficiency is around 20 %. n=3

*3.3.3.2.5 **RED6** in HEK 293 T17*

In order to improve this low transfection efficiency, the highly transfectable HEK 293 T17 line was used. These cells were co-transfected with the **RED6** system (Figure 68), the GFP reporter and the gRNA plasmids and were exposed to continuous red or infrared illumination for 24 hours. The GFP reporter plasmid alone was transfected as control.

From the fluorescence images in Figure 72 it is clear that the number cells overexpressing GFP under red illumination (fluorescence images and flow cytometry plots - Figure 72) was significantly higher when compared to the images/plots in Figure 70 where **RED6** was transfected in HEK 293. As shown by the flow cytometry graph in Figure 72 (left), this was translated in higher up-regulation efficiency of the **RED6** system: the change of the cell line resulted in a ≈4 times higher GFP overexpression level. The analysis in Figure 72 (right) highlights in fact that a transfection efficiency between 50% and 60% could be achieved compared to the previously 20%.

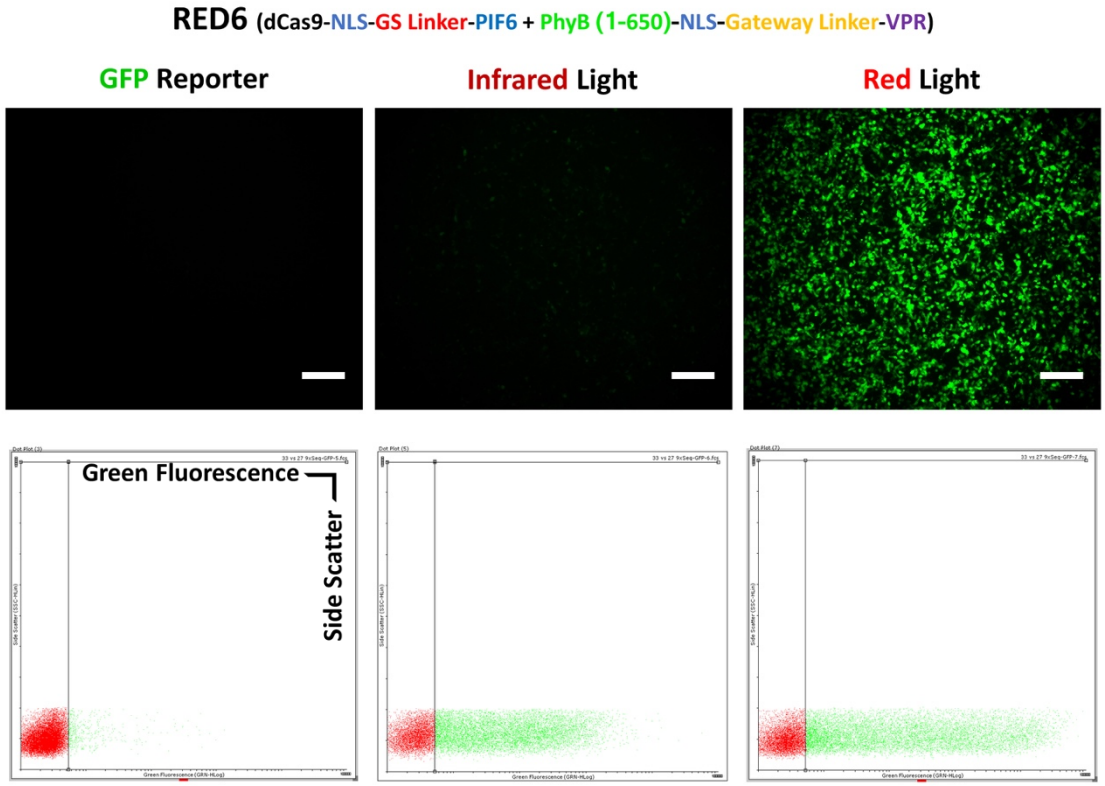

Figure 72 - Continues in the next page...

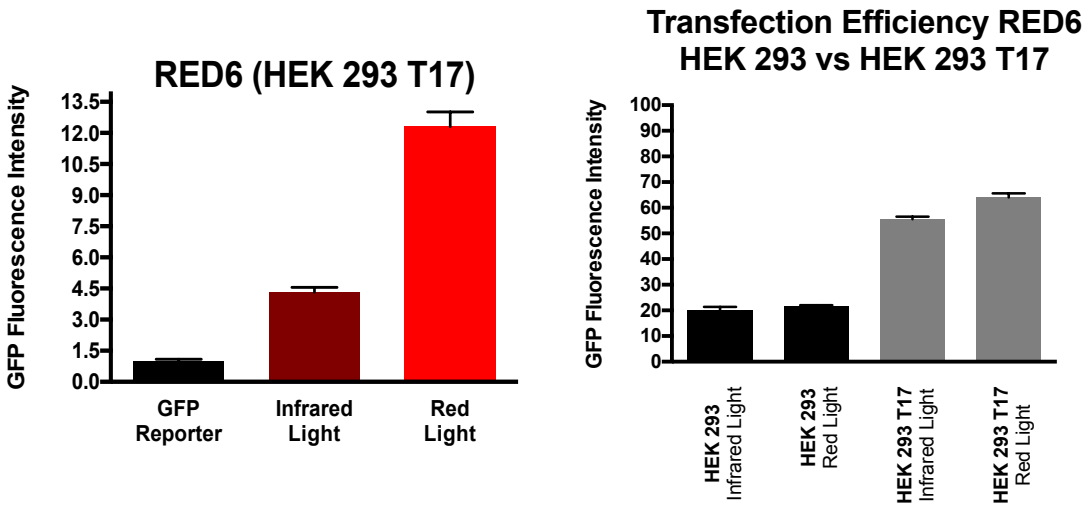

Figure 72 - **RED6** GFP up-regulation in HEK 293 T17 cells. Fluorescence images and flow cytometry analysis of **RED6** co-transfected in HEK 293 T17 cells with the GFP reporter and the gRNA plasmids and illuminated with red or infrared light (for 24 hours after the addition of PCB). The GFP reporter plasmid alone was transfected as control. It is visible that in this line, the number cells overexpressing GFP under red illumination is higher when compared to the transfection in HEK 293 cells (Figure 70). This result is confirmed by the flow cytometry graphs. The only change of the cell line results in a transfection efficiency between 50% and 60% which is translated in a ≈4 times higher GFP overexpression (n=3, statistically significant when compared to cells transfected with the GFP reporter alone or with **RED6** under infrared illumination, ANOVA - $p<0.05$). These data suggest that the efficiency of the transfection is actually a limiting factor for a proper functioning of the Red Light CRISPR system. The flow cytometry plots represent the number of cells below (red) and above (green) an arbitrary GFP threshold (0.5% of un-transfected cells - Material and Method section, chapter 5). Scale Bar, 200 μm.

These data suggested that the efficiency of the transfection is actually a limiting factor for a proper functioning of the Red Light CRISPR system.

*3.3.3.2.6 **RED7***

A further modification to the activator plasmid PhyB (1-650)-VPR was made. In particular, the NLS-gateway linker was replaced by a 10 aminoacid polyglycine-serine (GS) flexible linker used for previously published PhyB fusion proteins [105, 106]: PhyB (1-650)-GS Linker-VPR (Plasmids 22 - Supplementary Material - Chapter 6 - Section 6.2.2). This version of the system, **RED7** (Table 7 and Figure 73), was co-transfected in HEK 293 T17 cells but, compared to **RED6** (Figure 72), no improvements were detected in both the fluorescence microscopy and flow cytometry analysis (Figure 74).

RED7	dCas9-NLS-GS Linker-PIF6
	PhyB (1-650)-GS Linker-VPR

Figure 73 - Plasmids structure of the **RED7** system.

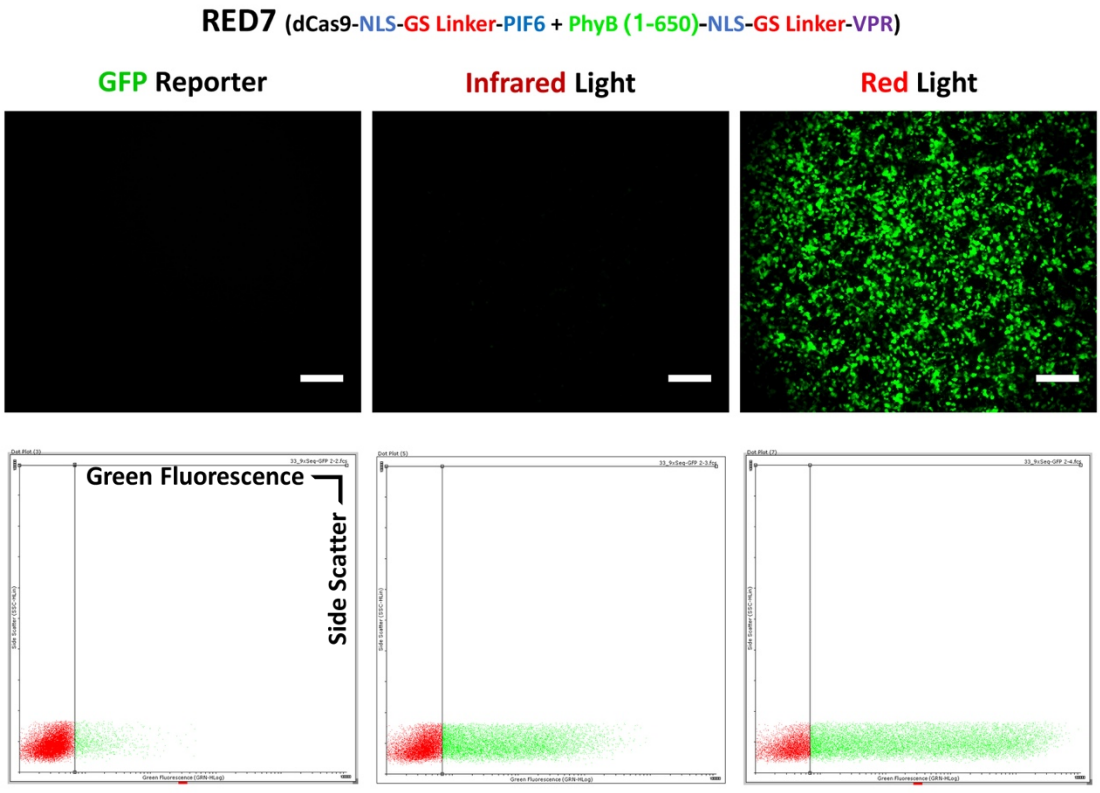

Figure 74 - Continues in the next page...

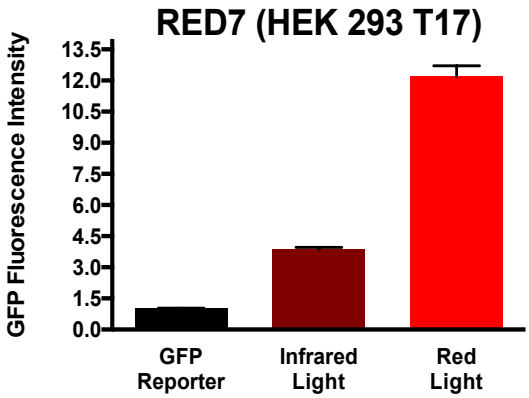

Figure 74 - **RED7** GFP up-regulation in HEK 293 T17 cells. Fluorescence images and flow cytometry analysis (n=4) of **RED7** co-transfected in HEK 293 cells with the GFP reporter and the gRNA plasmids and illuminated with red or infrared light (for 24 hours after the addition of PCB). The GFP reporter plasmid alone was transfected as control. From both the images and the flow cytometry graph it can be observed that there is not a significant difference between **RED6** (Figure 70) and **RED7** in terms of GFP up-regulation efficiency (**RED6** red light vs **RED7** red light, **RED6** infrared light vs **RED7** infrared light, **RED6** GFP reporter vs **RED7** GFP reporter non-statistically significant, ANOVA - $p>0.05$). The flow cytometry plots represent the number of cells below (red) and above (green) an arbitrary GFP threshold (0.5% of un-transfected cells - Material and Method section, chapter 5). Scale Bar, 200 μm.

*3.3.3.2.7 **RED7** vs dCas9-PIF6 Fusion Proteins*

The **RED7** version of the system produced very promising results, however, because the up-regulation rate was strictly related with the transfection efficiency, all the previously developed dCas9-PIF6 fusion proteins (From **RED1**, **RED2**, **RED3**, **RED4** and **RED5**) were compared in HEK 293 T17 in combination with the activator plasmid from **RED7**: PhyB (1-650)-GS Linker-VPR (Plasmids 22 - Supplementary Material - Chapter 6 - Section 6.2.2). In addition, a further CRISPR plasmid was assembled which consisted in dCas9 (from Chavez *at al.* [70]) with the N- and C-terminus fused to two PIF6 proteins separated by the 10 aminoacid polyglycine-serine (GS) flexible linker used in **RED6** and **RED7**: PIF6-GS Linker-dCas9-NLS-GS Linker-PIF6 (Figure 75) (Plasmids 20 - Supplementary Material - Chapter 6 - Section 6.2.2).

Figure 75 - CRISPR plasmid with dCas9 with the N- and C-terminus fused to two PIF6 proteins separated by a 10 aminoacid polyglycine-serine (GS) flexible linker.

Low passage HEK 293 T17 cells were co-transfected with the **RED7** activator plasmid (Figure 75) and the different dCas9-PIF6 fusion proteins together with the GFP reporter and the gRNA plasmids. Transfected cells were exposed to continuous red or infrared illumination for 24 hours. The GFP reporter plasmid alone was transfected as control.

The fluorescence images and the flow cytometry plots in Figure 76 confirmed that the highest GFP up-regulation was achieved with the **RED7** system. This was also quantified by flow cytometry analysis. As shown in Figure 77, the **RED7** system under red illumination induced the highest GFP up-regulation equal to ≈17.5 times the signal from the GFP reporter alone. The other pairs induced an equal GFP overexpression only around 7.5 times. From the graph in Figure 77, it was also interesting to notice that in all the systems, the de-activating infrared illumination was producing a similar low level of background fluorescence only ≈2.5 times higher than the GFP reporter alone signal. This is a very positive outcome: this difference, as mentioned before, is probably not strong enough to up-regulate any endogenous gene of interest which means that, as

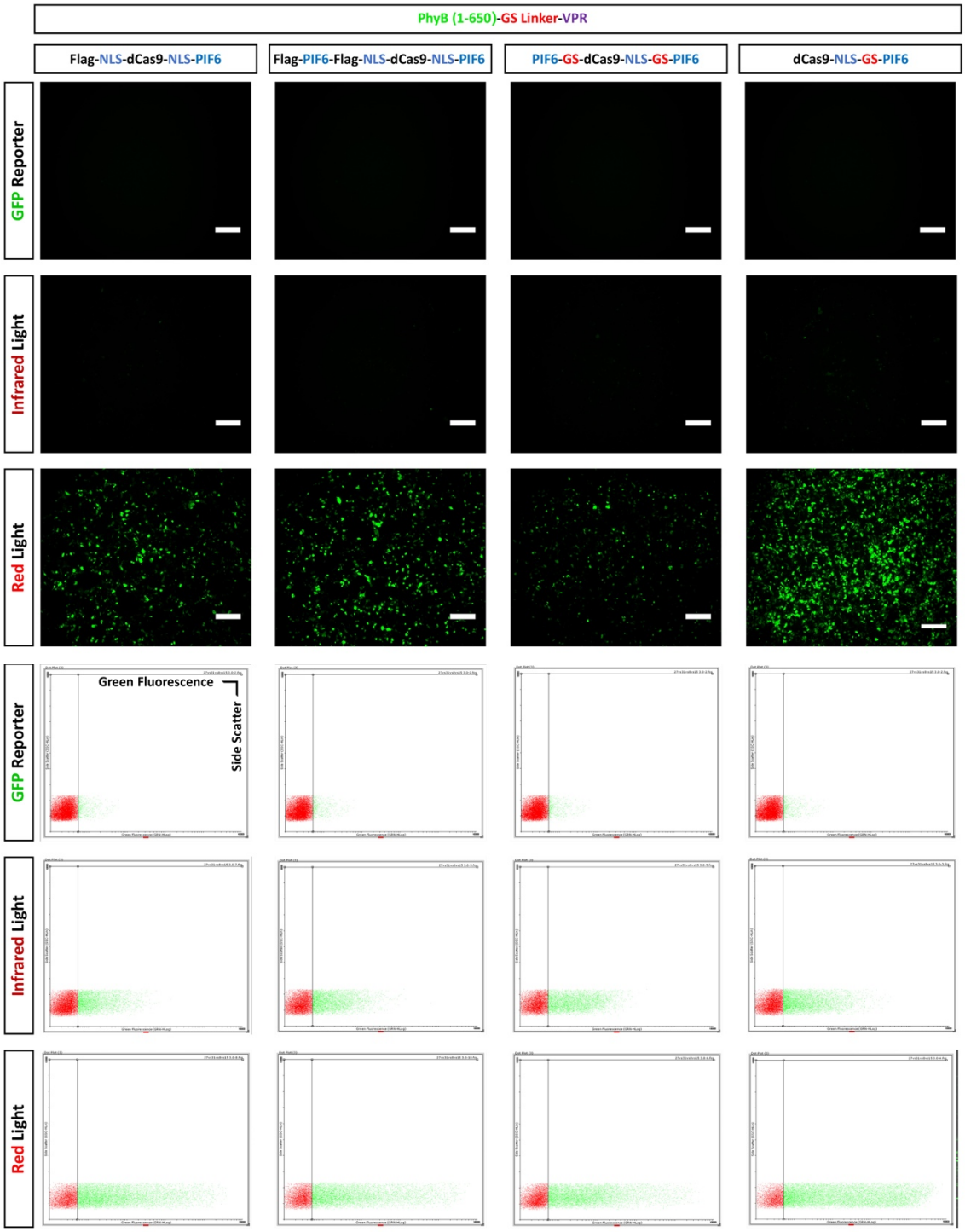

Figure 76 - Fluorescence microscopy comparison between **RED7** and different dCas9-PIF6 fusion proteins in combination with the **RED7** activator plasmid. The activator plasmid PhyB (1-650)-GS Linker-VPR (**RED7**) was co-transfected in HEK 293 T17 cells with the GFP reporter and the gRNA plasmids in combination with the different dCas9-PIF6 fusion proteins previously developed Flag-NLS-dCas9-NLS-PIF6 (**RED1**/**RED2** - Figure 59), Flag-PIF6-Flag-NLS-dCas9-NLS-PIF6 (**RED3**/**RED4**/**RED5** - Figures 61, 65 and 66)**,** dCas9-NLS-GS Linker-PIF6 (**RED6**/**RED7** - Figures 68 and 73) and the newly assembled PIF6-GS Linker-dCas9-NLS-GS Linker-PIF6 (Figure 75). The GFP reporter plasmid alone was transfected as control. The images indicate that the highest GFP up-regulation is achieved with the **RED7** system (red rectangle). The flow cytometry plots represent the number of cells below (red) and above (green) an arbitrary GFP threshold (0.5% of un-transfected cells - Material and Method section, chapter 5). Scale Bar, 200 μm.

required, infrared illumination is maintaining the system in the de-activated form. Moreover, as shown in the next section (3.3.3.2.8), the fluorescence background level of the system under infrared illumination is comparable with the GFP reporter fluorescent basal level.

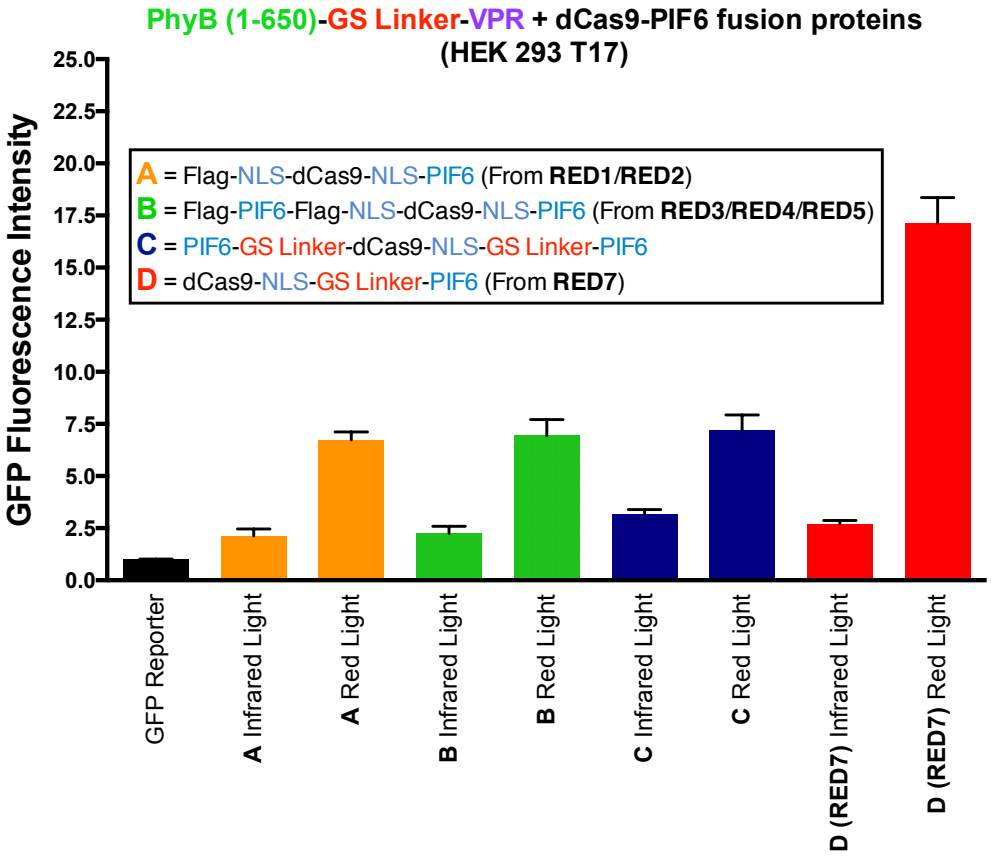

Figure 77 - Flow cytometry analysis of the samples in Figure 76. The activator plasmid PhyB (1-650)-GS Linker-VPR (**RED7**) was co-transfected in HEK 293 T17 cells with the GFP reporter and the gRNA plasmids in combination with the different dCas9-PIF6 fusion proteins indicated with the letters A, B, C and D. While A, B and D were previously used in **RED1/RED2**, **RED3/RED4/RED5** and **RED7** respectively, C is a newly assembled version. All these combinations were illuminated with red or infrared light for a 24 hours period (after the addition of PCB). The GFP reporter plasmid alone was transfected as control. The data confirmed that the highest GFP up-regulation is achieved with the **RED7** system (≈18 times over the GFP reporter alone signal).

*3.3.3.2.8 **RED7**, the promising version of the Red Light CRISPR System.*

This section of the thesis described the process behind the development of the Red Light CRISPR system that leaded to the assembly of **RED7** as a promising optogenetics tool for the control of gene expression using light. The graph and plots in Figure 78 below quantifies the efficiency of **RED7** from an average of four independent experiments where the light-induced up-regulation of the GFP reporter was measured by flow cytometry (in HEK 293 T17 cells). Importantly, while the GFP overexpression under red illumination is statistically significant ($p<0.0001$) when compared to both the system under infrared light and the GFP reporter alone, the GFP up-regulation induced by infrared light is not statistically significant when related to the fluorescence signal from the GFP reporter alone. The next section, 3.3.4, will analyse the main feature of the Red Light CRISPR system: the spatial resolution.

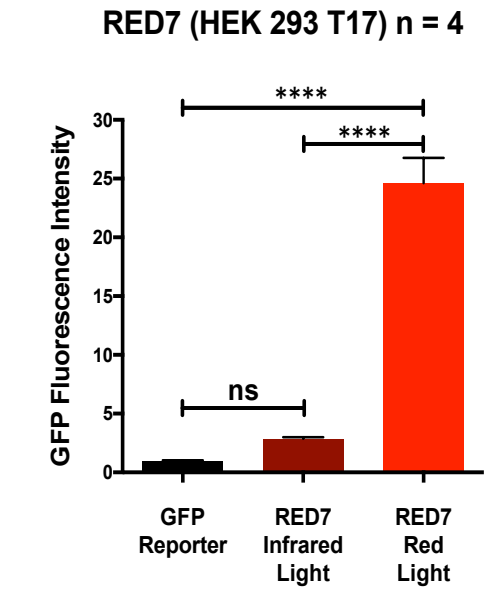

Figure 78 - Flow cytometry analysis (n=4) of **RED7**, the final version of the Red Light CRISPR system. HEK 293 T17 cells were co-transfected with the **RED7** system, the GFP reporter and the gRNA plasmids and were exposed to continuous red or infrared illumination for 24 hours. The GFP reporter plasmid alone was transfected as control. **RED7** is able to induce a statistically significant GFP up-regulation when compared to both the cells transfected with the GFP reporter alone or with **RED7** under infrared illumination (ANOVA - $p<0.0001$). Importantly, the GFP overexpression of RED7 under infrared illumination is not statistically significant when compared to the cells transfected with the GFP reporter alone (ANOVA - $p>0.05$). The flow cytometry plots represent the number of cells below (red) and above (green) an arbitrary GFP threshold (0.5% of un-transfected cells - Material and Method section, chapter 5).

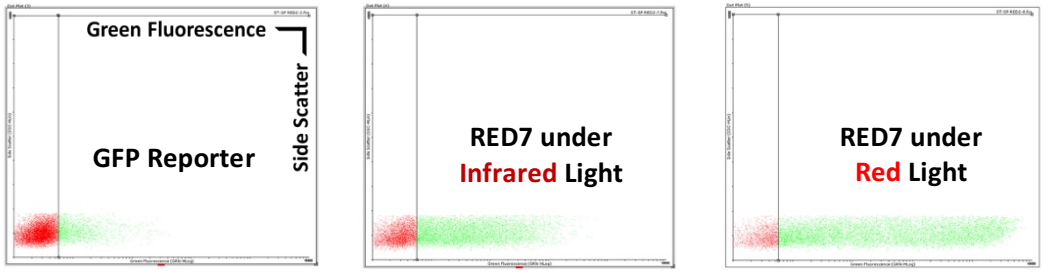

3.3.4 The Spatial Resolution of the Red Light CRISPR System

The main advantage of the Red Light CRISPR tool over the established dCas9-based systems (e.g. dCas9-VPR) for the up-regulation of genes of interest is the precise spatial resolution. **RED7** can be activated not only at a specific time, but the gene of interest up-regulation can also be confined to a precise region. This can be simply achieved by directing the red activating light to a selected area of the cells transfected with the system and a proper gRNA plasmid(s).

In order to demonstrate the spatial resolution capability of the Red Light CRISPR system, the LED box described in section 3.3.2 was modified. In particular, the red LEDs were placed close to each other to form a uniform illuminated surface. The experiments were performed in 6 well culture plates which were positioned over the LEDs at a variable distance (6-8 cm) depending on the LEDs number and the size of the illuminated area.
As shown in Figure 79A, to precisely select the confined region of up-regulation, a pattern was printed in black and white on transparent papers. Consequently, only the white area resulted in a transparent mask that was allowing red light to pass through.
As illustrated in Figure 79B, the printed mask was placed directly under the 6 well plate with the transfected cells and all was positioned over the LED box inside the cell culture incubator.

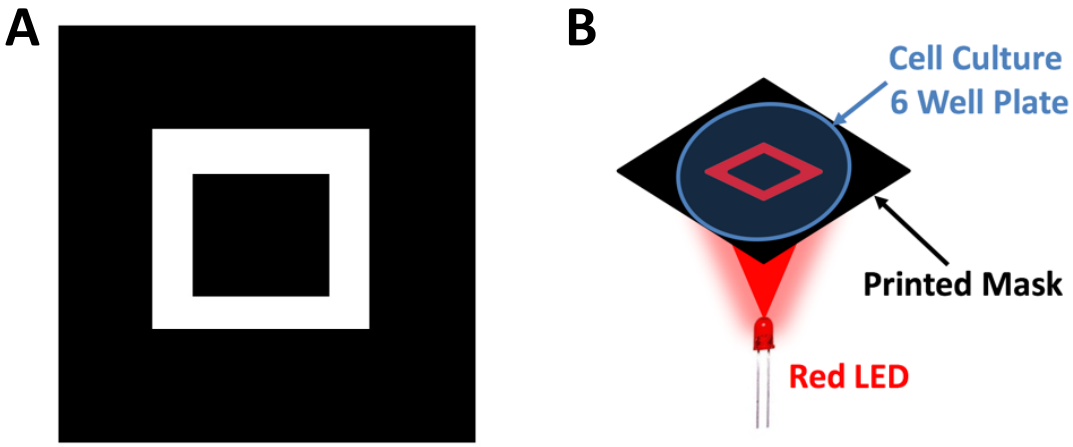

Figure 79 - Red Light CRISPR system spatial activation experimental procedure. (A) Black and white mask for a precise illumination pattern. It will be printed on transparent papers so that only the white area results in a transparent mask that allows red light to pass through. (B) To perform the experiments, the printed mask is placed directly under the 6 well plate with the transfected cells and this assembly is positioned over an LED box inside the cell culture incubator.

The pattern was exposed to red illumination for a period of 24h with a reduced 0.080/0.100 mW/cm^2 light intensity (section 3.3.2) as the walls and the lid of the culture plate could generate potentially activating light reflections. In addition, to minimise this possible issue, the lid of the 6 well plate was removed and replaced with a custom-made dark box placed directly in the incubator over the LED box and the 6 well plate.

The result of this experiment can be visualized in Figure 80 where the cells transfected with the **RED7** system, the GFP reporter and the gRNA plasmids were exposed to continuous red illumination for 24 hours through the mask in Figure 79A.
The well plate was fully covered by a dense monolayer of cells (Figure 80A, C, D and E) but only the one illuminated with red light through the mask were actually highly overexpressing the GFP reporter (Figure 80B, C, D and E).
As shown in Figure 81, the same experiment was repeated with different masks and the same result was obtained.

This section of the thesis suggested that the Red Light CRISPR system is capable of a highly spatial resolution. This optogenetics approach could lead to new possibilities in perturbative experiments aiming to study the dynamic interaction of a group of cells with their neighbours. Moreover, with a more precise control of the light at the micrometre level (e.g. Digital Micromirror Devices - DMDs), these experiments could be performed even at a single cell level.

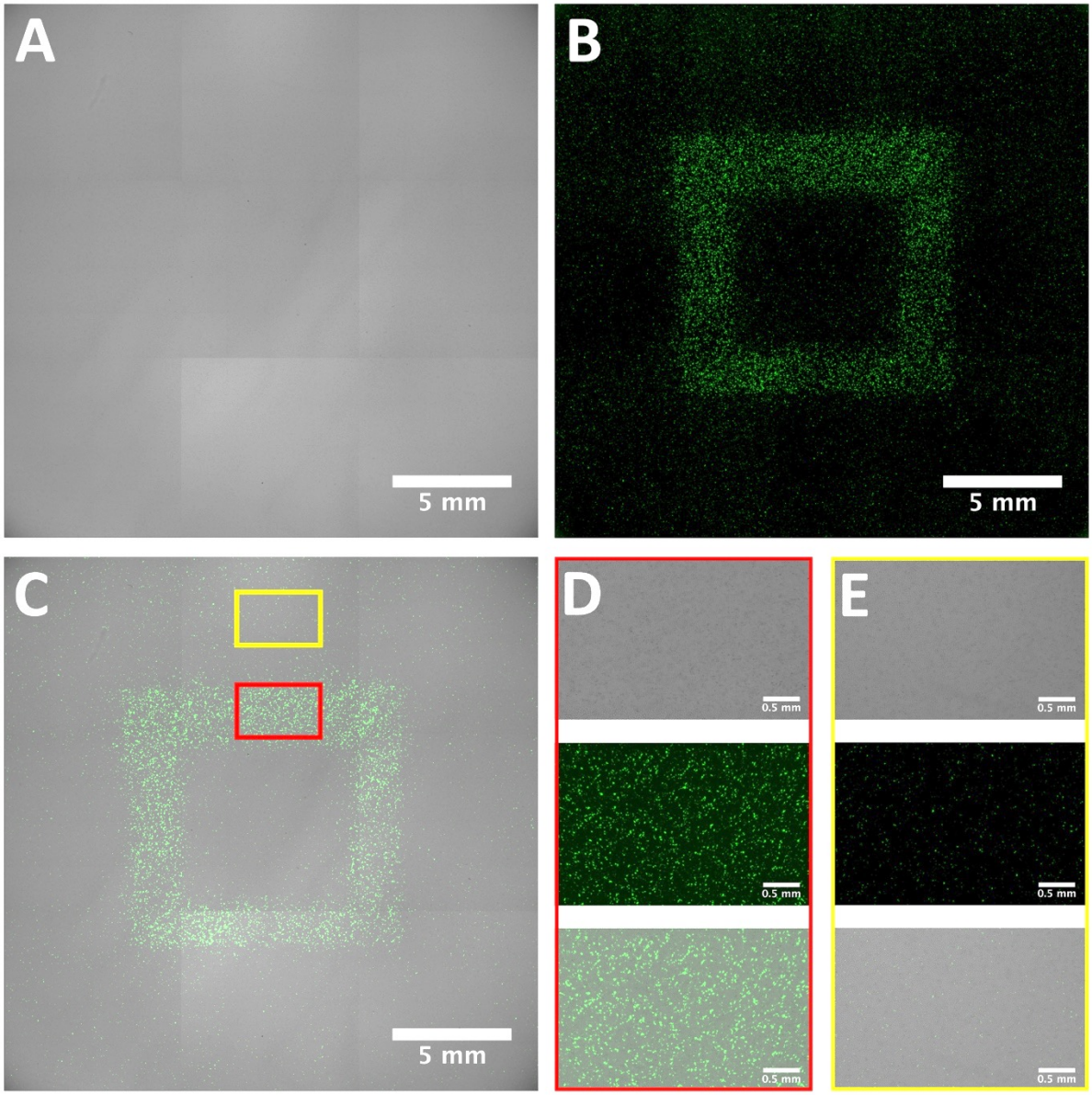

Figure 80 - Spatial activation of the Red Light CRISPR system. (A, B, C) Brightfield (A), fluorescence (B) and merged (C) images of HEK 293 cells co-transfected in a well from a 6 well plate with the **RED7** system, the GFP reporter and the gRNA plasmids and exposed to continuous red illumination for 24 hours through the mask shown in Figure 79A. (D, E) Brightfield, fluorescence and merged images of the two illuminated and non-illuminated regions indicated in (C) by the red and yellow rectangles respectively. The plate is fully covered by a dense monolayer of cells but only the one illuminated with red light through the mask were actually highly overexpressing the GFP reporter.

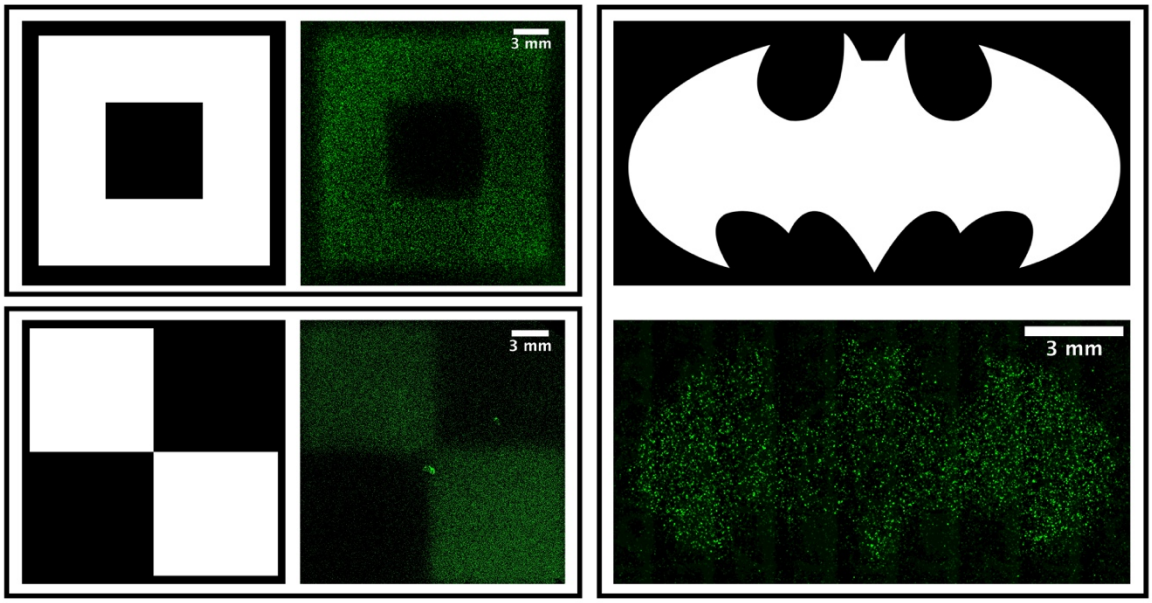

Figure 81 - Spatial activation of the Red Light CRISPR system through different masks than the one in Figures 79 and 80.

3.3.5 Orthogonal Optogenetics with Light CRISPR Systems

As mention in section 3.2, the CRISPR system is a flexible, efficient and easy to use genome engineering tool that was discovered in bacteria. Even though the Cas9 protein from *Streptococcus Pyogenes* (SPCas9) is the most studied and used, there are other bacteria species able to code for Cas9 proteins that are responding to specific gRNA Protospacer Adjacent Motif (PAM) sequences different from the *Streptococcus Pyogenes* NGG PAM [61, 108]. For instance, the Cas9 from *Streptococcus Thermophilus* (STCas9) is responding to a NNAGAAW PAM sequence (W = A or T). It means that SPCas9 transfected in cells together with STgRNA will not generate any genome modification as this protein will not be able to recognise the DNA target because of the PAM sequence mismatch. This process is equal also in the opposite case (STCas9 with SPgRNA). It follows that CRISPR systems from different bacteria species are fully orthogonal between each other in a PAM-dependent manner [61].

This multiplex approach has been successfully used to precisely label and simultaneously follow the dynamics of different chromosomal loci which are targeted by different Cas9 species fused with diverse fluorescent proteins [109]. Interestingly, orthogonal Cas9 proteins have also been fused to transcription activators for epigenetic DNA modification. An example is the work published by Esvelt *et al*.[61] where a fluorescent reporter has been orthogonally up-regulated by SPdCas9 or STdCas9 fused with the transcription activator VP64 and driven by specific SP or STgRNAs. Therefore, it is now possible in principle to simultaneously target and control different genes of interest.

However, this process is limited as the orthogonal CRISPR systems are lacking in spatiotemporal resolution. The ability to control the expression of multiple genes in space and time is fundamental as cellular processes are not arranged in a random fashion but are regulated following specific combinations of genetic patterns [101, 102]. The expression level of one or multiple genes in various cells and tissues can induce significantly different effects depending on both time and space [103].

As presented in the previous sections, the Red Light CRISPR system allows for a precise spatial control. Moreover, its activation and de-activation is only related to red or infrared illumination and therefore it can be controlled at will in a time-dependent

manner. It follows that the orthogonality in light-based CRISPR inducible systems can have an important impact as multiple gene (or set of genes) could be precisely and independently controlled in terms of both space and time.

This section of the thesis describes a potential multiplex approach based on light inducible orthogonal CRISPR systems with the aim of controlling the expression level of two different reporter genes in a spatiotemporally resolved manner. This project was the result of a collaboration with a colleague at the University of St Andrews, Rebeca Diaz, who provided plasmids of an improved and orthogonal version of the blue light-based (470 nm) CRISPR system previously published by Polstein *et al*. [85]. In particular, the CRYptochome 2 (CRY2) from *Arabidopsis Thaliana* was fused with the transcription activator VPR and the dCas9 protein from *Streptococcus Thermophilus* (STdCas9) was fused with the CRY2 counterpart, CIB1. In this way, this system should be fully orthogonal to the **RED7** system described in this thesis.

The first step was to verify the CRISPR orthogonality of the SPdCas9-based **RED7** with the gRNA for the STdCas9 protein. Therefore, HEK 293 T17 cells were transfected with the GFP reporter plasmid alone as control and co-transfected with the **RED7** system, the GFP reporter and the SPgRNA plasmid. Importantly, the GFP reporter eight repetitions that represents the SPdCas9 binding site (Figure 63), also contains a target for STdCas9. In fact, the NNAGAAW *Streptococcus Thermophilus* PAM sequence can be found within the repetitions in the form 5'-GTCGAGAAACTGCAAAAGGT**CGAGAAA**-3'. A suitable STgRNA plasmid targeting the sequence above was thus assembled. Therefore, **RED7** and the GFP reporter construct were co-transfected also with this STgRNA plasmid responsive for STdCas9. All the mentioned conditions, except the GFP reporter alone, were exposed to red or infrared light for 24 hours.

The result of this experiment can be visualized in Figure 82.

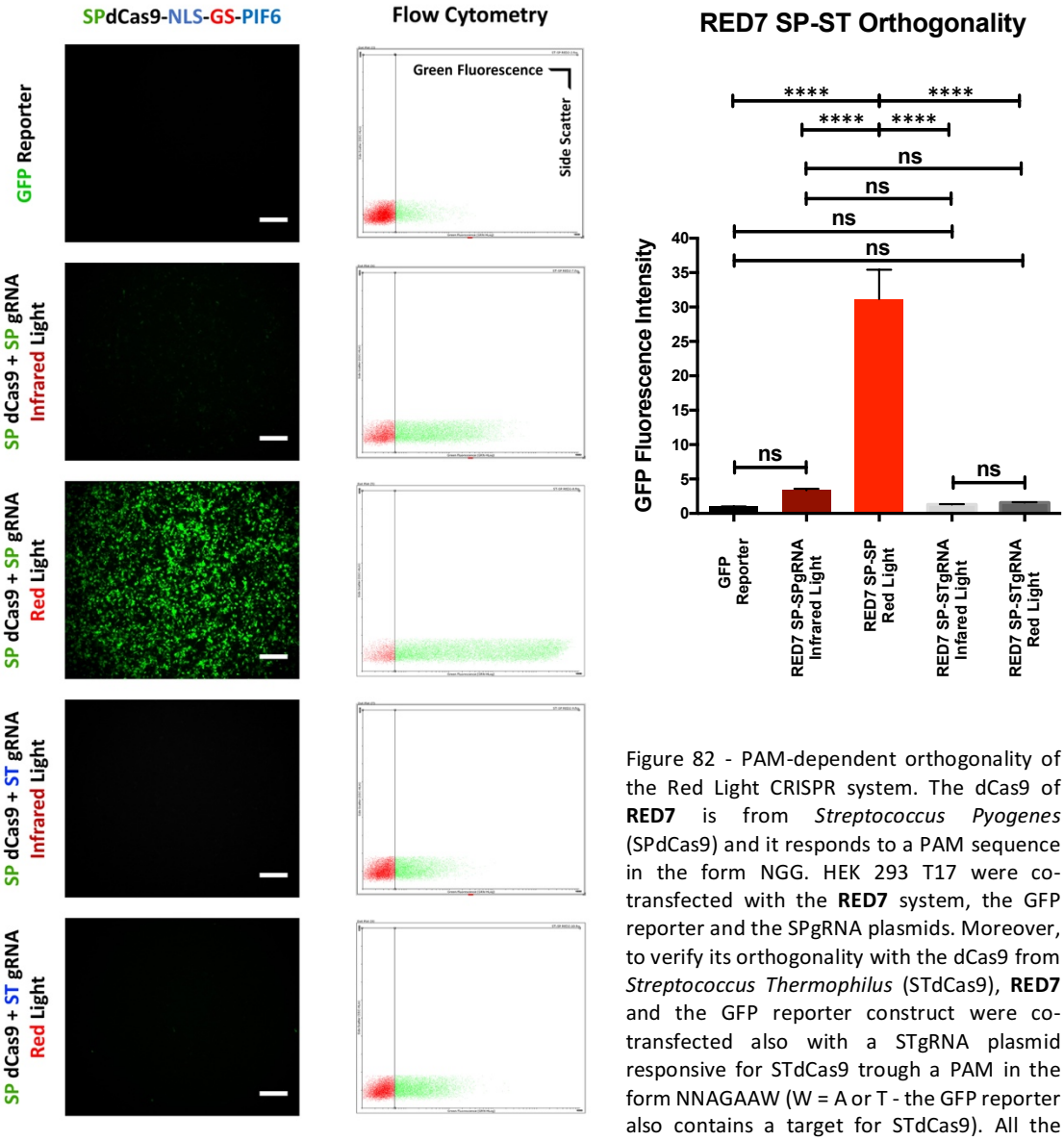

Figure 82 - PAM-dependent orthogonality of the Red Light CRISPR system. The dCas9 of **RED7** is from *Streptococcus Pyogenes* (SPdCas9) and it responds to a PAM sequence in the form NGG. HEK 293 T17 were co-transfected with the **RED7** system, the GFP reporter and the SPgRNA plasmids. Moreover, to verify its orthogonality with the dCas9 from *Streptococcus Thermophilus* (STdCas9), **RED7** and the GFP reporter construct were co-transfected also with a STgRNA plasmid responsive for STdCas9 trough a PAM in the form NNAGAAW (W = A or T - the GFP reporter also contains a target for STdCas9). All the mentioned conditions were exposed to red or infrared light for 24 hours (after the addition of PCB). The GFP reporter plasmid alone was transfected as control. From the fluorescence images, it is evident that **RED7** is inducing a significant up-regulation of the GFP reporter only when coupled with the SPgRNA and under red illumination. The flow cytometry analysis in the graph primarily confirms that **RED7** is not active with STgRNAs. In addition, it importantly shows that there is not a statistically significant difference between the GFP reporter alone signal, **RED7** under infrared illumination and the system coupled with STgRNA illuminated with either red or infrared light. These results suggest that the Red Light CRISPR system is actually orthogonal to the CRISPR system from *Streptococcus Thermophilus* depending on the PAM sequence. Scale Bar, 200 µm. The flow cytometry plots represent the number of cells below (red) and above (green) an arbitrary GFP threshold (0.5% of un-transfected cells - Material and Method section, chapter 5). (**** $p<0.0001$ - ANOVA).

From the fluorescence images, it is evident that **RED7** induced a significant up-regulation of the GFP reporter only when coupled with the SPgRNA and under red illumination. This suggests that the Red Light CRISPR system is actually orthogonal to the CRISPR system from *Streptococcus Thermophilus*. In order to quantify this, further experiments

were performed (plots in Figure 82). The results are summarized in the flow cytometry graph in Figure 82. This analysis primarily confirmed that **RED7** is not active with STgRNAs. Moreover, it importantly showed that there is not a statistically significant difference between the GFP reporter alone signal, **RED7** under infrared illumination and the system coupled with STgRNA illuminated with either red or infrared light.

These experiments suggested that if both the systems are present in a cell together with their gRNA plasmids, they can be independently controlled with red or blue light. It means that the expression of genes of interests could be controlled in space and time in a very precise manner. However, it has to be mentioned that in order to properly work, the red and the blue systems have to be orthogonal also in terms of light wavelength. The CRY2-CIB1 pair of proteins have been reported to interact with each other only with wavelength lower than 500 nm with major excitation peaks at ≈470 nm or ≈360 nm [78]. PhyB and PIF6 instead, are very sensitive to red or infrared light but a reduced level of interaction has been reported to happen also under UV light (311 nm) and, more importantly, under blue illumination at 465 nm [110]. Nevertheless, this activation can be easily compensated by shining simultaneously blue and infrared light [110].

In order to evaluate these features of the PhyB and PIF6 pair, HEK 293 cells were co-transfected with the **RED7** system, the GFP reporter and the SPgRNA plasmids. Transfected cells were exposed to red (660 nm), infrared (740 nm), blue (470 nm) or blue and infrared simultaneous (470 + 740 nm) light for 24 hours. Importantly, because the CRY2-CIB1 pair does not require continuous illumination as **RED7**, the 470 nm light was pulsed (1 pulse every 15 seconds) with a power of 16 mW/cm^2 [85].Moreover, the **RED7** system was also illuminated with red light (660 nm) for only 3 hours followed by 21 hours in the dark (Dark) to evaluate if, as previously reported [80], a shorter period of illumination was sufficient to fully exploit the power of the system. The same experiment was performed with 3 hours of red illumination followed by 21 hours under infrared light.

The results of this experiment are displayed by the flow cytometry analysis in Figure 83. First of all, it is important to mentioned that this experiment was performed in HEK 293 cells and therefore the GFP reporter up-regulation level is not as high as in Figure 78.

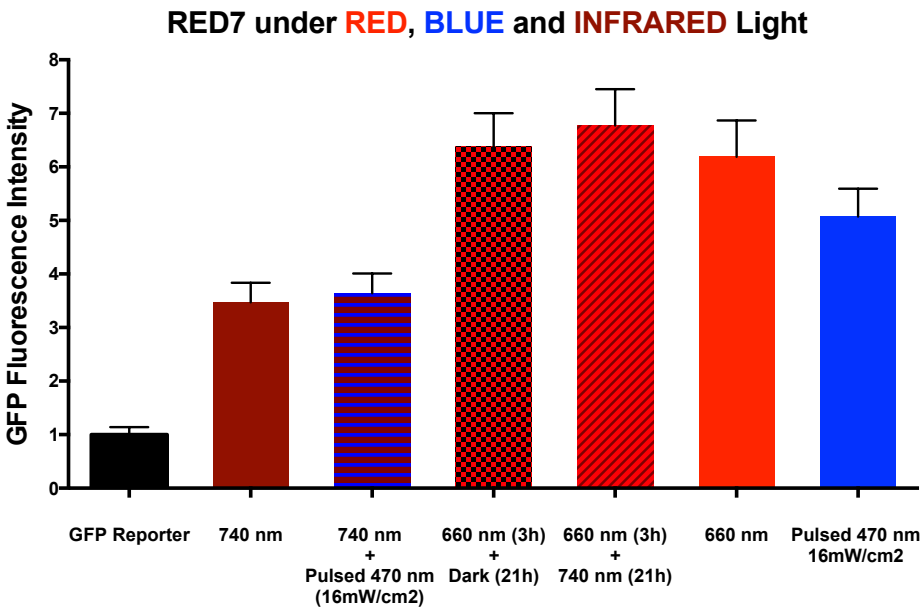

Figure 83 - Light wavelength-dependent orthogonality of the Red Light CRISPR system. PhyB and PIF6 are very sensitive to red (660 nm) or infrared (740 nm) light but a reduced level of interaction has been reported to happen also under UV light (311 nm) and, more importantly, under blue illumination at 465 nm. Nevertheless, this activation can be easily compensated by shining simultaneously blue and infrared light. This was verified by flow cytometry. HEK 293 cells were co-transfected with the **RED7** system, the GFP reporter and the SPgRNA plasmids. Transfected cells were exposed to red (660 nm), infrared (740 nm), blue (470 nm) or blue and infrared simultaneous (470 + 740 nm) light for 24 hours. Moreover, the **RED7** system was also illuminated with red light (660 nm) for only 3 hours followed by 21 hours in the dark (Dark) to evaluate if, as previously reported, a shorter period of illumination was sufficient to fully exploit the up-regulating power of the system. The same experiment was performed with 3 hours of red illumination followed by 21 hours under infrared light. The GFP reporter plasmid alone was transfected as control. The blue-infrared combination is actually maintaining the GFP overexpression at the same level as when **RED7** is under the only infrared light. It can also be observed that 3 or 24 hours of continuous red illumination are sufficient to achieve an equal level of GFP up-regulation when followed by either a dark period or infrared illumination. Finally, the results show that, even though with a reduced efficiency, also the blue light (470 nm) is able to activate the **RED7** system. Importantly, because the CRY2-CIB1 pair does not require continuous illumination as **RED7** (section 3.3.2), the 470 nm light was pulsed (1 pulse every 15 seconds) with a power of 16 mW/cm^2.

However, the main focus was to evaluate the activation level under the simultaneous blue and infrared illumination (470 + 740 nm). The results confirmed that this combination was actually maintaining the GFP overexpression at the same level as when **RED7** was under the only infrared light. Moreover, it was observed that 3 or 24 hours of continuous red illumination were sufficient to achieve an equal level of GFP up-regulation when followed by either a dark period or infrared illumination. This latter result is strictly gene/protein dependent. An illumination of red light for 3 hours is certainly sufficient to up-regulate GFP but if this process is followed by 21 hours of

infrared illumination, the **RED7** system is de-activated and thus the induced gene transcription is blocked. If a protein requires more time than GFP to be transcribed, it will not possible to reach an equal red light induced overexpression level. In addition, even if the 21 hours of 740 nm illumination is de-activating the system, the GFP signal is not decreasing. It is because the half-life of this fluorescent protein is around 24 hours and therefore, in order to observe a significant decrease in the intensity, a longer period of time (e.g. 48 hours) is required before performing the flow cytometry analysis. Valid alternative ways of studying the de-activation process of the Red Light CRISPR system could be either the use of a destabilised version of GFP (EGFPd2) that has a half-life of only 2 hours or performing real time PCR experiments.

Finally, the results showed that, even though with a reduced efficiency, also the pulsed blue light (470 nm at 16 mW/cm^2) was able to activate the **RED7** system.

Overall, these experiments demonstrated that **RED7** and the blue system were orthogonal in terms of both CRISPR species and light wavelength but only if blue and infrared illumination were simultaneously on. These findings suggested that the two systems could be in principle used together to achieve a precise and independent control of different genes of interest in terms of both space and time. The GFP and mCherry reporter plasmids previously used in this work (Figures 57 and 63) were selected as the targets for a proof-of-concept experiment aiming to test the light wavelength-dependent orthogonality of the red and blue CRISPR systems.

If the only temporal resolution is desired, the cells transfected with the two systems can be illuminated with blue and infrared light when the activation of the blue system is required or with red light when the **RED7** action is needed.

If instead the spatial resolution is desired, there are in general two types of protocols that depends on the accuracy of the illumination source. For instance, the use of Digital Micromirror Devices (DMDs) coupled with an optical microscope can guarantee micrometre precision over a large field of view and therefore different areas can be simultaneously illuminated with either red or infrared and blue light (Figure 84A). In the other case, as shown for the spatial resolution experiments in section 3.3.4, a sequential

illumination is required because the use of simultaneous red illumination with blue and infrared light will not allow the activation of the **RED7** system (because infrared is de-activating the system). This is why the previous evaluation of the minimum red illumination time for an efficient **RED7** GFP up-regulation was fundamental (Figure 83). With the illumination setup used in this work (LED box - section 3.3.2), a micrometre precise illumination could not be achieved. Therefore, in order to reach a precise spatial resolution, a sequential approach exploiting a different solution based on the colour theory had to be used. It is known that red light is blocked by blue filters, blue light is instead blocked by yellow filters. Vice versa, the blue filter allows blue light to pass through and yellow filter does the same for red light (Figure 84B). For instance, in case

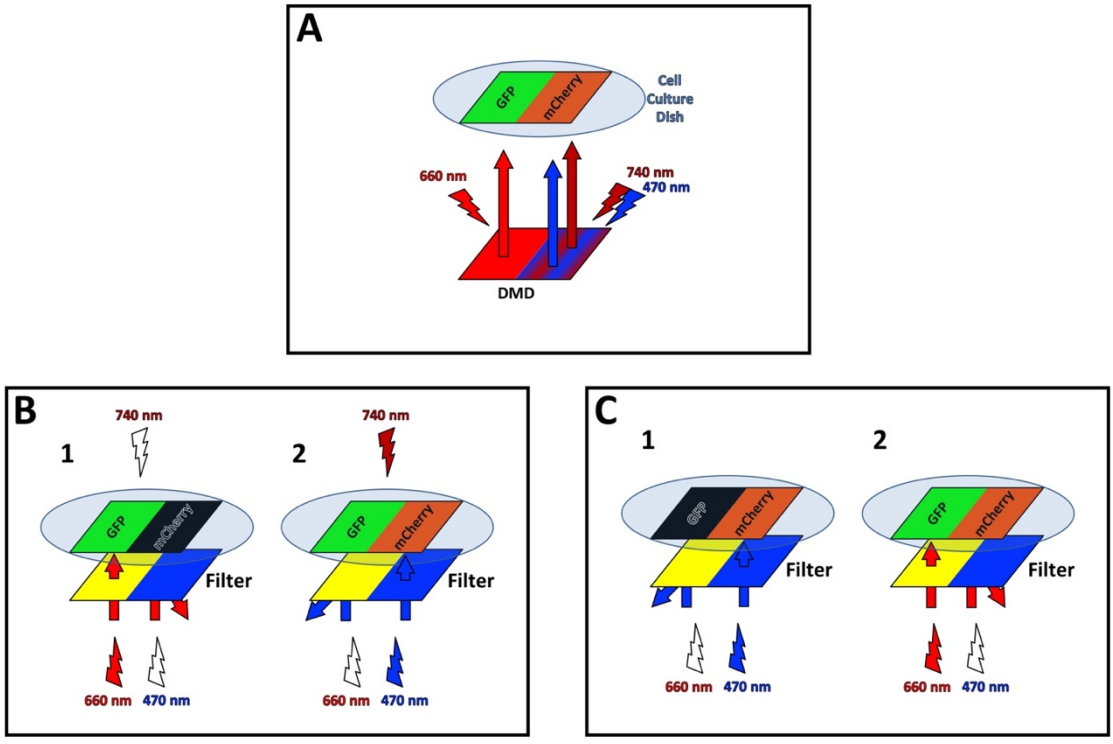

Figure 84 - Diagrams for light wavelength-dependent orthogonality in spatial activation experiments between the Red Light CRISPR system and the blue light CRY2-CIB1 CRISPR system. The red system is controlling the expression level of GFP, the blue system of mCherry. (A) The use of a Digital Micromirror Device (DMD) can guarantee micrometre precision illumination pattern and different areas can be simultaneously illuminated with either red (660 nm) or infrared and blue (740+470 nm) light inducing an accurate GFP/mCherry spatially separate up-regulation. If this or a similar precision device is not available, there are two options that require a sequential illumination approach based on the colour theory: red light is blocked by blue filters, blue light is instead stopped by yellow filters. Vice versa, the blue filter allows blue light to pass through and yellow filter does the same for red light. In the first approach (B1), red light (660 nm) is switched on first and it induces GFP up-regulation only in the region masked with a yellow filter. The wavelength is then changed (B2) to simultaneous blue (470 nm) and infrared (740 nm - from the top) and mCherry can be overexpressed only in the area masked with a blue filter. The second approach (C) does not require infrared illumination. Blue light (470 nm) is switched on first (C1) and it induces mCherry up-regulation only in the region masked with a blue filter. The wavelength is then changed (C2) to red (660 nm) and GFP can be overexpressed only in the area masked with a yellow filter.

of the GFP protein, the **RED7** system could be activated with a 3 hours red illumination followed by a 21 hours period of simultaneous infrared and blue illumination for mCherry overexpression (Figure 84B). With another approach, the CRY2-CIB1 system can be activated with blue light first and then, after the addition of PCB, red light (minimum 3 hours) can be used to switch on the **RED7** system (Figure 84C). The advantage is that infrared LEDs are not required.

The latter is the strategy (Figure 84C) used in the spatial resolution experiment with the two CRISPR orthogonal systems. In order to create a suitable light filter, a bicolour blue and yellow mask was printed on transparent paper as shown in Figure 85A. The power of blue and red light was evaluated with a power metre to make sure that the blue filter was blocking red light but allowing a sufficient level of blue light and, vice versa, that the yellow filter was blocking blue light but allowing red light to pass through. Because

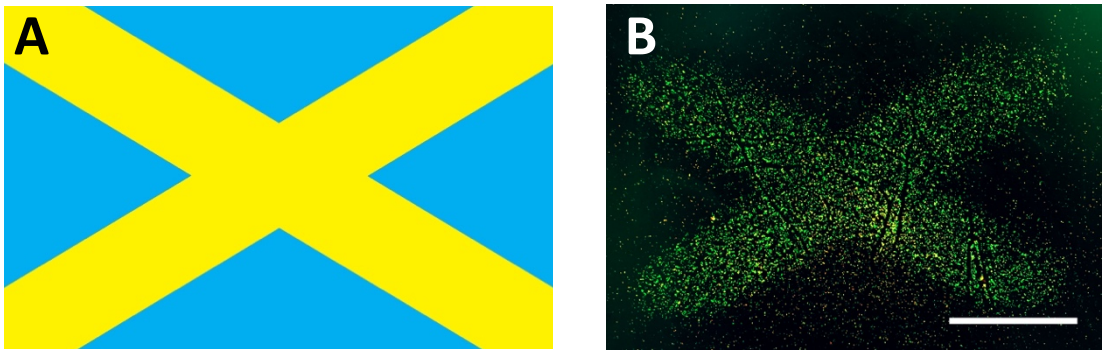

Figure 85 - Light wavelength-dependent orthogonal spatial activation of the red and blue CRISPR systems. (A) Blue and yellow mask for a precise orthogonal illumination pattern. (B) Fluorescence image of HEK 293 T17cells co-transfected in a well from a 6 well plate with the **RED7** system, the blue system, the GFP reporter, the mCherry reporter and the SPgRNA and STgRNA plasmids. Because transfecting both the systems in HEK 293 T17 cells with Lipofectamine 3000 was not feasible due to the big size of the plasmids, two different wells of a 6 well plate were first transfected with the two systems separately and then mixed together. The experiment was performed using the bi-colour mask in (A) and following the sequential approach illustrated in Figure 84C. As expected, the **RED7** system induced GFP up-regulation in a light wavelength-based space resolved manner. However, further experiments have to be performed (by Rebeca Diaz) aiming to more precisely characterised the CRY2-CIB1-based blue light system since a significant/visible mCherry overexpression is not detected. Blue light, 1 pulse every 15 seconds with a power of 16 mW/cm^2 for 12 hours. Red light, continuous red illumination at 80 μW/cm^2 for 3 hours followed by 21 hours of dark. Scale Bar, 0.5 mm.

transfecting both the systems in HEK 293 T17 cells with Lipofectamine 3000 was not feasible due to the big size of the plasmids, two different wells of a 6 well plate were first transfected with the two systems separately and then mixed together. In particular, **RED7** was co-transfected with the GFP reporter (Figure 63) and the SPgRNA plasmids,

the blue system with the mCherry reporter (Figure 57) and the STgRNA plasmids. Pulsed Blue light was switched on for a 12 hours period followed by 3 hours of red illumination.

As shown in Figure 85B, this experiment suggests that, as expected, the **RED7** system induced GFP up-regulation in a light wavelength-based space resolved manner. However, further experiments have to be performed by Rebeca Diaz aiming to more precisely characterised her CRY2-CIB1-based system since a significant/visible mCherry overexpression could not be detected.

3.4 The Red Light CRISPR System in 3D Cell Culture Models

One of the main advantages of the Red Light CRISPR system is that it is based on the PhyB-PIF6 pair of proteins that are sensitive to red light. This feature is very important mostly when 3D cell culture models are considered as red light can penetrate deeper in thick samples/tissues when compared to lower wavelength such as UV or blue light [81]. It follows that the Red Light CRISPR system developed in this work has the potential to be exploited in optogenetics experiments that require a precise control of genes expression in cell culture models that more closely mimic human tissues. As mentioned in Chapters 1 and 2, these 3D models require dedicated imaging systems, especially if the samples need to be alive for long periods of time. Light sheet microscopy emerged as one of the most suitable techniques to serve this purpose [32]. The HT-LISH microscope developed in this work, apart from its main application in high throughput imaging studies, was capable to acquire stack of images in multiple dimensions (3D, 4D and 5D). The HT-LISH microscope and the Red Light CRISPR system developed and described in this thesis have therefore the potential of working together in a synergistic manner.

This section is first evaluating if the Red Light CRISPR system can be expressed in cellular spheroid when transfected with Lipofectamine 3000 and is then proposing a HT-LISH microscope implementation aiming to lay the foundation for future on-stage HT-LISH microscope-based optogenetics experiments on 3D models. In particular, the upgraded microscope has been used to perform experiments aiming to optically control the expression level of genes of interest in cellular spheroids with the Red Light CRISPR system.

3.4.1 The Red Light CRISPR System in cellular spheroids

The first step was to evaluate whether the Red Light CRISPR system could be transfected with Lipofectamine 3000 and activated in 3D cell culture models. For this purpose, HEK 293 T17 cellular spheroids of 200 μm in size were used. The **RED7** system, the GFP reporter and the gRNA plasmids were transfected while plating the cells in an ultra-low attachment 96-well round bottom cell culture plate for the generation of the spheroids (Material and Methods - Chapter 5). After a 24 hours period, the well plate was positioned on top of the LED box inside the culture incubator and the spheroids were exposed to continuous red or infrared illumination for 24 hours. The HT-LISH was then used to image these samples. The images in Figure 86 displays the Maximum Intensity Projection (MIP) of two HEK 293 T17 cellular spheroids exposed to infrared or red light.

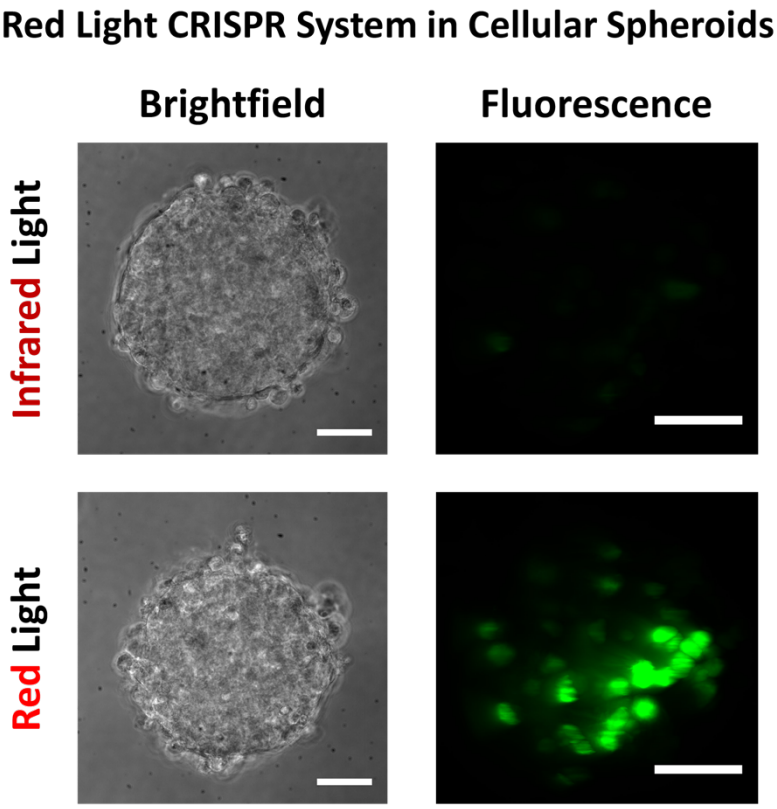

Figure 86 - The Red Light CRISPR System in Cellular Spheroids. Brightfield and fluorescence images of the **RED7** system, the GFP reporter and the gRNA plasmids transfected in ≈200 μm HEK 293 T17 cellular spheroids. After 24 hours, the spheroids were incubated in PCB for 1 hour and then transferred on top of the LED box inside the culture incubator. The samples were exposed to continuous red or infrared illumination for 24 hours. The HT-LISH was then used to image these samples. Despite a low transfection efficiency, the fluorescence images (Maximum Intensity Projection) show that the **RED7** system under red illumination is inducing a clear GFP up-regulation compared to the spheroid illuminated with infrared light, wavelength that, maintains the system in the off state. Scale bar, 50 μm.

Despite a low transfection efficiency, it was evident that the **RED7** system under red illumination was inducing a clear GFP up-regulation compared to the spheroid illuminated with infrared light, a wavelength that, as expected, was maintaining the system in the off state. These data suggest that the Red Light CRISPR system could be exploited also in 3D *in vitro* cell culture models such as cellular spheroids. Probably, if bigger and thus more scattering samples are used, a higher illumination power is required for the activation/de-activation. In addition, the experiment confirmed that the maximum transfection efficiency that can be achieved with Lipofectamine 3000 is limited by the plasmids size.

3.4.2 Implementing the HT-LISH microscope for Optogenetics Experiments

The challenge was now to implement the HT-LISH microscope so that optogenetics studies could be performed directly on the microscope stage, including the experiments with the Red Light CRISPR system. In this way, 3D samples (but also 2D monolayers) could be grown and monitored/imaged over time directly on the microscope while different wavelength of light are used to control the optogenetics tools expressed in the specimens.

In order to introduce this upgrade to the HT-LISH microscope, a DLP® LightCrafter™4500 (National Instruments) was used. It is a projector that include red, blue and green LEDs and a Digital Micromirror Device (DMD) that can be used to precisely direct the light. The DMD consists of an array of small mirrors that can be singularly and independently switched between a on or off position so that any light pattern can be generated and projected. It means that if the DMD is conjugate with the focal plane of the objective O1 (Figure 87), the light coming from the LightCrafter can be precisely shaped at the sample level.

The diagram of the HT-LISH optogenetics upgrade is shown in Figure 87. The parts list of all the components used in this system can be found in the Supplementary Material (Chapter 6 - Section 6.1.1).

A dichroic mirror reflecting red light and allowing lower wavelength to pass through was mounted after the tube lens TL1. The DMD plane (IP8) had to be conjugate to the image plane labelled as IP6 which in turns was conjugate with the focal plane (FP) of O1 (Figure 87). Importantly, the FOV of the HT-LISH microscope is of 250 μm in X and 257 μm in Y; the DMD size is instead of 8706 μm in X and 6965 μm in Y (Micromirror XY size 6.637 μm - DMD pixel size 1140 in X and 912 in Y). If the DMD is installed directly at the IP6 level, its size at the sample level (FP) is de-magnified 40 times (O1 is a 40X) and therefore its dimensions will be 218 μm in X and 174 μm in Y. While the size covers almost the entire FOV of the HT-LISH microscope along the X direction (250 vs 218), the situation is different for the vertical dimension (257 vs 174). In order to cover the entire FOV, a magnification of 1.5x can be used (257/174) as it will result in a DMD XY size of 327.8

μm and 261 μm at the O1 focal plane (FP) level. To achieve that, a single f=125 mm lens labelled as L7 was used (Figure 87). In particular, the lens L7 was installed at 313 mm after the IP6 and the DMD at 208 mm from the lens L7 (M=313/208=1.5x). In addition, also a compact CCD camera was mounted in this optical path (IP7) through a 50:50 light splitter. In this way, any pattern projected on the focal plane (FP) or the samples illuminated with Brightfield light could be visualised (even if not entirely as the compact CCD camera sensor is smaller) (Figure 87).

Both the DMD and the light wavelengths can be controlled with the LightCrafter

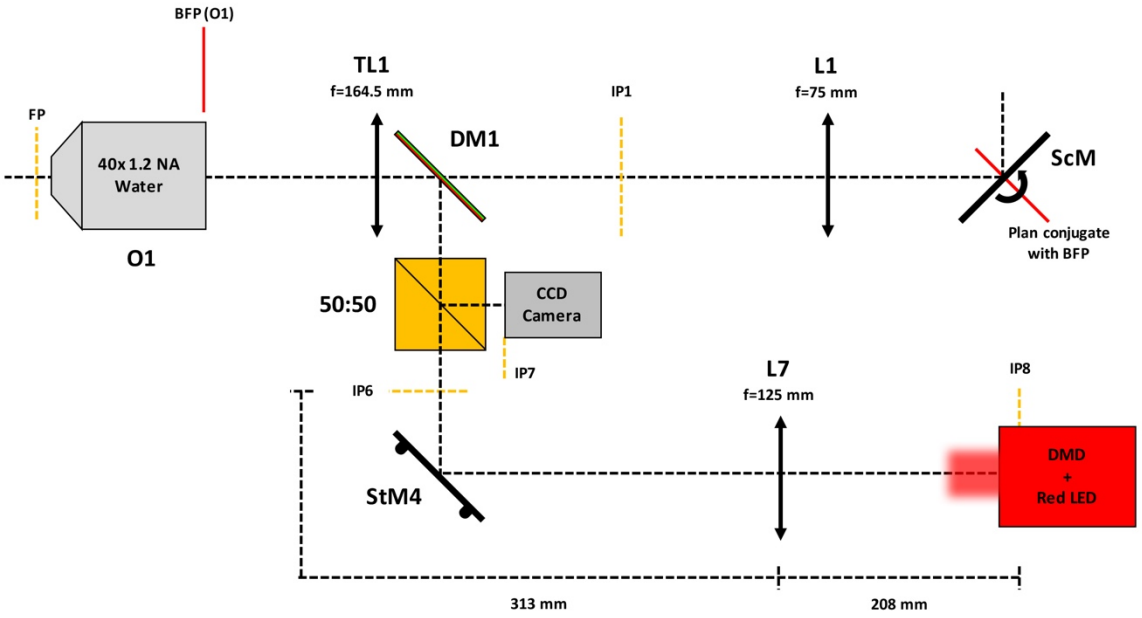

Figure 87 - Diagram of the Digital Micromirror Device (DMD) optical path. O, Objective; FP, Focal Plane; BFP, Back Focal Plane; TL, Tube Lens; IP, Image Plane; L, Lens; ScM, Scanning Mirror; DM, Dichroic Mirror; StM, Steering Mirror; 50:50, Lights Splitter.

software from National Instruments. The red light power was measured with a power meter (Thorlabs PM100USB) and was set to ≈300 $\mu W/cm^2$.

In order to test the DMD alignment and its ability to project light patterns at the focal plane level, a glass bottom cell culture dish was covered with a marker that could be excited with red light. The different light masks projected were imaged with the compact

CCD camera. As shown in Figure 88, the DMD was capable of illuminating the full area or only precise regions of the FOV.

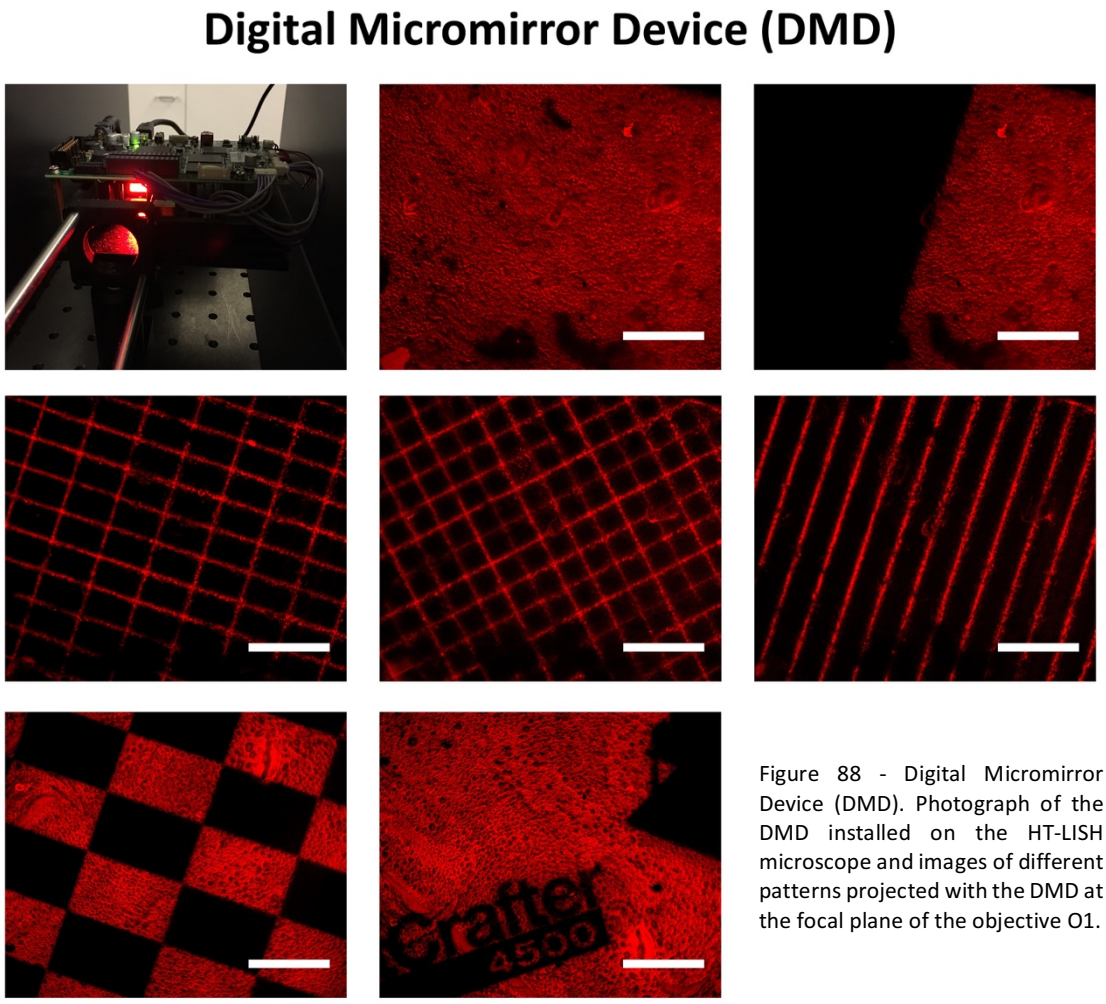

Figure 88 - Digital Micromirror Device (DMD). Photograph of the DMD installed on the HT-LISH microscope and images of different patterns projected with the DMD at the focal plane of the objective O1.

3.4.3 On-stage optical control of gene expression with the Red Light CRISPR System in cellular spheroids

The next step was to activate the Red Light CRISPR system expressed in HEK 293 T17 cellular spheroids directly on the stage of the implemented HT-LISH microscope. Therefore, the **RED7** system, the GFP reporter and the gRNA plasmids were transfected while plating the cells in an ultra-low attachment 96-well round bottom cell culture plate for the generation of the spheroids (Material and Methods - Chapter 5). After a 24 hours period, the PCB was added to the culture media and the spheroids were left for 1 hour in the cell incubator. The samples were then transferred into a glass bottom culture plate and suspended in a solution of low melting point agarose (to minimize any movement on the microscope stage). These processes were performed in dark condition or under a green safelight (Material and Methods - Chapter 5). The dish was then transferred to the stage top incubator on the HT-LISH microscope stage and, under infrared illumination, the compact CCD camera was used to focus a spheroid in the FOV. A custom-made dark box was positioned on top of the dish to block any possible room activating light. The LightCrafter were then switched on so that the entire FOV was illuminated with red light. After a 24 hours period, the spheroid was imaged with the HT-LISH microscope.

The result of this experiment can be visualized in Figure 89. The Maximum Intensity Projections (MIP) of the HEK 293 T17 cellular spheroid suggested that the Red Light CRISPR system could be activated directly on the implemented HT-LISH microscope stage.

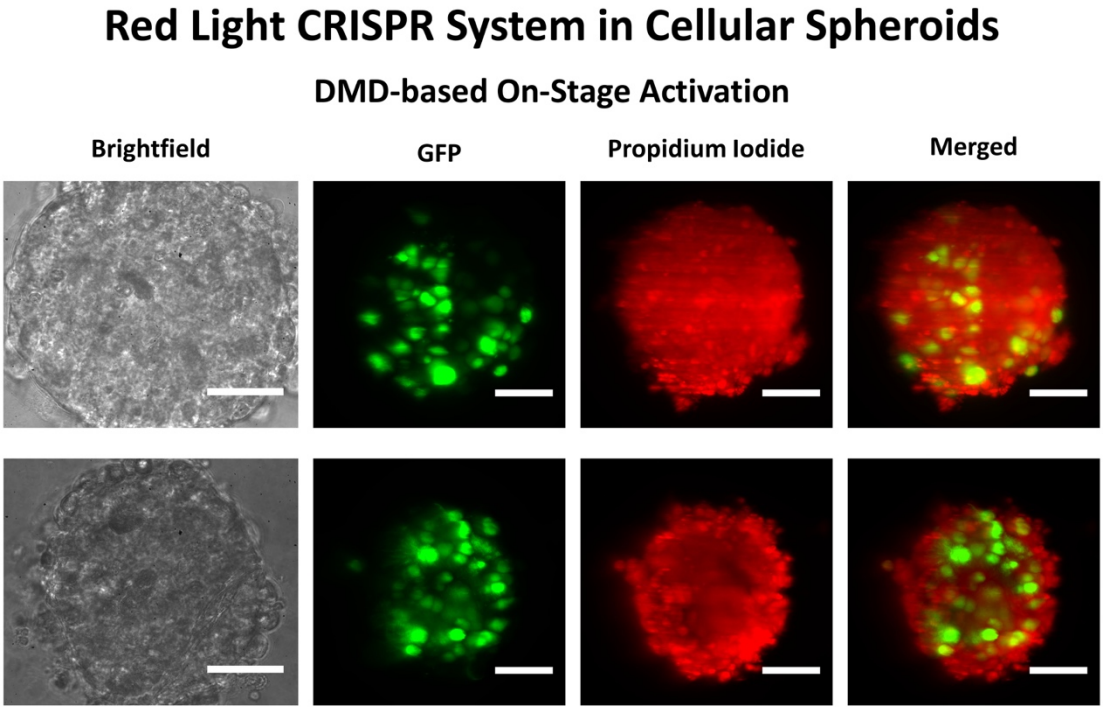

Figure 89 - DMD-based on-stage activation of the Red Light CRISPR System expressed in Cellular Spheroids. Brightfield and fluorescence images of the **RED7** system, the GFP reporter and the gRNA plasmids were transfected in ≈200 μm HEK 293 T17 cellular spheroids. After 24 hours, the spheroids were incubated in PCB for 1 hour and then transferred on the stage top incubator of the HT-LISH microscope. The DMD was used to illuminate the samples with red light directly on the microscope stage. After the illumination period, the spheroids were fixed and the nuclei were stained with Propidium Iodide (red channel). The fluorescence images (Maximum Intensity Projection) show that the DMD-based on-stage illumination successfully activated the Red Light CRISPR system transfected in cellular spheroids. Scale bar, 50 μm.

3.5 Discussion and Future Directions

One of the aim of this thesis project was to develop a light inducible CRISPR/dCas9 system for gene regulation experiments to overcome the lack in spatial and temporal resolution of the direct dCas9-Transcription Regulators (dCas9-TRs) fusions proteins that cannot be switched on or off at will. When this PhD project started in 2014, the inducible promoters available to control the CRISPR system expression did not carry this important feature. This chapter presented the development and the characterization of the Red Light CRISPR/dCas9 system, a novel CRISPR-based optogenetics tool for gene regulation experiments that uses red or infrared light as external triggers. The Red Light CRISPR system can be precisely controlled in space and time as it can be selectively targeted to small populations of cells (spatial resolution) or be activated and de-activated at will (temporal resolution). The system consists of two separate plasmids and was designed around a pair of protein from the plant *Arabidopsis Thaliana* that bind to each other when irradiated with red light at 660 nm and separate if illuminated with infrared light at 740 nm: the Phytochrome B (PhyB) and the Phytochrome-Interacting Factor 6 (PIF6). In general, light sensitive protein pairs have been previously used to develop light inducible gene regulation tools based on Zinc Fingers (ZFNs), Transcription Activator-Like Effector Nucleases (TALEN) or Tetracycline Repressor/Operator (TetR/tetO) systems. However, compared to the efficient and simple to use type II CRISPR/Cas9 system, ZNFs or TALEN need complex and time-consuming protein engineering and the TetR system requires a specific number of tet operator (tetO) repeats upstream the gene of interest sequence. For the CRISPR-based inducible system developed in this work, PIF6 was fused to the “dead” Cas9 protein from *Streptococcus Pyogenes* (SPdCas9) and PhyB to the transcription activator VPR. When a specifically designed gRNA is transfected in cells together with the Red Light CRISPR system, the SPdCas9 protein recognises and binds to the DNA target determined by the gRNA sequence. Under infrared light at 740 nm (or in dark condition), the system is not active; only the use of red illumination at 660 nm results in a stable PhyB-PIF6 bond and thus in the transcription up-regulation of the targeted gene of interest.

As described in section 3.3.3, there were several factors that influenced the proper development of the Red light CRISPR system and seven different versions had to be studied before obtaining promising results with the system named **RED7**.

First of all, based on the literature, the phytochrome B was used in two different truncated forms, PhyB (1-908), corresponding to the first 908 amino acids and PhyB (1-650), corresponding to the only first 650 amino acids. Even though both these versions were reported to well interact with the PIF counterpart, the Red Light CRISPR system was capable of inducing a significant fluorescence reporter up-regulation only with PhyB (1-650). This could be clearly observed in section 3.3.3.2.3 from the analysis of the **RED5** version of the system where, in comparison with the previous **RED3** and **RED4** constructs (section 3.3.3.2.2), the only switch of PhyB (1-908) with PhyB (1-650) resulted in an evident and detectable GFP reporter up-regulation. PhyB (1-650) was therefore used also in the next version of the Red Light CRISPR system, **RED6** and **RED7**.

A second factor that was thought to be important for the correct development of the Red Light CRISPR system was the presence of Nuclear Localization sequences (NLSs) in the plasmids as both dCas9-PIF6 and PhyB-VPR require to be present in the cellular nucleus at the same time; the dCas9-PIF6 fusion protein must be localized in the nucleus in order to bind to the DNA target and PhyB-VPR must translocate into the nucleus to bind to PIF6 and thus induce the VPR activity. Even though in the different versions of the system a variable number of NLSs were used (**RED3**, 3 + 1 in VPR; **RED4**, 6 + 1 in VPR; **RED5**, 3 + 1 in VPR; **RED6**, 2 + 1 in VPR - sections 3.3.3.2.2, 3.3.3.2.3 and 3.3.3.2.4), only one NLS per plasmid was observed to be necessary. In fact, the heights GFP reporter up-regulation was achieved with **RED7** where only one NLS was present in the dCas9-PIF6 fusion and one in the PhyB (1-650)-VPR plasmid within the VPR sequence (sections 3.3.3.2.6 and 3.3.3.2.8).

A further parameter that was considered when developing the Red Light CRISPR system was the number of PIF6 fused to dCas9. In principle, linking two PIF6 proteins to dCas9, one upstream and one downstream, could attract two PhyB-VPR fusion proteins and thus induce higher upregulation of the targeted gene of interest. The **RED3**, **RED4** and **RED5** versions were based on this design (sections 3.3.3.2.2 and 3.3.3.2.3) however this

approach did not improve the system efficiency (this was further confirmed by the experiment in section 3.3.3.2.7). In fact, the heights GFP reporter up-regulation was achieved with the **RED6** and **RED7** systems where only one PIF6 protein was fused downstream dCas9 (sections 3.3.3.2.5, 3.3.3.2.6 and 3.3.3.2.8).

Protein misfolding was another parameter that had to be considered; in a fusion construct, it is important that all protein involved can fold properly when linked together. For this reason, the insertion of polyglycine-serine (GS) flexible linkers in-between the fusion proteins were used. When focusing on the PhyB (1-650)-VPR fusion proteins, the insertion of a GS linker between PhyB (1-650) and VPR in **RED7** (section 3.3.3.2.6) did not improve the efficiency of the system compared to **RED6** (section 3.3.3.2.5) and the GFP reporter up-regulation level remained the same indicating that both the proteins were folding correctly. The situation was instead different when considering the CRISPR part of the system. From the experiment in section 3.3.3.2.7, the use of GS linkers in-between the dCas9 fusion with two PIF6 proteins did not change the system efficiency. However, when considering the direct dCas9-PIF6 fusion proteins, the Red Light CRISPR system was able to induce a more than two times higher up-regulation level when a GS linker was inserted between dCas9 and PIF6. This indicates that a better dCas9-PIF6 folding together with a better PhyB-PIF6 binding could be achieved.

A final and very important result that emerged from the characterization of the Red Light CRISPR system was related to transfection efficiency which has proved to be a fundamental and highly discriminating factor for a proper functioning of the system. This is due to the big plasmid size of both dCas9-PIF6 and PhyB-VPR constructs which are therefore difficult to transfect in cells with Lipofectamine 3000. It was demonstrated in sections 3.3.3.2.4 and 3.3.3.2.5 where the **RED6** version of the system was transfected in HEK 293 or in the more efficient HEK 293 T17 cells. From these experiments, it can be clearly observed that a higher transfection efficiency (≈60%) results in a much higher GFP reporter up-regulation level (≈ 4 times compared to a transfection efficiency of ≈20%) thus indicating that transfection efficiency is a limiting factor for the Red Light CRISPR system. The immediate solution to this possible issue can be the use of viral plasmids for a highly efficient delivery of the system into the cells.

In summary, all the characterization experiments performed in section 3.3.3 lead to the establishment of **RED7** as the final and promising version of the Red Light CRISPR system. The CRISPR part of this tool includes one NLS and a GS linker in-between the dCas9 and one PIF6 protein; the activator plasmid contains a GS linker between PhyB (1-650) and the transcription activator VPR and one NLS within the VRP sequence. This final version of the system was capable of significantly induce a GFP reporter up-regulation ≈25 times higher than the fluorescence basal level (section 3.3.3.2.8).

One of the main features of optogenetics-based tools is that light is used as external trigger to activate (or de-activate) these types of systems at will in a very selective manner by simply shining light in precise regions of interest. The Red Light CRISPR system is an optogenetics tool and as such it retains the mentioned above characteristic. In particular it allows for an accurate up-regulation of gRNA-targeted gene(s) of interest in a space-resolved manner. Section 3.3.4 reports the results of dedicated experiments aiming to test and demonstrate the spatial resolution capabilities of the Red Light CRISPR system. In particular, the **RED7** version was transfected in HEK 293 T17 cells and was activated through different red illumination patterns only in precise areas of the culture dish. As shown in Figures 80 and 81, the GFP was precisely overexpressed only within the illuminated areas while the cells that did not received any activating light maintained a fluorescence signal close to the basal level.

The experiments in sections 3.3.3 and 3.3.4 suggest that the Red Light CRISPR system has the potential to be a valuable optogenetics tool in biomedical research where there is the need to precisely control defined events in space and time with the aim to directly interact and modify cellular behaviour and thus study the mechanisms behind biological processes. The Red Light CRISPR system developed in this work which fuses together the non-invasive and highly spatiotemporal resolved technique of optogenetics with the "easy to use" and efficient CRISPR approach, could help understanding the relationship between gene(s) expression and cell/tissue malfunction/disease. In principle, any genetic pathway can be targeted through the simple CRISPR-based method and then

up-regulated in a time and/or space-dependent manner. This optogenetics approach has the potential to open new experimental avenues in perturbative studies on the significance of spatial and temporal heterogeneity of cell populations and the dynamic interaction of a cell or a group of cells with its/their neighbours. In particular, the use of such optogenetics tool could be applied to evaluate how small genetic perturbations in different cell populations influence the local and global properties, dynamics and fate decisions of the whole ensemble or for instance to discriminate what are the spatiotemporal conditions and circumstances that promote a given type of cell behaviour. In addition, with a more precise control of the red activating light at the micrometre level (e.g. with the use of Digital Micromirror Devices - DMDs), Red Light CRISPR system-based experiments could be performed even at a single cell level. Interestingly, even though the current **RED7** version of the system contains the transcription activator VPR and thus enables gene up-regulation experiments, it could be sufficient to replace this transcription activator with for instance the Kruppel associated box (KRAB) to also achieve a precise optical gene down-regulation.

It is important to mention that after this PhD project has started, in the beginning of 2015 Polstein *et al*. [85] and Nihongaki *et al*. [86] published a conceptually similar system in which light-inducible CRISPR/SP-dCas9 was created using a pair of blue light sensitive *Arabidopsis Thaliana* proteins, CRYptochrome2 (CRY2) and CIBN/CIB1. When irradiated with blue light (470 nm), CRY2 undergoes a conformational change and subsequently recruits its interacting partner CIBN/CIB1. By fusing SP-dCas9 with CRY2 and CIB1 with a transcription activator (VP64/p65), they could upregulate genes of interest by illuminating the system with blue light to trigger dimerization of CRY2 and CIMN/CIB1. Although conceptually similar to the CRY2-CIBN/CIB1 systems mentioned above, the Red Light CRISPR system provides additional active on/off switching control by using light sensitive proteins that can be activated by red light and deactivated under infrared illumination. Moreover, red-shifted wavelengths penetrate tissues much deeper than for instance blue or UV light with also much lower phototoxicity, a key feature if long term live imaging experiments need to be performed. In addition, the choice of a red shifted pair of light sensitive proteins is even more significant if the light activation is

combined with fluorescence microscopy in which blue light is commonly used for imaging of GFP-based fluorophores.

Importantly, the Red Light CRISPR system allows to target multiple genes of interest in a gRNA-dependent manner with high spatial and temporal resolution but the expression level of each gene cannot be controlled at different time points unless the gRNAs are transfected in the samples in different periods. However, the CRISPR system has a great advantage over other gene editing technologies: there are several species of Cas9 proteins that respond to specific gRNAs. Orthogonal dCas9 proteins have been fused to transcription regulators to achieve epigenetic DNA modification which means that, in principle, it is now possible to simultaneously target and control different genes of interest with different dCas9-TR-gRNA combinations. Nevertheless, also these orthogonal dCas9-TR fusion proteins do not offer any spatiotemporal control. It follows that CRISPR orthogonality in light-based CRISPR inducible tools such as the Red Light CRISPR system could have an important impact as multiple genes could be independently controlled in terms of both space and time. Section 3.3.5 of this work describes a potential optogenetics multiplex approach based on two light inducible CRISPR systems, the RED Light CRISPR system and an orthogonal STdCas9-based tool developed by a colleague at the University of St Andrews, Rebeca Diaz. This approach was possible because of the variety of light sensitive optogenetics proteins that were available. In fact, a fundamental requirement for the simultaneous use of light inducible systems is that the activating light of one tool must not overlap and thus activate the other(s). Even though a proof-of-concept experiment with multiple optogenetics tools that respond to different wavelengths of light was previously reported by Muller *et al*. [110, 111], currently there are no publications showing a combined use of CRISPR-based optogenetics systems for precise spatiotemporally resolve multiple gene regulation experiments. The ST CRISPR system relies on two different proteins form *Arabidopsis Thaliana* that interact with each other only when illuminated with blue light at 470 nm: CIB1 and the CRYptochome 2 (CRY2). In particular, CRY2 is fused with the transcription activator VPR and the STdCas9 protein is fused with the CRY2 counterpart, CIB1. It

follows that the Red Light CRISPR system and the CRY2-CIB1-based ST CRISPR tool should be orthogonal in terms of both gRNA species (SP vs ST) and activating light (660/740 nm vs 470 nm). The actual gRNA-dependent orthogonality of the Red Light CRISPR system was first verified with the experiments in Figure 82 (section 3.3.5) which confirmed that **RED7** was only responding to the gRNA specific for SPdCas9. The orthogonality in terms of wavelength was instead evaluated with the experiment in Figure 83 (section 3.3.5) where it emerged that blue illumination at 470 nm is inducing a minor PhyB-PIF6 interaction. However, if combined with simultaneous infrared illumination at 740 nm, blue light is not capable of activating the Red Light CRISPR system. Therefore, while in terms of gRNA the two red and blue light-based systems are fully orthogonal, their combined used is possible only if considering the activating wavelengths overlap: when exploiting the blue system, blue and infrared light must be simultaneously on so that only this system is active. Red illumination can instead be used to activate only the Red Light CRISPR system as the CRY2-CIB1-based ST CRISPR tool is not sensitive to this wavelength. These findings suggest that if both the systems are present in a cell, they could be simultaneously controlled with different light wavelengths and thus the expression of different genes of interest defined by specific SP or STgRNAs could be controlled independently in space and time. This can be achieved only if two or more separated regions are illuminated with different light wavelengths: simultaneous blue, infrared and red light on a single area will result in the only activation of the CRY2-CIB1 system as infrared illumination will is de-activate the Red Light CRISPR system. The probably most efficient way to perform this type of optogenetics experiments is to use very accurate illumination patterns. This can be for instance achieved with a Digital Micromirror Device (DMD), an array of small mirrors that can be independently controlled so that different regions can be simultaneously illuminated with different wavelengths of light with micrometre precision. The use of such device in combination with an optical microscope could allow for a precise and simultaneous activation of the Red Light CRISPR system and the CRY2-CIB1-based ST CRISPR tool in different areas of a culture dish by shining red or blue+infrared light (Figure 84A - section 3.3.5) thus enabling selective optogenetics-based multiple gene regulation experiments. If a similar

device allowing simultaneous illumination in different areas with different wavelengths of light is not available, the only possible solution is to follow one of the sequential approaches presented in Figure 84B and C (section 3.3.5) as the use of simultaneous red illumination with blue+infrared light will not allow the activation of the Red Light CRISPR system (because infrared is de- activating the system). A sequential approach was applied to the experiment in Figure 85 (section 3.3.5) where a bi-colour mask acting as a light filter was used to sequentially activate first with blue and then with red light the two inducible CRISPR system which were controlling a mCherry and a GFP reporters respectively. This was only possible because the Red Light CRISPR system is light sensitive only with PhycoCyanoBilin (PCB) and therefore, any illumination before the addition of this chromophore, will not activate the system. It is important to mention that this experiment aimed at evaluating the orthogonality of the two optogenetics tools in terms of wavelengths as it was not possible to simultaneously introduce in cells both the systems with a Lipofectamine 3000-based transfection (due to the large size of the plasmids). As already mentioned, the use of viral plasmids can be the immediate solution to this issue. The two systems were therefore separately transfected in two different populations of cells that were after mixed together. This experiment primarily confirms that the Red Light CRISPR system can be used for space resolved experiments in combination with other optogenetics tools as the GFP reporter was up-regulated only in the masked region illuminated with red light. This experiment also indicates that the CRY2-CIB1-based ST CRISPR tool needs further study as it did not induce any evident mCherry reporter up-regulation.

In regard to applications involving the use of the Red Light CRISPR tool in combination with other light orthogonal systems, a better and more efficient solution could be the switch of the PhyB-PIF6 pair with the very recently published red-infrared light sensitive bacterial proteins, BphP1-PpsR2 [112]. BphP1 and PpsR2 interact under infrared light at 740 nm and detach if irradiated with red light at 650 nm. This can offer two main advantages over the PhyB-PIF6 pair. First, there will not be any wavelength overlapping issues with the more common blue light optogenetic systems (such as the CRY2-CIB1-based ST CRISPR tool) for multiplex optogenetics experiments [112]. Second, because of

the higher penetration capabilities of infrared light, compared to the PhyB-PIF6 pair the novel BphP1-PpsR2 pair was demonstrated to be more efficiently activated also at different depth in scattering tissues [112] thus allowing to perform optogenetics gene regulation experiments also in more complex and biologically-relevant 3D cell culture models. In addition to these features, it is interesting to mention that the BphP1-PpsR2 pair is always light sensitive and it does not need any external chromophore. As explained in section 3.3.1, the PCB dependency of the current version of the Red Light CRISPR system can be considered as a disadvantage or as an advantage depending on the experimental applications. The PCB must be added every time an experiment need to be performed, it is very light-sensitive and, if the system is required to be activated for longer periods, PCB has to be replaced every 24 hours. The use of the chromophore-free BphP1-PpsR2 pair can overcome this issue. However, as explained before, transfection efficiency can be a limiting factor for the Red Light CRISPR system. There are two possible solution to minimize this issue: first, as previously mentioned, the use of viral plasmids to deliver the system will certainly increase the transfection and thus also the system efficiency. Second, a simpler method could be the generation of cell lines stably expressing the Red Light CRISPR system at high level. In this letter case, the PCB dependency offers a valuable advantage as the stable lines could be cultured under normal ambient light conditions since the system could not be activated without the presence of PCB in the culture media. On the contrary, cells stably expressing a chromophore-free system (e.g. BphP1-PpsR2 pair) will be always ready to be activated by ambient light and therefore the cell lines have to be handled with more care. In summary, the assembly of a further Red Light CRISPR system around the novel red/infrared light sensitive pair of protein BphP1-PpsR2 could extend the experimental possibility of the optogenetics tool developed in this work as different applications might require different optogenetics features. For instance, in multiplex experiments with the CRY2-CIB1-based tool, a BphP1-PpsR2-based system will be more indicated due to the absence of activating wavelength overlap.

As mentioned before in this work, one of the main advantages of the Red Light CRISPR system is that it is based on a pair of proteins that are sensitive to red light. This feature

is very important when 3D cell culture models are considered as red light can penetrate deeper in thick samples/tissues when compared to lower wavelength such as UV or blue light. Therefore, the Red Light CRISPR system has the potential to be exploited in optogenetics experiments that require a precise control of genes expression in cell culture models that more closely mimic human tissues. The PhyB-PIF pair of proteins have been successfully expressed in zebrafish to induce a light-based protein translocation [104] but never for optogenetics CRISPR-based experiments aiming to regulate the gene expression levels. Section 3.4.1 intended to evaluate whether the Red Light CRISPR system could be transfected and activated in 3D cell culture models, in this specific case in HEK 293 T17 cellular spheroids, to up-regulate the GFP reporter. As in 2D cells monolayers, the transfection efficiency achieved with Lipofectamine 3000 was not very high and therefore, as mentioned before, viral transduction or the generation of a stable cell line could certainly help to overcome this issue. Nevertheless, Figure 86 shows that there is a noticeable difference between the spheroids illuminated with red or infrared light. The sample under red illumination exhibits a clear GFP overexpression suggesting that the gene up-regulating capabilities of the Red Light CRISPR system can be potentially exploited also in more complex 3D cell culture models. Importantly, it seems that a strong activation of the system is limited to the bottom part of the spheroid which is the side directly in front of the illumination source. This can suggest that a probably higher red light power is necessary to fully penetrate and thus activate the system along the entire volume of the sample. It can be anticipated that in the experiment described in section 3.3.4 the red light power was increased to ≈300 $\mu W/cm^2$ (instead of 0.080/0.100 mW/cm^2) and a more uniform volumetric activation pattern could be achieved.

Section 3.4.1 suggest that the Red Light CRISPR system can be expressed and activated in 3D samples and therefore genetic perturbative experiment aiming at regulating the gene expression in a precise spatiotemporal manner could be performed also in biologically-relevant 3D models. The next step was to develop a system that was both capable of generating precise illumination patterns and simultaneously able to image 3D specimens. In this regard, sections 3.4.2 and 3.4.3 are proposing a HT-LISH

microscope implementation aiming to lay the foundation for future on-stage HT-LISH microscope-based optogenetics experiments on 3D models. In particular, as shown in Figures 87 and 88 in section 3.4.2, a Digital Micromirror Device (DMD) coupled with a RGB (Red, Blue and Green) LED light source was installed so that a variety of precise illumination patterns can be projected at the focal plane of the objective O1. This HT-LISH upgrade capabilities in terms of optogenetics experiments was evaluated in section 3.4.3 where the Red Light CRISPR system expressed in cellular spheroids were activated directly on the microscope stage. The samples were grown on the HT-LISH system in the stage top incubator and illuminated with the red light projected by the DMD. As shown in Figure 89, the GFP reporter expressed in the spheroids could be successfully up-regulated. These results primarily confirmed that the Red Light CRISPR system can be also exploited in more complex 3D samples and, as mentioned before, also suggested that with a higher red illumination power (≈300 $\mu W/cm^2$) the Red Light CRISPR system can be activated in the whole spheroid volume. This indicates that samples with different optical densities and dimensions might require specific settings of red light power that need to be evaluated prior the experiments.

In addition, the outcomes of section 3.4.3 highlighted that the HT-LISH implementation described in section 3.4.2 is actually adding promising optogenetics capabilities to the system. The variety of micrometre-precise illumination patterns (such as the examples in Figure 88) that can be projected through the DMD at the microscope focal plane level have the potential to offer full control over any optogenetic tool expressed in the specimens. Specific regions of the samples can be selectively illuminated with activating (or de-activating) light and thus any light sensitive protein can be controlled in space and time even with single cell precision. Moreover, due to the fast acquisition speed, the HT-LISH coupled with the DMD/LED upgrade could also become a versatile system for optogenetics-based functional studies that require to follow rapid cellular processes overtime. For instance, the currently available optogenetic tools for the non-invasive stimulation of neuronal cultures (e.g. Channelrhodopsin variants) could be expressed and activated in 3D samples; if coupled with functional fluorescent reporters, such as the genetically encoded calcium indicators, volumetric neuronal functional studies could

be performed in more biologically-relevant 3D models with precise spatiotemporal control and potentially also with a HTI approach.

In summary, this chapter described the development and the characterization of the Red Light CRISPR system, a novel molecular biology tool that links together the non-invasive and highly spatiotemporal resolved technique of optogenetics with the “easy to use” and efficient CRISPR approach. The Red Light CRISPR system has the potential to open new experimental avenues in perturbative studies on the significance of spatial and temporal heterogeneity of cell populations and the dynamic interaction of a cell or a group of cells with its/their neighbours. The expression of this system is not limited to 2D cell monolayers but it can be also expressed and activated in more biologically-relevant 3D cell culture models. Moreover, with a micrometre-precise control of the red activating light with for instance a Digital Micromirror Device (DMD), Red Light CRISPR system-based experiments could be performed even at a single cell level. In addition, this chapter also proposes a simple but efficient upgrade of the HT-LISH microscope developed in this work which lays the foundation for on-stage non-invasive optogenetics experiments in 3D *in vitro* cell culture models with high spatiotemporal control and potential high throughput functional studies.

Chapter 4

Discussion and Conclusion

This PhD thesis project had multiple aims which were focused on microscopy, in relation to High Throughput Imaging (HTI), and molecular biology, in regard to optogenetics-based genome engineering.

Chapter 2 proposed a first prototype of the HT-LISH microscope, a versatile single objective light sheet microscope for the imaging of 3D samples that possesses different imaging capabilities and is thus indicated for various applications. As other light sheet microscopes, the HT-LISH is capable to perform a fast image acquisition of biologically-relevant 3D cell culture model in 3 dimensions (3D - xyz), 3 dimensions with multiple channels (3D - xyzc) and in 4/5 dimensions (3D over time/multi-channel - 4/5D - xyz(c)t). However, the HT-LISH microscope was specifically thought and developed as a solution to bring together light sheet microscopy and 3D cell culture models with the currently available High Throughput/Content Screening (HTS/HCS) platforms. The current HT-LISH prototype design allows for (semi-)automated volumetric (3D, 4D or 5D) image acquisition of 3D specimens cultured in commercially available multi (or single) well plate formats as in most of the HTS/HCS systems. With further software, hardware and optical implementations, this prototype system has the potential to become a valuable light sheet microscopy-based tool in the HTI pipeline where the study of more biologically-relevant 3D cell culture models is required. One of the main advantages of the HT-LISH system is that it is fully compatible with any currently available inverted microscope: as schematized in Figure 52 (Section 2.5), the HT-LISH can be seen as an external box of limited size that can be easily attached through their side port(s). This is fundamental as inverted microscopes are widely spread in various microscopy based HTI stations used by industries or phenotypic screening centres as well as in most of the academic laboratories. It follows that inverted microscope-based HTI platform could be potentially implemented with the HT-LISH functionality without substantially changing their structure. This compatibility feature is even more relevant when considering smaller academic realities that might not afford the expensive 3D HTI machines

currently available on the market, but still require a certain level of throughput for an automated imaging of multiple 3D samples. These laboratories could implement their inverted microscope with the HT-LISH box and thus have access to a versatile platform that offers the possibility to image single or multiple 3D samples in 3, 4 or 5 dimensions (x, y, z, multi-channel, over time) with high acquisition speed while maintains the classic epi-fluorescence or Brightfield microscopy features if needed. A further advantage of the HT-LISH microscope is that the system is very user friendly. Even though it is a first prototype, the use of all the microscope features, from the basic 3D imaging to the more complex acquisition of multiple 3D samples, it is very simple and not more challenging than operating a confocal microscope. In addition, the hardware/optical implementations described in Section 3.4 (Chapter 3), add to the HT-LISH microscope the possibility to perform non-invasive optogenetics experiments on 2D or 3D samples even with singe cell precision. In conclusion, although further work is required to improve the prototype, its overall design and operation could make the HT-LISH a versatile and user-friendly microscopy multi-station with a fast light sheet-based 3D (xyz), 4D (xyzt), 5D (xyzct) and optogenetics imaging capabilities that could also bring the HTI approach of 3D specimens in any laboratory, academic and non, that are provided with an inverted microscope/inverted microscopy-based platform. Once fully implemented the HT- LISH could become a very powerful, versatile and affordable inverted microscopy “add-on” that might have a future impact in 3D imaging and 3D HTI-based research (e.g. drug or genetic screening) in both academia and industry.

Chapter 3 described the development of the Red Light CRISPR system, a novel optogenetics tool for gene regulation experiments that add precise spatiotemporal control to the CRISPR system. It relies on the interaction of the Phytochrome B (PhyB) and Phytochrome-Interacting Factor 6 (PIF6), two light sensitive protein from the plant *Arabidopsis Thaliana* that dimerize under red light at 660 nm and separate when illuminated with infrared light at 740 nm. The experimental characterization suggested that the Red Light CRISPR system has the potential to be a valuable optogenetics tool in biomedical research where there is the need to precisely control defined events in space

and time with the aim to directly interact and modify cellular behaviour and thus study the mechanisms behind biological processes. The Red Light CRISPR system developed in this work which fuses together the non-invasive and highly spatiotemporal resolved technique of optogenetics with the “easy to use” and efficient CRISPR approach, could help understanding the relationship between gene(s) expression and cell/tissue malfunction/disease. In principle, any genetic pathway can be targeted through the simple CRISPR-based method and then up-regulated in a time and/or space-dependent manner. This optogenetics approach has the potential to open new experimental avenues in perturbative studies on the significance of spatial and temporal heterogeneity of cell populations and the dynamic interaction of a cell or a group of cells with its/their neighbours. In addition, the Red Light CRISPR system can be exploited in both 2D or 3D cell culture models and, with a more precise control of the red activating light at the micrometre level (e.g. with the use of Digital Micromirror Devices - DMDs), Red Light CRISPR system-based experiments could be performed even at a single cell level. Moreover, this tool can be used in combination with other orthogonal CRISPR-based optogenetics systems for multiplex gene regulation experiments (mostly if the PhyB-PIF6 pair of proteins will be switched with the newly published infrared/red light sensitive protein pair BphP1-PpsR2). To conclude, the Red Light CRISPR system is joining the already available range of optogenetics tools that enable a precise and non-invasive external control of the CRISPR system and in particular it introduces for the first time a red/infrared light CRISPR inducible system.

Chapter 5

Materials and Methods

5.1 Cell Culture

5.1.1 HEK 293/HEK 293 T17

5.1.2 HeLa-FUCCI

5.2 Transfection of the Red Light CRISPR System in 2D HEK 293/HEK 293 T17 culture

5.3 HEK 293 T17 cellular spheroids and Red Light CRISPR System transfection

5.4 Fluorescent Beads Three-Dimensional distribution

5.5 HeLa-FUCCI Three-Dimensional distribution

5.6 HeLa-FUCCI Cellular Spheroids

5.7 PCB handling

5.8 Cloning

5.9 DNA Plasmid Sequencing

5.10 Epi-fluorescence Microscopy Analysis

5.11 Flow Cytometry Analysis

5.1 Cell Culture

5.1.1 HEK 293/HEK 293 T17

HEK 293/ HEK 293 T17 cells (ATCC CRL-1573/ATCC CRL-11288) are grown in 25 cm^2 cell culture flasks (Nunclon Delta Surface) with Dulbecco's Modified Eagle Medium: Nutrient Mixture F-12 without Phenol Red (DMEM/F-12 - Gibco) containing 10% Fetal Bovine Serum (FBS - Gibco) and penicillin-streptomycin (Gibco). When 80/90% confluent, the medium is removed and 1X Phosphate Buffered Saline (PBS - Gibco) is added to remove any medium traces; the PBS is then aspirated and 0.5 mL of TrypLE are added to the flask that is incubated at 37°C and 5% CO_2. Once cells are detached, different volumes of complete DMEM/F-12 are added to the flask depending on the needs.
When the cells have to be split, 1.5 mL of media is added and the cells are transferred into a new flask with fresh media: different subcultures ratios are used depending on requirements. Finally, the cells are moved back into the incubator at 37°C and 5% CO_2.

5.1.2 HeLa-FUCCI

HeLa cells stably expressing the FUCCI constructs cells are grown in 25 cm^2 cell culture flasks (Nunclon Delta Surface) with Dulbecco's Modified Eagle Medium: Nutrient Mixture F-12 without Phenol Red (DMEM/F-12 - Gibco) and containing 10% Fetal Bovine Serum (FBS - Gibco) and penicillin-streptomycin (Gibco). When 80/90% confluent, the medium is removed and 1X Phosphate Buffered Saline (PBS - Gibco) is added to remove any medium traces; the PBS is then aspirated and 0.5 mL of TrypLE are added to the flask that is incubated at 37°C and 5% CO_2. Once cells are detached, different volumes of complete DMEM/F-12 without Phenol Red are added to the flask depending on the needs.
When the cells have to be split, 1.5 mL of media is added and the cells are transferred into a new flask with fresh media: different subcultures ratios are used depending on requirements. Finally, the cells are moved back into the incubator at 37°C and 5% CO_2.

5.2 Transfection of the Red Light CRISPR System in 2D HEK 293/HEK 293 T17 culture

All transfections are carried out with a reverse approach using Lipofectamine 3000 (Life Technologies). During the splitting procedure, after cells are detached, fresh complete DMEM/F-12 (without Phenol Red - Gibco) is added to a final concentration of 8/9 mL depending on the cell confluence ratio. From the cell mix obtained, 100 μL per well (2.9-3.2 $x10^4$ cells/well) are plated in black walls 96 well plates (Perkin Elmer 6005182). For space resolved experiments, after cells are detached, fresh complete DMEM/F-12 is added to a final concentration of 5/6 mL depending on the cell confluence ratio. From the cell mix obtained, 2 mL are plated in a 6 well plate (8.2-9.5 $x10^5$ cells/well) (Corning Costar 3516). Transfections are performed following the Lipofectamine 3000 company protocol; the DNA ratio used for the Red Light CRISPR system are the following: CRISPR plasmid (dCas9-PIF6): 3, Activator plasmid (PhyB-TR): 2, Reporter plasmid: 1 and gRNA plasmid: 4.

5.3 HEK 293 T17 cellular spheroids and Red Light CRISPR System transfection

In order to generate HEK 297 T17 (ATCC CRL-11288) cellular spheroids, a variable number of cells (150, 250 or 500) depending on the wanted spheroids size are plated in ultra-low attachment 96-well round bottom cell culture plate (Corning Costar 7007). At the same time, the Red Light CRISPR system with reporter and gRNA plasmids is transfected with Lipofectamine 3000 (Life Technologies) following the protocol described in the above paragraph. After a 24 hours period, cells are incubated for 1 hour in fresh warm DMEM/F-12 medium (without Phenol Red - Gibco) containing PCB (see below PCB handling). The well plate is then positioned on top of the LED box inside the culture incubator and the spheroids are exposed to continuous red or infrared illumination for 24 hours. Alternatively, for the on-stage activation experiments, after the PCB incubation, the spheroids are embedded in a solution of low melting point agarose, transferred to glass bottom dishes, positioned in the HT-LISH microscope stage top incubator and illuminated with the DMD system. For the automated imaging of

multiple spheroids, the samples are transferred to a glass bottom 96 well plate (Corning 4580).

5.4 Fluorescent Beads Three-Dimensional distribution

In order to create a 3D distribution, 200 μm fluorescent beads are first diluted in water and then mixed with a 1X low melting point agarose solution. The mix is transferred to a glass bottom well plate (FluoroDish - WPI World Precision Instruments) and the sample is ready for imaging. The low melting point agarose solution is produced in water and it maintains the liquid form if stored in the cell culture incubator at 37 degrees.

5.5 HeLa-FUCCI Three-Dimensional distribution

In order to create a 3D distribution, a HeLa-FUCCI cells in suspension are mixed with a 1X low melting point agarose (Sigma A9414) solution. The mix is transferred to a glass bottom well plate and the sample is ready for imaging. The low melting point agarose solution is produced in DMEM/F12 without Phenol Red medium (Gibco) and it maintains the liquid form if stored in the cell culture incubator at 37 degrees.

5.6 HeLa-FUCCI Cellular Spheroids

In order to generate HeLa-FUCCI cellular spheroids, a variable number of cells (150, 250 or 500) depending on the wanted spheroids size are plated in ultra-low attachment 96-well round bottom cell culture plate (Corning Costar 7007). After a 24/48 hours period, the spheroids are ready for the imaging process. For time lapse experiments, spheroids are embedded in a solution of low melting point agarose (Sigma A9414).

5.7 PCB handling

Phycocyanobilin (PCB) 25 mg powder was obtained from LivChem.

It was diluted in 1.42 mL of DMSO (Molecular Probes) (at a concentration of 30 mM), aliquoted into 0.6mL tubes and stored at -20°C. Prior to use, 24 h post transfection, PCB is thawed at room temperature and diluted in fresh warm DMEM/F-12 cell culture medium to obtain the optimal final concentration of 15 μM. The medium of the transfected cells is removed and replaced with this PCB-medium. The cell plate is then incubated in complete dark (aluminium foil is used to cover the plate) for 1 h at 37°C 5% CO_2.

Importantly, the handling of PCB has to be carried out in absence of room light or under green light, otherwise it can be oxidized and cannot bind to PhyB. For this reason, all the steps involving PCB, from the thawing to the incubation steps, were performed under green LED light.

5.8 Cloning

All the plasmid constructs are built following the same strategy. The plasmids assembled in this work are listed in the Supplementary Material section (Chapter 6) of this thesis. The free sequence editor software "A Plasmid Editor" (ApE) is used to plan the work. Nanodrop (Thermo Scientific) is used to determine each DNA concentration.

First of all, for each plasmid that has to be assembled/modified, suitable restriction enzymes are chosen. Digestions are then performed using New England Biolabs (NEB) restriction endonucleases and the products are run by electrophoresis on a 1x agarose-TAE-SYBRSafe (ThermoFisher Scientific) gel. If the plasmid backbone (part of the plasmid containing the bacterial antibiotic resistance) has to be used, after digestion it is dephosphorylated using the NEB Calf Intestinal Phosphatase (CIP).

The band of interest is then extracted from the gel under UV light and the DNA is purified using the Quiagen Gel Extraction Kit.

In order to make most of the constructs, the Polymerase Chain Reaction (PCR) is used to amplify the DNA fragments of interest; all the reactions are performed using the G-Storm Thermal Cycler system. NEB Phusion High-Fidelity or NEB Q5 High-Fidelity DNA polymerases are used following the manufacturer protocols. All the primers for the PCRs are ordered from the Eurofins Genomic company. The amplified fragments obtained are

run by electrophoresis on a 1x agarose-TAE-SYBRSafe (ThermoFisher Scientific) gel, the bands are then extracted from the gel under UV light and the DNA is purified using the Qiagen Gel Extraction Kit. Before ligation, the DNA fragment is digested with NEB restriction endonucleases.

For some plasmids, instead of using a PCR, a pair of annealed complementary oligos or a gene fragment is used to complete the construct (all purchased from Eurofins Genomics).

All the ligation steps are performed with NEB T4 Ligase (NEB) and the products are then transformed using Life Technologies Library Efficiency DH5α Competent Cells following the manufacturer protocol. For each ligation, a control is performed by adding only the vector to the ligation mix.

The Bacteria are then spread and streaked onto an agarose-antibiotic Petri dish and incubated at 37°C for 12-18 hours. Some grown colonies are then picked and checked by PCR using the Bioline MyTaq DNA Polymerase. One or more positive colonies are transferred in a liquid LB broth-antibiotic solution (5 mL for MiniPrep or 100 mL for MidiPrep) and incubated at 37°C for 12-18 hours. The DNA is then extracted using the Qiagen Mini or Midi kit.

5.9 DNA Plasmid Sequencing

All created plasmids were sequenced using the Dundee DNA Sequencing Service: http://dnaseq.bioch.dundee.ac.uk/home.html

5.10 Epi-fluorescence Microscopy Analysis

A Nikon Eclipse Ti epi-fluorescence microscope is used for a first screening to evaluate the Red Light CRISPR system activity after the transient transfection in HEK 293/ HEK 293 T17 cells. The fluorescence signal coming from a gRNA-targeted fluorescent reporter plasmid is observed in different fields of view. A control well of cells transfected with the reporter plasmid alone is used to set an appropriate exposure time of the microscope camera; the fluorescence coming from the wells transfected

with the system are then compared with the control while maintaining the same microscope settings. If there is a clear detectable difference in terms of fluorescent signal between the reporter plasmid alone and the activated/non-activated (Red light/Infrared light) system, a flow cytometry analysis is performed and thus the efficiency is precisely quantified.

5.11 Flow Cytometry Analysis

In order to quantify the variation in the GFP reporter fluorescence intensities due to the Red Light CRISPR systems activation, flow cytometry analysis is performed using a Millipore Guava easyCyte system. Briefly, 24 hours after illumination with red/infrared light, cells in the 96 well plate are washed with 1X PBS (Gibco), detached with TrypLE and re-suspended in fresh DMEM/F-12. Cells are then transferred into a 96 well plate with round bottom wells and centrifuged for 5 minutes at ~1700 rpm. They are then re-suspended in 1x PBS and loaded into the Guava system. The data obtained are analysed using Flowing Software 2 (http://www.flowingsoftware.com). Figure 90 shows the flow cytometry analysis strategy used in the project. The first step is to select only the live cells from the total events analysed. To do that, forward scatter versus side scatter values of wild type (WT) un-transfected (UT) HEK 293/ HEK 293 T17 cells are plotted in a dot plot and live cells can be distinguished as they are displayed in a clear big population (Figure 21A). After that, a gating strategy on live cells for the GFP intensities has to be chosen: it means that only the live cells over the threshold selected are considered positive for GFP expression. In the example in Figure 21B, live WT UT cells are used to set the threshold: GFP intensities versus cell count are plotted in a histogram. The same gate has to be applied to all samples scanned and information about the GFP positive cells is given in terms of percentage of cells over the threshold and their GFP GeoMean value (Figure 21C). For all the experiments, the gate is set to ≈0.5% of the live WT UT cells.

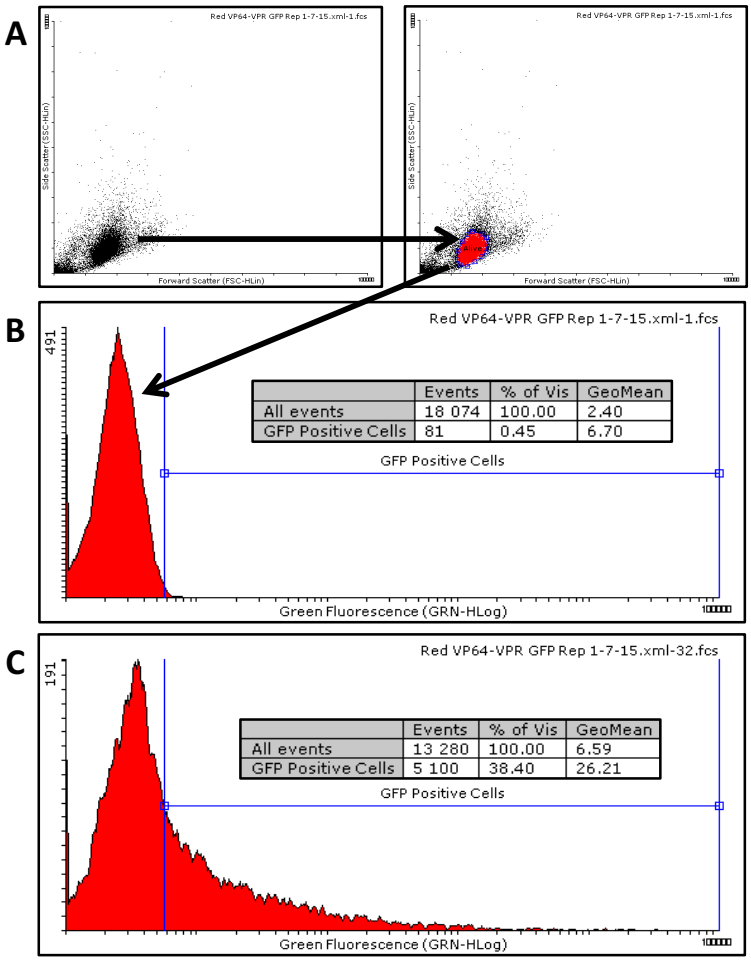

Figure 90 - Schematic workflow for the flow cytometry analysis.
(A) Live cells are selected using a dot plot displaying Side Scatter vs Forward Scatter of un-transfected cells. (B) Gating strategy is defined based on a histogram displaying GFP Intensity vs Cell Count of the live cell population. (C)The selected threshold is used to gate the samples scanned to obtain data about percentage of cells over the threshold and GFP GeoMean values.

Chapter 6

Supplementary Material

6.1 HT-LISH Microscope

6.1.1 HT-LISH Microscope Table of Parts

6.1.2 Matlab Script for Frame Alignment

6.1.3 LabVIEW Diagram

6.2 Red Light CRISPR System

6.2.1 Arduino UNO Script

6.2.2 List of Plasmids, Plasmids Assembly Strategy and Plasmids Sequence

6.2.3 GFP Reporter and PCB Controls

6.1 HT-LISH Microscope

6.1.1 HT-LISH Microscope Table of Parts

Item Symbol	Description	Brand	Code/Model
O1	Objective 1 - 40X 1.2 NA Water	Zeiss	
TL1	Zeiss Tube Lens	Zeiss	
L1	Achromatic Doublets f=75mm Ø1"	Thorlabs	AC254-075-A-ML
ScM	Scanning Mirror + Galvo + Servo	Cambridge Technologies	6M2412B40S100S1, 6240HA, 67124H-1, 611240, 6010-25-040
L2	Achromatic Doublets f=100mm Ø1"	Thorlabs	AC254-100-A-ML
TL2	Achromatic Doublets f=200mm Ø1"	Thorlabs	AC254-200-A-ML
O2	Objective 2 - 40X 0.95 NA Air	Nikon	
O3	Objective 3 - 40x 0.6 NA Air LWD	Nikon	
Filter Wheel	6-Position Motorized Filter Wheels for Ø1" Optics	Thorlabs	FW102C
Emission Filter FITC	535/45	Nikon	
Emission Filter Texas Red	630/60	Nikon	
TL3	Achromatic Doublets f=200mm	Thorlabs	AC254-200-A-ML
sCMOS Camera	Andor Zyla 5.5 sCMOS Camera	Andor	Zyla 5.5 sCMOS
DM	25 mm x 36 mm Longpass Dichroic Mirror, 505 nm Cutoff	Thorlabs	DMLP505R
	Dichroic Mirror Cage Mounts		C4W + FFM1 + B4C
L3	Achromatic Doublets f=100mm Ø1"	Thorlabs	AC254-100-A-ML
StM1	Steering Mirror Mount	Thorlabs	KCB1C/M
	Mirror	Thorlabs	PF10-03-P01
L4	Achromatic Doublets f=200mm Ø1"	Thorlabs	AC254-200-A-ML
Cyl	Cylindrical Lens f = 50 mm, Ø1"	Thorlabs	ACY254-050-A
	Cylindrical Lens Ø1" Rotation Mount	Thorlabs	RSP1X15/M
Slit	Adjustable Mechanical Slit	Thorlabs	VA100C/M
StM3	Steering Mount	Thorlabs	KCB1C/M
	Mirror	Thorlabs	PF10-03-P01
StM2	Steering Mount	Thorlabs	KCB1C/M
	Mirror	Thorlabs	PF10-03-P01
L6	Achromatic Doublets f=250mm Ø1"	Thorlabs	AC254-250-A-ML
L5	Achromatic Doublets f=75mm Ø1"	Thorlabs	AC254-075-A-ML
Laser 488 nm	iBeam Smart Laser 488 nm	Toptica Photonics	iBeam Smart 488-S
Motorized Stage	Motorized Stage	Marzhauser	SCAN IM 130 x 85 00-24-625-0000
Stage Top Incubator	Stage Top Incubator	okolab	H301-K-FRAME
DAQ Card 1	USB Data Acquisition Card	National Instrument ™	3008
DAQ Card 2	USB Data Acquisition Card	National Instrument ™	6211
Projector	DLP® LightCrafter™ 4500	Texas Instruments	DLP® LightCrafter™ 4500
L7	Achromatic Doublets f=125mm Ø1"	Thorlabs	AC254-125-A-ML
DM1	625 nm edge BrightLine single-edge short-pass dichroic beamsplitter	Laser 2000	FF625-SDi01-25x36
	Dichroic Mirror Cage Mounts	Thorlabs	C4W + FFM1 + B4C
Compact Camera	USB3 Vision CMOS, 5.1 MP, Mono, Cased	Sentech	STC-MBS500U3V
Other Items	**Description**	**Brand**	**Code/Model**
Objectives Mount Adapters	Adapter with External SM1 Threads and Internal M25 x 0.75 Threads	Thorlabs	SM1A12
Objectives Mount Adapters	Adapter with External SM1 Threads and Internal M27 x 0.75 Threads	Thorlabs	SM1A17
XY Mounts	XY Translator with Micrometer Drives, Metric	Thorlabs	ST1XY-S/M
Camera Mount Adapters	Adapter with External C-Mount Threads and External SM1 Threads	Thorlabs	SM1A39
Screws	M6 Cap Screw and Hardware Kit	Thorlabs	HW-KIT2/M
Posts	Ø12.7 mm Stainless Steel Optical Posts - Metric	Thorlabs	TRXX/M
Posts Holders	Standard Ø1/2" Post Holders	Thorlabs	PHXX/M
Posts Holders Bases	Standard Bases	Thorlabs	BA1/M - BA2/M - BA1S/M
Rods	ER Assembly Rods for 30 mm and 60 mm Cage Systems	Thorlabs	ERX
Cage Plates	SM1-Threaded Standard Cage Plates	Thorlabs	CP02/M - CP02T/M
Table Clamps	General-Purpose Table Clamps	Thorlabs	CL5 - CL5A
Post	Ø1.5" Dynamically Damped Post, 8" Long, Metric	Thorlabs	DP8A/M
BIG Clamp	Large Ø1.5" Post Mounting Clamp	Thorlabs	C1545/M
Cage Mount		Thorlabs	C4W
Heat Sink	Custom-made Heat Sink for Laser Box		

6.1.2 Matlab Script for Frame Alignment

```
%-------open the stack/image-------------

fname_root='Folder\';
f_name_core = [fname_root 'File Name'] ;
fname=[f_name_core 'File Type such as .tif'];
info = imfinfo(fname);
imageStack = [];
numberOfImages = length(info);

%prepare correction/shift

n_frames=numberOfImages;
dz_um=0.1; %[dz in microns]
scalingfactor = 1
pixel_size_height=0.122/scalingfactor; %pixel size height [in microns]
dz=dz_um/pixel_size_height;  %[in pixels]
angle=55/180*pi();% angle beta

fname_save_stack=[f_name_core 'Name to save new file ']

%apply correction

for current_frame = 1:numberOfImages


    currentImage = imread(fname, current_frame, 'Info', info);

size_x=size(currentImage,1);
size_y=size(currentImage,2);
New Image Size=zeros(size_x,size_y+round((n_frames-1)*sin(angle)*dz));


    corrected_frame=New Image Size;
 corrected_frame(:,round((current_frame-
1)*sin(angle)*dz)+1:round((current_frame-1)*sin(angle)*dz)+size_y)=
currentImage(:,:);


 imwrite(uint16(corrected_frame), fname_save_stack, 'writemode',
'append');



end;
```

6.1.3 LabVIEW Diagram

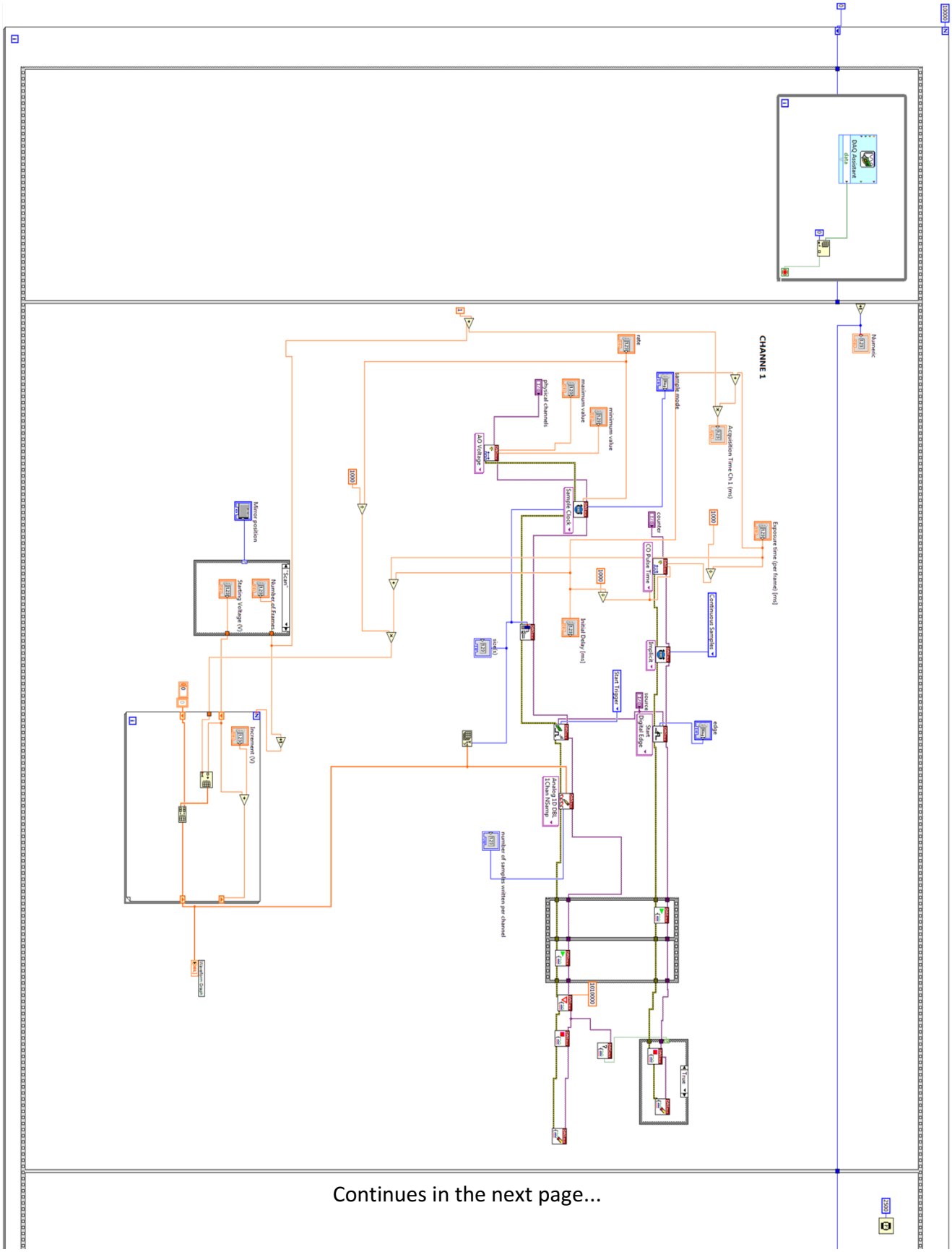

Continues in the next page...

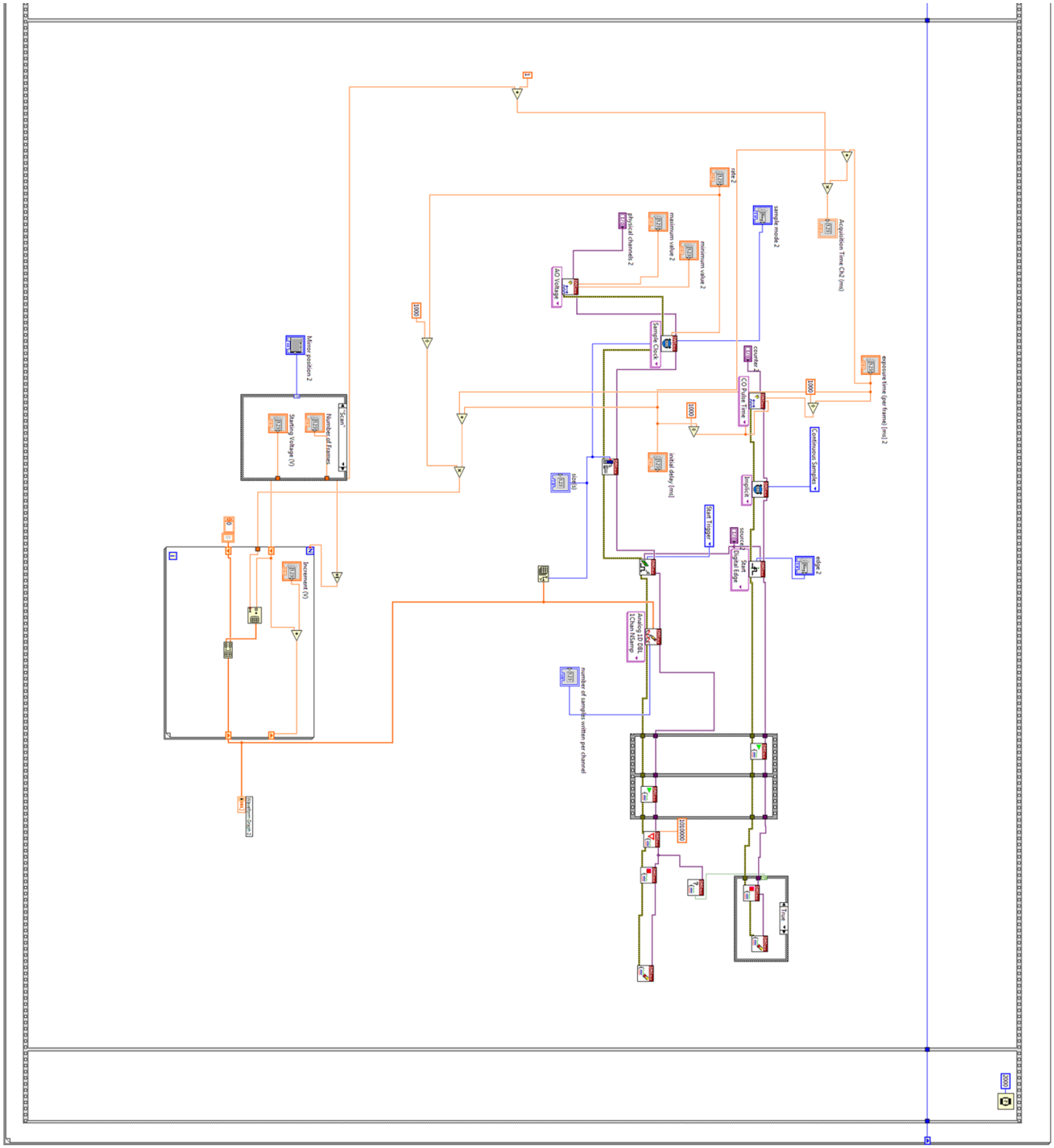
rate 2
physical channels 2
maximum value 2
minimum value 2
sample mode 2
Acquisition Time Ch2 (ms)
AO Voltage
Sample Clock
counter 1
exposure time (per frame) (ms) 2
CO Pulse Time
1000
initial delay (ms)
Continuous Samples
sample
Start Trigger
source
Start Signal Edge
edge 2
Analog 1D DBL 1Chan NSamp
number of samples written per channel
1000000
True
Mirror position 2
Starting Voltage (V)
Number of Frames
"Scan"
Increment (0)
Position Out 2

6.2 Red Light CRISPR System

6.2.1 Arduino UNO Script

```
int LED_Pins[] = {3,5,6,9,10,11}; // PINS 3,5,6,9,10,11 support PWM so can set Power level

float LED_Periods[] = {1,1,1,1,1,1}; //in SECONDS
float LED_PulseDurations[] = {1,1,1,1,1,1}; //in SECONDS
int LED_Powers[] = {35,23,23,35,35,35};// PERCENTAGE (0-100)
unsigned long LED_Illumination_duration[]={720,720,720,720,720,720}; // duration of
illumination in MINUTES
unsigned long LED_Illumination_start[]={50,50,50,50,50,50}; // start of illumination in
MINUTES

unsigned long t_zero=millis();
// the setup routine runs once when you press reset:
void setup() {
  Serial.begin(9600);

  for (int LED_no = 0; LED_no < 6; LED_no++)  {
    pinMode(LED_Pins[LED_no], OUTPUT);
  }
}
// the loop routine runs over and over again forever:
void loop() {
  unsigned long t_now=millis();
  unsigned long t_phase;

  for (int LED_no = 0; LED_no < 6; LED_no++)  {

    t_phase=t_now % int(LED_Periods[LED_no]*1000);
    unsigned long
t_end=(LED_Illumination_duration[LED_no]+LED_Illumination_start[LED_no])*60000;
  if ((t_phase<LED_PulseDurations[LED_no]*1000)&&((t_now-t_zero)<(t_end))&&((t_now-
t_zero)>LED_Illumination_start[LED_no]*60000))
 { analogWrite(LED_Pins[LED_no],int(LED_Powers[LED_no]*255/100) );
 Serial.println(LED_no);Serial.println("ON");Serial.println((t_now-
t_zero));Serial.println((t_end));
  }else
  {digitalWrite(LED_Pins[LED_no], LOW);
  Serial.println(LED_no);Serial.println("OFF");Serial.println((t_now-
t_zero));Serial.println((t_end));

}
  }
}
```

6.2.2 List of Plasmids, Plasmids Assembly Strategy and Plasmids Sequence

1 - Addgene #47107	pcDNA-dCas9-VP64	[68]
2 - Addgene #22474	pCMV-PIF6APB-mYFP	[105]
3 - Addgene #47457	LITE2.0 EF1a-NLS (alpha-imp)-CRY2PHR-NLS-VP64-2A-GFP	[78]
4 - Addgene #22275	pCMV-PhyB(1-908)-10aaLinker-mCherry	[105]
5 - Addgene #63798	SP-dCas9-VPR	[70]
6 - SPgRNA-9xSeq2	SPgRNA for 9xSeq2.	Rebeca Diaz
7 - 9xSeq2-mCherry Reporter	mCherry Reporter Plasmid with a SPgRNA target sequence repeated 8 times.	Rebeca Diaz
8 - 9xSeq2-GFP Reporter	GFP Reporter Plasmid with a SPgRNA target sequence repeated 8 times.	Rebeca Diaz
9 - SPgRNA-9xSeq2	SPgRNA for 9xSeq2.	Rebeca Diaz
10 - pcDNA-Flag-NLS-dCas9-NLS-PIF6 RED1/RED2	Digest plasmid 1 with AscI and XbaI (pcDNA-dCas9). Amplify PIF6 with PCR from plasmid 2 with the following primers: F 5' GAGAGAGGCGCGCCTTCTTACCAACCGATTATTGT 3' and R 5' GAGAGATCTAGACTAGTCAACATGTTTATTGCTTTC 3'. Digest with AscI and XbaI. Ligate.	This Project
11 - EF1a-PhyB(1-908)-NLS-VP64-2A-GFP	Digest plasmid 3 with NheI and KpnI-HF (EF1a-NLS-VP64-2A-GFP). Amplify PhyB(1-908) with PCR from plasmid 4 with the following primers: F 5' GAGAGACTTGGTACCATGGTTTCCGGAG 3' and R 5' GAGAGAGCTAGCGAATTCGCTCGGGATTTGCAAG 3'. Digest with NheI and KpnI-HF. Ligate.	This Project
12 - pcDNA-PhyB(1-908)-NLS-VP64-2A-GFP RED1	Digest plasmid 2 with KpnI-HF and NotI-HF (pcDNA Backbone). Amplify PhyB(1-908)-NLS-VP64-2A-GFP with PCR from plasmid 11 with the following primers: F 5' GAGAGAGGTACC ATGGTTTCCGGAGTC 3' and R 5' GAGAGAGCGGCCGCTTACTTGTACAGCTCGTCCATGCC 3'. Digest with KpnI-HF and NotI-HF. Ligate.	This Project
13 - pcDNA-NLSx3-GS-PhyB(1-908)-NLS-VP64-2A-GFP RED2	Digest plasmid 12 with KpnI-HF (pcDNA-PhyB(1-908)-NLS-VP64-2A-GFP). Digest the Gene Fragment NLSx3-GS (5'GAGAGAGGTACCATGGCCAGCCCTAAGAAAAAGCGAAAGGTTGAGGCCTCCGCTTCTCCAAAGAAAAAA	This Project

	CGCAAGGTCGAAGCCAGCGCCTCTCCGAAAAAGAA AAGCAAAGTGGAAGCCAGCGGTACTGGTGGGTCCG GGTCATCCGGAGGGTCTGGAGGAAGCGGAGGCTCC GGAGGTACCGAGAGA3') with KpnI-HF. Ligate.	
14 - pcDNA-Flag-PIF6-Flag-NLS-dCas9-NLS-PIF6 RED3/RED4/RED5	Digest plasmid 10 with ClaI and SacII (pcDNA-NLS-dCas9-NLS-PIF6). Digest the Gene Fragment PIF6 (5'GAGAGAATCGATATGATGTTCTTACCAACCGATT ATTGTTGCAGGTTAAGCGATCAAGAGTATATGGAGC TTGTGTTTGAGAATGGCCAGATTCTTGCAAAGGGCC AAAGATCCAACGTTTCTCTGCATAATCAACGTACCAA ATCGATCATGGATTTGTATGAGGCAGAGTATAACGA GGATTTCATGAAGAGTATCATCCATGGTGGTGGTGG TGCCATCACAAATCTCGGGGACACGCAGGTTGTTCC ACAAAGTCATGTTGCTGCTGCCCATGAAACAAACAT GTTGGAAAGCAATAAACATGTTGACCATcaCGATTAC AAGGATGACGATGACAAGATGGCCCCCAAGAAGAA GAGGAAGGTGGGCCGCGGGAGAGA 3') with ClaI and SacII. Ligate.	This Project
15 - pcDNA-PhyB(1-908)-NLS-Gateway Linker-VPR RED3	Digest plasmid 12 with NheI and NotI-HF (pcDNA-PhyB(1-908)). Amplify NLS-VPR with PCR from plasmid 5 with the following primers: F 5' GAGAGAGCTAGCAGCAGGGCTGACCCCAAGAAGAA G 3' and R 5'GAGAGAGCGGCCGCTCATCAAAACAGAGATGTGT CGAAGATGGA 3'. Digest with NheI and NotI-HF. Ligate.	This Project
16 - pcDNA-NLSx3-GS-PhyB(1-908)-NLS-Gateway Linker-VPR RED4	Digest plasmid 14 with NheI and NotI-HF (pcDNA-NLSx3-GS-PhyB(1-908)). Amplify NLS-VPR with PCR from plasmid 5 with the following primers: F 5' GAGAGAGCTAGCAGCAGGGCTGACCCCAAGAAGAA G 3' and R 5'GAGAGAGCGGCCGCTCATCAAAACAGAGATGTGT CGAAGATGGA 3'. Digest with NheI and NotI-HF. Ligate.	This Project
17 - pcDNA-PhyB(1-650)-NLS-Gateway Linker-VPR RED5	Digest plasmid 15 with NheI and KpnI-HF (pcDNA-NLS-VPR). Amplify PhyB(1-650) with PCR from plasmid 4 with the following primers: F 5' GAGAGACTTGGTACCATGGTTTCCGGAG 3' and R 5' GAGAGAGCTAGCACCTAACTCATCAATCCCCTGTTC 3'. Digest with NheI and KpnI-HF. Ligate.	This Project

18 - pcDNA-dCas9-NLS	Digest plasmid 2 with KpnI-HF and NotI-HF (pcDNA Backbone). Amplify dCas9-NLS with PCR from plasmid 5 with the following primers: F 5' GAGAGAGGTACCATGGACAAGAAGTACTCCATTGGG 3' and R 5' GAGAGAGCGGCCGCTTATTAACCGGTCACCTTCCTCTTCTTCTTGGGGTC 3'. Digest with KpnI-HF and NotI-HF. Ligate.	This Project
19 - pcDNA-dCas9-NLS-GS Linker-PIF6 RED6/RED7	Digest plasmid 18 with AgeI and XbaI (pcDNA-dCas9-NLS). Digest the Gene Fragment PIF6 (5' GAGAGAACCGGTGATAGTGCTGGTAGTGCTGGTAGTGCTGGTATGATGTTCTTACCAACCGATTATTGTTGCAGGTTAAGCGATCAAGAGTATATGGAGCTTGTGTTTGAGAATGGCCAGATTCTTGCAAAGGGCCAAAGATCCAACGTTTCTCTGCATAATCAACGTACCAAATCGATCATGGATTTGTATGAGGCAGAGTATAACGAGGATTTCATGAAGAGTATCATCCATGGTGGTGGTGGTGCCATCACAAATCTCGGGGACACGCAGGTTGTTCCACAAAGTCATGTTGCTGCTGCCCATGAAACAAACATGTTGGAAAGCAATAAACATGTTGACTAATAATCTAGAGAGAGA3') with AgeI and XbaI. Ligate.	This Project
20 - pcDNA-PIF6-GS-dCas9-NLS-GS Linker-PIF6	Digest plasmid 19 with KpnI (pcDNA-dCas9-NLS-GS Linker-PIF6). Digest the Gene Fragment PIF6 (5' GAGAGAGGTACCATGATGTTCTTACCAACCGATTATTGTTGCAGGTTAAGCGATCAAGAGTATATGGAGCTTGTGTTTGAGAATGGCCAGATTCTTGCAAAGGGCCAAAGATCCAACGTTTCTCTGCATAATCAACGTACCAAATCGATCATGGATTTGTATGAGGCAGAGTATAACGAGGATTTCATGAAGAGTATCATCCATGGTGGTGGTGGTGCCATCACAAATCTCGGGGACACGCAGGTTGTTCCACAAAGTCATGTTGCTGCTGCCCATGAAACAAACATGTTGGAAAGCAATAAACATGTTGACGATAGTGCTGGTAGTGCTGGTAGTGCTGGTGGTACCGAGAGA3') with KpnI. Ligate.	This Project
21 - pcDNA-PhyB(1-908)-GS Linker-VPR	Digest plasmid 4 with KpnI-HF and ApaI (pcDNA Backbone). Amplify KpnI-PhyB(1-908)-GS Linker-NotI with PCR from plasmid 4 with the following primers: F 5' GAGAGACTTGGTACCATGGTTTCCGGAG 3' and R 5' GAGAGAGCGGCCGCTACCAGCACTACCAGCACTAC 3'. Digest with KpnI-HF and NotI-HF.	This Project

	Amplify NotI-VPR-ApaI with PCR from plasmid 5 with the following primers: F 5' GAGAGAGCGGCCGCGGTTCCGGACGGGCTGACGCA 3' and R 5' GAGAGAGGGCCCTCAAAACAGAGATGTGTCGAAGA TGGACAG 3'. Digest with NotI-HF and ApaI. Ligate.	
22 - pcDNA-PhyB(1-650)-GS Linker-VPR RED7	Digest plasmid 21 with KpnI-HF and EcoRI (pcDNA-GS Linker-VPR). Amplify KpnI-PhyB(1-650)-EcoRI with PCR from plasmid 4 with the following primers: F 5' GAGAGACTTGGTACCATGGTTTCCGGAG 3' and R 5' GAGAGAGAATTCACCTAACTCATCAATCCCCTGTTC 3'. Digest with KpnI-HF and NotI-HF. Ligate.	This Project

7 - 9xSeq2-mCherry Reporter

AAACTGCAAAAGGTCGAGAAACTGCAAAAGGTCGAGAAACTGCAAAAGGTCGAGAAACTGCAAAAGGTCGAGA
AACTGCAAAAGGTCGAGAAACTGCAAAAGGTCGAGAAACTGCAAAAGGTCGAGAAACTGCAAAAGGTCGAGAA
ACTGCAAAAGAGATCTGGTAGGCGTGTACGGTGGGAGGTCTATATAAGCAGAGCTCGTTTAGTGAACCGTCAGAT
CAAGCTTGGCATTCCGGTACTGTTGGTAAAGCCACCATGAGCCACCATGGTGAGCAAGGGCGAGGAGGATAACA
TGGCCATCATCAAGGAGTTCATGCGCTTCAAGGTGCACATGGAGGGCTCCGTGAACGGCCACGAGTTCGAGATCG
AGGGCGAGGGCGAGGGCCGCCCCTACGAGGGCACCCAGACCGCCAAGCTGAAGGTGACCAAGGGTGGCCCCCT
GCCCTTCGCCTGGGACATCCTGTCCCCTCAGTTCATGTACGGCTCCAAGGCCTACGTGAAGCACCCCGCCGACATC
CCCGACTACTTGAAGCTGTCCTTCCCCGAGGGCTTCAAGTGGGAGCGCGTGATGAACTTCGAGGACGGCGGCGTG
GTGACCGTGACCCAGGACTCCTCCCTGCAGGACGGCGAGTTCATCTACAAGGTGAAGCTGCGCGGCACCAACTTC
CCCTCCGACGGCCCCGTAATGCAGAAGAAGACCATGGGCTGGGAGGCCTCCTCCGAGCGGATGTACCCCGAGGA
CGGCGCCCTGAAGGGCGAGATCAAGCAGAGGCTGAAGCTGAAGGACGGCGGCCACTACGACGCTGAGGTCAAG
ACCACCTACAAGGCCAAGAAGCCCGTGCAGCTGCCCGGCGCCTACAACGTCAACATCAAGTTGGACATCACCTCCC
ACAACGAGGACTACACCATCGTGGAACAGTACGAACGCGCCGAGGGCCGCCACTCCACCGGCGGCATGGATGAA
TTGTACAAATAG

8 - 9xSeq2-GFP Reporter

AAACTGCAAAAGGTCGAGAAACTGCAAAAGGTCGAGAAACTGCAAAAGGTCGAGAAACTGCAAAAGGTCGAGA
AACTGCAAAAGGTCGAGAAACTGCAAAAGGTCGAGAAACTGCAAAAGGTCGAGAAACTGCAAAAGGTCGAGAA
ACTGCAAAAGAGATCTGGTAGGCGTGTACGGTGGGAGGTCTATATAAGCAGAGCTCGTTTAGTGAACCGTCAGAT
CAAGCTTGGCATTCCGGTACTGTTGGTAAAGCCACCATGGTGAGCAAGGGCGAGGAGCTGTTCACCGGGGTGGT
GCCCATCCTGGTCGAGCTGGACGGCGACGTAAACGGCCACAAGTTCAGCGTGTCCGGCGAGGGCGAGGGCGATG
CCACCTACGGCAAGCTGACCCTGAAGTTCATCTGCACCACCGGCAAGCTGCCCGTGCCCTGGCCCACCCTCGTGAC
CACCCTGACCTACGGCGTGCAGTGCTTCAGCCGCTACCCCGACCACATGAAGCAGCACGACTTCTTCAAGTCCGCC
ATGCCCGAAGGCTACGTCCAGGAGCGCACCATCTTCTTCAAGGACGACGGCAACTACAAGACCCGCGCCGAGGTG
AAGTTCGAGGGCGACACCCTGGTGAACCGCATCGAGCTGAAGGGCATCGACTTCAAGGAGGACGGCAACATCCT
GGGGCACAAGCTGGAGTACAACTACAACAGCCACAACGTCTATATCATGGCCGACAAGCAGAAGAACGGCATCA
AGGTGAACTTCAAGATCCGCCACAACATCGAGGACGGCAGCGTGCAGCTCGCCGACCACTACCAGCAGAACACCC
CCATCGGCGACGGCCCCGTGCTGCTGCCCGACAACCACTACCTGAGCACCCAGTCCGCCCTGAGCAAAGACCCCA

ACGAGAAGCGCGATCACATGGTCCTGCTGGAGTTCGTGACCGCCGCCGGGATCACTCTCGGCATGGACGAGCTGT
ACAAGTAA

9 - SPgRNA-9xSeq2

TTTCCCATGATTCCTTCATATTTGCATATACGATACAAGGCTGTTAGAGAGATAATTGGAATTAATTTGACTGTAAA
CACAAAGATATTAGTACAAAATACGTGACGTAGAAAGTAATAATTTCTTGGGTAGTTTGCAGTTTTAAAATTATGT
TTTAAAATGGACTATCATATGCTTAtCGTAACTTGAAAGTATTTCGATTTCTTGGCTTTATATATCTTGTGGAAAGGA
CGAAACACCGAAAGGTCGAGAAACTGCAAAGTTTTAGAGCTAGAAATAGCAAGTTAAAATAAGGCTAGTCCGTTA
TCAACTTGAAAAAGTGGCACCGAGTCGGTGCTTTTTTT

10 - Flag-NLS-dCas9-NLS-PIF6

GACTACAAAGACCATGACGGTGATTATAAAGATCATGACATCGATTACAAGGATGACGATGACAAGATGGCCCCC
AAGAAGAAGAGGAAGGTGGGCCGCGGAATGGATAAGAAATACTCAATAGGCTTAGCTATCGGCACAAATAGCGT
CGGATGGGCGGTGATCACTGATGAATATAAGGTTCCGTCTAAAAAGTTCAAGGTTCTGGGAAATACAGACCGCCA
CAGTATCAAAAAAAATCTTATAGGGGCTCTTTTATTTGACAGTGGAGAGACAGCGGAAGCGACTCGTCTCAAACG
GACAGCTCGTAGAAGGTATACACGTCGGAAGAATCGTATTTGTTATCTACAGGAGATTTTTTCAAATGAGATGGC
GAAAGTAGATGATAGTTTCTTTCATCGACTTGAAGAGTCTTTTTTGGTGGAAGAAGACAAGAAGCATGAACGTCAT
CCTATTTTTGGAAATATAGTAGATGAAGTTGCTTATCATGAGAAATATCCAACTATCTATCATCTGCGAAAAAAATT
GGTAGATTCTACTGATAAAGCGGATTTGCGCTTAATCTATTTGGCCTTAGCGCATATGATTAAGTTTCGTGGTCATT
TTTTGATTGAGGGAGATTTAAATCCTGATAATAGTGATGTGGACAAACTATTTATCCAGTTGGTACAAACCTACAA
TCAATTATTTGAAGAAAACCCTATTAACGCAAGTGGAGTAGATGCTAAAGCGATTCTTTCTGCACGATTGAGTAAA
TCAAGACGATTAGAAAATCTCATTGCTCAGCTCCCCGGTGAGAAGAAAAATGGCTTATTTGGGAATCTCATTGCTT
TGTCATTGGGTTTGACCCCTAATTTTAAATCAAATTTTGATTTGGCAGAAGATGCTAAATTACAGCTTTCAAAAGAT
ACTTACGATGATGATTTAGATAATTTATTGGCGCAAATTGGAGATCAATATGCTGATTTGTTTTTGGCAGCTAAGA
ATTTATCAGATGCTATTTTACTTTCAGATATCCTAAGAGTAAATACTGAAATAACTAAGGCTCCCCTATCAGCTTCA
ATGATTAAACGCTACGATGAACATCATCAAGACTTGACTCTTTTAAAAGCTTTAGTTCGACAACAACTTCCAGAAAA
GTATAAAGAAATCTTTTTTGATCAATCAAAAAACGGATATGCAGGTTATATTGATGGGGGAGCTAGCCAAGAAGA
ATTTTATAAATTTATCAAACCAATTTTAGAAAAAATGGATGGTACTGAGGAATTATTGGTGAAACTAAATCGTGAA
GATTTGCTGCGCAAGCAACGGACCTTTGACAACGGCTCTATTCCCCATCAAATTCACTTGGGTGAGCTGCATGCTA
TTTTGAGAAGACAAGAAGACTTTTATCCATTTTTAAAAGACAATCGTGAGAAGATTGAAAAAATCTTGACTTTTCG
AATTCCTTATTATGTTGGTCCATTGGCGCGTGGCAATAGTCGTTTTGCATGGATGACTCGGAAGTCTGAAGAAACA
ATTACCCCATGGAATTTTGAAGAAGTTGTCGATAAAGGTGCTTCAGCTCAATCATTTATTGAACGCATGACAAACTT
TGATAAAAATCTTCCAAATGAAAAAGTACTACCAAAACATAGTTTGCTTTATGAGTATTTTACGGTTTATAACGAAT
TGACAAAGGTCAAATATGTTACTGAAGGAATGCGAAAACCAGCATTTCTTTCAGGTGAACAGAAGAAAGCCATTG
TTGATTTACTCTTCAAAACAAATCGAAAAGTAACCGTTAAGCAATTAAAAGAAGATTATTTCAAAAAAATAGAATG
TTTTGATAGTGTTGAAATTTCAGGAGTTGAAGATAGATTTAATGCTTCATTAGGTACCTACCATGATTTGCTAAAAA
TTATTAAAGATAAAGATTTTTTGGATAATGAAGAAAATGAAGATATCTTAGAGGATATTGTTTTAACATTGACCTTA
TTTGAAGATAGGGAGATGATTGAGGAAAGACTTAAAACATATGCTCACCTCTTTGATGATAAGGTGATGAAACAG
CTTAAACGTCGCCGTTATACTGGTTGGGGACGTTTGTCTCGAAAATTGATTAATGGTATTAGGGATAAGCAATCTG
GCAAAACAATATTAGATTTTTTGAAATCAGATGGTTTTGCCAATCGCAATTTTATGCAGCTGATCCATGATGATAGT
TTGACATTTAAAGAAGACATTCAAAAAGCACAAGTGTCTGGACAAGGCGATAGTTTACATGAACATATTGCAAATT
TAGCTGGTAGCCCTGCTATTAAAAAAGGTATTTTACAGACTGTAAAAGTTGTTGATGAATTGGTCAAAGTAATGGG
GCGGCATAAGCCAGAAAATATCGTTATTGAAATGGCACGTGAAAATCAGACAACTCAAAAGGGCCAGAAAAATTC
GCGAGAGCGTATGAAACGAATCGAAGAAGGTATCAAAGAATTAGGAAGTCAGATTCTTAAAGAGCATCCTGTTG
AAAATACTCAATTGCAAAATGAAAAGCTCTATCTCTATTATCTCCAAAATGGAAGAGACATGTATGTGGACCAAGA
ATTAGATATTAATCGTTTAAGTGATTATGATGTCGATGCCATTGTTCCACAAAGTTTCCTTAAAGACGATTCAATAG
ACAATAAGGTCTTAACGCGTTCTGATAAAAATCGTGGTAAATCGGATAACGTTCCAAGTGAAGAAGTAGTCAAAA
AGATGAAAAACTATTGGAGACAACTTCTAAACGCCAAGTTAATCACTCAACGTAAGTTTGATAATTTAACGAAAGC
TGAACGTGGAGGTTTGAGTGAACTTGATAAAGCTGGTTTTATCAAACGCCAATTGGTTGAAACTCGCCAAATCACT
AAGCATGTGGCACAAATTTTGGATAGTCGCATGAATACTAAATACGATGAAAATGATAAACTTATTCGAGAGGTTA
AAGTGATTACCTTAAAATCTAAATTAGTTTCTGACTTCCGAAAAGATTTCCAATTCTATAAAGTACGTGAGATTAAC
AATTACCATCATGCCCATGATGCGTATCTAAATGCCGTCGTTGGAACTGCTTTGATTAAGAAATATCCAAAACTTGA

ATCGGAGTTTGTCTATGGTGATTATAAAGTTTATGATGTTCGTAAAATGATTGCTAAGTCTGAGCAAGAAATAGGC
AAAGCAACCGCAAAATATTTCTTTTACTCTAATATCATGAACTTCTTCAAAACAGAAATTACACTTGCAAATGGAGA
GATTCGCAAACGCCCTCTAATCGAAACTAATGGGGAAACTGGAGAAATTGTCTGGGATAAAGGGCGAGATTTTGC
CACAGTGCGCAAAGTATTGTCCATGCCCCAAGTCAATATTGTCAAGAAAACAGAAGTACAGACAGGCGGATTCTC
CAAGGAGTCAATTTTACCAAAAAGAAATTCGGACAAGCTTATTGCTCGTAAAAAAGACTGGGATCCAAAAAAATA
TGGTGGTTTTGATAGTCCAACGGTAGCTTATTCAGTCCTAGTGGTTGCTAAGGTGGAAAAAGGGAAATCGAAGAA
GTTAAAATCCGTTAAAGAGTTACTAGGGATCACAATTATGGAAAGAAGTTCCTTTGAAAAAAATCCGATTGACTTT
TTAGAAGCTAAAGGATATAAGGAAGTTAAAAAAGACTTAATCATTAAACTACCTAAATATAGTCTTTTTGAGTTAG
AAAACGGTCGTAAACGGATGCTGGCTAGTGCCGGAGAATTACAAAAAGGAAATGAGCTGGCTCTGCCAAGCAAA
TATGTGAATTTTTTATATTTAGCTAGTCATTATGAAAAGTTGAAGGGTAGTCCAGAAGATAACGAACAAAAACAAT
TGTTTGTGGAGCAGCATAAGCATTATTTAGATGAGATTATTGAGCAAATCAGTGAATTTTCTAAGCGTGTTATTTTA
GCAGATGCCAATTTAGATAAAGTTCTTAGTGCATATAACAAACATAGAGACAAACCAATACGTGAACAAGCAGAA
AATATTATTCATTTATTTACGTTGACGAATCTTGGAGCTCCCGCTGCTTTTAAATATTTTGATACAACAATTGATCGT
AAACGATATACGTCTACAAAAGAAGTTTTAGATGCCACTCTTATCCATCAATCCATCACTGGTCTTTATGAAACACG
CATTGATTTGAGTCAGCTAGGAGGTGACCCAATTGCCGGATCCAAGGCTAGCCCGAAAAAGAAACGCAAAGTTGG
GCGCGCCTTCTTACCAACCGATTATTGTTGCAGGTTAAGCGATCAAGAGTATATGGAGCTTGTGTTTGAGAATGGC
CAGATTCTTGCAAAGGGCCAAAGATCCAACGTTTCTCTGCATAATCAACGTACCAAATCGATCATGGATTTGTATG
AGGCAGAGTATAACGAGGATTTCATGAAGAGTATCATCCATGGTGGTGGTGGTGCCATCACAAATCTCGGGGACA
CGCAGGTTGTTCCACAAAGTCATGTTGCTGCTGCCCATGAAACAAACATGTTGGAAAGCAATAAACATGTTGACTA
G

12 - PhyB(1-908)-NLS-VP64-2A-GFP

ATGGTTTCCGGAGTCGGGGGTAGTGGCGGTGGCCGTGGCGGTGGCCGTGGCGGAGAAGAAGAACCGTCGTCAA
GTCACACTCCTAATAACCGAAGAGGAGGAGAACAAGCTCAATCGTCGGGAACGAAATCTCTCAGACCAAGAAGC
AACACTGAATCAATGAGCAAAGCAATTCAACAGTACACCGTCGACGCAAGACTCCACGCCGTTTTCGAACAATCCG
GCGAATCAGGGAAATCATTCGACTACTCACAATCACTCAAAACGACGACGTACGGTTCCTCTGTACCTGAGCAACA
GATCACAGCTTATCTCTCTCGAATCCAGCGAGGTGGTTACATTCAGCCTTTCGGATGTATGATCGCCGTCGATGAA
TCCAGTTTCCGGATCATCGGTTACAGTGAAAACGCCAGAGAAATGTTAGGGATTATGCCTCAATCTGTTCCTACTCT
TGAGAAACCTGAGATTCTAGCTATGGGAACTGATGTGAGATCTTTGTTCACTTCTTCGAGCTCGATTCTACTCGAGC
GTGCTTTCGTTGCTCGAGAGATTACCTTGTTAAATCCGGTTTGGATCCATTCCAAGAATACTGGTAAACCGTTTTAC
GCCATTCTTCATAGGATTGATGTTGGTGTTGTTATTGATTTAGAGCCAGCTAGAACTGAAGATCCTGCGCTTTCTAT
TGCTGGTGCTGTTCAATCGCAGAAACTCGCGGTTCGTGCGATTTCTCAGTTACAGGCTCTTCCTGGTGGAGATATT
AAGCTTTTGTGTGACACTGTCGTGGAAAGTGTGAGGGACTTGACTGGTTATGATCGTGTTATGGTTTATAAGTTTC
ATGAAGATGAGCATGGAGAAGTTGTAGCTGAGAGTAAACGAGATGATTTAGAGCCTTATATTGGACTGCATTATC
CTGCTACTGATATTCCTCAAGCGTCAAGGTTCTTGTTTAAGCAGAACCGTGTCCGAATGATAGTAGATTGCAATGC
CACACCTGTTCTTGTGGTCCAGGACGATAGGCTAACTCAGTCTATGTGCTTGGTTGGTTCTACTCTTAGGGCTCCTC
ATGGTTGTCACTCTCAGTATATGGCTAACATGGGATCTATTGCGTCTTTAGCAATGGCGGTTATAATCAATGGAAA
TGAAGATGATGGGAGCAATGTAGCTAGTGGAAGAAGCTCGATGAGGCTTTGGGGTTTGGTTGTTTGCCATCACAC
TTCTTCTCGCTGCATACCGTTTCCGCTAAGGTATGCTTGTGAGTTTTTGATGCAGGCTTTCGGTTTACAGTTAAACAT
GGAATTGCAGTTAGCTTTGCAAATGTCAGAGAAACGCGTTTTGAGAACGCAGACACTGTTATGTGATATGCTTCTG
CGTGACTCGCCTGCTGGAATTGTTACACAGAGTCCCAGTATCATGGACTTAGTGAAATGTGACGGTGCAGCATTTC
TTTACCACGGGAAGTATTACCCGTTGGGTGTTGCTCCTAGTGAAGTTCAGATAAAAGATGTTGTGGAGTGGTTGCT
TGCGAATCATGCGGATTCAACCGGATTAAGCACTGATAGTTTAGGCGATGCGGGGTATCCCGGTGCAGCTGCGTT
AGGGGATGCTGTGTGCGGTATGGCAGTTGCATATATCACAAAAAGAGACTTTCTTTTTTGGTTTCGATCTCACACT
GCGAAAGAAATCAAATGGGGAGGCGCTAAGCATCATCCGGAGGATAAAGATGATGGGCAACGAATGCATCCTCG
TTCGTCCTTTCAGGCTTTTCTTGAAGTTGTTAAGAGCCGGAGTCAGCCATGGGAAACTGCGGAAATGGATGCGATT
CACTCGCTCCAGCTTATTCTGAGAGACTCTTTTAAAGAATCTGAGGCGGCTATGAACTCTAAAGTTGTGGATGGTG
TGGTTCAGCCATGTAGGGATATGGCGGGGGAACAGGGGATTGATGAGTTAGGTGCAGTTGCAAGAGAGATGGTT
AGGCTCATTGAGACTGCAACTGTTCCTATATTCGCTGTGGATGCCGGAGGCTGCATCAATGGATGGAACGCTAAG
ATTGCAGAGTTGACAGGTCTCTCAGTTGAAGAAGCTATGGGGAAGTCTCTGGTTTCTGATTTAATATACAAAGAGA
ATGAAGCAACTGTCAATAAGCTTCTTTCTCGTGCTTTGAGAGGGGACGAGGAAAAGAATGTGGAGGTTAAGCTGA
AAACTTTCAGCCCCGAACTACAAGGGAAAGCAGTTTTTGTGGTTGTGAATGCTTGTTCCAGCAAGGACTACTTGAA
CAACATTGTCGGCGTTTGTTTTGTTGGACAAGACGTTACTAGTCAGAAAATCGTAATGGATAAGTTCATCAACATA

CAAGGAGATTACAAGGCTATTGTACATAGCCCAAACCCTCTAATCCCGCCAATTTTTGCTGCTGACGAGAACACGT
GCTGCCTGGAATGGAACATGGCGATGGAAAAGCTTACGGGTTGGTCTCGCAGTGAAGTGATTGGGAAAATGATT
GTCGGGGAAGTGTTTGGGAGCTGTTGCATGCTAAAGGGTCCTGATGCTTTAACCAAGTTCATGATTGTATTGCATA
ATGCGATTGGTGGCCAAGATACGGATAAGTTCCCTTTCCCATTCTTTGACCGCAATGGGAAGTTTGTTCAGGCTCT
ATTGACTGCAAACAAGCGGGTTAGCCTCGAGGGAAAGGTTATTGGGGCTTTCTGTTTCTTGCAAATCCCGAGCGA
ATTCGCTAGCCCCAAGAAGAAGAGAAAGGTGGAGGCCAGCGGTTCCGGACGGGCTGACGCATTGGACGATTTTG
ATCTGGATATGCTGGGAAGTGACGCCCTCGATGATTTTGACCTTGACATGCTTGGTTCGGATGCCCTTGATGACTT
TGACCTCGACATGCTCGGCAGTGACGCCCTTGATGATTTCGACCTGGACATGCTGATTAACTCTAGAGGCAGTGGA
GAGGGCAGAGGAAGTCTGCTAACATGCGGTGACGTCGAGGAGAATCCTGGCCCAGTGAGCAAGGGCGAGGAGC
TGTTCACCGGGGTGGTGCCCATCCTGGTCGAGCTGGACGGCGACGTAAACGGCCACAAGTTCAGCGTGTCCGGC
GAGGGCGAGGGCGATGCCACCTACGGCAAGCTGACCCTGAAGTTCATCTGCACCACCGGCAAGCTGCCCGTGCCC
TGGCCCACCCTCGTGACCACCCTGACCTACGGCGTGCAGTGCTTCAGCCGCTACCCCGACCACATGAAGCAGCACG
ACTTCTTCAAGTCCGCCATGCCCGAAGGCTACGTCCAGGAGCGCACCATCTTCTTCAAGGACGACGGCAACTACAA
GACCCGCGCCGAGGTGAAGTTCGAGGGCGACACCCTGGTGAACCGCATCGAGCTGAAGGGCATCGACTTCAAGG
AGGACGGCAACATCCTGGGGCACAAGCTGGAGTACAACTACAACAGCCACAACGTCTATATCATGGCCGACAAGC
AGAAGAACGGCATCAAGGTGAACTTCAAGATCCGCCACAACATCGAGGACGGCAGCGTGCAGCTCGCCGACCAC
TACCAGCAGAACACCCCCATCGGCGACGGCCCCGTGCTGCTGCCCGACAACCACTACCTGAGCACCCAGTCCGCCC
TGAGCAAAGACCCCAACGAGAAGCGCGATCACATGGTCCTGCTGGAGTTCGTGACCGCCGCCGGGATCACTCTCG
GCATGGACGAGCTGTACAAGTAA

13 - NLSx3-GS-PhyB(1-908)-NLS-VP64-2A-GFP

ATGGCCAGCCCTAAGAAAAAGCGAAAGGTTGAGGCCTCCGCTTCTCCAAAGAAAAAACGCAAGGTCGAAGCCAG
CGCCTCTCCGAAAAAGAAAAGCAAAGTGGAAGCCAGCGGTACTGGTGGGTCCGGGTCATCCGGAGGGTCTGGAG
GAAGCGGAGGCTCCGGAGGTACCATGGTTTCCGGAGTCGGGGGTAGTGGCGGTGGCCGTGGCGGTGGCCGTGG
CGGAGAAGAAGAACCGTCGTCAAGTCACACTCCTAATAACCGAAGAGGAGGAGAACAAGCTCAATCGTCGGGAA
CGAAATCTCTCAGACCAAGAAGCAACACTGAATCAATGAGCAAAGCAATTCAACAGTACACCGTCGACGCAAGAC
TCCACGCCGTTTTCGAACAATCCGGCGAATCAGGGAAATCATTCGACTACTCACAATCACTCAAAACGACGACGTA
CGGTTCCTCTGTACCTGAGCAACAGATCACAGCTTATCTCTCTCGAATCCAGCGAGGTGGTTACATTCAGCCTTTCG
GATGTATGATCGCCGTCGATGAATCCAGTTTCCGGATCATCGGTTACAGTGAAAACGCCAGAGAAATGTTAGGGA
TTATGCCTCAATCTGTTCCTACTCTTGAGAAACCTGAGATTCTAGCTATGGGAACTGATGTGAGATCTTTGTTCACT
TCTTCGAGCTCGATTCTACTCGAGCGTGCTTTCGTTGCTCGAGAGATTACCTTGTTAAATCCGGTTTGGATCCATTC
CAAGAATACTGGTAAACCGTTTTACGCCATTCTTCATAGGATTGATGTTGGTGTTGTTATTGATTTAGAGCCAGCTA
GAACTGAAGATCCTGCGCTTTCTATTGCTGGTGCTGTTCAATCGCAGAAACTCGCGGTTCGTGCGATTTCTCAGTTA
CAGGCTCTTCCTGGTGGAGATATTAAGCTTTTGTGTGACACTGTCGTGGAAAGTGTGAGGGACTTGACTGGTTAT
GATCGTGTTATGGTTTATAAGTTTCATGAAGATGAGCATGGAGAAGTTGTAGCTGAGAGTAAACGAGATGATTTA
GAGCCTTATATTGGACTGCATTATCCTGCTACTGATATTCCTCAAGCGTCAAGGTTCTTGTTTAAGCAGAACCGTGT
CCGAATGATAGTAGATTGCAATGCCACACCTGTTCTTGTGGTCCAGGACGATAGGCTAACTCAGTCTATGTGCTTG
GTTGGTTCTACTCTTAGGGCTCCTCATGGTTGTCACTCTCAGTATATGGCTAACATGGGATCTATTGCGTCTTTAGC
AATGGCGGTTATAATCAATGGAAATGAAGATGATGGGAGCAATGTAGCTAGTGGAAGAAGCTCGATGAGGCTTT
GGGGTTTGGTTGTTTGCCATCACACTTCTTCTCGCTGCATACCGTTTCCGCTAAGGTATGCTTGTGAGTTTTTGATG
CAGGCTTTCGGTTTACAGTTAAACATGGAATTGCAGTTAGCTTTGCAAATGTCAGAGAAACGCGTTTTGAGAACGC
AGACACTGTTATGTGATATGCTTCTGCGTGACTCGCCTGCTGGAATTGTTACACAGAGTCCCAGTATCATGGACTT
AGTGAAATGTGACGGTGCAGCATTTCTTTACCACGGGAAGTATTACCCGTTGGGTGTTGCTCCTAGTGAAGTTCAG
ATAAAAGATGTTGTGGAGTGGTTGCTTGCGAATCATGCGGATTCAACCGGATTAAGCACTGATAGTTTAGGCGAT
GCGGGGTATCCCGGTGCAGCTGCGTTAGGGGATGCTGTGTGCGGTATGGCAGTTGCATATATCACAAAAAGAGA
CTTTCTTTTTTGGTTTCGATCTCACACTGCGAAAGAAATCAAATGGGGAGGCGCTAAGCATCATCCGGAGGATAAA
GATGATGGGCAACGAATGCATCCTCGTTCGTCCTTTCAGGCTTTTCTTGAAGTTGTTAAGAGCCGGAGTCAGCCAT
GGGAAACTGCGGAAATGGATGCGATTCACTCGCTCCAGCTTATTCTGAGAGACTCTTTTAAAGAATCTGAGGCGG
CTATGAACTCTAAAGTTGTGGATGGTGTGGTTCAGCCATGTAGGGATATGGCGGGGGAACAGGGGATTGATGAG
TTAGGTGCAGTTGCAAGAGAGATGGTTAGGCTCATTGAGACTGCAACTGTTCCTATATTCGCTGTGGATGCCGGA
GGCTGCATCAATGGATGGAACGCTAAGATTGCAGAGTTGACAGGTCTCTCAGTTGAAGAAGCTATGGGGAAGTCT
CTGGTTTCTGATTTAATATACAAAGAGAATGAAGCAACTGTCAATAAGCTTCTTTCTCGTGCTTTGAGAGGGGACG
AGGAAAAGAATGTGGAGGTTAAGCTGAAAACTTTCAGCCCCGAACTACAAGGGAAAGCAGTTTTTGTGGTTGTGA

ATGCTTGTTCCAGCAAGGACTACTTGAACAACATTGTCGGCGTTTGTTTTGTTGGACAAGACGTTACTAGTCAGAA
AATCGTAATGGATAAGTTCATCAACATACAAGGAGATTACAAGGCTATTGTACATAGCCCAAACCCTCTAATCCCG
CCAATTTTTGCTGCTGACGAGAACACGTGCTGCCTGGAATGGAACATGGCGATGGAAAAGCTTACGGGTTGGTCT
CGCAGTGAAGTGATTGGGAAAATGATTGTCGGGGAAGTGTTTGGGAGCTGTTGCATGCTAAAGGGTCCTGATGC
TTTAACCAAGTTCATGATTGTATTGCATAATGCGATTGGTGGCCAAGATACGGATAAGTTCCCTTTCCCATTCTTTG
ACCGCAATGGGAAGTTTGTTCAGGCTCTATTGACTGCAAACAAGCGGGTTAGCCTCGAGGGAAAGGTTATTGGGG
CTTTCTGTTTCTTGCAAATCCCGAGCGAATTCGCTAGCCCCAAGAAGAAGAGAAAGGTGGAGGCCAGCGGTTCCG
GACGGGCTGACGCATTGGACGATTTTGATCTGGATATGCTGGGAAGTGACGCCCTCGATGATTTTGACCTTGACAT
GCTTGGTTCGGATGCCCTTGATGACTTTGACCTCGACATGCTCGGCAGTGACGCCCTTGATGATTTCGACCTGGAC
ATGCTGATTAACTCTAGAGGCAGTGGAGAGGGCAGAGGAAGTCTGCTAACATGCGGTGACGTCGAGGAGAATCC
TGGCCCAGTGAGCAAGGGCGAGGAGCTGTTCACCGGGGTGGTGCCCATCCTGGTCGAGCTGGACGGCGACGTAA
ACGGCCACAAGTTCAGCGTGTCCGGCGAGGGCGAGGGCGATGCCACCTACGGCAAGCTGACCCTGAAGTTCATC
TGCACCACCGGCAAGCTGCCCGTGCCCTGGCCCACCCTCGTGACCACCCTGACCTACGGCGTGCAGTGCTTCAGCC
GCTACCCCGACCACATGAAGCAGCACGACTTCTTCAAGTCCGCCATGCCCGAAGGCTACGTCCAGGAGCGCACCA
TCTTCTTCAAGGACGACGGCAACTACAAGACCCGCGCCGAGGTGAAGTTCGAGGGCGACACCCTGGTGAACCGC
ATCGAGCTGAAGGGCATCGACTTCAAGGAGGACGGCAACATCCTGGGGCACAAGCTGGAGTACAACTACAACAG
CCACAACGTCTATATCATGGCCGACAAGCAGAAGAACGGCATCAAGGTGAACTTCAAGATCCGCCACAACATCGA
GGACGGCAGCGTGCAGCTCGCCGACCACTACCAGCAGAACACCCCCATCGGCGACGGCCCCGTGCTGCTGCCCGA
CAACCACTACCTGAGCACCCAGTCCGCCCTGAGCAAAGACCCCAACGAGAAGCGCGATCACATGGTCCTGCTGGA
GTTCGTGACCGCCGCCGGGATCACTCTCGGCATGGACGAGCTGTACAAGTAA

14 - Flag-PIF6-Flag-NLS-dCas9-NLS-PIF6

ATGGACTACAAAGACCATGACGGTGATTATAAAGATCATGACATCGATATGATGTTCTTACCAACCGATTATTGTT
GCAGGTTAAGCGATCAAGAGTATATGGAGCTTGTGTTTGAGAATGGCCAGATTCTTGCAAAGGGCCAAAGATCCA
ACGTTTCTCTGCATAATCAACGTACCAAATCGATCATGGATTTGTATGAGGCAGAGTATAACGAGGATTTCATGAA
GAGTATCATCCATGGTGGTGGTGGTGCCATCACAAATCTCGGGGACACGCAGGTTGTTCCACAAAGTCATGTTGC
TGCTGCCCATGAAACAAACATGTTGGAAAGCAATAAACATGTTGACCATCACGATTACAAGGATGACGATGACAA
GATGGCCCCCAAGAAGAAGAGGAAGGTGGGCCGCGGAATGGATAAGAAATACTCAATAGGCTTAGCTATCGGCA
CAAATAGCGTCGGATGGGCGGTGATCACTGATGAATATAAGGTTCCGTCTAAAAAGTTCAAGGTTCTGGGAAATA
CAGACCGCCACAGTATCAAAAAAAATCTTATAGGGGCTCTTTTATTTGACAGTGGAGAGACAGCGGAAGCGACTC
GTCTCAAACGGACAGCTCGTAGAAGGTATACACGTCGGAAGAATCGTATTTGTTATCTACAGGAGATTTTTTCAAA
TGAGATGGCGAAAGTAGATGATAGTTTCTTTCATCGACTTGAAGAGTCTTTTTTGGTGGAAGAAGACAAGAAGCA
TGAACGTCATCCTATTTTTGGAAATATAGTAGATGAAGTTGCTTATCATGAGAAATATCCAACTATCTATCATCTGC
GAAAAAAATTGGTAGATTCTACTGATAAAGCGGATTTGCGCTTAATCTATTTGGCCTTAGCGCATATGATTAAGTTT
CGTGGTCATTTTTTGATTGAGGGAGATTTAAATCCTGATAATAGTGATGTGGACAAACTATTTATCCAGTTGGTAC
AAACCTACAATCAATTATTTGAAGAAAACCCTATTAACGCAAGTGGAGTAGATGCTAAAGCGATTCTTTCTGCACG
ATTGAGTAAATCAAGACGATTAGAAAATCTCATTGCTCAGCTCCCCGGTGAGAAGAAAAATGGCTTATTTGGGAA
TCTCATTGCTTTGTCATTGGGTTTGACCCCTAATTTTAAATCAAATTTTGATTTGGCAGAAGATGCTAAATTACAGCT
TTCAAAAGATACTTACGATGATGATTTAGATAATTTATTGGCGCAAATTGGAGATCAATATGCTGATTTGTTTTTGG
CAGCTAAGAATTTATCAGATGCTATTTTACTTTCAGATATCCTAAGAGTAAATACTGAAATAACTAAGGCTCCCCTA
TCAGCTTCAATGATTAAACGCTACGATGAACATCATCAAGACTTGACTCTTTTAAAAGCTTTAGTTCGACAACAACT
TCCAGAAAAGTATAAAGAAATCTTTTTTGATCAATCAAAAAACGGATATGCAGGTTATATTGATGGGGGAGCTAG
CCAAGAAGAATTTTATAAATTTATCAAACCAATTTTAGAAAAAATGGATGGTACTGAGGAATTATTGGTGAAACTA
AATCGTGAAGATTTGCTGCGCAAGCAACGGACCTTTGACAACGGCTCTATTCCCCATCAAATTCACTTGGGTGAGC
TGCATGCTATTTTGAGAAGACAAGAAGACTTTTATCCATTTTTAAAAGACAATCGTGAGAAGATTGAAAAAATCTT
GACTTTTCGAATTCCTTATTATGTTGGTCCATTGGCGCGTGGCAATAGTCGTTTTGCATGGATGACTCGGAAGTCTG
AAGAAACAATTACCCCATGGAATTTTGAAGAAGTTGTCGATAAAGGTGCTTCAGCTCAATCATTTATTGAACGCAT
GACAAACTTTGATAAAAATCTTCCAAATGAAAAAGTACTACCAAAACATAGTTTGCTTTATGAGTATTTTACGGTTT
ATAACGAATTGACAAAGGTCAAATATGTTACTGAAGGAATGCGAAAACCAGCATTTCTTTCAGGTGAACAGAAGA
AAGCCATTGTTGATTTACTCTTCAAAACAAATCGAAAAGTAACCGTTAAGCAATTAAAAGAAGATTATTTCAAAAA
AATAGAATGTTTTGATAGTGTTGAAATTTCAGGAGTTGAAGATAGATTTAATGCTTCATTAGGTACCTACCATGATT
TGCTAAAAATTATTAAAGATAAAGATTTTTTGGATAATGAAGAAAATGAAGATATCTTAGAGGATATTGTTTTAAC
ATTGACCTTATTTGAAGATAGGGAGATGATTGAGGAAAGACTTAAAACATATGCTCACCTCTTTGATGATAAGGTG

ATGAAACAGCTTAAACGTCGCCGTTATACTGGTTGGGGACGTTTGTCTCGAAAATTGATTAATGGTATTAGGGATA
AGCAATCTGGCAAAACAATATTAGATTTTTTGAAATCAGATGGTTTTGCCAATCGCAATTTTATGCAGCTGATCCAT
GATGATAGTTTGACATTTAAAGAAGACATTCAAAAAGCACAAGTGTCTGGACAAGGCGATAGTTTACATGAACAT
ATTGCAAATTTAGCTGGTAGCCCTGCTATTAAAAAAGGTATTTTACAGACTGTAAAAGTTGTTGATGAATTGGTCA
AAGTAATGGGGCGGCATAAGCCAGAAAATATCGTTATTGAAATGGCACGTGAAAATCAGACAACTCAAAAGGGC
CAGAAAAATTCGCGAGAGCGTATGAAACGAATCGAAGAAGGTATCAAAGAATTAGGAAGTCAGATTCTTAAAGA
GCATCCTGTTGAAAATACTCAATTGCAAAATGAAAAGCTCTATCTCTATTATCTCCAAAATGGAAGAGACATGTAT
GTGGACCAAGAATTAGATATTAATCGTTTAAGTGATTATGATGTCGATGCCATTGTTCCACAAAGTTTCCTTAAAGA
CGATTCAATAGACAATAAGGTCTTAACGCGTTCTGATAAAAATCGTGGTAAATCGGATAACGTTCCAAGTGAAGA
AGTAGTCAAAAAGATGAAAAACTATTGGAGACAACTTCTAAACGCCAAGTTAATCACTCAACGTAAGTTTGATAAT
TTAACGAAAGCTGAACGTGGAGGTTTGAGTGAACTTGATAAAGCTGGTTTTATCAAACGCCAATTGGTTGAAACTC
GCCAAATCACTAAGCATGTGGCACAAATTTTGGATAGTCGCATGAATACTAAATACGATGAAAATGATAAACTTAT
TCGAGAGGTTAAAGTGATTACCTTAAAATCTAAATTAGTTTCTGACTTCCGAAAAGATTTCCAATTCTATAAAGTAC
GTGAGATTAACAATTACCATCATGCCCATGATGCGTATCTAAATGCCGTCGTTGGAACTGCTTTGATTAAGAAATA
TCCAAAACTTGAATCGGAGTTTGTCTATGGTGATTATAAAGTTTATGATGTTCGTAAAATGATTGCTAAGTCTGAGC
AAGAAATAGGCAAAGCAACCGCAAAATATTTCTTTTACTCTAATATCATGAACTTCTTCAAAACAGAAATTACACTT
GCAAATGGAGAGATTCGCAAACGCCCTCTAATCGAAACTAATGGGGAAACTGGAGAAATTGTCTGGGATAAAGG
GCGAGATTTTGCCACAGTGCGCAAAGTATTGTCCATGCCCCAAGTCAATATTGTCAAGAAAACAGAAGTACAGAC
AGGCGGATTCTCCAAGGAGTCAATTTTACCAAAAAGAAATTCGGACAAGCTTATTGCTCGTAAAAAAGACTGGGA
TCCAAAAAAATATGGTGGTTTTGATAGTCCAACGGTAGCTTATTCAGTCCTAGTGGTTGCTAAGGTGGAAAAAGG
GAAATCGAAGAAGTTAAAATCCGTTAAAGAGTTACTAGGGATCACAATTATGGAAAGAAGTTCCTTTGAAAAAAA
TCCGATTGACTTTTTAGAAGCTAAAGGATATAAGGAAGTTAAAAAAGACTTAATCATTAAACTACCTAAATATAGT
CTTTTTGAGTTAGAAAACGGTCGTAAACGGATGCTGGCTAGTGCCGGAGAATTACAAAAAGGAAATGAGCTGGCT
CTGCCAAGCAAATATGTGAATTTTTTATATTTAGCTAGTCATTATGAAAAGTTGAAGGGTAGTCCAGAAGATAACG
AACAAAAACAATTGTTTGTGGAGCAGCATAAGCATTATTTAGATGAGATTATTGAGCAAATCAGTGAATTTTCTAA
GCGTGTTATTTTAGCAGATGCCAATTTAGATAAAGTTCTTAGTGCATATAACAAACATAGAGACAAACCAATACGT
GAACAAGCAGAAAATATTATTCATTTATTTACGTTGACGAATCTTGGAGCTCCCGCTGCTTTTAAATATTTTGATAC
AACAATTGATCGTAAACGATATACGTCTACAAAAGAAGTTTTAGATGCCACTCTTATCCATCAATCCATCACTGGTC
TTTATGAAACACGCATTGATTTGAGTCAGCTAGGAGGTGACCCAATTGCCGGATCCAAGGCTAGCCCGAAAAAGA
AACGCAAAGTTGGGCGCGCCTTCTTACCAACCGATTATTGTTGCAGGTTAAGCGATCAAGAGTATATGGAGCTTGT
GTTTGAGAATGGCCAGATTCTTGCAAAGGGCCAAAGATCCAACGTTTCTCTGCATAATCAACGTACCAAATCGATC
ATGGATTTGTATGAGGCAGAGTATAACGAGGATTTCATGAAGAGTATCATCCATGGTGGTGGTGGTGCCATCACA
AATCTCGGGGACACGCAGGTTGTTCCACAAAGTCATGTTGCTGCTGCCCATGAAACAAACATGTTGGAAAGCAAT
AAACATGTTGACTAG

15 - PhyB(1-908)-NLS-Gateway Linker-VPR

ATGGTTTCCGGAGTCGGGGGTAGTGGCGGTGGCCGTGGCGGTGGCCGTGGCGGAGAAGAAGAACCGTCGTCAA
GTCACACTCCTAATAACCGAAGAGGAGGAGAACAAGCTCAATCGTCGGGAACGAAATCTCTCAGACCAAGAAGC
AACACTGAATCAATGAGCAAAGCAATTCAACAGTACACCGTCGACGCAAGACTCCACGCCGTTTTCGAACAATCCG
GCGAATCAGGGAAATCATTCGACTACTCACAATCACTCAAAACGACGACGTACGGTTCCTCTGTACCTGAGCAACA
GATCACAGCTTATCTCTCTCGAATCCAGCGAGGTGGTTACATTCAGCCTTTCGGATGTATGATCGCCGTCGATGAA
TCCAGTTTCCGGATCATCGGTTACAGTGAAAACGCCAGAGAAATGTTAGGGATTATGCCTCAATCTGTTCCTACTCT
TGAGAAACCTGAGATTCTAGCTATGGGAACTGATGTGAGATCTTTGTTCACTTCTTCGAGCTCGATTCTACTCGAGC
GTGCTTTCGTTGCTCGAGAGATTACCTTGTTAAATCCGGTTTGGATCCATTCCAAGAATACTGGTAAACCGTTTTAC
GCCATTCTTCATAGGATTGATGTTGGTGTTGTTATTGATTTAGAGCCAGCTAGAACTGAAGATCCTGCGCTTTCTAT
TGCTGGTGCTGTTCAATCGCAGAAACTCGCGGTTCGTGCGATTTCTCAGTTACAGGCTCTTCCTGGTGGAGATATT
AAGCTTTTGTGTGACACTGTCGTGGAAAGTGTGAGGGACTTGACTGGTTATGATCGTGTTATGGTTTATAAGTTTC
ATGAAGATGAGCATGGAGAAGTTGTAGCTGAGAGTAAACGAGATGATTTAGAGCCTTATATTGGACTGCATTATC
CTGCTACTGATATTCCTCAAGCGTCAAGGTTCTTGTTTAAGCAGAACCGTGTCCGAATGATAGTAGATTGCAATGC
CACACCTGTTCTTGTGGTCCAGGACGATAGGCTAACTCAGTCTATGTGCTTGGTTGGTTCTACTCTTAGGGCTCCTC
ATGGTTGTCACTCTCAGTATATGGCTAACATGGGATCTATTGCGTCTTTAGCAATGGCGGTTATAATCAATGGAAA
TGAAGATGATGGGAGCAATGTAGCTAGTGGAAGAAGCTCGATGAGGCTTTGGGGTTTGGTTGTTTGCCATCACAC
TTCTTCTCGCTGCATACCGTTTCCGCTAAGGTATGCTTGTGAGTTTTTGATGCAGGCTTTCGGTTTACAGTTAAACAT

GGAATTGCAGTTAGCTTTGCAAATGTCAGAGAAACGCGTTTTGAGAACGCAGACACTGTTATGTGATATGCTTCTG
CGTGACTCGCCTGCTGGAATTGTTACACAGAGTCCCAGTATCATGGACTTAGTGAAATGTGACGGTGCAGCATTTC
TTTACCACGGGAAGTATTACCCGTTGGGTGTTGCTCCTAGTGAAGTTCAGATAAAAGATGTTGTGGAGTGGTTGCT
TGCGAATCATGCGGATTCAACCGGATTAAGCACTGATAGTTTAGGCGATGCGGGGTATCCCGGTGCAGCTGCGTT
AGGGGATGCTGTGTGCGGTATGGCAGTTGCATATATCACAAAAAGAGACTTTCTTTTTTGGTTTCGATCTCACACT
GCGAAAGAAATCAAATGGGGAGGCGCTAAGCATCATCCGGAGGATAAAGATGATGGGCAACGAATGCATCCTCG
TTCGTCCTTTCAGGCTTTTCTTGAAGTTGTTAAGAGCCGGAGTCAGCCATGGGAAACTGCGGAAATGGATGCGATT
CACTCGCTCCAGCTTATTCTGAGAGACTCTTTTAAAGAATCTGAGGCGGCTATGAACTCTAAAGTTGTGGATGGTG
TGGTTCAGCCATGTAGGGATATGGCGGGGGAACAGGGGATTGATGAGTTAGGTGCAGTTGCAAGAGAGATGGTT
AGGCTCATTGAGACTGCAACTGTTCCTATATTCGCTGTGGATGCCGGAGGCTGCATCAATGGATGGAACGCTAAG
ATTGCAGAGTTGACAGGTCTCTCAGTTGAAGAAGCTATGGGGAAGTCTCTGGTTTCTGATTTAATATACAAAGAGA
ATGAAGCAACTGTCAATAAGCTTCTTTCTCGTGCTTTGAGAGGGGACGAGGAAAAGAATGTGGAGGTTAAGCTGA
AAACTTTCAGCCCCGAACTACAAGGGAAAGCAGTTTTTGTGGTTGTGAATGCTTGTTCCAGCAAGGACTACTTGAA
CAACATTGTCGGCGTTTGTTTTGTTGGACAAGACGTTACTAGTCAGAAAATCGTAATGGATAAGTTCATCAACATA
CAAGGAGATTACAAGGCTATTGTACATAGCCCAAACCCTCTAATCCCGCCAATTTTTGCTGCTGACGAGAACACGT
GCTGCCTGGAATGGAACATGGCGATGGAAAAGCTTACGGGTTGGTCTCGCAGTGAAGTGATTGGGAAAATGATT
GTCGGGGAAGTGTTTGGGAGCTGTTGCATGCTAAAGGGTCCTGATGCTTTAACCAAGTTCATGATTGTATTGCATA
ATGCGATTGGTGGCCAAGATACGGATAAGTTCCCTTTCCCATTCTTTGACCGCAATGGGAAGTTTGTTCAGGCTCT
ATTGACTGCAAACAAGCGGGTTAGCCTCGAGGGAAAGGTTATTGGGGCTTTCTGTTTCTTGCAAATCCCGAGCGA
ATTCGCTAGCAGCAGGGCTGACCCCAAGAAGAAGAGGAAGGTGTCGCCAGGGATCCGTCGACTTGACGCGTTGA
TATCAACAAGTTTGTACAAAAAAGCAGGCTACAAAGAGGCCAGCGGTTCCGGACGGGCTGACGCATTGGACGATT
TTGATCTGGATATGCTGGGAAGTGACGCCCTCGATGATTTTGACCTTGACATGCTTGGTTCGGATGCCCTTGATGA
CTTTGACCTCGACATGCTCGGCAGTGACGCCCTTGATGATTTCGACCTGGACATGCTGATTAACTCTAGAAGTTCC
GGATCTCCGAAAAAGAAACGCAAAGTTGGTAGCCAGTACCTGCCCGACACCGACGACCGGCACCGGATCGAGGA
AAAGCGGAAGCGGACCTACGAGACATTCAAGAGCATCATGAAGAAGTCCCCCTTCAGCGGCCCCACCGACCCTAG
ACCTCCACCTAGAAGAATCGCCGTGCCCAGCAGATCCAGCGCCAGCGTGCCAAAACCTGCCCCCCAGCCTTACCCC
TTCACCAGCAGCCTGAGCACCATCAACTACGACGAGTTCCCTACCATGGTGTTCCCCAGCGGCCAGATCTCTCAGG
CCTCTGCTCTGGCTCCAGCCCCTCCTCAGGTGCTGCCTCAGGCTCCTGCTCCTGCACCAGCTCCAGCCATGGTGTCT
GCACTGGCTCAGGCACCAGCACCCGTGCCTGTGCTGGCTCCTGGACCTCCACAGGCTGTGGCTCCACCAGCCCCTA
AACCTACACAGGCCGGCGAGGGCACACTGTCTGAAGCTCTGCTGCAGCTGCAGTTCGACGACGAGGATCTGGGA
GCCCTGCTGGGAAACAGCACCGATCCTGCCGTGTTCACCGACCTGGCCAGCGTGGACAACAGCGAGTTCCAGCAG
CTGCTGAACCAGGGCATCCCTGTGGCCCCTCACACCACCGAGCCCATGCTGATGGAATACCCCGAGGCCATCACCC
GGCTCGTGACAGGCGCTCAGAGGCCTCCTGATCCAGCTCCTGCCCCTCTGGGAGCACCAGGCCTGCCTAATGGAC
TGCTGTCTGGCGACGAGGACTTCAGCTCTATCGCCGATATGGATTTCTCAGCCTTGCTGGGCTCTGGCAGCGGCAG
CCGGGATTCCAGGGAAGGGATGTTTTTGCCGAAGCCTGAGGCCGGCTCCGCTATTAGTGACGTGTTTGAGGGCCG
CGAGGTGTGCCAGCCAAAACGAATCCGGCCATTTCATCCTCCAGGAAGTCCATGGGCCAACCGCCCACTCCCCGCC
AGCCTCGCACCAACACCAACCGGTCCAGTACATGAGCCAGTCGGGTCACTGACCCCGGCACCAGTCCCTCAGCCA
CTGGATCCAGCGCCCGCAGTGACTCCCGAGGCCAGTCACCTGTTGGAGGATCCCGATGAAGAGACGAGCCAGGC
TGTCAAAGCCCTTCGGGAGATGGCCGATACTGTGATTCCCCAGAAGGAAGAGGCTGCAATCTGTGGCCAAATGGA
CCTTTCCCATCCGCCCCCAAGGGGCCATCTGGATGAGCTGACAACCACACTTGAGTCCATGACCGAGGATCTGAAC
CTGGACTCACCCCTGACCCCGGAATTGAACGAGATTCTGGATACCTTCCTGAACGACGAGTGCCTCTTGCATGCCA
TGCATATCAGCACAGGACTGTCCATCTTCGACACATCTCTGTTTTGA

16 - NLSx3-GS-PhyB(1-908)-NLS-Gateway Linker-VPR

ATGGCCAGCCCTAAGAAAAAGCGAAAGGTTGAGGCCTCCGCTTCTCCAAAGAAAAAACGCAAGGTCGAAGCCAG
CGCCTCTCCGAAAAAGAAAAGCAAAGTGGAAGCCAGCGGTACTGGTGGGTCCGGGTCATCCGGAGGGTCTGGAG
GAAGCGGAGGCTCCGGAGGTACCATGGTTTCCGGAGTCGGGGGTAGTGGCGGTGGCCGTGGCGGTGGCCGTGG
CGGAGAAGAAGAACCGTCGTCAAGTCACACTCCTAATAACCGAAGAGGAGGAGAACAAGCTCAATCGTCGGGAA
CGAAATCTCTCAGACCAAGAAGCAACACTGAATCAATGAGCAAAGCAATTCAACAGTACACCGTCGACGCAAGAC
TCCACGCCGTTTTCGAACAATCCGGCGAATCAGGGAAATCATTCGACTACTCACAATCACTCAAAACGACGACGTA
CGGTTCCTCTGTACCTGAGCAACAGATCACAGCTTATCTCTCTCGAATCCAGCGAGGTGGTTACATTCAGCCTTTCG
GATGTATGATCGCCGTCGATGAATCCAGTTTCCGGATCATCGGTTACAGTGAAAACGCCAGAGAAATGTTAGGGA
TTATGCCTCAATCTGTTCCTACTCTTGAGAAACCTGAGATTCTAGCTATGGGAACTGATGTGAGATCTTTGTTCACT

TCTTCGAGCTCGATTCTACTCGAGCGTGCTTTCGTTGCTCGAGAGATTACCTTGTTAAATCCGGTTTGGATCCATTC
CAAGAATACTGGTAAACCGTTTTACGCCATTCTTCATAGGATTGATGTTGGTGTTGTTATTGATTTAGAGCCAGCTA
GAACTGAAGATCCTGCGCTTTCTATTGCTGGTGCTGTTCAATCGCAGAAACTCGCGGTTCGTGCGATTTCTCAGTTA
CAGGCTCTTCCTGGTGGAGATATTAAGCTTTTGTGTGACACTGTCGTGGAAAGTGTGAGGGACTTGACTGGTTAT
GATCGTGTTATGGTTTATAAGTTTCATGAAGATGAGCATGGAGAAGTTGTAGCTGAGAGTAAACGAGATGATTTA
GAGCCTTATATTGGACTGCATTATCCTGCTACTGATATTCCTCAAGCGTCAAGGTTCTTGTTTAAGCAGAACCGTGT
CCGAATGATAGTAGATTGCAATGCCACACCTGTTCTTGTGGTCCAGGACGATAGGCTAACTCAGTCTATGTGCTTG
GTTGGTTCTACTCTTAGGGCTCCTCATGGTTGTCACTCTCAGTATATGGCTAACATGGGATCTATTGCGTCTTTAGC
AATGGCGGTTATAATCAATGGAAATGAAGATGATGGGAGCAATGTAGCTAGTGGAAGAAGCTCGATGAGGCTTT
GGGGTTTGGTTGTTTGCCATCACACTTCTTCTCGCTGCATACCGTTTCCGCTAAGGTATGCTTGTGAGTTTTTGATG
CAGGCTTTCGGTTTACAGTTAAACATGGAATTGCAGTTAGCTTTGCAAATGTCAGAGAAACGCGTTTTGAGAACGC
AGACACTGTTATGTGATATGCTTCTGCGTGACTCGCCTGCTGGAATTGTTACACAGAGTCCCAGTATCATGGACTT
AGTGAAATGTGACGGTGCAGCATTTCTTTACCACGGGAAGTATTACCCGTTGGGTGTTGCTCCTAGTGAAGTTCAG
ATAAAAGATGTTGTGGAGTGGTTGCTTGCGAATCATGCGGATTCAACCGGATTAAGCACTGATAGTTTAGGCGAT
GCGGGGTATCCCGGTGCAGCTGCGTTAGGGGATGCTGTGTGCGGTATGGCAGTTGCATATATCACAAAAAGAGA
CTTTCTTTTTTGGTTTCGATCTCACACTGCGAAAGAAATCAAATGGGGAGGCGCTAAGCATCATCCGGAGGATAAA
GATGATGGGCAACGAATGCATCCTCGTTCGTCCTTTCAGGCTTTTCTTGAAGTTGTTAAGAGCCGGAGTCAGCCAT
GGGAAACTGCGGAAATGGATGCGATTCACTCGCTCCAGCTTATTCTGAGAGACTCTTTTAAAGAATCTGAGGCGG
CTATGAACTCTAAAGTTGTGGATGGTGTGGTTCAGCCATGTAGGGATATGGCGGGGGAACAGGGGATTGATGAG
TTAGGTGCAGTTGCAAGAGAGATGGTTAGGCTCATTGAGACTGCAACTGTTCCTATATTCGCTGTGGATGCCGGA
GGCTGCATCAATGGATGGAACGCTAAGATTGCAGAGTTGACAGGTCTCTCAGTTGAAGAAGCTATGGGGAAGTCT
CTGGTTTCTGATTTAATATACAAAGAGAATGAAGCAACTGTCAATAAGCTTCTTTCTCGTGCTTTGAGAGGGGACG
AGGAAAAGAATGTGGAGGTTAAGCTGAAAACTTTCAGCCCCGAACTACAAGGGAAAGCAGTTTTTGTGGTTGTGA
ATGCTTGTTCCAGCAAGGACTACTTGAACAACATTGTCGGCGTTTGTTTTGTTGGACAAGACGTTACTAGTCAGAA
AATCGTAATGGATAAGTTCATCAACATACAAGGAGATTACAAGGCTATTGTACATAGCCCAAACCCTCTAATCCCG
CCAATTTTTGCTGCTGACGAGAACACGTGCTGCCTGGAATGGAACATGGCGATGGAAAAGCTTACGGGTTGGTCT
CGCAGTGAAGTGATTGGGAAAATGATTGTCGGGGAAGTGTTTGGGAGCTGTTGCATGCTAAAGGGTCCTGATGC
TTTAACCAAGTTCATGATTGTATTGCATAATGCGATTGGTGGCCAAGATACGGATAAGTTCCCTTTCCCATTCTTTG
ACCGCAATGGGAAGTTTGTTCAGGCTCTATTGACTGCAAACAAGCGGGTTAGCCTCGAGGGAAAGGTTATTGGGG
CTTTCTGTTTCTTGCAAATCCCGAGCGAATTCGCTAGCAGCAGGGCTGACCCCAAGAAGAAGAGGAAGGTGTCGC
CAGGGATCCGTCGACTTGACGCGTTGATATCAACAAGTTTGTACAAAAAAGCAGGCTACAAAGAGGCCAGCGGTT
CCGGACGGGCTGACGCATTGGACGATTTTGATCTGGATATGCTGGGAAGTGACGCCCTCGATGATTTTGACCTTG
ACATGCTTGGTTCGGATGCCCTTGATGACTTTGACCTCGACATGCTCGGCAGTGACGCCCTTGATGATTTCGACCT
GGACATGCTGATTAACTCTAGAAGTTCCGGATCTCCGAAAAAGAAACGCAAAGTTGGTAGCCAGTACCTGCCCGA
CACCGACGACCGGCACCGGATCGAGGAAAAGCGGAAGCGGACCTACGAGACATTCAAGAGCATCATGAAGAAGT
CCCCCTTCAGCGGCCCCACCGACCCTAGACCTCCACCTAGAAGAATCGCCGTGCCCAGCAGATCCAGCGCCAGCGT
GCCAAAACCTGCCCCCCAGCCTTACCCCTTCACCAGCAGCCTGAGCACCATCAACTACGACGAGTTCCCTACCATG
GTGTTCCCCAGCGGCCAGATCTCTCAGGCCTCTGCTCTGGCTCCAGCCCCTCCTCAGGTGCTGCCTCAGGCTCCTGC
TCCTGCACCAGCTCCAGCCATGGTGTCTGCACTGGCTCAGGCACCAGCACCCGTGCCTGTGCTGGCTCCTGGACCT
CCACAGGCTGTGGCTCCACCAGCCCCTAAACCTACACAGGCCGGCGAGGGCACACTGTCTGAAGCTCTGCTGCAG
CTGCAGTTCGACGACGAGGATCTGGGAGCCCTGCTGGGAAACAGCACCGATCCTGCCGTGTTCACCGACCTGGCC
AGCGTGGACAACAGCGAGTTCCAGCAGCTGCTGAACCAGGGCATCCCTGTGGCCCCTCACACCACCGAGCCCATG
CTGATGGAATACCCCGAGGCCATCACCCGGCTCGTGACAGGCGCTCAGAGGCCTCCTGATCCAGCTCCTGCCCCTC
TGGGAGCACCAGGCCTGCCTAATGGACTGCTGTCTGGCGACGAGGACTTCAGCTCTATCGCCGATATGGATTTCTC
AGCCTTGCTGGGCTCTGGCAGCGGCAGCCGGGATTCCAGGGAAGGGATGTTTTTGCCGAAGCCTGAGGCCGGCT
CCGCTATTAGTGACGTGTTTGAGGGCCGCGAGGTGTGCCAGCCAAAACGAATCCGGCCATTTCATCCTCCAGGAA
GTCCATGGGCCAACCGCCCACTCCCCGCCAGCCTCGCACCAACACCAACCGGTCCAGTACATGAGCCAGTCGGGT
CACTGACCCCGGCACCAGTCCCTCAGCCACTGGATCCAGCGCCCGCAGTGACTCCCGAGGCCAGTCACCTGTTGG
AGGATCCCGATGAAGAGACGAGCCAGGCTGTCAAAGCCCTTCGGGAGATGGCCGATACTGTGATTCCCCAGAAG
GAAGAGGCTGCAATCTGTGGCCAAATGGACCTTTCCCATCCGCCCCCAAGGGGCCATCTGGATGAGCTGACAACC
ACACTTGAGTCCATGACCGAGGATCTGAACCTGGACTCACCCCTGACCCCGGAATTGAACGAGATTCTGGATACCT
TCCTGAACGACGAGTGCCTCTTGCATGCCATGCATATCAGCACAGGACTGTCCATCTTCGACACATCTCTGTTTTGA

17 - PhyB(1-650)-NLS-Gateway Linker-VPR

ATGGTTTCCGGAGTCGGGGGTAGTGGCGGTGGCCGTGGCGGTGGCCGTGGCGGAGAAGAAGAACCGTCGTCAA
GTCACACTCCTAATAACCGAAGAGGAGGAGAACAAGCTCAATCGTCGGGAACGAAATCTCTCAGACCAAGAAGC
AACACTGAATCAATGAGCAAAGCAATTCAACAGTACACCGTCGACGCAAGACTCCACGCCGTTTTCGAACAATCCG
GCGAATCAGGGAAATCATTCGACTACTCACAATCACTCAAAACGACGACGTACGGTTCCTCTGTACCTGAGCAACA
GATCACAGCTTATCTCTCTCGAATCCAGCGAGGTGGTTACATTCAGCCTTTCGGATGTATGATCGCCGTCGATGAA
TCCAGTTTCCGGATCATCGGTTACAGTGAAAACGCCAGAGAAATGTTAGGGATTATGCCTCAATCTGTTCCTACTCT
TGAGAAACCTGAGATTCTAGCTATGGGAACTGATGTGAGATCTTTGTTCACTTCTTCGAGCTCGATTCTACTCGAGC
GTGCTTTCGTTGCTCGAGAGATTACCTTGTTAAATCCGGTTTGGATCCATTCCAAGAATACTGGTAAACCGTTTTAC
GCCATTCTTCATAGGATTGATGTTGGTGTTGTTATTGATTTAGAGCCAGCTAGAACTGAAGATCCTGCGCTTTCTAT
TGCTGGTGCTGTTCAATCGCAGAAACTCGCGGTTCGTGCGATTTCTCAGTTACAGGCTCTTCCTGGTGGAGATATT
AAGCTTTTGTGTGACACTGTCGTGGAAAGTGTGAGGGACTTGACTGGTTATGATCGTGTTATGGTTTATAAGTTTC
ATGAAGATGAGCATGGAGAAGTTGTAGCTGAGAGTAAACGAGATGATTTAGAGCCTTATATTGGACTGCATTATC
CTGCTACTGATATTCCTCAAGCGTCAAGGTTCTTGTTTAAGCAGAACCGTGTCCGAATGATAGTAGATTGCAATGC
CACACCTGTTCTTGTGGTCCAGGACGATAGGCTAACTCAGTCTATGTGCTTGGTTGGTTCTACTCTTAGGGCTCCTC
ATGGTTGTCACTCTCAGTATATGGCTAACATGGGATCTATTGCGTCTTTAGCAATGGCGGTTATAATCAATGGAAA
TGAAGATGATGGGAGCAATGTAGCTAGTGGAAGAAGCTCGATGAGGCTTTGGGGTTTGGTTGTTTGCCATCACAC
TTCTTCTCGCTGCATACCGTTTCCGCTAAGGTATGCTTGTGAGTTTTTGATGCAGGCTTTCGGTTTACAGTTAAACAT
GGAATTGCAGTTAGCTTTGCAAATGTCAGAGAAACGCGTTTTGAGAACGCAGACACTGTTATGTGATATGCTTCTG
CGTGACTCGCCTGCTGGAATTGTTACACAGAGTCCCAGTATCATGGACTTAGTGAAATGTGACGGTGCAGCATTTC
TTTACCACGGGAAGTATTACCCGTTGGGTGTTGCTCCTAGTGAAGTTCAGATAAAAGATGTTGTGGAGTGGTTGCT
TGCGAATCATGCGGATTCAACCGGATTAAGCACTGATAGTTTAGGCGATGCGGGGTATCCCGGTGCAGCTGCGTT
AGGGGATGCTGTGTGCGGTATGGCAGTTGCATATATCACAAAAAGAGACTTTCTTTTTTGGTTTCGATCTCACACT
GCGAAAGAAATCAAATGGGGAGGCGCTAAGCATCATCCGGAGGATAAAGATGATGGGCAACGAATGCATCCTCG
TTCGTCCTTTCAGGCTTTTCTTGAAGTTGTTAAGAGCCGGAGTCAGCCATGGGAAACTGCGGAAATGGATGCGATT
CACTCGCTCCAGCTTATTCTGAGAGACTCTTTTAAAGAATCTGAGGCGGCTATGAACTCTAAAGTTGTGGATGGTG
TGGTTCAGCCATGTAGGGATATGGCGGGGGAACAGGGGATTGATGAGTTAGGTGCTAGCAGCAGGGCTGACCCC
AAGAAGAAGAGGAAGGTGTCGCCAGGGATCCGTCGACTTGACGCGTTGATATCAACAAGTTTGTACAAAAAAGC
AGGCTACAAAGAGGCCAGCGGTTCCGGACGGGCTGACGCATTGGACGATTTTGATCTGGATATGCTGGGAAGTG
ACGCCCTCGATGATTTTGACCTTGACATGCTTGGTTCGGATGCCCTTGATGACTTTGACCTCGACATGCTCGGCAGT
GACGCCCTTGATGATTTCGACCTGGACATGCTGATTAACTCTAGAAGTTCCGGATCTCCGAAAAAGAAACGCAAA
GTTGGTAGCCAGTACCTGCCCGACACCGACGACCGGCACCGGATCGAGGAAAAGCGGAAGCGGACCTACGAGAC
ATTCAAGAGCATCATGAAGAAGTCCCCCTTCAGCGGCCCCACCGACCCTAGACCTCCACCTAGAAGAATCGCCGTG
CCCAGCAGATCCAGCGCCAGCGTGCCAAAACCTGCCCCCCAGCCTTACCCCTTCACCAGCAGCCTGAGCACCATCA
ACTACGACGAGTTCCCTACCATGGTGTTCCCCAGCGGCCAGATCTCTCAGGCCTCTGCTCTGGCTCCAGCCCCTCCT
CAGGTGCTGCCTCAGGCTCCTGCTCCTGCACCAGCTCCAGCCATGGTGTCTGCACTGGCTCAGGCACCAGCACCCG
TGCCTGTGCTGGCTCCTGGACCTCCACAGGCTGTGGCTCCACCAGCCCCTAAACCTACACAGGCCGGCGAGGGCA
CACTGTCTGAAGCTCTGCTGCAGCTGCAGTTCGACGACGAGGATCTGGGAGCCCTGCTGGGAAACAGCACCGATC
CTGCCGTGTTCACCGACCTGGCCAGCGTGGACAACAGCGAGTTCCAGCAGCTGCTGAACCAGGGCATCCCTGTGG
CCCCTCACACCACCGAGCCCATGCTGATGGAATACCCCGAGGCCATCACCCGGCTCGTGACAGGCGCTCAGAGGC
CTCCTGATCCAGCTCCTGCCCCTCTGGGAGCACCAGGCCTGCCTAATGGACTGCTGTCTGGCGACGAGGACTTCAG
CTCTATCGCCGATATGGATTTCTCAGCCTTGCTGGGCTCTGGCAGCGGCAGCCGGGATTCCAGGGAAGGGATGTT
TTTGCCGAAGCCTGAGGCCGGCTCCGCTATTAGTGACGTGTTTGAGGGCCGCGAGGTGTGCCAGCCAAAACGAAT
CCGGCCATTTCATCCTCCAGGAAGTCCATGGGCCAACCGCCCACTCCCCGCCAGCCTCGCACCAACACCAACCGGT
CCAGTACATGAGCCAGTCGGGTCACTGACCCCGGCACCAGTCCCTCAGCCACTGGATCCAGCGCCCGCAGTGACT
CCCGAGGCCAGTCACCTGTTGGAGGATCCCGATGAAGAGACGAGCCAGGCTGTCAAAGCCCTTCGGGAGATGGC
CGATACTGTGATTCCCCAGAAGGAAGAGGCTGCAATCTGTGGCCAAATGGACCTTTCCCATCCGCCCCCAAGGGG
CCATCTGGATGAGCTGACAACCACACTTGAGTCCATGACCGAGGATCTGAACCTGGACTCACCCCTGACCCCGGA
ATTGAACGAGATTCTGGATACCTTCCTGAACGACGAGTGCCTCTTGCATGCCATGCATATCAGCACAGGACTGTCC
ATCTTCGACACATCTCTGTTTTGA

19 - dCas9-NLS-GS Linker-PIF6

ATGGACAAGAAGTACTCCATTGGGCTCGCTATCGGCACAAACAGCGTCGGCTGGGCCGTCATTACGGACGAGTAC
AAGGTGCCGAGCAAAAAATTCAAAGTTCTGGGCAATACCGATCGCCACAGCATAAAGAAGAACCTCATTGGCGCC
CTCCTGTTCGACTCCGGGGAGACGGCCGAAGCCACGCGGCTCAAAAGAACAGCACGGCGCAGATATACCCGCAG
AAAGAATCGGATCTGCTACCTGCAGGAGATCTTTAGTAATGAGATGGCTAAGGTGGATGACTCTTTCTTCCATAGG
CTGGAGGAGTCCTTTTTGGTGGAGGAGGATAAAAAGCACGAGCGCCACCCAATCTTTGGCAATATCGTGGACGA
GGTGGCGTACCATGAAAAGTACCCAACCATATATCATCTGAGGAAGAAGCTTGTAGACAGTACTGATAAGGCTGA
CTTGCGGTTGATCTATCTCGCGCTGGCGCATATGATCAAATTTCGGGGACACTTCCTCATCGAGGGGGACCTGAAC
CCAGACAACAGCGATGTCGACAAACTCTTTATCCAACTGGTTCAGACTTACAATCAGCTTTTCGAAGAGAACCCGA
TCAACGCATCCGGAGTTGACGCCAAAGCAATCCTGAGCGCTAGGCTGTCCAAATCCCGGCGGCTCGAAAACCTCA
TCGCACAGCTCCCTGGGGAGAAGAAGAACGGCCTGTTTGGTAATCTTATCGCCCTGTCACTCGGGCTGACCCCCAA
CTTTAAATCTAACTTCGACCTGGCCGAAGATGCCAAGCTTCAACTGAGCAAAGACACCTACGATGATGATCTCGAC
AATCTGCTGGCCCAGATCGGCGACCAGTACGCAGACCTTTTTTTGGCGGCAAAGAACCTGTCAGACGCCATTCTGC
TGAGTGATATTCTGCGAGTGAACACGGAGATCACCAAAGCTCCGCTGAGCGCTAGTATGATCAAGCGCTATGATG
AGCACCACCAAGACTTGACTTTGCTGAAGGCCCTTGTCAGACAGCAACTGCCTGAGAAGTACAAGGAAATTTTCTT
CGATCAGTCTAAAAATGGCTACGCCGGATACATTGACGGCGGAGCAAGCCAGGAGGAATTTTACAAATTTATTAA
GCCCATCTTGGAAAAAATGGACGGCACCGAGGAGCTGCTGGTAAAGCTTAACAGAGAAGATCTGTTGCGCAAAC
AGCGCACTTTCGACAATGGAAGCATCCCCCACCAGATTCACCTGGGCGAACTGCACGCTATCCTCAGGCGGCAAG
AGGATTTCTACCCCTTTTTGAAAGATAACAGGGAAAAGATTGAGAAAATCCTCACATTTCGGATACCCTACTATGT
AGGCCCCCTCGCCCGGGGAAATTCCAGATTCGCGTGGATGACTCGCAAATCAGAAGAGACCATCACTCCCTGGAA
CTTCGAGGAAGTCGTGGATAAGGGGGCCTCTGCCCAGTCCTTCATCGAAAGGATGACTAACTTTGATAAAAATCT
GCCTAACGAAAAGGTGCTTCCTAAACACTCTCTGCTGTACGAGTACTTCACAGTTTATAACGAGCTCACCAAGGTC
AAATACGTCACAGAAGGGATGAGAAAGCCAGCATTCCTGTCTGGAGAGCAGAAGAAAGCTATCGTGGACCTCCTC
TTCAAGACGAACCGGAAAGTTACCGTGAAACAGCTCAAAGAAGACTATTTCAAAAAGATTGAATGTTTCGACTCTG
TTGAAATCAGCGGAGTGGAGGATCGCTTCAACGCATCCCTGGGAACGTATCACGATCTCCTGAAAATCATTAAAG
ACAAGGACTTCCTGGACAATGAGGAGAACGAGGACATTCTTGAGGACATTGTCCTCACCCTTACGTTGTTTGAAG
ATAGGGAGATGATTGAAGAACGCTTGAAAACTTACGCTCATCTCTTCGACGACAAAGTCATGAAACAGCTCAAGA
GGCGCCGATATACAGGATGGGGGCGGCTGTCAAGAAAACTGATCAATGGGATCCGAGACAAGCAGAGTGGAAA
GACAATCCTGGATTTTCTTAAGTCCGATGGATTTGCCAACCGGAACTTCATGCAGTTGATCCATGATGACTCTCTCA
CCTTTAAGGAGGACATCCAGAAAGCACAAGTTTCTGGCCAGGGGGACAGTCTTCACGAGCACATCGCTAATCTTG
CAGGTAGCCCAGCTATCAAAAAGGGAATACTGCAGACCGTTAAGGTCGTGGATGAACTCGTCAAAGTAATGGGA
AGGCATAAGCCCGAGAATATCGTTATCGAGATGGCCCGAGAGAACCAAACTACCCAGAAGGGACAGAAGAACAG
TAGGGAAAGGATGAAGAGGATTGAAGAGGGTATAAAAGAACTGGGGTCCCAAATCCTTAAGGAACACCCAGTTG
AAAACACCCAGCTTCAGAATGAGAAGCTCTACCTGTACTACCTGCAGAACGGCAGGGACATGTACGTGGATCAGG
AACTGGACATCAATCGGCTCTCCGACTACGACGTGGCTGCTATCGTGCCCCAGTCTTTTCTCAAAGATGATTCTATT
GATAATAAAGTGTTGACAAGATCCGATAAAGCTAGAGGGAAGAGTGATAACGTCCCCTCAGAAGAAGTTGTCAA
GAAAATGAAAAATTATTGGCGGCAGCTGCTGAACGCCAAACTGATCACACAACGGAAGTTCGATAATCTGACTAA
GGCTGAACGAGGTGGCCTGTCTGAGTTGGATAAAGCCGGCTTCATCAAAAGGCAGCTTGTTGAGACACGCCAGAT
CACCAAGCACGTGGCCCAAATTCTCGATTCACGCATGAACACCAAGTACGATGAAAATGACAAACTGATTCGAGA
GGTGAAAGTTATTACTCTGAAGTCTAAGCTGGTCTCAGATTTCAGAAAGGACTTTCAGTTTTATAAGGTGAGAGAG
ATCAACAATTACCACCATGCGCATGATGCCTACCTGAATGCAGTGGTAGGCACTGCACTTATCAAAAAATATCCCA
AGCTTGAATCTGAATTTGTTTACGGAGACTATAAAGTGTACGATGTTAGGAAAATGATCGCAAAGTCTGAGCAGG
AAATAGGCAAGGCCACCGCTAAGTACTTCTTTTACAGCAATATTATGAATTTTTTCAAGACCGAGATTACACTGGCC
AATGGAGAGATTCGGAAGCGACCACTTATCGAAACAAACGGAGAAACAGGAGAAATCGTGTGGGACAAGGGTA
GGGATTTCGCGACAGTCCGGAAGGTCCTGTCCATGCCGCAGGTGAACATCGTTAAAAAGACCGAAGTACAGACC
GGAGGCTTCTCCAAGGAAAGTATCCTCCCGAAAAGGAACAGCGACAAGCTGATCGCACGCAAAAAAGATTGGGA
CCCCAAGAAATACGGCGGATTCGATTCTCCTACAGTCGCTTACAGTGTACTGGTTGTGGCCAAAGTGGAGAAAGG
GAAGTCTAAAAAACTCAAAAGCGTCAAGGAACTGCTGGGCATCACAATCATGGAGCGATCAAGCTTCGAAAAAAA
CCCCATCGACTTTCTCGAGGCGAAAGGATATAAAGAGGTCAAAAAAGACCTCATCATTAAGCTTCCCAAGTACTCT
CTCTTTGAGCTTGAAAACGGCCGGAAACGAATGCTCGCTAGTGCGGGCGAGCTGCAGAAAGGTAACGAGCTGGC
ACTGCCCTCTAAATACGTTAATTTCTTGTATCTGGCCAGCCACTATGAAAAGCTCAAAGGGTCTCCCGAAGATAAT
GAGCAGAAGCAGCTGTTCGTGGAACAACACAAACACTACCTTGATGAGATCATCGAGCAAATAAGCGAATTCTCC
AAAAGAGTGATCCTCGCCGACGCTAACCTCGATAAGGTGCTTTCTGCTTACAATAAGCACAGGGATAAGCCCATCA

GGGAGCAGGCAGAAAACATTATCCACTTGTTTACTCTGACCAACTTGGGCGCGCCTGCAGCCTTCAAGTACTTCGA
CACCACCATAGACAGAAAGCGGTACACCTCTACAAAGGAGGTCCTGGACGCCACACTGATTCATCAGTCAATTAC
GGGGCTCTATGAAACAAGAATCGACCTCTCTCAGCTCGGTGGAGACAGCAGGGCTGACCCCAAGAAGAAGAGGA
AGGTGACCGGTGATTCCGCCGGGTCCGCAGGTTCAGCTGGCATGATGTTCTTACCAACCGATTATTGTTGCAGGTT
AAGCGATCAAGAGTATATGGAGCTTGTGTTTGAGAATGGCCAGATTCTTGCAAAGGGCCAAAGATCCAACGTTTC
TCTGCATAATCAACGTACCAAATCGATCATGGATTTGTATGAGGCAGAGTATAACGAGGATTTCATGAAGAGTATC
ATCCATGGTGGTGGTGGTGCCATCACAAATCTCGGGGACACGCAGGTTGTTCCACAAAGTCATGTTGCTGCTGCCC
ATGAAACAAACATGTTGGAAAGCAATAAACATGTTGACTAA

20 - PIF6-GS-dCas9-NLS-GS Linker-PIF6

ATGATGTTCTTACCAACCGATTATTGTTGCAGGTTAAGCGATCAAGAGTATATGGAGCTTGTGTTTGAGAATGGCC
AGATTCTTGCAAAGGGCCAAAGATCCAACGTTTCTCTGCATAATCAACGTACCAAATCGATCATGGATTTGTATGA
GGCAGAGTATAACGAGGATTTCATGAAGAGTATCATCCATGGTGGTGGTGGTGCCATCACAAATCTCGGGGACAC
GCAGGTTGTTCCACAAAGTCATGTTGCTGCTGCCCATGAAACAAACATGTTGGAAAGCAATAAACATGTTGACGG
ATCTTCTGGAGGAAGCATGGATAAGAAATACTCAATAGGCTTAGCTATCGGCACAAATAGCGTCGGATGGGCGGT
GATCACTGATGAATATAAGGTTCCGTCTAAAAAGTTCAAGGTTCTGGGAAATACAGACCGCCACAGTATCAAAAA
AAATCTTATAGGGGCTCTTTTATTTGACAGTGGAGAGACAGCGGAAGCGACTCGTCTCAAACGGACAGCTCGTAG
AAGGTATACACGTCGGAAGAATCGTATTTGTTATCTACAGGAGATTTTTTCAAATGAGATGGCGAAAGTAGATGA
TAGTTTCTTTCATCGACTTGAAGAGTCTTTTTTGGTGGAAGAAGACAAGAAGCATGAACGTCATCCTATTTTTGGAA
ATATAGTAGATGAAGTTGCTTATCATGAGAAATATCCAACTATCTATCATCTGCGAAAAAAAATTGGTAGATTCTACT
GATAAAGCGGATTTGCGCTTAATCTATTTGGCCTTAGCGCATATGATTAAGTTTCGTGGTCATTTTTTGATTGAGGG
AGATTTAAATCCTGATAATAGTGATGTGGACAAACTATTTATCCAGTTGGTACAAACCTACAATCAATTATTTGAAG
AAAACCCTATTAACGCAAGTGGAGTAGATGCTAAAGCGATTCTTTCTGCACGATTGAGTAAATCAAGACGATTAGA
AAATCTCATTGCTCAGCTCCCCGGTGAGAAGAAAAATGGCTTATTTGGGAATCTCATTGCTTTGTCATTGGGTTTGA
CCCCTAATTTTAAATCAAATTTTGATTTGGCAGAAGATGCTAAATTACAGCTTTCAAAAGATACTTACGATGATGAT
TTAGATAATTTATTGGCGCAAATTGGAGATCAATATGCTGATTTGTTTTTGGCAGCTAAGAATTTATCAGATGCTAT
TTTACTTTCAGATATCCTAAGAGTAAATACTGAAATAACTAAGGCTCCCCTATCAGCTTCAATGATTAAACGCTACG
ATGAACATCATCAAGACTTGACTCTTTTAAAAGCTTTAGTTCGACAACAACTTCCAGAAAAGTATAAAGAAATCTTT
TTTGATCAATCAAAAAACGGATATGCAGGTTATATTGATGGGGGAGCTAGCCAAGAAGAATTTTATAAATTTATCA
AACCAATTTTAGAAAAAATGGATGGTACTGAGGAATTATTGGTGAAACTAAATCGTGAAGATTTGCTGCGCAAGC
AACGGACCTTTGACAACGGCTCTATTCCCCATCAAATTCACTTGGGTGAGCTGCATGCTATTTTGAGAAGACAAGA
AGACTTTTATCCATTTTTAAAAGACAATCGTGAGAAGATTGAAAAAATCTTGACTTTTCGAATTCCTTATTATGTTG
GTCCATTGGCGCGTGGCAATAGTCGTTTTGCATGGATGACTCGGAAGTCTGAAGAAACAATTACCCCATGGAATTT
TGAAGAAGTTGTCGATAAAGGTGCTTCAGCTCAATCATTTATTGAACGCATGACAAACTTTGATAAAAATCTTCCA
AATGAAAAAGTACTACCAAAACATAGTTTGCTTTATGAGTATTTTACGGTTTATAACGAATTGACAAAGGTCAAAT
ATGTTACTGAAGGAATGCGAAAACCAGCATTTCTTTCAGGTGAACAGAAGAAAGCCATTGTTGATTTACTCTTCAA
AACAAATCGAAAAGTAACCGTTAAGCAATTAAAAGAAGATTATTTCAAAAAAATAGAATGTTTTGATAGTGTTGAA
ATTTCAGGAGTTGAAGATAGATTTAATGCTTCATTAGGTACCTACCATGATTTGCTAAAAATTATTAAAGATAAAG
ATTTTTTGGATAATGAAGAAAATGAAGATATCTTAGAGGATATTGTTTTAACATTGACCTTATTTGAAGATAGGGA
GATGATTGAGGAAAGACTTAAAACATATGCTCACCTCTTTGATGATAAGGTGATGAAACAGCTTAAACGTCGCCGT
TATACTGGTTGGGGACGTTTGTCTCGAAAATTGATTAATGGTATTAGGGATAAGCAATCTGGCAAAACAATATTAG
ATTTTTTGAAATCAGATGGTTTTGCCAATCGCAATTTTATGCAGCTGATCCATGATGATAGTTTGACATTTAAAGAA
GACATTCAAAAAGCACAAGTGTCTGGACAAGGCGATAGTTTACATGAACATATTGCAAATTTAGCTGGTAGCCCT
GCTATTAAAAAAGGTATTTTACAGACTGTAAAAGTTGTTGATGAATTGGTCAAAGTAATGGGGCGGCATAAGCCA
GAAAATATCGTTATTGAAATGGCACGTGAAAATCAGACAACTCAAAAGGGCCAGAAAAATTCGCGAGAGCGTAT
GAAACGAATCGAAGAAGGTATCAAAGAATTAGGAAGTCAGATTCTTAAAGAGCATCCTGTTGAAAATACTCAATT
GCAAAATGAAAAGCTCTATCTCTATTATCTCCAAAATGGAAGAGACATGTATGTGGACCAAGAATTAGATATTAAT
CGTTTAAGTGATTATGATGTCGATGCCATTGTTCCACAAAGTTTCCTTAAAGACGATTCAATAGACAATAAGGTCTT
AACGCGTTCTGATAAAAATCGTGGTAAATCGGATAACGTTCCAAGTGAAGAAGTAGTCAAAAAGATGAAAAACTA
TTGGAGACAACTTCTAAACGCCAAGTTAATCACTCAACGTAAGTTTGATAATTTAACGAAAGCTGAACGTGGAGGT
TTGAGTGAACTTGATAAAGCTGGTTTTATCAAACGCCAATTGGTTGAAACTCGCCAAATCACTAAGCATGTGGCAC
AAATTTTGGATAGTCGCATGAATACTAAATACGATGAAAATGATAAACTTATTCGAGAGGTTAAAGTGATTACCTT
AAAATCTAAATTAGTTTCTGACTTCCGAAAAGATTTCCAATTCTATAAAGTACGTGAGATTAACAATTACCATCATG

CCCATGATGCGTATCTAAATGCCGTCGTTGGAACTGCTTTGATTAAGAAATATCCAAAACTTGAATCGGAGTTTGT
CTATGGTGATTATAAAGTTTATGATGTTCGTAAAATGATTGCTAAGTCTGAGCAAGAAATAGGCAAAGCAACCGC
AAAATATTTCTTTTACTCTAATATCATGAACTTCTTCAAAACAGAAATTACACTTGCAAATGGAGAGATTCGCAAAC
GCCCTCTAATCGAAACTAATGGGGAAACTGGAGAAATTGTCTGGGATAAAGGGCGAGATTTTGCCACAGTGCGCA
AAGTATTGTCCATGCCCCAAGTCAATATTGTCAAGAAAACAGAAGTACAGACAGGCGGATTCTCCAAGGAGTCAA
TTTTACCAAAAAGAAATTCGGACAAGCTTATTGCTCGTAAAAAAGACTGGGATCCAAAAAAATATGGTGGTTTTGA
TAGTCCAACGGTAGCTTATTCAGTCCTAGTGGTTGCTAAGGTGGAAAAAGGGAAATCGAAGAAGTTAAAATCCGT
TAAAGAGTTACTAGGGATCACAATTATGGAAAGAAGTTCCTTTGAAAAAAATCCGATTGACTTTTTAGAAGCTAAA
GGATATAAGGAAGTTAAAAAAGACTTAATCATTAAACTACCTAAATATAGTCTTTTTGAGTTAGAAAACGGTCGTA
AACGGATGCTGGCTAGTGCCGGAGAATTACAAAAAGGAAATGAGCTGGCTCTGCCAAGCAAATATGTGAATTTTT
TATATTTAGCTAGTCATTATGAAAAGTTGAAGGGTAGTCCAGAAGATAACGAACAAAAACAATTGTTTGTGGAGC
AGCATAAGCATTATTTAGATGAGATTATTGAGCAAATCAGTGAATTTTCTAAGCGTGTTATTTTAGCAGATGCCAAT
TTAGATAAAGTTCTTAGTGCATATAACAAACATAGAGACAAACCAATACGTGAACAAGCAGAAAATATTATTCATT
TATTTACGTTGACGAATCTTGGAGCTCCCGCTGCTTTTAAATATTTTGATACAACAATTGATCGTAAACGATATACG
TCTACAAAAGAAGTTTTAGATGCCACTCTTATCCATCAATCCATCACTGGTCTTTATGAAACACGCATTGATTTGAG
TCAGCTAGGAGGTGACCCAATTGCCGGATCCAAGGCTAGCCCGAAAAAGAAACGCAAAGTTACCGGTTCTGGAG
GAAGCATGATGTTCTTACCAACCGATTATTGTTGCAGGTTAAGCGATCAAGAGTATATGGAGCTTGTGTTTGAGAA
TGGCCAGATTCTTGCAAAGGGCCAAAGATCCAACGTTTCTCTGCATAATCAACGTACCAAATCGATCATGGATTTG
TATGAGGCAGAGTATAACGAGGATTTCATGAAGAGTATCATCCATGGTGGTGGTGGTGCCATCACAAATCTCGGG
GACACGCAGGTTGTTCCACAAAGTCATGTTGCTGCTGCCCATGAAACAAACATGTTGGAAAGCAATAAACATGTT
GACTAA

22 - PhyB(1-650)-GS Linker-VPR

ATGGTTTCCGGAGTCGGGGGTAGTGGCGGTGGCCGTGGCGGTGGCCGTGGCGGAGAAGAAGAACCGTCGTCAA
GTCACACTCCTAATAACCGAAGAGGAGGAGAACAAGCTCAATCGTCGGGAACGAAATCTCTCAGACCAAGAAGC
AACACTGAATCAATGAGCAAAGCAATTCAACAGTACACCGTCGACGCAAGACTCCACGCCGTTTTCGAACAATCCG
GCGAATCAGGGAAATCATTCGACTACTCACAATCACTCAAAACGACGACGTACGGTTCCTCTGTACCTGAGCAACA
GATCACAGCTTATCTCTCTCGAATCCAGCGAGGTGGTTACATTCAGCCTTTCGGATGTATGATCGCCGTCGATGAA
TCCAGTTTCCGGATCATCGGTTACAGTGAAAACGCCAGAGAAATGTTAGGGATTATGCCTCAATCTGTTCCTACTCT
TGAGAAACCTGAGATTCTAGCTATGGGAACTGATGTGAGATCTTTGTTCACTTCTTCGAGCTCGATTCTACTCGAGC
GTGCTTTCGTTGCTCGAGAGATTACCTTGTTAAATCCGGTTTGGATCCATTCCAAGAATACTGGTAAACCGTTTTAC
GCCATTCTTCATAGGATTGATGTTGGTGTTGTTATTGATTTAGAGCCAGCTAGAACTGAAGATCCTGCGCTTTCTAT
TGCTGGTGCTGTTCAATCGCAGAAACTCGCGGTTCGTGCGATTTCTCAGTTACAGGCTCTTCCTGGTGGAGATATT
AAGCTTTTGTGTGACACTGTCGTGGAAAGTGTGAGGGACTTGACTGGTTATGATCGTGTTATGGTTTATAAGTTTC
ATGAAGATGAGCATGGAGAAGTTGTAGCTGAGAGTAAACGAGATGATTTAGAGCCTTATATTGGACTGCATTATC
CTGCTACTGATATTCCTCAAGCGTCAAGGTTCTTGTTTAAGCAGAACCGTGTCCGAATGATAGTAGATTGCAATGC
CACACCTGTTCTTGTGGTCCAGGACGATAGGCTAACTCAGTCTATGTGCTTGGTTGGTTCTACTCTTAGGGCTCCTC
ATGGTTGTCACTCTCAGTATATGGCTAACATGGGATCTATTGCGTCTTTAGCAATGGCGGTTATAATCAATGGAAA
TGAAGATGATGGGAGCAATGTAGCTAGTGGAAGAAGCTCGATGAGGCTTTGGGGTTTGGTTGTTTGCCATCACAC
TTCTTCTCGCTGCATACCGTTTCCGCTAAGGTATGCTTGTGAGTTTTTGATGCAGGCTTTCGGTTTACAGTTAAACAT
GGAATTGCAGTTAGCTTTGCAAATGTCAGAGAAACGCGTTTTGAGAACGCAGACACTGTTATGTGATATGCTTCTG
CGTGACTCGCCTGCTGGAATTGTTACACAGAGTCCCAGTATCATGGACTTAGTGAAATGTGACGGTGCAGCATTTC
TTTACCACGGGAAGTATTACCCGTTGGGTGTTGCTCCTAGTGAAGTTCAGATAAAAGATGTTGTGGAGTGGTTGCT
TGCGAATCATGCGGATTCAACCGGATTAAGCACTGATAGTTTAGGCGATGCGGGGTATCCCGGTGCAGCTGCGTT
AGGGGATGCTGTGTGCGGTATGGCAGTTGCATATATCACAAAAAGAGACTTTCTTTTTTGGTTTCGATCTCACACT
GCGAAAGAAATCAAATGGGGAGGCGCTAAGCATCATCCGGAGGATAAAGATGATGGGCAACGAATGCATCCTCG
TTCGTCCTTTCAGGCTTTTCTTGAAGTTGTTAAGAGCCGGAGTCAGCCATGGGAAACTGCGGAAATGGATGCGATT
CACTCGCTCCAGCTTATTCTGAGAGACTCTTTTAAAGAATCTGAGGCGGCTATGAACTCTAAAGTTGTGGATGGTG
TGGTTCAGCCATGTAGGGATATGGCGGGGGAACAGGGGATTGATGAGTTAGGTGAATTCGATAGTGCTGGTAGT
GCTGGTAGTGCTGGTAGCGGCCGCGGTTCCGGACGGGCTGACGCATTGGACGATTTTGATCTGGATATGCTGGG
AAGTGACGCCCTCGATGATTTTGACCTTGACATGCTTGGTTCGGATGCCCTTGATGACTTTGACCTCGACATGCTCG
GCAGTGACGCCCTTGATGATTTCGACCTGGACATGCTGATTAACTCTAGAAGTTCCGGATCTCCGAAAAAGAAACG
CAAAGTTGGTAGCCAGTACCTGCCCGACACCGACGACCGGCACCGGATCGAGGAAAAGCGGAAGCGGACCTACG

AGACATTCAAGAGCATCATGAAGAAGTCCCCCTTCAGCGGCCCCACCGACCCTAGACCTCCACCTAGAAGAATCGC
CGTGCCCAGCAGATCCAGCGCCAGCGTGCCAAAACCTGCCCCCCAGCCTTACCCCTTCACCAGCAGCCTGAGCACC
ATCAACTACGACGAGTTCCCTACCATGGTGTTCCCCAGCGGCCAGATCTCTCAGGCCTCTGCTCTGGCTCCAGCCCC
TCCTCAGGTGCTGCCTCAGGCTCCTGCTCCTGCACCAGCTCCAGCCATGGTGTCTGCACTGGCTCAGGCACCAGCA
CCCGTGCCTGTGCTGGCTCCTGGACCTCCACAGGCTGTGGCTCCACCAGCCCCTAAACCTACACAGGCCGGCGAG
GGCACACTGTCTGAAGCTCTGCTGCAGCTGCAGTTCGACGACGAGGATCTGGGAGCCCTGCTGGGAAACAGCACC
GATCCTGCCGTGTTCACCGACCTGGCCAGCGTGGACAACAGCGAGTTCCAGCAGCTGCTGAACCAGGGCATCCCT
GTGGCCCCTCACACCACCGAGCCCATGCTGATGGAATACCCCGAGGCCATCACCCGGCTCGTGACAGGCGCTCAG
AGGCCTCCTGATCCAGCTCCTGCCCCTCTGGGAGCACCAGGCCTGCCTAATGGACTGCTGTCTGGCGACGAGGAC
TTCAGCTCTATCGCCGATATGGATTTCTCAGCCTTGCTGGGCTCTGGCAGCGGCAGCCGGGATTCCAGGGAAGGG
ATGTTTTTGCCGAAGCCTGAGGCCGGCTCCGCTATTAGTGACGTGTTTGAGGGCCGCGAGGTGTGCCAGCCAAAA
CGAATCCGGCCATTTCATCCTCCAGGAAGTCCATGGGCCAACCGCCCACTCCCCGCCAGCCTCGCACCAACACCAA
CCGGTCCAGTACATGAGCCAGTCGGGTCACTGACCCCGGCACCAGTCCCTCAGCCACTGGATCCAGCGCCCGCAG
TGACTCCCGAGGCCAGTCACCTGTTGGAGGATCCCGATGAAGAGACGAGCCAGGCTGTCAAAGCCCTTCGGGAG
ATGGCCGATACTGTGATTCCCCAGAAGGAAGAGGCTGCAATCTGTGGCCAAATGGACCTTTCCCATCCGCCCCCAA
GGGGCCATCTGGATGAGCTGACAACCACACTTGAGTCCATGACCGAGGATCTGAACCTGGACTCACCCCTGACCC
CGGAATTGAACGAGATTCTGGATACCTTCCTGAACGACGAGTGCCTCTTGCATGCCATGCATATCAGCACAGGACT
GTCCATCTTCGACACATCTCTGTTTTGA

6.2.3 GFP Reporter and PCB Controls

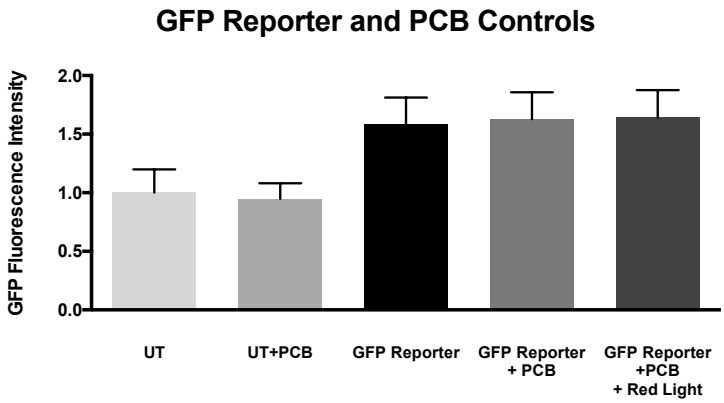

GFP Reporter characterization. In order to be certain that the addition of PCB in the culture media was not influencing its fluorescence signal, the GFP reporter was transfected in HEK 293 cells and the fluorescence level was analysed by flow cytometry. The following conditions were considered: UT, UT+PCB, GFP Reporter, GFP Reporter+PCB and GFP Reporter+PCB+Red Light. UT, un-transfected cells; PCB, *PhycoCyanoBilin.*

References

1. Pereira, D.A. and J.A. Williams, *Origin and evolution of high throughput screening.* British Journal of Pharmacology, 2007. **152**(1): p. 53-61.
2. Taylor, D.L., *Past, Present, and Future of High Content Screening and the Field of Cellomics*, in *High Content Screening: A Powerful Approach to Systems Cell Biology and Drug Discovery*, D.L. Taylor, J.R. Haskins, and K.A. Giuliano, Editors. 2006, Humana Press: Totowa, NJ. p. 3-18.
3. Singh, S., A.E. Carpenter, and A. Genovesio, *Increasing the Content of High-Content Screening:An Overview.* Journal of Biomolecular Screening, 2014. **19**(5): p. 640-650.
4. Boutros, M., F. Heigwer, and C. Laufer, *Microscopy-Based High-Content Screening.* Cell, 2015. **163**(6): p. 1314-1325.
5. Lang, P., et al., *Cellular imaging in drug discovery.* Nature Reviews Drug Discovery, 2006. **5**: p. 343.
6. Hood, L. and R.M. Perlmutter, *The impact of systems approaches on biological problems in drug discovery.* Nature Biotechnology, 2004. **22**: p. 1215.
7. Mattiazzi Usaj, M., et al., *High-Content Screening for Quantitative Cell Biology.* Trends in Cell Biology, 2016. **26**(8): p. 598-611.
8. Zanella, F., J.B. Lorens, and W. Link, *High content screening: seeing is believing.* Trends in Biotechnology, 2010. **28**(5): p. 237-245.
9. Daub, A., P. Sharma, and S. Finkbeiner, *High-Content Screening of Primary Neurons: Ready for Prime Time.* Current opinion in neurobiology, 2009. **19**(5): p. 537-543.
10. Lee, J.A. and E.L. Berg, *Neoclassic Drug Discovery:The Case for Lead Generation Using Phenotypic and Functional Approaches.* Journal of Biomolecular Screening, 2013. **18**(10): p. 1143-1155.
11. Haney, S.A., et al., *High-content screening moves to the front of the line.* Drug Discovery Today, 2006. **11**(19): p. 889-894.
12. Bickle, M., *The beautiful cell: high-content screening in drug discovery.* Analytical and Bioanalytical Chemistry, 2010. **398**(1): p. 219-226.
13. Alsehli, H., et al., *The emerging importance of high content screening for future therapeutics.* Journal of Microscopy and Ultrastructure, 2017.
14. Kenny, H.A., et al., *Quantitative high throughput screening using a primary human three-dimensional organotypic culture predicts in vivo efficacy.* Nature Communications, 2015. **6**: p. 6220.
15. Wang, J., et al., *Anti-gastric cancer activity in three-dimensional tumor spheroids of bufadienolides.* Scientific Reports, 2016. **6**: p. 24772.
16. Fang, Y. and R.M. Eglen, *Three-Dimensional Cell Cultures in Drug Discovery and Development.* Slas Discovery, 2017. **22**(5): p. 456-472.
17. Page, H., P. Flood, and E. Reynaud, *Three-dimensional tissue cultures: current trends and beyond.* Cell and Tissue Research, 2013. **352**(1): p. 123-131.
18. Pampaloni, F., E.G. Reynaud, and E.H.K. Stelzer, *The third dimension bridges the gap between cell culture and live tissue.* Nat Rev Mol Cell Biol, 2007. **8**(10): p. 839-845.

19. Li, S., et al., *Genomic analysis of smooth muscle cells in three-dimensional collagen matrix.* The FASEB Journal, 2002. **17**(1): p. 97-99.
20. Krausz, E., et al., *Translation of a Tumor Microenvironment Mimicking 3D Tumor Growth Co-culture Assay Platform to High-Content Screening.* Journal of Biomolecular Screening, 2013. **18**(1): p. 54-66.
21. Pampaloni, F., N. Ansari, and E.H.K. Stelzer, *High-resolution deep imaging of live cellular spheroids with light-sheet-based fluorescence microscopy.* Cell and Tissue Research, 2013. **352**(1): p. 161-177.
22. Nelson, C.M. and M.J. Bissell, *Of Extracellular Matrix, Scaffolds, and Signaling: Tissue Architecture Regulates Development, Homeostasis, and Cancer.* Annual Review of Cell and Developmental Biology, 2006. **22**(1): p. 287-309.
23. Griffith, L.G. and M.A. Swartz, *Capturing complex 3D tissue physiology in vitro.* Nat Rev Mol Cell Biol, 2006. **7**(3): p. 211-224.
24. Abbott, A., *Cell culture: Biology's new dimension.* Nature, 2003. **424**(6951): p. 870-872.
25. Cukierman, E., et al., *Taking Cell-Matrix Adhesions to the Third Dimension.* Science, 2001. **294**(5547): p. 1708-1712.
26. Justice, B.A., N.A. Badr, and R.A. Felder, *3D cell culture opens new dimensions in cell-based assays.* Drug Discovery Today, 2009. **14**(1): p. 102-107.
27. Li, L., et al., *High-throughput Imaging: Focusing In On Drug Discovery in 3D.* Methods (San Diego, Calif.), 2016. **96**: p. 97-102.
28. Clevers, H., *Modeling Development and Disease with Organoids.* Cell, 2016. **165**(7): p. 1586-1597.
29. Graf, B.W. and S.A. Boppart, *Imaging and Analysis of Three-Dimensional Cell Culture Models.* Methods in molecular biology (Clifton, N.J.), 2010. **591**: p. 211-227.
30. Swoger, J., F. Pampaloni, and E.H.K. Stelzer, *Light-Sheet-Based Fluorescence Microscopy for Three-Dimensional Imaging of Biological Samples.* Cold Spring Harbor Protocols, 2014. **2014**(1): p. pdb.top080168.
31. Keller, P.J. and E.H.K. Stelzer, *Quantitative in vivo imaging of entire embryos with Digital Scanned Laser Light Sheet Fluorescence Microscopy.* Current Opinion in Neurobiology, 2008. **18**(6): p. 624-632.
32. *Method of the Year 2014.* Nature Methods, 2014. **12**: p. 1.
33. Olarte, O.E., et al., *Light-sheet microscopy: a tutorial.* Advances in Optics and Photonics, 2018. **10**(1): p. 111-179.
34. Gutiérrez-Heredia, L., P.M. Flood, and E.G. Reynaud, *Light Sheet Fluorescence Microscopy: beyond the flatlands.* Current Microscopy Contributions to Advances in Science and Technology, 2012. **2**: p. 838-847.
35. Weber, M. and J. Huisken, *Light sheet microscopy for real-time developmental biology.* Current Opinion in Genetics & Development, 2011. **21**(5): p. 566-572.
36. Reynaud, E.G., et al., *Light sheet-based fluorescence microscopy: more dimensions, more photons, and less photodamage.* HFSP Journal, 2008. **2**(5): p. 266-275.

37. Keller, P.J., et al., *Digital Scanned Laser Light-Sheet Fluorescence Microscopy (DSLM) of Zebrafish and Drosophila Embryonic Development.* Cold Spring Harbor Protocols, 2011. **2011**(10): p. pdb.prot065839.
38. Huisken, J. and D.Y.R. Stainier, *Selective plane illumination microscopy techniques in developmental biology.* Development (Cambridge, England), 2009. **136**(12): p. 1963-1975.
39. Huisken, J., et al., *Optical Sectioning Deep Inside Live Embryos by Selective Plane Illumination Microscopy.* Science, 2004. **305**(5686): p. 1007-1009.
40. Pitrone, P.G., et al., *OpenSPIM: an open-access light-sheet microscopy platform.* Nature Methods, 2013. **10**(7): p. 598-599.
41. Reynaud, E.G., et al., *Guide to light-sheet microscopy for adventurous biologists.* Nature Methods, 2015. **12**(1): p. 30-34.
42. Greger, K., J. Swoger, and E.H.K. Stelzer, *Basic building units and properties of a fluorescence single plane illumination microscope.* Review of Scientific Instruments, 2007. **78**(2): p. 023909.
43. Elisa, Z., et al., *Technical implementations of light sheet microscopy.* Microscopy Research and Technique, 2017. **0**(0): p. 1-18.
44. Gualda, E.J., et al., *SPIM-fluid: open source light-sheet based platform for high-throughput imaging.* Biomedical Optics Express, 2015. **6**(11): p. 4447-4456.
45. Wang, H., M.L. Russa, and L.S. Qi, *CRISPR/Cas9 in Genome Editing and Beyond.* Annual Review of Biochemistry, 2016. **85**(1): p. 227-264.
46. Carroll, D., *Genome editing: progress and challenges for medical applications.* Genome Medicine, 2016. **8**(1): p. 120.
47. McMahon, M.A., M. Rahdar, and M. Porteus, *Gene editing: not just for translation anymore.* Nature Methods, 2012. **9**(1): p. 28-31.
48. Marx, J., *New Bacterial Defense Against Phage Invaders Identified.* Science, 2007. **315**(5819): p. 1650-1651.
49. Haft, D.H., et al., *A Guild of 45 CRISPR-Associated (Cas) Protein Families and Multiple CRISPR/Cas Subtypes Exist in Prokaryotic Genomes.* PLoS Computational Biology, 2005. **1**(6): p. e60.
50. Barrangou, R., et al., *CRISPR Provides Acquired Resistance Against Viruses in Prokaryotes.* Science, 2007. **315**(5819): p. 1709-1712.
51. Pennisi, E., *The CRISPR Craze.* Science, 2013. **341**(6148): p. 833-836.
52. Bhaya, D., M. Davison, and R. Barrangou, *CRISPR-Cas Systems in Bacteria and Archaea: Versatile Small RNAs for Adaptive Defense and Regulation.* Annual Review of Genetics, 2011. **45**(1): p. 273-297.
53. Zhang, F., Y. Wen, and X. Guo, *CRISPR/Cas9 for genome editing: progress, implications and challenges.* Human Molecular Genetics, 2014. **23**(R1): p. R40-6.
54. Terns, M.P. and R.M. Terns, *CRISPR-based adaptive immune systems.* Current Opinion in Microbiology, 2011. **14**(3): p. 321-327.
55. Mojica, F.J., et al., *Short motif sequences determine the targets of the prokaryotic CRISPR defence system.* Microbiology, 2009. **155**(Pt 3): p. 733-40.

56. Deveau, H., J.E. Garneau, and S. Moineau, *CRISPR/Cas System and Its Role in Phage-Bacteria Interactions.* Annual Review of Microbiology, 2010. **64**(1): p. 475-493.
57. Makarova, K.S., et al., *Evolution and classification of the CRISPR–Cas systems.* Nature Review Microbiology, 2011. **9**(6): p. 467-477.
58. Jinek, M., et al., *A Programmable Dual-RNA–Guided DNA Endonuclease in Adaptive Bacterial Immunity.* Science, 2012. **337**(6096): p. 816-821.
59. Chylinski, K., et al., *Classification and evolution of type II CRISPR-Cas systems.* Nucleic Acids Res, 2014. **42**(10): p. 6091-105.
60. Liu, L. and X.D. Fan, *CRISPR-Cas system: a powerful tool for genome engineering.* Plant Molecular Biology, 2014. **85**(3): p. 209-18.
61. Esvelt, K.M., et al., *Orthogonal Cas9 proteins for RNA-guided gene regulation and editing.* Nature Methods, 2013. **10**(11): p. 1116-1121.
62. Ran, F.A., et al., *In vivo genome editing using Staphylococcus aureus Cas9.* Nature, 2015. **520**(7546): p. 186-191.
63. Cong, L., et al., *Multiplex genome engineering using CRISPR/Cas systems.* Science, 2013. **339**(6121): p. 819-23.
64. Mali, P., et al., *RNA-Guided Human Genome Engineering via Cas9.* Science, 2013. **339**(6121): p. 823-826.
65. Doudna, J.A. and E. Charpentier, *The new frontier of genome engineering with CRISPR-Cas9.* Science, 2014. **346**(6213).
66. Qi, L.S., et al., *Repurposing CRISPR as an RNA-guided platform for sequence-specific control of gene expression.* Cell, 2013. **152**(5): p. 1173-83.
67. Gilbert, L.A., et al., *CRISPR-mediated modular RNA-guided regulation of transcription in eukaryotes.* Cell, 2013. **154**(2): p. 442-51.
68. Perez-Pinera, P., et al., *RNA-guided gene activation by CRISPR-Cas9-based transcription factors.* Nature Methods, 2013. **10**(10): p. 973-6.
69. Mali, P., et al., *CAS9 transcriptional activators for target specificity screening and paired nickases for cooperative genome engineering.* Nature Biotechnology, 2013. **31**(9): p. 833-8.
70. Chavez, A., et al., *Highly efficient Cas9-mediated transcriptional programming.* Nature Methods, 2015. **12**(4): p. 326-328.
71. Tanenbaum, Marvin E., et al., *A Protein-Tagging System for Signal Amplification in Gene Expression and Fluorescence Imaging.* Cell, 2014. **159**(3): p. 635-646.
72. Gilbert, L.A., et al., *Genome-Scale CRISPR-Mediated Control of Gene Repression and Activation.* Cell, 2014. **159**(3): p. 647-61.
73. Tischer, D. and O.D. Weiner, *Illuminating cell signalling with optogenetic tools.* Nature Reviews Molecular Cell Biology, 2014. **15**(8): p. 551-558.
74. Deisseroth, K., *Optogenetics.* Nature Methods, 2011. **8**(1): p. 26-29.
75. Pastrana, E., *Optogenetics: controlling cell function with light.* Nature Methods, 2011. **8**(1): p. 24-25.
76. Beyer, H.M., et al., *Optogenetic control of signaling in mammalian cells.* Biotechnology Journal, 2014. **10**(2): p. 273-283.
77. Muller, K., et al., *Optogenetics for gene expression in mammalian cells.* Biological Chemistry, 2015. **396**(2): p. 145-52.

78. Konermann, S., et al., *Optical control of mammalian endogenous transcription and epigenetic states.* Nature, 2013. **500**(7463): p. 472-6.
79. Polstein, L.R. and C.A. Gersbach, *Light-inducible spatiotemporal control of gene activation by customizable zinc finger transcription factors.* Journal of the American Chemical Society, 2012. **134**(40): p. 16480-3.
80. Muller, K., et al., *A red/far-red light-responsive bi-stable toggle switch to control gene expression in mammalian cells.* Nucleic Acids Research, 2013. **41**(7): p. e77.
81. Müller, K., M.D. Zurbriggen, and W. Weber, *Control of gene expression using a red- and far-red light–responsive bi-stable toggle switch.* Nature Protocols, 2014. **9**(3): p. 622-632.
82. Gupta, R.M. and K. Musunuru, *Expanding the genetic editing tool kit: ZFNs, TALENs, and CRISPR-Cas9.* Journal of Clinical Investigation, 2014. **124**(10): p. 4154-61.
83. Hemphill, J., et al., *Optical Control of CRISPR/Cas9 Gene Editing.* Journal of the American Chemical Society, 2015. **137**(17): p. 5642–5645.
84. Nihongaki, Y., et al., *Photoactivatable CRISPR-Cas9 for optogenetic genome editing.* Nat Biotech, 2015. **advance online publication**.
85. Polstein, L.R. and C.A. Gersbach, *A light-inducible CRISPR-Cas9 system for control of endogenous gene activation.* Nature Chemical Biology, 2015. **11**(3): p. 198-200.
86. Nihongaki, Y., et al., *CRISPR-Cas9-based Photoactivatable Transcription System.* Chemistry & Biology, 2015. **22**(2): p. 169-174.
87. Jain, P.K., et al., *Development of Light-Activated CRISPR Using Guide RNAs with Photocleavable Protectors.* Angewandte Chemie International Edition, 2016. **55**(40): p. 12440-12444.
88. Hughes, R.M., et al., *Light-mediated control of DNA transcription in yeast.* Methods, 2012. **58**(4): p. 385-91.
89. Dunsby, C., *Optically sectioned imaging by oblique plane microscopy.* Optics Express, 2008. **16**(25): p. 20306-20316.
90. Bouchard, M.B., et al., *Swept confocally-aligned planar excitation (SCAPE) microscopy for high-speed volumetric imaging of behaving organisms.* Nature Photonics, 2015. **9**(2): p. 113-119.
91. Cutrale, F. and E. Gratton, *Inclined Selective Plane Illumination Microscopy (iSPIM) adaptor for conventional microscopes.* Microscopy Research and Technique, 2012. **75**(11): p. 1461-1466.
92. Kumar, S., et al., *High-speed 2D and 3D fluorescence microscopy of cardiac myocytes.* Optics Express, 2011. **19**(15): p. 13839-13847.
93. Maioli, V., et al., *Time-lapse 3-D measurements of a glucose biosensor in multicellular spheroids by light sheet fluorescence microscopy in commercial 96-well plates.* Scientific Reports, 2016. **6**: p. 37777.
94. Sikkel, M.B., et al., *High speed sCMOS-based oblique plane microscopy applied to the study of calcium dynamics in cardiac myocytes.* Journal of Biophotonics, 2016. **9**(3): p. 311-323.

95. Voleti, V., et al. *SCAPE microscopy for high-speed volumetric functional imaging of the awake, behaving brain*. in *Biomedical Optics Congress 2016*. 2016. Fort Lauderdale, Florida: Optical Society of America.
96. Sakaue-Sawano, A., et al., *Visualizing Spatiotemporal Dynamics of Multicellular Cell-Cycle Progression.* Cell, 2008. **132**(3): p. 487-498.
97. Hande, K.R., *Etoposide: four decades of development of a topoisomerase II inhibitor.* European Journal of Cancer, 1998. **34**(10): p. 1514-1521.
98. Heck, M.M., W.N. Hittelman, and W.C. Earnshaw, *Differential expression of DNA topoisomerases I and II during the eukaryotic cell cycle.* Proceedings of the National Academy of Sciences of the United States of America, 1988. **85**(4): p. 1086-1090.
99. Sakaue-Sawano, A., et al., *Drug-induced cell cycle modulation leading to cell-cycle arrest, nuclear mis-segregation, or endoreplication.* BMC Cell Biology, 2011. **12**: p. 2-2.
100. Laurent, J., et al., *Multicellular tumor spheroid models to explore cell cycle checkpoints in 3D.* BMC Cancer, 2013. **13**(1): p. 73.
101. Brieke, C., et al., *Light-Controlled Tools.* Angewandte Chemie International Edition, 2012. **51**(34): p. 8446-8476.
102. Gao, Y., et al., *Complex transcriptional modulation with orthogonal and inducible dCas9 regulators.* Nature Methods, 2016. **13**: p. 1043.
103. Johnson, H.E. and J.E. Toettcher, *Illuminating developmental biology with cellular optogenetics.* Current Opinion in Biotechnology, 2018. **52**: p. 42-48.
104. Beyer, H.M., et al., *Red Light-Regulated Reversible Nuclear Localization of Proteins in Mammalian Cells and Zebrafish.* ACS Synthetic Biology, 2015. **4**: p. 951-958.
105. Levskaya, A., et al., *Spatiotemporal control of cell signalling using a light-switchable protein interaction.* Nature, 2009. **461**(7266): p. 997-1001.
106. Toettcher, J.E., et al., *Light control of plasma membrane recruitment using the Phy–Pif system.* Methods in Enzymology, 2011. **497**: p. 409-423.
107. Maeder, M.L., et al., *CRISPR RNA-guided activation of endogenous human genes.* Nature Methods, 2013. **10**(10): p. 977-9.
108. Braff, J.L., et al., *Characterization of Cas9–Guide RNA Orthologs.* Cold Spring Harbor Protocols, 2016. **2016**(5): p. 422-425.
109. Ma, H., et al., *Multicolor CRISPR labeling of chromosomal loci in human cells.* Proceedings of the National Academy of Science of the USA, 2015. **112**(10): p. 3002-3007.
110. Müller, K., et al., *Multi-chromatic control of mammalian gene expression and signaling.* Nucleic Acids Research, 2013. **41**(12): p. e124.
111. Müller, K., et al., *Orthogonal Optogenetic Triple-Gene Control in Mammalian Cells.* ACS Synthetic Biology, 2014. **3**(11): p. 796-801.
112. Kaberniuk, A.A., A.A. Shemetov, and V.V. Verkhusha, *A bacterial phytochrome-based optogenetic system controllable with near-infrared light.* Nature Methods, 2016. **13**(7): p. 591-597.